The Dissertation Committee for Evan Joseph Ramos
certifies that this is the approved version of the following dissertation:

# Toward a Mechanistic Understanding of Silicate Weathering and Li Transfer Across Landscapes, Past and Present

Committee:

Daniel O. Breecker, Co-Supervisor

Jaime D. Barnes, Co-Supervisor

Daniella M. Rempe

Joel P.L. Johnson

Brady Z. Foreman

# Toward a Mechanistic Understanding of Silicate Weathering and Li Transfer Across Landscapes, Past and Present

by

**Evan Joseph Ramos**

**Dissertation**

Presented to the Faculty of the Graduate School of

The University of Texas at Austin

in Partial Fulfillment

of the Requirements

for the Degree of

**Doctor of Philosophy**

**The University of Texas at Austin**

August 2021

To Patricia and Joseph, Matthew and Diane

# Acknowledgments

Making it out on the other side of PhD, at least partially intact and not completely jaded, is no small feat. But as I ruminate on my graduate career, I feel less responsible for my accomplishments and more so incredibly fortunate to have been surrounded by such supportive, intelligent, generous, funny, and kind people during this time. My growth and successes during my PhD are tied directly to this support system, and that cannot go without mention.

To my advisers, Dan and Jaime: you have been such immense sources of support and inspiration. I began my PhD with loose ideas of what I wanted to research, and you both effectively allowed me to stay in a holding pattern for year as I narrowed my interests. In many ways, this freedom you encouraged conveyed to me that you believed in my abilities as a scientist when I didn't necessary believe in myself. I always felt that I was your priority even though you both had countless other responsibilities as professors and as parents. You effectively adopted me as your surrogate science son, and the fact that you let me crash your family vacations in order to sample skarns in the Sierra Nevada and paleosols in the Bighorn Basin is a testament to that. Grad school is colored significantly by student-adviser relationships, and I am one of the lucky students who had kind and encouraging advisers. I hope that if I advise my own students that I can foster as excellent, positive, and inclusive spaces as you both have. Thank you for all that you do.

I'm fairly certain that I have assembled the nicest PhD committee of all

time. Collectively, they have bolstered my science and given me timely and careful attention. To Daniella, who actively included me in her research group meetings, made plenty of time to field my questions, gave practical advice about developing healthy work habits as an academic, and who ceaselessly burst with ideas that have propelled me down various rabbit holes; to Brady, whose feedback at a workshop and generous sharing of samples led to an entire chapter of my dissertation and who, without fail, provided swift and careful scientific feedback (embodied by returning me comments on Chapter 4 *while* doing fieldwork in 100° weather); and to Joel, who asked both the hardest and most important questions during my qualifying exam and subsequent committee meetings, gave me informal lessons on geomorphology at critical junctures when I was completing Chapter 2, and always had an open door and welcomed my questions; I am indebted to your support. Thank you all so much.

I've also been lucky to work among wonderful people in the Jackson School and at other institutions. Many faculty, researchers, and peers have left a mark and enriched my grad school experience: Marc Hesse, whose mentorship as my co-adviser during my MS fundamentally shifted the way I approach scientific problem solving; Staci Loewy, Aaron Satkoski, and John Lassiter, who graciously included me in their laboratories and through which allowed us to get Li isotope chemistry up and running at UT; Julia Clarke, whose course *Curiosity to Question* helped me approach manuscript writing more methodically and whose workshops were the first spaces I felt comfortable discussing my personal difficulties in graduate school, including dealing with imposter syndrome; Ginny Catania, whose course *Preparing Future Faculty* got my butt into gear when planning for job applications and whose establishment of the *Geoscience Empowerment Network* made a lasting impact on me in what I prioritize as a scientist; Rowan Martindale, who led the "Postdoc Party" last year that helped me land a job and whose leadership through *URGE* helped create safe spaces to discuss racism in the geosciences that uniquely fostered

bonds across broad constituencies in the Jackson School, from staff to undergrads to tenured faculty; current and past members of Barnes/Breecker/Hesse research groups – especially Jake Jordan, Michelle Gevedon, Jeff Cullen, Miguel Cisneros, Grace Beaudoin, Natasha Sekhon, and Fangliang Li – whose friendship, assistance, and willingness to goof off made group meetings fun and the occasional drudgery of research more tolerable; researchers at other institutions, particularly Scott Wing and Philip Gingerich, who provided scientific and logistical assistance during my field seasons in the Bighorn Basin and included me among the PETM cohort; members of the GeoFORCE staff, namely Dana Thomas and John Hash, who gave me opportunities to teach high schoolers and through which enriched me in ways that research often could not; educational team members of GeoFORCE academies, including Alissa Kotowski, Nick Soltis, and Enrique Reyes, who showed me how to engage students, act as an effective leader, and share responsibilities on an educational team; the countless other staff who helped me as a student, TA, and as an officer for GSEC, including Patrick Stafford, Camille Barraza, Georgia Sanders, and Kristen Tucek; and lastly, Philip Guerrero, who is the literal foundation of the Jackson School, who has staunchly advocated for me and graduate students in countless ways, who has saved my butt many times when I've absentmindedly forgotten to submit forms, and who I am lucky to call a friend. Sorry that we were never able to advance to the intramural softball playoffs, PG (go Austin Sed Rox!).

To my cat Beatrice: adopting you was the best impromptu decision I've ever made and I'm excited you'll be making the trip with me to Houston. Please, do not mess up my new furniture.

In my undergraduate and MS theses, I commemorated the music that I was listening to that helped me through the long nights of writing. In that spirit, here's an exhaustive list of the artists and albums that have kept me afloat during my PhD, some of whom I was lucky enough to see living in the live music hub of

Austin (sorry, this is more for me than for whoever else reads this): Frank Ocean's *Blonde*, Kendrick Lamar's *To Pimp a Butterfly*, *Untitled Unmastered*, and *DAMN.*, Fleet Foxes' *Crack-Up* and *Shore*, Alex G's *Rocket* and *House of Sugar*, My Bloody Valentine's *Loveless* and *m b v*, Badbadnotgood and MGMT's *LateNightTales* mixes, Dehd's *Flower of Devotion*, Deafheaven's *New Bermuda* and *Sunbather*, Iceage's *Plowing Into the Field of Love* and *You're Nothing*, Japenese Breakfast's *Jubilee* and *Soft Sounds From Another Planet*, Floating Point's *Eleania*, Boards of Canada's *Music Has The Right To Children*, DJ Koze's *Knock Knock*, Kanye West's *The Life of Pablo*, *My Beautiful Dark Twisted Fantasy* and *Yeezus*, Warehouse's *super low*, Freddie Gibbs and Madlib's *Bandana*, Hamilton Leithauser + Rostam's *I Had a Dream That You Were Mine*, The Avalanches's *Wildflower* and *Since I Left You*, Kamasi Washington's *The Epic* and *Heaven and Earth*, Yves Tumor's *Heaven To A Tortured Mind*, The Clientele's *Suburban Light*, Kaytranada's *99.9%* and *BUBBA*, The Microphone's *The Glow, Pt. 2* and *Microphones in 2020*, Mount Eerie's *A Crow Looked at Me*, Mannequin Pussy's *Patience*, Solange's *A Seat at the Table* and *When I Get Home*, Empath's *Active Listening: Night on Earth*, Joni Mitchell's *Blue* and *The Hissing of Summer Lawns*, Angel Olsen's *MY WOMAN*, Grimes's *Art Angels*, Neon Indian's *Vega Intl. Night School*, *Era Extaña*, and *Psychic Chasms*, Oso Oso's *basking in the glow*, Vince Staples' *Summertime '06* and *Big Fish Theory*, Tirzah's *Devotion*, Prince's *Sign O' The Times*, Saba's *CARE FOR ME*, Kevin Morby's *City Music*, R.E.M.'s *Murmur*, The Radio Dept.'s *Clinging to a Scheme*, Sampha's *Process*, Floating Points, Pharoah Sanders, and the London Symphony Orchestra's *Promises*, Soccer Mommy's *Clean*, Joey Purp's *iiiDrops*, Snail Mail's *Lush*, Lomelda's *Hannah*, Fuck Buttons's *Tarot Sport*, The Cure's *Disintegration*, Kaitlyn Aurelia Smith's *The Kid*, Radiohead's *In Rainbows*, Skee Mask's *Compro*, Tame Impala's *Currents*, A Tribe Called Quest's *Midnight Marauders* and *We Got It From Here ... Thank You 4 Your Service*, Jay Reatard's *Blood Visions*, Stereo-

lab's *Dots And Loops* and *Emperor Tomato Ketchup*, Thundercat's *Drunk*, Spirit of the Beehive's *Hypnic Jerks*, Tyler, The Creator's *Flower Boy* and *Call Me If You Get Lost*, Fiona Apple's *Fetch The Bolt Cutters*, Stella Donnelly's *Beware of the Dogs*, Moses Sumney's *Aromanticism* and *græ*, Jay Som's *Everybody Works*, The Internet's *Ego Death*, Wu Lyf's *Go Tell Fire To The Mountains*, Wilco's *Ode to Joy*, Amen Dunes's *Freedom*, Big Thief's *U.F.O.F.*, Gorillaz's *Plastic Beach*, The War on Drug's *A Deeper Understanding*, Teeb's *Anicca*, Crack Cloud's *Pain Olympics*, Jeff Parkers's *Suite for Max Brown*, Deerhunter's *Halcyon Digest*, Charly Bliss's *Young Enough*, Clairo's *Immunity*, Cocteau Twins's *Heaven or Las Vegas*, George Clanton's *Slide*, Kacey Musgraves's *Golden Hour*, Yo La Tengo's *I Can Hear The Heart Beating As One* and *There's A Riot Going On*, Faye Webster's *Atlanta's Millionaires Club* and *I Think I'm Funny haha*, Bon Iver's *22, A Million* and *i,i*, Animal Collective's *Feels*, Blood Orange's *Freetown Sound*, Crumb's *Jinx*, Jamie xx's *In Colour*, Brittany Howard's *Jaime*, King Geedorah's *Take Me To Your Leader*, Steve Lacy's *Steve Lacy's Demo*, Nick Hakim's *Green Twins*, Hovvdy's *Cranberry* and *Heavy Lifter*, Mount Kimbie's *Love What Survives*, King Krule's *The OOZ*, FKA twigs's *MAGDALENE*, Anderson .Paak's *Malibu*, Dry Cleaning's *New Long Leg*, Makaya McCraven and Gil Scott-Heron's *We're New Again*, Ariel Pink's *pom pom* and *Dedicated to Bobby Jameson*, Phoebe Bridger's *Punisher*, Nicolas Jaar's *Sirens*, Earl Sweatshirts *Some Rap Songs* and *Doris*, Beach Fossil's *Somersault*, Christian Scott's *Ancestral Recall*, M83's *Hurry Up, We're Dreaming*, Toro Y Moi's *Outer Peace*, Girlpool's *What Chaos Is Imaginary*, LCD Soundsystem's *Sound of Silver*, The Stroke's *Is This It*, Caribou's *Suddenly*, Helado Negro's *This Is How You Smile*, Noname's *Telefone*, Beach House's *7*, Youth Lagoon's *Wondrous Bughouse*, and Nx-Worries's *Yes Lawd!*.

Good friends are really hard to come by, and I've happened to make some of my best friends here at UT. First there's the "JSG Hall of Fame", which includes J.J.

Muñoz, Simon Scarpetta, Patrick Boyd, Tom Etzel, Nick Ettinger, Will Pinkston, and Lily Serach (honorary member), who were the first friends I made starting as a graduate student in 2015 and who are now some of my closest friends. Our bonds have been forged through collective struggle and festivities (typically involving Nick's Caesars) in our time as grad students, and I'm so thankful that I'll be living near some of you when I move to Houston. Then there are the "fourteeners", especially Sarah George, Tomas Capaldi, Margo Odlum, Chelsea Mackaman-Lofland, Jenny Harding, and Max Daniller-Varghese, who all had a year of grad school under their belts when I started and quickly became close friends and mentors to me. Whether it was at Backlot (fka Nasty's), Crown & Anchor, Growler USA, Lazarus, The Side Bar, Cheer Up Charlie's, Hotel Vegas, Barracuda, Barbarella's, or the Mohawk, we had fun times wherever we went. You all showed me how to make the most of grad school and I'm lucky to call you all friends. In addition to these folks, there is the posse of "Chicken Street", which includes Sophie Goliber, Scott Eckley, Brad Post, Sam Robbins, Stephen Ferencz, and Grace Guryan (among many of those aforementioned), whose friendship is tied closely to the dump of a house we all lived in for some stretch of time. You were all great friends and once the pandemic was in full swing, our bonds only ossified. The only great thing about us disbanding from the house and moving elsewhere is that I'll have cool places to visit. And lastly, there are my friends from high school who I've remained close with despite the distance between Texas and New York, especially Gus Kivotidis, Nick DeStefano, Andrew Flanagan, Matt Ogden, and Alex Toto. Whether in NY over the holidays or in Austin during your visits, our time spent together while I was in grad school grounded me and felt like reconnecting with my roots. People outside of NY don't talk nearly as much smack as you all, and I miss that big time. You guys are a special lot.

Lastly, to my wild and wonderful family: I could not have submitted myself to

this degree without your love and encouragement. Fortunately, my mom's cousins Janet and Nicole and their husband's Terry and Charles live in Austin and were amazing sources of comfort and escape. For the most part, though, moving away from NY meant limiting time with my closest family. Thankfully, our connections never dimmed. To my brother and sister, Cruz and Colleen, and my step siblings, Rita, Elizabeth, and Madison: your love means more than anything to me. Our get-togethers around Christmas have lifted my spirits, and I'm excited to see you all this Christmas after our pandemic-related hiatus. To my grandma, Evelyn: you are the best person I know and it's not even close. Not every 90-year-old can survive COVID and speak about it like it was water under the bridge. I have always looked up to you, and your profound goodness is inspirational. I love you like mad. And lastly, to my mom and dad, Patricia and Joseph, and my stepparents, Diane and Matt: you've given me more than I can ever repay. Even if you don't care about soils and the carbon cycle, all of my work herein and all that I will do is dedicated to you.

Evan Joseph Ramos

*The University of Texas at Austin*
*August 2021*

# Toward a Mechanistic Understanding of Silicate Weathering and Li Transfer Across Landscapes, Past and Present

Publication No. _____

Evan Joseph Ramos, Ph.D.
The University of Texas at Austin, 2021

Supervisors: Daniel O. Breecker, Jaime D. Barnes

Silicate weathering is a fundamental process that sculpts landscapes, provides nutrients for organisms, underpins life-sustaining biogeochemical cycles on Earth, and keeps Earth from entering a runaway greenhouse state. This process is influenced by the geologic and environmental conditions at the Earth's surface, therefore uniting many traditional geoscience subdisciplines and being an area of active research for nearly a century. It has been studied through observations of drainage catchments on continents, where most silicate weathering on Earth happens today. The geologic record also served as an important archive of this process, invariably recording the

conditions and processes occurring at the Earth's surface in the past and allowing for observations on timescales that studies of modern environments do not permit. Despite advancements in the process-based understanding of silicate weathering, considerable debate remains regarding its primary drivers, the relevance of silicate weathering in the evolution of Earth's climate, and the degree with which known modulators of silicate weathering can be constrained independently of one another.

The central focus of this dissertation is to expand upon the utility of lithium (Li) isotopes: a burgeoning isotope system that, when measured in geologic material, allows for a quantitative assessment of silicate weathering over a range of timescales. The dissertation is composed of three case studies which test the viability of Li isotopes in discerning the controls of silicate weathering, both in past and present environments. In turn, these studies help identify controls of silicate weathering in different Earth surface environments. The outcome of these studies are conceptual or mechanistic models for silicate weathering that either i) provide constraints for its controls or ii) yield a template with which to probe it with Li isotopes and other measurements.

# Contents

# List of Tables

# List of Figures

# Chapter 1

# Introduction

## 1.1 Silicate weathering

The geologic carbon cycle is governed by the transfer of carbon between the solid Earth and its overlying oceans, atmosphere, and biosphere. As carbon degasses from Earth's interior and accumulates in the exosphere, several mechanisms return carbon back to the solid Earth and allow Earth's surface to remain habitable throughout Earth's history. One such mechanism is the chemical weathering of silicate minerals in Earth's crust: a process which is relevant to climate modulation over $10^5$- and $10^6$-year timescales. When exposed to acid-bearing water (typically carbonic acid), silicate minerals are leached of monovalent and divalent cations (e.g., $Na^+$, $K^+$, $Mg^{2+}$, $Ca^{2+}$) that either remain in solution or are incorporated into authigenic (secondary) minerals. This alkalinity in water, when supplied to the ocean by rivers or through groundwater discharge, favors the formation of marine carbonates (mineral formula $(Ca,Mg)CO_3$) which acts as a net sink of atmospheric $CO_2$. This sequestration of $CO_2$ by silicate weathering is thus thought of as a climate stabilizer by counteracting excess input of $CO_2$ from the solid Earth. Studies of both modern and ancient surface environments, in addition to controlled experiments, have enabled the development of constitutive equations for silicate weathering.

### 1.1.1 Difficulties with silicate weathering in the modern

The loci of weathering on Earth include soils, fractured bedrock, and subaqueous continental margins, encompassing a large range of environmental and geologic conditions. At a fundamental level, however, silicate weathering is linked to the chemical and physical environment in which the reactions are taking place. The geometry and composition of weathering environments, alongside the nature of water-rock interactions therein, is influenced by climate, atmospheric $CO_2$ concentrations, tectonics, rock types, and terrestrial biota. These myriad factors and their effects on silicate weathering are encoded in surface environments today, as evidenced by the chemistry of river water and soils and the morphology of landscapes. Yet, it has been a longstanding challenge to independently distinguish these modulators from one another, and whether certain processes trump others in their influence on silicate weathering.

The development of new isotope systems, such as lithium (Li) isotopes, have greatly advanced our quantitative understanding of silicate weathering. Many traditional measurements like elemental concentration measurements of river water, although quantitative in nature, are often impacted by non-silicate element input that can make quantitative analyses of silicate weathering difficult. The use of non-traditional isotope systems, alongside common measurements, have led to an increasingly quantitative and nuanced understanding of silicate weathering, usually at the catchment scale. Results from these studies are like a tapestry, offering insights into the fundamental processes that influence that isotope system (such as Li isotopes) but not necessarily providing a comprehensive assessment of the processes or conditions that unify these varied results. Piecing together these findings is imperative for deducing primary controls of silicate weathering and imposing silicate weathering in global-scale Earth systems models of the carbon cycle.

### 1.1.2 Difficulties with silicate weathering in the past

The geologic record is composed of sedimentary rocks that variably document Earth surface conditions and silicate weathering. Unlike the modern, the geologic record permits a long-term (i.e., $> 10^4$ year) assessment of silicate weathering and an exploration of silicate weathering when the geologic, environmental, and biological conditions of the Earth were fundamentally different. However, several complications arise when interrogating the geologic record, such as the relative paucity of sedimentary rocks compared to modern surface environments, the stochasticity of what is preserved, and the potential biases (e.g., seasonal bias in mineral formation, bias of landscape elements preserved) of these records. These complications not only affect the interpretation of weathering-sensitive geochemical proxies (e.g., Li isotopes) but also obscure the interpretation of proxy data that inform environmental (e.g., mean annual precipitation and temperature) and geologic (e.g., sediment provenance) conditions at the Earth's surface in the past.

Despite these challenges, novel isotope measurements have reduced ambiguity in these records. Unlike traditional silicate weathering indices (e.g., Chemical Index of Alteration, Chemical Index of Weathering, $\sum$Bases/Al, smectite crystallinity index) that only qualitatively convey the intensity of silicate weathering, these new measurements can provide quantitative constraints on silicate weathering that illuminate potential controls and provide quantities (e.g., silicate weathering fluxes) that can be utilized in global carbon cycle models. Studies that have applied Li isotopes to sedimentary archives (e.g., Bastian et al., 2017; Dosseto et al., 2015) underscore the utility of these measurements in identifying silicate weathering controls, but more studies of ancient environments with Li isotopes are warranted to further parameterize silicate weathering over a wider range of environmental and geologic conditions. Moreover, the study of sedimentary rocks can enable broader spatial and temporal observations that would be otherwise prohibitive in the modern.

## 1.2 Overview of silicate weathering case studies

The central objectives of this dissertation are twofold: 1) to expand our understanding of silicate weathering by applying new Li isotopes in untested geologic settings and 2) to improve on the utility of Li isotopes to probe controls of silicate weathering. Importantly, these chapters aim to bridge knowledge gaps in our understanding of the long-term and modern day processes involved in silicate weathering by studying both ancient and modern weathering environments.

### 1.2.1 Li isotope compositions of river water informed by catchment properties

The past 30 years have seen the advancement and widespread use of Li isotope measurements of river water to discern the "style" of silicate weathering occurring within a drainage catchment. Because it is not fractionated directly by terrestrial organisms (Clergue et al., 2015; Pogge von Strandmann et al., 2016; Lemarchand et al., 2010; Schmitt et al., 2012) and is found predominantly in silicate minerals (e.g., Kisakűrek et al., 2005), Li and its isotopes are thought to be direct tracers of silicate weathering. Broadly, Li isotopes in river water are found to reflect the catchment-scale balance of congruent (solely mineral dissolution) and incongruent (mineral dissolution and secondary mineral formation) weathering reactions. The formation of secondary clays (or lack thereof) adequately explains the global distribution of reported Li isotope compositions. Yet, there are many proposed drivers of weathering congruency, including temperature, precipitation, lithology, fluid/mineral residence times, and weathering intensity. Chapter 2 represents a first attempt at synthesizing a global dataset of published river water Li isotope compositions and assessing what environmental/geologic conditions and processes can best explain the range of observations.

Through the compilation of these published data and the determination of

catchment-average climatic, lithologic, and morphometric properties for each river water sample, Chapter 2 evaluates how river water Li isotope compositions directly compare to catchment properties and how catchment properties compare to one another. This chapter utilizes statistical tools to gauge the significance of these relationships and subsequently employs numerical models of silicate weathering and Li isotope transfer to relate catchment properties with surface processes. What amounts from this study is a conceptual model (informed by theory and observations) that describes how river water Li isotope compositions change along the length of a river, from mountainous headwater catchments to peneplains farther downstream. Further, this study offers new hypotheses for drivers of silicate weathering and Li transfer in low-relief environments. These findings have been submitted as a revised manuscript to *Geochimica et Cosmochimica Acta* and are currently under review.

### 1.2.2 Rapid silicate weathering response in floodplains during the Paleocene-Eocene Thermal Maximum

During hyperthermal events in Earth's history, where massive amounts of $CO_2$ are injected from the solid Earth into the exposphere over geologically rapid ($10^4$-$10^5$ years) timescales, silicate weathering is observed to offset the massive $CO_2$ input. Most of these findings are derived from evidence of marine sedimentary rocks and Earth systems models, but there is comparatively little work chronicling the silicate weathering response on land during these hyperthermal events. With limited observations of these nonmarine archives, nuances of silicate weathering responses on land are overlooked. Chapter 3 seeks to expand our understanding of silicate weathering across the Paleocene-Eocene Thermal Maximum (PETM): a hyperthermal event that is often used as an analogue for anthropogenically induced climate change today.

By analyzing the elemental and Li isotope composition of ancient floodplain deposits in the Bighorn Basin, Wyoming (USA) that span the PETM, and comparing their composition to those of bedrock in the basin, this chapter documents changes in silicate weathering intensity during an abrupt change in climate. These measurements reveal a rapid and sustained increase in silicate weathering in response to the climatic perturbation, even after global climate has returned to its pre-perturbed state. Furthermore, these data, when contextualized alongside sedimentological features contained in the sedimentary deposits, show that this weathering response occurs within floodplains and that the magnitude of the response varies based on where the sediments were deposited in the paleo-floodplain. These findings newly demonstrate that weathering in floodplains actively responds to climate change and further reinforce the utility of Li isotopes in discerning weathering mechanisms. A manuscript containing these results is being prepared for submission to *Nature Geosciences*.

### 1.2.3 Sediment transport and silicate weathering in the Huerfano Basin (Colorado, USA) during the latest Paleocene and Early Eocene

Along with the Bighorn Basin (subject of Chapter 3) are a series north-south trending Laramide basins which variably contain Paleocene and Eocene-aged sedimentary deposits. One such basin is the Huerfano Basin which had a markedly similar climate to the Bighorn Basin during the early Paleogene (Sewall and Sloan, 2006). The Huerfano Basin differs with the Bighorn Basin in that it contains sediments sourced strictly from crystalline bedrock. Therefore, in discerning the controls of silicate weathering in the Huerfano Basin, Chapters 3 and 4 implicitly interrogate the role of lithology in silicate weathering.

Chapter 4 employs similar techniques utilized in Chapter 3, namely major

and trace element concentration measurements and Li isotope analyses. This chapter expands upon the previous chapter by analyzing both channel sandstones and overbank deposits (as opposed to solely overbank deposits in the previous chapter) to probe for influences of sediment transport and sediment chemistry on up-section weathering trends. These data, alongside published bedrock elemental concentrations and sedimentological information, yield two primary findings: 1) overbank deposits are derived from mafic-through-intermediate source rocks whereas channel sandstones are derived from intermediate-through-felsic source rocks; 2) despite inherent difference in source rock lithology, overbank and channel-fill deposits follow similar up-section trends in weathering proxies. These findings suggest that there was very little silicate weathering occurring in the basin during the Paleocene and Eocene. We posit the limited weathering is the result of two plausible mechanisms: 1) poor landscape stability (i.e., high river channel mobility) imposed by the lack of sediment cohesion among source sediments concomitant with low fluid flow in floodplain soils; 2) large sediment fluxes into the floodplain from the hinterland that either buried sediments faster than they can weather or bypassed the depositional system rapidly. Furthermore, these findings illustrate that source rock Li isotope compositions can impose a primary influence on sediment chemistry. These findings are currently being prepared for submission to a peer-reviewed journal.

# Chapter 2

# Li isotope composition of river water informed by catchment properties

The Li isotope composition of river water is a measure of the congruency of silicate weathering throughout a drainage catchment. The properties of drainage catchments that modulate the congruency of silicate weathering and transfer of Li across landscapes – including climate, lithology, morphometrics, and weathering intensity – have been individually discussed in previous studies, but not considered wholesale. In this study, we amass a global dataset of published river water Li isotope compositions (n = 757) and determine mean drainage catchment properties to test the hypothesis that weathering intensity, and not individual catchment properties, drives the range of globally observed river water $\delta^7$Li values. First, through linear regressions and analysis of variance, we find that although river water $\delta^7$Li values are not significantly correlated with individual catchment properties, the coupling of either climatic (mean annual temperature and precipitation) or morphometric (mean local relief, catchment area, and mean hillslope angles) properties with lithologic (rock type proportions) properties produce significant correlations (p-value $< 0.05$), underscoring the necessity of multiple catchment properties to describe the global range of river water $\delta^7$Li values. Second, to assess the empirical relationship

between river water $\delta^7$Li values and weathering intensity, we compute catchment-wide erosion and silicate weathering fluxes for all samples using both a steady-state and time-dependent weathering model. Although spanning a broad range of environments, all samples in the steady-state weathering model are predicted to have weathering intensities $< 10^{-1}$, which are values associated with high-relief, kinetically limited weathering environments. The time-dependent model, in contrast, ably predicts weathering intensities $> 10^{-1}$, often associated with low-relief, supply-limited weathering environments, but seldom predicts intensities $< 10^{1}$. Among the samples from the dataset that also have independent weathering intensity measurements, we discern that the steady-state model increasingly underestimates predicted weathering intensity as reported weathered intensity increases; in contrast, the time dependent model consistently overestimates weathering intensity, but approaches parity near high reported weathering intensities. These predictions, in conjunction with catchment properties, showcase the effects of plausible denudation mechanisms on river water $\delta^7$Li values; moreover, they suggest that the relationship between river water $\delta^7$Li values and weathering intensity may not be time-transgressive, having implications for how we interpret the secular evolution of ocean water $\delta^7$Li values.

## 2.1 Introduction

Chemical weathering of silicate minerals is a process that plays a central role in life-sustaining element cycles and the modulation of Earth's climate on million-year time scales (e.g., Berner et al., 1983; Chamberlin, 1899; Hilton and West, 2020; Urey, 1952; Walker et al., 1981). Stable lithium (Li) isotope measurements are gaining traction across the geosciences in part due to their increasing utility as a direct proxy for silicate weathering, which is underscored by three critical observations: (1) Li is predominantly found in silicate minerals (e.g., Kisakűrek et al., 2005); (2) Li partitioning and isotope fractionation are largely driven by the

formation of secondary minerals (such as clay minerals and sesquioxides) from the incongruent weathering of primary silicates, where $^{6}$Li is preferentially incorporated over $^{7}$Li into the surface and crystallographic sites of secondary minerals (Hindshaw et al., 2019; Pistiner and Henderson, 2003; Tardy et al., 1972; Vigier et al., 2008; Wimpenny et al., 2010); and (3) Li isotopes undergo no direct fractionation by the terrestrial biomass, including rooting plants and algae (Clergue et al., 2015; Lemarchand et al., 2010; Pogge von Strandmann et al., 2016; Schmitt et al., 2012). The sensitivity of Li isotope transfer to secondary mineral formation has fostered advances in our quantitative understanding of the congruency of silicate weathering in modern surface environments and in the geologic past (e.g., Dellinger et al., 2015, 2017; Pogge von Strandmann et al., 2017b,c and references therein).

The catchment-wide balance of congruent and incongruent silicate weathering yields a $>$ 40‰ range of river water $\delta^{7}$Li values (Tomascak et al., 2016; Fig. 2.1A), hereon denoted as $\delta^{7}\mathrm{Li}_{f}$ (subscript f corresponds to "fluid"). As acid-bearing fluids flow through the Critical Zone, they chemically react with exposed minerals and discharge solutes into rivers. The alkalinity of river water thus reflects an integrated signature of chemical weathering occurring throughout a drainage catchment. In catchments where congruent weathering of silicates dominates and secondary mineral formation is suppressed, $\delta^{7}\mathrm{Li}_{f}$ values are low and approach those of catchment rocks (average value of $0 \pm 5$ ‰; Teng et al., 2004; Sauzéat et al., 2015). Contrarily, when $^{6}$Li from water is preferentially incorporated into newly formed secondary minerals, $\delta^{7}\mathrm{Li}_{f}$ values can reach values as high as $\sim$ 25 ‰, in accordance with equilibrium fractionation factors between water and secondary phyllosilicates at Earth surface temperatures (Vigier et al., 2008). Batch (closed-system) fractionation or Rayleigh (open-system) fractionation (e.g., Bouchez et al., 2013) can yield $\delta^{7}\mathrm{Li}_{f}$ values between these congruent and incongruent weathering endmember scenarios. Rayleigh fractionation, likely mediated by open-system fluid flow (e.g., Bohlin and

Bickle, 2019) and continuous removal of weathering product can drive $\delta^7\text{Li}_f$ values $> 40$ ‰ which exceed reported water-clay per mil fractionation factors (17-20 ‰; Vigier et al., 2008). Adsorption of Li to surface sites can also increase $\delta^7\text{Li}_f$ values, but the low fraction of aqueous Li ($\approx$ 5–16 %) that is adsorbed compared to Li that is crystallographically incorporated suggests it minimally affects $\delta^7\text{Li}_f$ values (Li et al., 2020; Pogge von Strandmann et al., 2019). These endmember models adequately describe observed ranges of $\delta^7\text{Li}_f$ values in previous studies, but the environmental or geologic conditions for which these models apply – including climate, tectonics, rock type, and landscape morphometrics – remain actively debated.

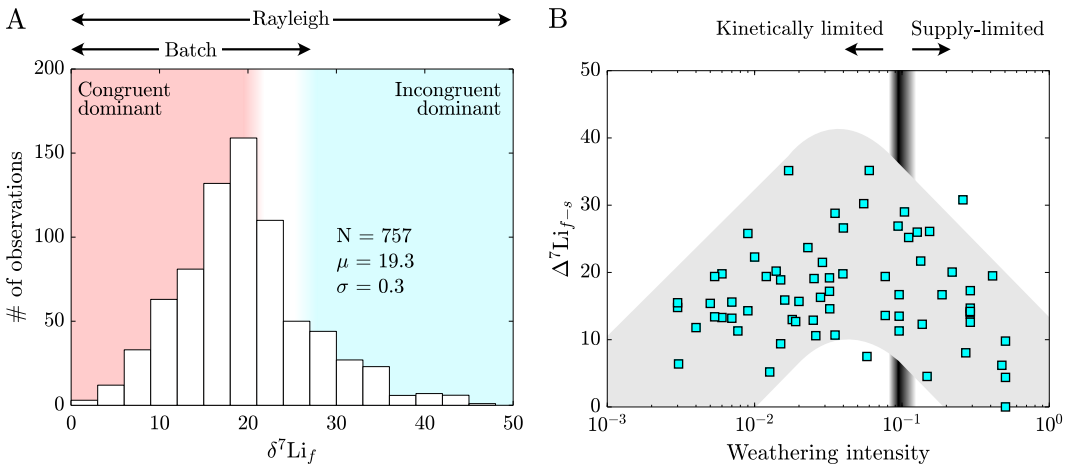


Figure 2.1: (A) Histogram of published river water $\delta^7$Li values with sample population $N$, population mean $\mu$, and standard error $\sigma$ inset. Domains for weathering congruency are listed and the ranges over which Rayleigh and batch fractionation models are indicated by arrows above the histogram plot. (B) Empirical relationship between river water $\delta^7$Li values (presented relative to source rock $\delta^7$Li values) and weathering intensity (Dellinger et al., 2015). The black vertical band corresponds to the boundary between kinetically limited and supply-limited weathering regimes (Dellinger et al., 2017; West et al., 2005).

Climate is canonically invoked as primary driver of silicate weathering and thus has been attributed as a control in Li isotope studies. Application of Li isotopes to sediment and speleothem paleoclimate records reveal inverse correlations between

$\delta^7$Li values and $\delta^{18}$O archives from benthic sediments and ice cores (Dosseto et al., 2015; Pogge von Strandmann et al., 2017b; Ryu et al., 2014). Coupled $\delta^7$Li and $\delta^{18}$O values suggest that changes in the congruency of silicate weathering are in accordance with Milankovitch climate cycles, where hot and wet interglacial periods enhance congruent weathering and cold and dry glacial periods subdue congruent weathering (Pogge von Strandmann et al., 2020). These studies that employ Li isotopes mostly attribute temperature variations as the cause for $\delta^7$Li variations, but the monotonic relationships among precipitation, temperature, and silicate weathering fluxes imply that precipitation could also be responsible for this variation (Godsey et al., 2009; Ibarra et al., 2016; Kump et al., 2000; Maher and Chamberlain, 2014). When modern weathering environments are considered, the influence of climate on $\delta^7\text{Li}_f$ values become less clear. For example, seasonal variations in river discharge causes perceptible changes in $\delta^7\text{Li}_f$ values (e.g., Gou et al., 2019; Henchiri et al., 2016), but the range of $\delta^7\text{Li}_f$ values that are observed are less than the entire range of $\delta^7\text{Li}_f$ values found in large river systems. Moreover, transcontinental river systems at high and low latitudes exhibit a similarly wide range of $\delta^7\text{Li}_f$ values despite their distinct differences in climate (Murphy et al., 2019). These observations imply that variations in climate cannot fully explain changes in silicate weathering and how climate is conveyed through Li isotope ratios.

The role of tectonics in the continental Li cycle on Earth, much like climate, has been studied through observations of ancient archives and modern systems, yielding similarly confounding results. Cenozoic seawater chemistry reflects long-term ($10^6$ – $10^7$ yr) changes in elemental cycles on Earth, with riverine alkalinity input playing a primary role in its evolution (e.g., Misra and Froelich, 2012). Significant increases in seawater $\delta^7$Li values during the Cenozoic have thus been attributed to tectonically induced weathering changes during Himalayan uplift, similar to changes observed with other weathering-sensitive geochemical proxies such as

$^{87}Sr/^{86}Sr$ and $^{187}Os/^{188}Os$ (e.g., Peucker-Ehrenbrink and Ravizza, 2000; Raymo and Ruddiman, 1992). However, the generation of continental relief during Himalayan uplift as the primary driver for changes in global weathering congruency remains contested (e.g., Colleps et al., 2018; Li and West, 2014; Pogge von Strandmann et al., 2017a; Rugenstein et al., 2019; Vigier and Goddéris, 2015), owing largely to the inextricable connection of tectonics, climate, and surface processes (e.g., West et al., 2005; Riebe et al., 2017; Whipple, 2009). In modern environments, evidence of an inverse relationship between uplift rate and $\delta^7Li_f$ values suppose a direct effect of tectonics on Li transfer (Pogge von Strandmann and Henderson, 2015), but often concomitant with changes in uplift are changes in climate and depositional setting that influence how sediments and fluids interact. In sum, the coupling of tectonics and climate, among other important properties of drainage catchments, complicate how to apportion the influence of each driver on $\delta^7Li_f$ values.

Drainage catchment lithology (i.e., rock types) and their paleogeographic and tectonic settings are increasingly proposed as an important driver of silicate weathering (e.g., Li et al., 2016; Macdonald et al., 2019). The lithology through which subsurface fluids flow can impact the stoichiometry of weathering reactions (e.g., Dellinger et al., 2015; Henchiri et al., 2016; Pogge von Strandmann et al., 2017b; Winnick et al., 2019) and impart diagnostic $\delta^7Li_f$ values. However, less is understood about the extent to which lithologic modulations of $\delta^7Li_f$ values are due to their physical and/or chemical erodibility. The physical erodibility of rocks within a catchment is dependent on rock strength, surface roughness, and mineralogy (e.g., Howard et al., 1994; Small et al., 2015). As a result, these physical properties modulate the mean local relief and sediment grain size distributions within catchments, influencing the timescales over which acid-bearing fluids and minerals interact and thereby dictating the modes of denudation in a catchment (e.g., Maher and Chamberlain, 2014; Portenga and Bierman, 2011). Although an influence on physical

erosion, the chemical erodibility of rocks within catchment depends largely on mineralogy, temperature, and fluid availability, all of which directly affect river water chemistry. Reaction rates as well as the types of secondary minerals that form as a byproduct of chemical weathering influence the transfer of Li between solid and aqueous phases (Winnick et al., 2019).

Catchment morphometric properties – which are integrative expressions of climate, lithology, and tectonics – have been indirectly related to $\delta^7\text{Li}_f$ values. Most studies have argued that integrative metrics, such as erosion (Bouchez et al., 2013; Pogge von Strandmann and Henderson, 2015) and fluid residence time (Liu et al., 2015; Manaka et al., 2017; Meier et al., 2017; Wanner et al., 2014), drive $\delta^7\text{Li}_f$ values. Not directly considered in Li isotope studies, however, is catchment relief, which is thought to be a principal driver of fluid (Małoszewski and Zuber, 1982; McGuire et al., 2005) and mineral (e.g., Montgomery and Brandon, 2002) residence time. Moreover, fluid and mineral residence times ($\sim$ 1/erosion rate) share similar increases with decreasing relief (Maher and Chamberlain, 2014; Portenga and Bierman, 2011) that further complicate their individual influences on $\delta^7\text{Li}_f$ values. Before processes can be invoked, direct comparisons of relief (and other river drainage morphometric properties) with $\delta^7\text{Li}_f$ values are warranted.

Of all proposed environmental controls on $\delta^7\text{Li}_f$ values, silicate weathering intensity (Bouchez et al., 2014; Dellinger et al., 2014; Huh et al., 2001) and its close relationship with landscape position appears to mechanistically explain the range of $\delta^7\text{Li}_f$ values. Defined as the ratio of silicate weathering to the sum of silicate weathering and physical erosion (Bouchez et al., 2014), silicate weathering intensity is observed to span 3 orders of magnitude among samples from several transcontinental rivers (Dellinger et al., 2015; Fig. 2.1B). At low weathering intensities, congruent weathering is the dominant mode of silicate weathering and is often associated with high-relief, kinetically limited weathering environments (Dellinger et al.,

2015). Similarly, congruent weathering is favored at high weathering intensities, but the low $\delta^7Li_f$ values are attributed to the dissolution of secondary minerals in low-relief continental interior, supply limited weathering environments (Dellinger et al., 2015; Henchiri et al., 2016). Intermediate weathering intensities are found to have high relative $\delta^7Li_f$ values, which is argued to be the result of weathering in floodplains (Dellinger et al., 2015; Pogge von Strandmann and Henderson, 2015). This empirical relationship between $\delta^7Li_f$ values and weathering intensity is potentially powerful because it suggests that past silicate weathering fluxes can be quantified if ancient river water $\delta^7Li$ values and erosional fluxes are determined. Some studies are beginning to apply this relationship to probe drivers of secular variations in the geologic carbon cycle (e.g., Rugenstein et al., 2019) while others are pointing to additional factors, such as annual to millennial changes in weathering intensity (Ferrier and West, 2017; Ferrier and Perron, 2020; Gou et al., 2019; Pogge von Strandmann et al., 2020), that muddle this relationship. Ultimately, the extent to which the relationship between $\delta^7Li_f$ values and weathering intensity applies broadly to rivers worldwide is a primary focus of this study.

Here we compile a global dataset of published Li isotope river water samples to identify key relationships between river water chemistry ($\delta^7Li_f$ values, Li concentrations, and Li/Na ratios) and drainage catchment properties. Specifically, we test the hypothesis that silicate weathering intensity, and not individual drainage catchment properties, can adequately describe the range of observed $\delta^7Li_f$ values by (1) determining catchment-averaged climate (mean annual precipitation and temperature), lithology (exposed bedrock geology), and morphometrics (catchment area, mean local relief, and hillslope angles); (2) utilizing various statistical tests to quantify the strength of variable correlations on a global dataset; and (3) predicting silicate weathering intensity using catchment-average properties. Through these observations and predictions, we highlight the inherently coupled nature of drainage

catchment properties and the continued need to refine drivers of river water chemistry across landscapes.

## 2.2 Methods

### 2.2.1 Global Li river chemistry database construction

The global dataset consists of published $\delta^7Li_f$ values ($n_{samples}$ = 757, $n_{studies}$ = 27; Table 2.1) and respective sampling locations (Fig. 2.2). A subset of the data includes river dissolved Li concentrations ($n_{samples}$ = 737) and a lesser number of studies ($n_{samples}$ = 574) report dissolved Li and Na concentrations alongside $\delta^7Li_f$ values. The sample set includes rivers in all climate zones (including monsoonal climates), draining a wide range of bedrock types, and flowing through a variety of geomorphic settings. Most samples come from well-studied transcontinental river systems with a smaller number of samples from Critical Zone observatories or smaller streams. Data from dry or seasonally wet climates, from Africa, Europe, and the southern hemisphere are underrepresented. Nevertheless, on average, the river water samples come from sedimentary rock-dominated catchments with moderate relief and temperate climates, characteristic of most environments presently at the Earth's surface (Fig. 2.2). Due to gaps in geospatial data around the polar regions, we do not include samples from Antarctica (Witherow et al., 2010; $n_{samples}$ = 6) in our subsequent analyses. To query weathering signals in the river water data, we correct $\delta^7Li_f$ values by accounting for source rock $\delta^7Li$ values and consider Li input from non-silicate sources. Corrections for source rock chemistry are presented as $\Delta^7Li_{f-s}$ where

$$\Delta^7Li_{f-s} = \delta^7Li_f - \delta^7Li_s \tag{2.1}$$

and subscript "s" corresponds to "source rocks". Because different bedrock types can exhibit a >10 ‰ range in $\delta^7$Li values (Tomascak et al., 2016), we constrained $\delta^7Li_s$ values using reported Li isotope composition of river bedload sediments (e.g., Dellinger et al., 2014). We do not consider reported river suspended load $\delta^7$Li values because suspended sediments often geochemically bias towards more negative values relative to their source rocks (e.g., Lupker et al., 2012; Dellinger et al., 2017). When a range of $\delta^7Li_s$ values are reported for a given sample set, we compute $\Delta^7Li_{f-s}$ based on the mean of the $\delta^7Li_s$ values. When the $\delta^7Li_s$ values are not reported alongside $\delta^7Li_f$ values, we assume a narrow range of $\delta^7Li_s$ values between 1.0 – 3.2 ‰, representative of most of the upper continental crust (Tomascak et al., 2016). To test the validity of our correction, we computed $\delta^7Li_s$ values as a weighted average of exposed bedrock types, assigning each rock type to have a median $\delta^7$Li value and Li concentration. $\Delta^7Li_{f-s}$ values are mostly within 2 ‰ of those computed assuming a $\delta^7Li_s$ value of the upper continental crust (see Figs. A.1-A.2, Table A.1 and methods therein). Because the assumptions of $\delta^7Li_s$ values and Li concentrations are tenuous, we elect to use the former computation for $\delta^7Li_s$ values. Lastly, $\delta^7Li_f$ values can be influenced by the input of Li through rainfall, aerosols (e.g., Pogge von Strandmann et al., 2006), hot springs (e.g., Rad et al., 2013), evaporites (e.g., Dellinger et al., 2015), and anthropogenic activities including agriculture (e.g., Choi et al., 2019; Millot and Négrel, 2021). When available, we choose data that have been already corrected for non-silicate Li input in the original publication ($n_{samples}$ = 222, or 29% of all samples).

### 2.2.2 Determining catchment geometries and extracting geopspatial information

Sample locations are crucial for determining drainage catchment geometries. When studies do not report coordinates of sampling locations, latitudes and longitudes

| Study name | Continent | Country/Major drainage | n |
|---|---|---|---|
| Bagard et al., 2015 | AS | Ganges-Brahmaputra | 26 |
| Bohlin and Bickle, 2019 | AS | Himalaya (Alaknanda) | 23 |
| Clergue et al., 2015 | SA | Lesser Antilles | 4 |
| Dellinger et al., 2015 | SA | Amazon | 42 |
| Gou et al., 2019 | AS | Yellow | 60 |
| Henchiri et al., 2014 | EU, AU (OC), AF | Azores (EU), Java (AU), Reunion (AF) | 9 |
| Henchiri et al., 2016 | AF | Congo | 10 |
| Hindshaw et al., 2018 | EU | Svalbard | 20 |
| Huh et al., 1998 | SA, NA, AS | Amazon (SA), Orinoco (SA), Mississippi (NA), Mackenzie (NA), Ganges-Brahmaputra (AS), Lena (AS), Yellow (AS), Qiatong (AS), Baikal (AS), Jordan (AS) | 41 |
| Huh et al., 2001 | SA, AS | Orinoco (SA), Anadyr (AS), Indus (AS) | 12 |
| Kisakűrek et al., 2005 | AS | Himalaya | 44 |
| Lemarchand et al., 2010 | EU | Strengbach | 28 |
| Liu et al., 2015 | NA | Columbia | 31 |
| Longley, 2018 | AS | Chao Phraya | 96 |
| Manaka et al., 2017 | AS | Ganges-Brahamputra | 21 |
| Meier et al., 2017 | AS | Gunt | 65 |
| Millot et al., 2010 | NA | Mackenzie | 40 |
| Murphy et al., 2019 | AS | Lena | 71 |
| Pogge von Strandmann and Henderson, 2015 | AU (OC) | Southern Apls (New Zealand) | 17 |
| Pogge von Strandmann et al., 2006 | EU | Iceland | 23 |
| Pogge von Strandmann et al., 2010 | EU | Azores | 13 |
| Pogge von Strandmann et al., 2017a | AS | Ganges | 49 |
| Rad et al., 2013 | SA | Lesser Antilles | 5 |
| Vigier et al., 2009 | EU | Iceland | 20 |
| Wang et al., 2015 | AS | Yangtze | 30 |
| Weynell et al., 2017 | AS | Dongqu | 24 |
| Witherow et al., 2010 | AN | – | 20 |

Table 2.1: List of studies included in this compilation and location information. Note that some studies include analysis ground water, ice water, or water from thermal springs, which are not used in this study. AS: Asia; AF: Africa; AU: Australia; AN: Antarctica; EU: Europe; OC: Oceania; NA: North America; SA: South America.

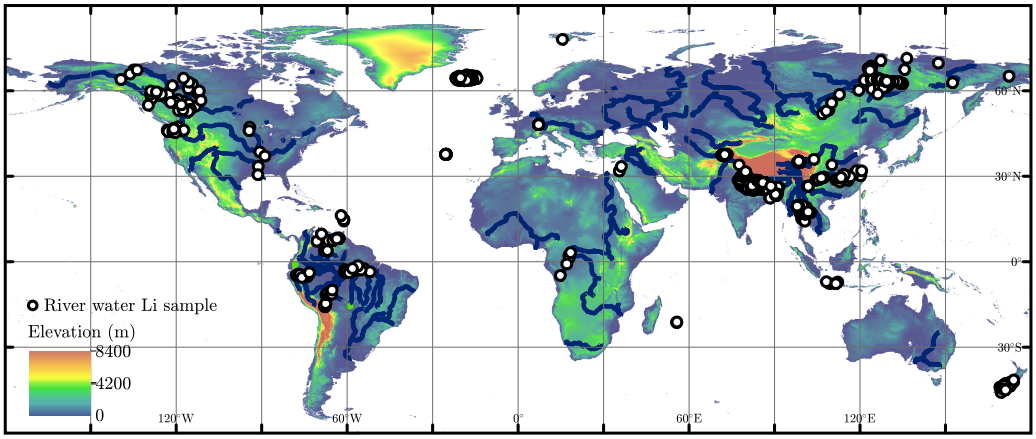


Figure 2.2: Map of global river water $\delta^7\text{Li}_f$ samples synthesized in this study. Global elevation map (meters above sea level) with river water $\delta^7\text{Li}_f$ sample locations (white circles) and major rivers (blue lines).

were estimated by relating sample location descriptions (e.g., city names, landmarks) and/or map illustrations of sample locations to the largest nearby river reaches.

Individual catchments for each river sample were designated using ArcGIS (ArcHydro tool extension), 30 arcsecond-resolution HYDRO1k global digital elevation data, Flow Accumulation, and Flow Direction rasters (Greenlee, 1987; Jenson and Domingue, 1988; Tarboton et al., 1991; Verdin et al., 2011). The generated watershed polygon was used to extract geospatial information from other global databases including climatic (precipitation and temperature), lithologic (exposed bedrock proportions), and morphometric (mean local relief, mean catchment hillslope angles, and catchment area) information. We refer to the geospatial measurements as "catchment variables" and characterize them as either a climatic, lithologic, or morphometric "catchment property" (Table 2.2).

Climate proxies, including mean annual temperature (MAT) and precipitation (MAP) data, were derived from 1 km (∼30 arcsecond) spatially resolved and monthly interpolated climate measurements from 1970–2000 included in the World-

| Catchment property | Variable | Mean | Median | Range | S.D. | $1\sigma$ error |
|---|---|---|---|---|---|---|
| River chemistry | $\delta^7Li_f$ (‰ LSVEC) | 19.5 | 18.9 | 44.3 | 7.4 | 0.3 |
| | $\Delta^7Li_{f-s}$ | 17.9 | 16.9 | 44.3 | 7.2 | 0.3 |
| | $\log_{10}$ [Li/Na] | -3.09 | -2.97 | 4.4 | 0.79 | 0.03 |
| | $\log_{10}$ [Li (ppm)] | -2.62 | -2.72 | 6.11 | 0.85 | 0.03 |
| Climate | MAT (°C) | 8.5 | 8.8 | 43.1 | 12.8 | 0.5 |
| | MAP (mm) | 1024.6 | 951.8 | 3575 | 614.4 | 22.4 |
| Morphometrics | $\log_{10}$ [area ($km^2$)] | 3 | 2.8 | 6.7 | 1.9 | 0.1 |
| | Mean hillslope (°) | 12.4 | 11 | 43.1 | 8.6 | 0.3 |
| | Local relief (m) | 469 | 357 | 2161.8 | 425 | 15.5 |
| Lithology | Sedimentary (%) | 47 | 42.8 | 100 | 43.1 | 1.6 |
| | Sediments (%) | 13.8 | 0 | 100 | 27.8 | 1 |
| | Metamorphic (%) | 15.2 | 0 | 100 | 28.3 | 1 |
| | Plutonic (%) | 9.8 | 0 | 100 | 21.3 | 0.8 |
| | Volcanic (%) | 13.1 | 0 | 100 | 30 | 1.1 |
| | Mafic (%) | 9.8 | 0 | 100 | 26.7 | 1 |
| | Intermediate (%) | 3.1 | 0 | 100 | 15.6 | 0.6 |
| | Felsic (%) | 10 | 0.1 | 100 | 21.2 | 0.8 |
| | Other (%) | 1.1 | 0 | 100 | 8.1 | 0.3 |

Table 2.2: Catchment-wide variables and river water chemistry for global dataset. "Other" corresponds to areas with glaciers, water bodies, or no data.

Clim 2 database (Fick and Hijmans, 2017). These MAT and MAP data do not correspond to the MAT and MAP at the time the waters were sampled.

Lithologic data were compiled from the 1:3,750,000 area-weighted scale (∼1.5 km resolution) global lithology map GLiM (Hartmann and Moosdorf, 2012), which allows for the delineation of contributing surface areas for all lithologic units within each catchment. We consider the relative proportions of 12 different rock types including sedimentary rocks (siliciclastic, mixed siliciclastic, pyroclastic, carbonate, and evaporite), plutonic rocks (mafic, intermediate, and felsic), volcanic rocks (mafic, intermediate, and felsic), metamorphic rocks, and unconsolidated sediments in a drainage catchment. The catchment area consisting of glaciers/ice, water bodies, and areas with no data is negligible for all samples. Further, the number of samples with plutonic and volcanic rock-dominated (i.e., proportions ≥75%) catchments is small and thus we could not interrogate the differences between felsic and

mafic rock-dominated catchments with much statistical significance. All lithologic data for each catchment are presented as proportions.

Lastly, for morphometric data, we consider catchment area, mean flow lengths, mean local relief, and mean hillslope angles using the 30 arcsecond HYDRO1k digital elevation data (Verdin et al., 2011). Mean local mean relief was computed across the land surface by averaging the elevation over a 3 km-diameter circular area, except for data from Guadaloupe (Rad et al., 2013) that required a 1 km diameter averaging window due to the demonstrably small area of the island on which samples were gathered. Mean hillslope angles were determined from a study that computed global hillslope angles on a 3 arcsecond DEM (Larsen et al., 2014b). For each sample, we compute a catchment-wide minimum, maximum, mean, and standard deviation for all climatic and morphometric variables. All catchment variables are compared against river water chemistry ($\delta^7\mathrm{Li}_f$ values, Li concentrations, and Li/Na ratios) (Table A.1).

### 2.2.3 Statistical analyses

To discern statistical trends among river water chemistry and catchment properties, we utilize linear regressions and two-way analysis of variance (ANOVA). All catchment variables exhibit skewed, non-normal distributions making many useful parametric tests, including principal component analysis, not suitable. We instead utilize non-parametric statistical tests that convey the significance of variable correlations (i.e., linear regressions) and the statistical similarity between various sample populations (i.e., ANOVA).

Linear regressions enable us to compare the strength of variable correlations among geochemical, climatic, and morphometric data. We compute the Spearman rank-order correlation (Spearman's $\rho$) to quantify the significance of the monotonicity among these variables. Variable pairs with $\rho > 0.1$ exhibit a significant direct

relationship, variables pairs with $\rho < -0.1$ exhibit a significant inverse relationship, and variable pairs with $|\rho| < 0.1$ exhibit no monotonicity.

Two-way ANOVA enables us to assess the strength of variable correlations using categorical data, allowing us to consider the effect of lithology on geochemical data. For each catchment variable (i.e., independent variable), we define categories in which geochemical data ($\Delta^7\text{Li}_{f-s}$ and $\log_{10}$ Li/Na) are grouped and then test the difference among category medians and distributions. This method enables us to determine if "main effects" or "interaction effects" exist among catchment variables, where the former represents a statistically significant direct effect of a catchment variable on geochemical data and the latter represents a statistically significant combined effect of two catchment variables (see Section A.1.2 for a further description of the technique). For lithologic data, we only consider catchments that are dominated by $\geq$75% areal exposure one rock type, and "mixed" catchments that do not have $\geq$50% areal exposure of any one rock type. These constraints define our categories for lithology, and we therefore do not test if individual rock type proportions (e.g., sedimentary rocks) have main effects on geochemical data.

### 2.2.4 Modeling silicate weathering

Silicate weathering intensity was computed for samples for which climatic, lithologic, and morphometric were gathered (nsamples= 748). Computing weathering intensity relies upon the estimation of both erosion and silicate weathering fluxes. To compute erosion fluxes, we applied an empirically derived power law relationship (Montgomery and Brandon, 2002) where

$$E = \rho_{soil} a S^b, \tag{2.2}$$

$E$ is erosion (t km$^{-2}$ yr$^{-1}$), $\rho_{soil}$ is soil density (kg m$^{-3}$), $S$ is mean local relief (m), and $a$ and $b$ are empirical constants (unitless). To compute silicate weathering

fluxes, we use two modeling approaches: one which assumes steady state erosion and silicate weathering (West, 2012) and another which allows for transience in erosion and silicate weathering (*sensu* Bouchez et al., 2013; Ferrier and Kirchner, 2008).

### Steady state weathering and erosion

To assess steady state weathering, we employ a parametric weathering equation specifically derived for continental-scale weathering estimates (West, 2012). In this formulation, the supply of fresh, un-weathered bedrock from erosion is assumed to be the primary driver of silicate weathering. The parametric equation is presented as

$$W = E\chi_m \cdot \Big\{1 - \exp\Big[ - K \cdot \big(1 - \exp(k_w \cdot Q)\big) \cdots \exp\Big(\frac{E_a}{\mathrm{R}T} - \frac{E_a}{\mathrm{R}T_0}\Big) \cdot \frac{(\frac{\rho_{soil} z}{E})^{\sigma+1}}{\sigma + 1}\Big]\Big\} \quad (2.3)$$

where $W$ is the silicate weathering flux (t km$^{-2}$ yr$^{-1}$), $\chi_m$ is the molar fraction of mono or divalent silicate cations found in eroding sediment (mol mol$^{-1}$), and each term between the curly braces corresponds broadly to kinetic effects that modify the maximum silicate weathering flux ($W_{max} = E\chi_m$; West et al., 2005). Details regarding the derivation of these terms can be found in West (2012) and references therein, but briefly put, the amalgamation of terms represents the cumulative effects of fluid flow, temperature, weathering zone thickness, and mineral surface area and residence time on mineral dissolution rates.

The catchment variables that are passed as input to Eqs. 2.2 and 2.3 include MAT ($T$), MAP ($Q$), mean local relief ($S$, $E$, $z$), and source rock proportions ($\chi_m$) (Fig. 2.3A). Without making crude assumptions that relate catchment-wide MAT and MAP to evapotranspiration, we assume that MAP is equivalent to subsurface fluid flow rates Q (m yr$^{-1}$). Moreover, we assume a nominal range of $\chi_m$ values for

each of the 5 dominant rock types (Rudnick and Gao, 2003) and then compute a weighted average $\chi_m$ for each catchment. To compute weathering zone thickness $z$ (m), we elect to assume that relief is equal to the weathering zone thickness because other formulations where z is a function of erosion-driven soil production rates (e.g., Heimsath et al., 1997; Larsen et al., 2014a) predict extremely low weathering intensities (Fig. A.3). All other empirical constants ($K$, $k_w$, $E_a$, $\sigma + 1$) are assumed to have a value between the 66% confidence interval determined by West (2012) (Table 2.3). To account for the range of values for empirical constant and the standard deviation of catchment-average variables, we use a Monte Carlo approach (50,000 iterations) to compute a range of weathering intensities for each sample; all $W$, $E$, and weathering intensity computations are presented as means of the 50,000 individual computations. Lastly, we compute weathering intensity simply by taking the ratio of $W$ and $W + E$ such that

$$\text{Weathering intensity} = \frac{W}{W + E}. \tag{2.4}$$

Model results using this formulation are hereafter referred to as "W2012" results (after West, 2012).

### Time-dependent weathering and erosion

To assess the effects of time-dependent weathering and erosion on silicate weathering intensity, we modify and numerically model a series of partial differential equations that describe changes in silicate weathering as a function of soil thickness, erosion, and sediment deposition (Bouchez et al., 2013; Ferrier and Kirchner, 2008; Heimsath et al., 1997). The change in soil (i.e., weathering zone) thickness $z$ (m) over time $t$ (yr) can be expressed as

$$\rho_{soil}\frac{dz}{dt} = \epsilon_0 \exp(-\alpha z) + D - (E + W) \tag{2.5}$$

| Variable | Description | Units | Values(s)[a] | Distribution[b] | Reference[c] |
|---|---|---|---|---|---|
| $\rho_{soil}$ | Soil density | kg m$^{-3}$ | 2000[b] | | |
| $a$ | Constant | 1 | 1.4E-6 | | MB2002 |
| $b$ | Constant | 1 | 1.8 | | MB2002 |
| $E$ | Erosion | t km$^{-2}$ yr$^{-1}$ | Calculated | | |
| $W$ | Weathering | t km$^{-2}$ yr$^{-1}$ | Calculated | | |
| $D$ | Deposition | t km$^{-2}$ yr$^{-1}$ | Calculated | | |
| $D_{max}$ | Max. deposition | t km$^{-2}$ yr$^{-1}$ | 2000 | | |
| | Cation fraction (sedimentary) | | [0.001, 0.04] | Uniform | |
| | Cation fraction (sediments) | | [0.001, 0.04] | Uniform | |
| $\chi_m$ | Cation fraction (metamorphic) | mol mol$^{-1}$ | [0.04, 0.13] | Uniform | RG2003 |
| | Cation fraction (plutonic) | | [0.04 0.13] | Uniform | |
| | Cation fraction (volcanic) | | [0.04, 0.13] | Uniform | |
| $K$ | Grain size/weathering | 1 | [7.6E-6, 1.2E-3] | Uniform | W2012 |
| $k_w$ | Role of water flow | 1 | [1.5E-6, 3E-3] | Uniform | W2012 |
| $E_a$ | Activation energy | kJ mol$^{-1}$ | [14.6, 79.2][d] | Uniform | W2012 |
| R | Gas constant | kJ mol$^{-1}$ K$^{-1}$ | 8.3146E-3 | | |
| $T_0$ | Mean surface temperature | K | 286 | | BC1994 |
| $z$ | Weathering zone thickness | m | Calculated | | |
| $\sigma + 1$ | Time dependence weathering | 1 | [0.66, 1.13] | Uniform | W2012 |
| $S$ | Relief | m | Input | Uniform | |
| $Q$ | Subsurface fluid flow | m yr$^{-1}$ | Input | Uniform | |
| $T$ | Temperature | K | Input | Uniform | |
| $\epsilon_0$ | Soil production rate | kg m$^{-2}$ yr$^{-1}$ | [.375, 15] | | H1997, L2014 |
| $\alpha$ | Soil production decay const. | m$^{-1}$ | 3 | | H1997; L2014 |
| $\gamma$ | Constant | 1 | 20 | | This study |

[a]variables with multiple values are minimum and maximum values; [b]applies to steady state weathering intensity calculations; [c]MB2002: Montgomery and Brandon (2002) - RG2003: Rudnick and Gao (2003) - W2012: West (2012) - BC1994: Brady and Carroll (1994) - H1997: Heimsath et al. (1997) - L2014: Larsen et al. (2014a); [d]see Table 2.4 for mineral-specific values

Table 2.3: Variables used in weathering intensity calculations

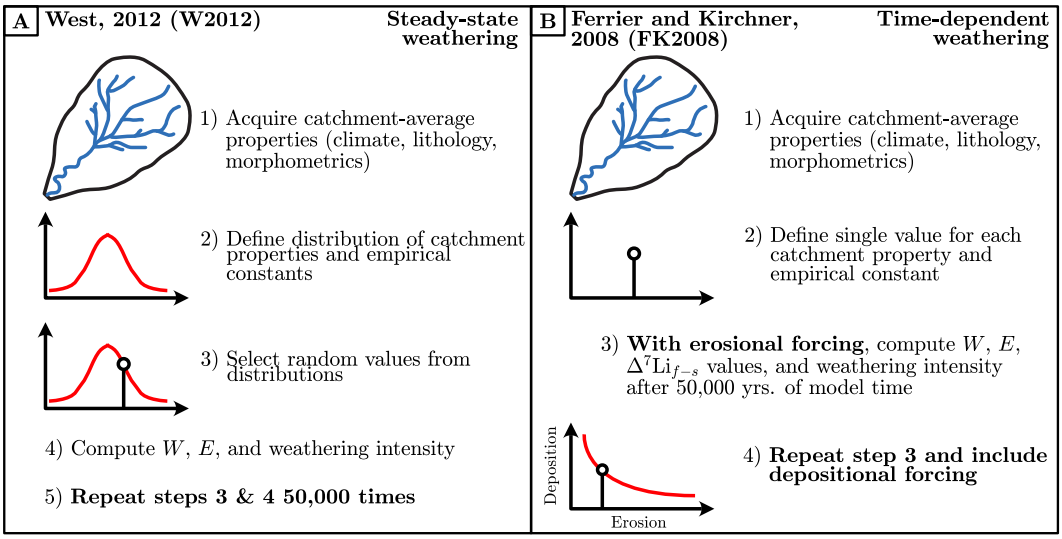


Figure 2.3: Workflows for the (A) steady-state weathering and (B) time-dependent weathering models for a given river sample.

where soil production rate $\epsilon_0$ (kg m$^{-2}$ yr$^{-1}$) and soil production decay constant $\alpha$ (m$^{-1}$) modulate the nonlinear growth of soil while $W$ and $E$ (t km$^{-2}$ yr$^{-1}$) remove soil mass and thus act to decrease soil thickness. We modified previous formulations to include sediment deposition $D$ (t km$^{-2}$ yr$^{-1}$) as another mode of sediment input into the weathering environment. This conservation of mass equation Eq. 2.5 also extends to mineral phase i and its molar concentration in soil $[X_i]_{soil}$ (mol kg$^{-1}$), which we express as

$$\begin{aligned}\frac{d[X_i]_{soil}}{dt} = {} & \frac{D + \exp(-\alpha z)}{\rho_{soil} z}\left([X_i]_s - [X_i]_{soil}\right) + \cdots \\ & \exp\left(\frac{E_{a_i}}{\mathrm{R}T} - \frac{E_{a_i}}{\mathrm{R}T_0}\right)\left\{\frac{\eta_i s_i}{\rho_{soil}} - \kappa_i A_i [X_i]_{soil}\right\} + \cdots \\ & [X_i]_{soil} \sum_{i+1}^{N} \exp\left(\frac{E_{a_{i+1}}}{\mathrm{R}T} - \frac{E_{a_{i+1}}}{\mathrm{R}T_0}\right)\left\{\kappa_{i+1} A_{i+1} [X_{i+1}]_{soil} w_{i+1} - \frac{\eta_{i+1} s_{i+1} w_{i+t}}{\rho_{soil}}\right\} \quad (2.6)\end{aligned}$$

where

$$\sum_{i+1}^{N} w_i[X_i] = 1, \tag{2.7}$$

$$\sum_{i+1}^{N} \rho_i w_i[X_i]_s = \rho_{soil}, \tag{2.8}$$

$s_i$ is the mineral formation rate (kg m$^{-3}$ yr$^{-1}$), $\kappa_i$ is the mineral dissolution rate (kg m$^{-2}$ yr$^{-1}$), $A_i$ is the mineral surface area (m$^2$ mol$^{-1}$), $w_i$ is the mineral molar mass (kg mol$^{-1}$),$\eta_i$ is a term which scales $s_i$ by the availability of primary minerals (mol mol$^{-1}$), and $N$ is the total number of mineral phases found in source sediments and soil. These equations implicitly assume that soils do not exhibit depth-dependent changes in mineralogy and instead treat soils as uniform reservoirs. Furthermore, by introducing D in Eq. 2.5, we assume that the chemistry of sediment input by deposition (atop soil) and of bedrock input by erosion (below soil) are identical. Note that we have included an Arrhenius term in Eq. 2.6 (*sensu* West, 2012) that modifies the rates of mineral dissolution and formation. We compute $\eta_i$ at each time step by comparing the proportion of biotite (bt), plagioclase (plag), and potassium feldspar (kspar) in source sediments to their proportions in soil such that

$$\eta_i = \frac{w_{bt}[X_{bt}]_{soil} + w_{plag}[X_{plag}]_{soil} + w_{kspar}[X_{kspar}]_{soil}}{w_{bt}[X_{bt}]_s + w_{plag}[X_{plag}]_s + w_{kspar}[X_{kspar}]_s}. \tag{2.9}$$

Eq. 2.9 is specifically designed for kaolinite (the only mineral that forms in this model) such that kaolinite formation occurs most quickly when the concentration of select primary minerals in soil are equal to those in source sediments. Because these constitutive equations track changes in soil mineralogy, we compute W at each time

step where

$$W = z\sum_{i}^{N}\exp\left(\frac{E_{a_i}}{\mathrm{R}T} - \frac{E_{a_i}}{\mathrm{R}T_0}\right)\left\{\kappa_i A_i [X_i]_s w_i \rho_i - \eta_i s_i w_i\right\}. \tag{2.10}$$

Moreover, we develop mass balance equations for Li and its isotopes (see Section A.1.3) and can thus predict $\Delta^7\mathrm{Li}_{f-s}$ values alongside weathering intensities.

Like the steady state weathering equation, the time-dependent weathering equations can be tailored to predict weathering intensities for each sample with climatic, lithologic, and morphometric information (Fig. 2.3B). Specifically, we pass MAT, mean local relief, and rock proportions as input to these equations. Although MAP is postulated to be related to soil production rates $\epsilon_0$ (Larsen et al., 2014a) and influences mineral dissolution rates (e.g., Maher, 2010; Kump et al., 2000), it is excluded from these weathering intensity calculations due to (1) a paucity of functional relationships between MAP and $\epsilon_0$ and (2) unclear connections between parameters in the steady state equation (Eq. 2.3) and time-dependent equations (Eqs. 2.5-2.6), respectively. For each of the major rock types we have defined, we simply assume that each major rock type is composed of varying proportions of quartz, plagioclase feldspar, potassium feldspar, biotite, kaolinite, and zircon (Table 2.4). A constant erosion rate, as determined through Eq. 2.2, is imposed over 50,000 years of model time and we initialize a soil thickness $z$ of 0.1 m. We solve Eqs. 2.5-2.6 with a fourth order Runge-Kutta method and report the predicted weathering intensities and $\Delta^7\mathrm{Li}_{f-s}$ values after 50,000 years of model time (when systems generally approach a steady state). Lastly, for each sample, we solve Eqs. 2.5–2.10 with and without the effect of sediment deposition $D$. We assume a nominal inverse relationship that relates $D$ to $E$, expressed as

$$D = D_{max}\frac{\exp\left(\gamma\frac{E_{max}-E}{E_{max}-E_{min}}\right)}{\exp(\gamma)-1} \tag{2.11}$$

| Variable | Description | Units | qtz | plag | kspar | bt | zir | kao |
|---|---|---|---|---|---|---|---|---|
| $\kappa$ | Mineral dissolution rate | mol $m^{-2}$ $yr^{-1}$ | 5E-8 | 5E-6 | 5E-7 | 2E-6 | 0 | 5E-8 |
| $A$ | Mineral surface area | $m^2$ $mol^{-1}$ | 2 | 117 | 26 | 1069 | 4 | 4776 |
| $w$ | Molar mass | kg $mol^{-1}$ | 0.0609 | 0.26544 | 0.27835 | 0.46460 | 0.18313 | 0.25818 |
| $s$ | Mineral formation rate | kg $m^{-3}$ $yr^{-1}$ | 0 | 0 | 0 | 0 | 0 | 0.51 |
| $\rho$ | Mineral density | kg $m^{-3}$ | 2650 | 2650 | 2560 | 3090 | 4600 | 2600 |
| $E_a$ | Activation energy | kJ $mol^{-1}$ | 84 | 73 | 50 | 42 | 54 | 61 |
| | Molar conc. (sedimentary) | | 6.550 | 0.1884 | 0.5389 | 0.4305 | 0.0005 | 0.7747 |
| | Molar conc. (sediments) | | 4.9908 | 0.1884 | 0.5389 | 0.4305 | 0.0005 | 1.1620 |
| $[X]_s$ | Molar conc. (metamorphic) | kg $mol^{-1}$ | 4.1588 | 1.5069 | 0.7185 | 0.3229 | 0.0005 | 0 |
| | Molar conc. (volcanic) | | 0.8321 | 2.6368 | 0.3593 | 0.3229 | 0.0005 | 0 |
| | Molar conc. (plutonic) | | 4.1588 | 1.5069 | 0.7185 | 0.3229 | 0.0005 | 0 |

Table 2.4: Mineral-specific properties used in time-dependent weathering intensity calculations. Refer to Table 2.5 for mineral abbreviations.

where $E_{max}$ is the maximum predicted erosion rate among samples in the global dataset, $E_{min}$ is the minimum predicted erosion rate among samples in the global dataset, $D_{max}$ is a nominal maximum deposition rate typical of foreland basins ($\sim$1 mm/yr aggradation rate), and $\gamma$ is a constant which modifies the concavity of the inverse relationship between $D$ and $E$.

Model results using this formulation are hereafter referred to as "FK2008" results.

## 2.3 Results

### 2.3.1 Global distributions of catchment properties and geochemical compositions

Catchment-wide properties and river water chemistry are reported as mean, median, range, and standard deviation/error (Table 2.2). We report a global mean $\Delta^7Li_{f-s}$ value of 17.9 ‰ ± 7.2 (1 standard deviation) with a range of 44.3 ‰. This mean value is comparable to the known per mil fractionation factor between water and clay at Earth surface temperature (17–19 ‰; Vigier et al., 2008). The average river Li/Na is $10^{-3.09\pm0.79}$, which is about 10 % of the upper continental crust Li/Na ($Li/Na_{UCC} = \sim10^{-2}$; Rudnick and Gao, 2003; Tomascak et al., 2016). River

catchment lithology is dominated by sedimentary rocks (mean 47 %) with moderate proportions (∼10-15 %) of metamorphic rocks, plutonic rocks, volcanic rocks, and unconsolidated sediment.

### 2.3.2 Linear regression and two-way ANOVA of global data

Linear regressions among climate (mean annual temperature and precipitation), morphometrics (hillslope angle, catchment area, mean local relief), and river water chemistry ($\log_{10}$ Li/Na, $\log_{10}$ Li, $\Delta^7\text{Li}_{f-s}$) quantify monotonic relationships in the global dataset (Fig. A.4). Strong variable correlations among certain catchment variables (e.g., hillslope angle and mean local relief) allow us to reduce the scope of variables considered hereafter, which includes MAT, MAP, catchment area, and mean local relief. Concerning solely $\Delta^7\text{Li}_{f-s}$ values, we find that no morphometric or climatic property exhibits a notably dominant relationship with $\Delta^7\text{Li}_{f-s}$ values (Fig. 2.4). We find weak monotonic relationships between $\Delta^7\text{Li}_{f-s}$ values and both mean local relief (Spearman's $\rho$ = -0.104) and MAT (Spearman's $\rho = 0.141$). $\text{Log}_{10}$ drainage catchment area (Spearman's $\rho = 0.123$) maintains a subsidiary relationship with $\Delta^7\text{Li}_{f-s}$ while MAP lacks a statistically significant correlation with $\Delta^7\text{Li}_{f-s}$ values (Spearman's $\rho = 0.021$). Notably, through ANOVA, we find that although none of the catchment variables have statistically significant main effects on $\Delta^7\text{Li}_{f-s}$ values, there are significant interaction effects among catchment properties (Fig. 2.4).

ANOVA of geochemical data reveals the significant coupling of lithology with other catchment properties and river water chemistry (Figs. 2.4 and 2.5; see Fig. A.5 for complete ANOVA results). Generally, we find two endmember environments that broadly correspond with rock erodibility. Crystalline rock-dominated catchments, which includes those with a majority of metamorphic and pluton rocks, tend to comprise small catchments with high relief and low MAT and MAP. Catch-

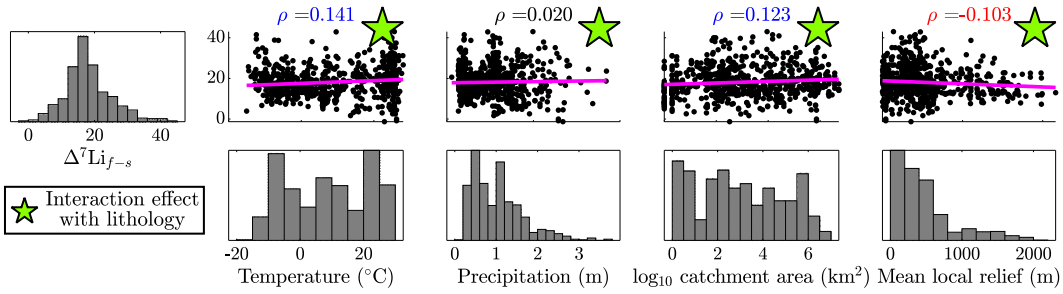


Figure 2.4: Correlation plots and histograms of continuous catchment variables against $\Delta^7Li_{f-s}$ values. Magenta lines represent least squares linear regressions and all values in the title of bivariate plots are Spearman's $\rho$ where values $> 0.1$ have a significant monotonic relationship that are either positive (blue), negative (red) correlations, or are $< 0.1$ and lack a significant monotonic relationship (black). Green stars indicate a significant interaction effect of a catchment variable and lithology on $\Delta^7Li_{f-s}$ values, as determined by ANOVA (p-value $< 0.05$).

ments with more erodible rocks, which includes those with unconsolidated sediments, volcanic, sedimentary, and mixed bedrocks, tend to have larger areas, lower relief, and higher MAT and MAP. The distribution of $\log_{10}$ Li/Na among different rock-dominated catchments is distinct, with metamorphic rock-dominated catchments having the highest $\log_{10}$ Li/Na, volcanic rock-dominated catchments having the lowest $\log_{10}$ Li/Na, and sedimentary, unconsolidated sediment, and mixed rock catchments containing intermediate and overlapping $\log_{10}$ Li/Na ranges (Fig. 2.5B). In contrast, the distributions of $\Delta^7Li_{f-s}$ values are indistinguishable among different rock-dominated catchments (Fig. 2.5A). The coupling of lithology with all other catchment variables yields significant interaction effects on $\Delta^7Li_{f-s}$; altogether, these tests reveal that there is not a catchment variable which has an overwhelmingly dominant relationship with $\Delta^7Li_{f-s}$ values.

### 2.3.3 Silicate weathering

The combined effect of catchment properties on $\Delta^7Li_{f-s}$ values are explored for river samples that have independent Li isotope and weathering intensity constraints

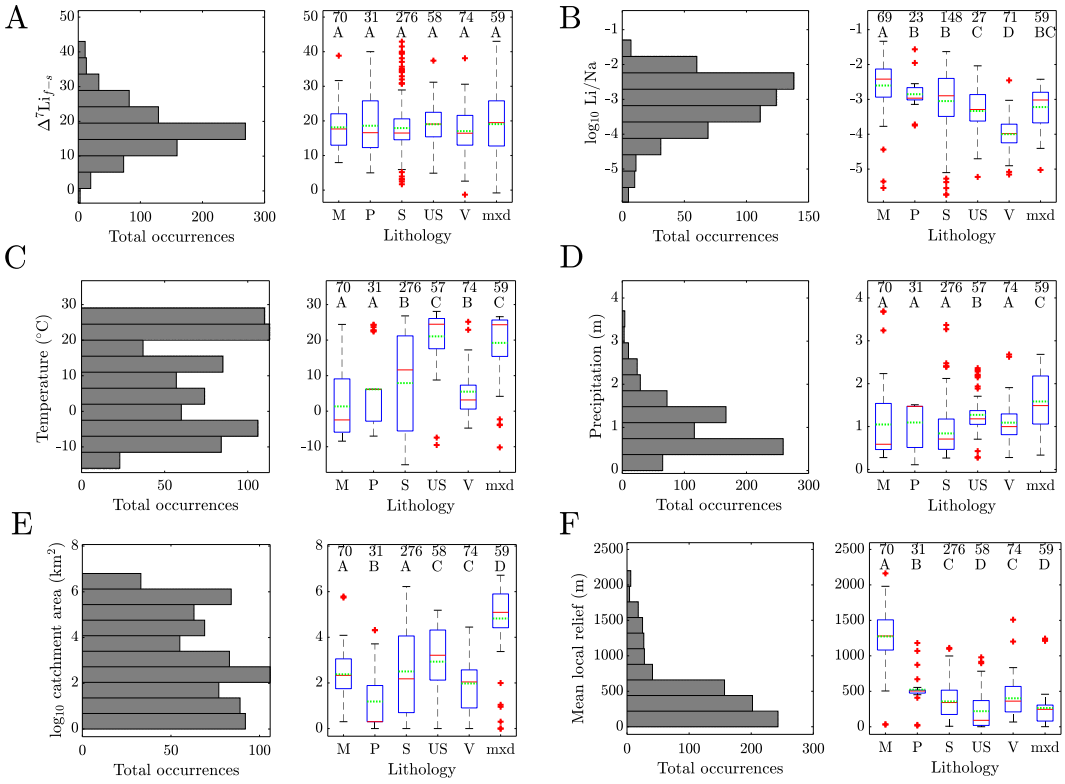


Figure 2.5: Global distribution of geochemical (A, B), climatic (C, D), and morphometric (E, F) catchment properties relative to lithology, shown as box-and-whisker plots that include quartile limits (red lines) means (green lines) for data subpopulations, outliers (red plus signs), total number of values in the distribution (upper numbers), and statistically similar groups (upper letters) where same letters indicate statistical similarity through the Wilcoxon rank sum test. Lithology abbreviations include metamorphic (M), plutonic (P), sedimentary (S), unconsolidated sediment (US), volcanic (V), and mixed (mxd) bedrock dominated catchments.

(Fig. 2.6). At low weathering intensities (values $< 10^{-1.5}$), catchments are typically cold, receive low relative amounts of precipitation, and have moderate relief. At high weathering intensities (values $> 10^{-1}$), catchments are typically warm, receive high relative amounts of precipitation, and have low relief. Samples with moderate weathering intensities tend to have catchment properties that fall variably between those of low and high weathering intensity regimes. These consistent trends in

catchment properties hint at plausible mechanisms that induce these trends, which further underscores the need to incorporate these properties into mechanistic models.

### Modeled silicate weathering intensity

Silicate weathering intensity was computed for all samples with extracted catchment property information (Fig. 2.7, 2.8A). All results from W2012 fall within kinetically limited weathering regimes, with weathering intensities spanning $\sim 10^{-4}$ to $10^{-1.3}$ that show direct relationships with MAT and MAP and an inverse relationship with mean local relief (Fig, 2.7). The changes in weathering intensity are greatest at the lowermost range of observed MAT ($< 0°$C), MAP ($< 1000$ mm), and relief ($< 1000$ m). These findings contrast with FK2008 model predictions that fall within supply-limited weathering regimes with $> 10^{-1}$ intensities. The few samples that have weathering intensities $< 10^{-1}$ are often at the soil formation limit, which occurs when soil mass removal (erosion $E$) exceeds soil mass addition (soil production rate $\epsilon_0$ + deposition $D$) (Fig 2.7F). The relationships between FK2008 modeled weathering intensity and both MAT and MAP are less obvious, where there are subtle increases in mean weathering intensity with MAT and MAP. In contrast, weathering intensity steeply decreases with increasing relief, suggesting that relief is the dominant driver of weathering intensity in this model (Fig. 2.7F). Weathering intensity estimates among FK2008 models with and without deposition are similar, with the inclusion of deposition generally increasing predicted weathering intensities. Increasing the soil production rate in the FK2008 models increases predicted weathering intensities for all samples, but the broad trends between weathering intensity and catchment properties remain the same (Fig. A.6).

Between W2012 and FK2008 model predictions, there are a dearth of predicted weathering intensities that fall within the moderate weathering intensity regime: approximately between weathering intensities of $10^{-1.6}$ and $10^{-1.1}$ where

the highest observed $\Delta^7Li_{f-s}$ values have been most readily identified (Fig. 2.8A). When modeled weathering intensities are compared to reported weathering intensities (Fig. 2.8B), two noteworthy trends arise. First, W2012 model predictions compare well with reported weathering intensities ($< 10^{-1}$) for kinetically limited weathering regimes yet increasingly underestimate weathering intensity as reported weathering intensities increase. Second, FK2008 model predictions consistently overestimate weathering intensity but become increasingly accurate as reported weathering intensities increase ($> 10^{-1}$). From these model-data comparisons, it appears that while W2012 more accurately represents kinetically limited weathering regimes, FK2008 more accurately represents supply-limited weathering regimes. We explore why this observation might be the case and discuss how it may relate to different modes of landscape denudation (see Section 2.4.3).

### Time-dependent modeled Li isotopes

Model-determined $\Delta^7Li_{f-s}$ values were found for all samples whose relief-driven erosion did not exceed the soil formation limit (Fig. 2.9). FK2008 models with and without deposition poorly agree with reported $\Delta^7Li_{f-s}$ values (Fig. 2.9A), where all results fall within a $\Delta^7Li_{f-s}$ range of 10 to 20 ‰. Among FK2008 models, there is significant agreement. Models that include deposition tend to predict slightly higher $\Delta^7Li_{f-s}$ values; the difference is greatest among samples who also have elevated mean local reliefs (Fig. 2.9B). For a better understanding in what drives this disagreement, we explore how each major catchment property individually affects predicted $\Delta^7Li_{f-s}$ values (see Section 2.4.1) and posit mechanisms that FK2008 might not capture (see Section 2.4.3).

## 2.4 Discussion

### 2.4.1 Catchment properties control on weathering intensities and river Li isotope compositions

The synthesis of W2012 and FK2008 results, corroborated by statistical analyses of global $\Delta^7Li_{f-s}$ values, underscore the combined and at times non-unique influence of climate, lithology, and morphometrics on river water chemistry (Figs. 2.4–2.6). Despite the overestimations of weathering intensity and narrow range of $\Delta^7Li_{f-s}$ values predicted by FK2008, we discern through sensitivity analyses how each of the primary input variables influence predicted weathering intensities and $\Delta^7Li_{f-s}$ values (Fig. 2.10).

Catchment-average temperature shows dual effects on $\Delta^7Li_{f-s}$ values and weathering intensity (Fig. 2.10B). With constant catchment-average erosion rates, soil formation rates, and uniform lithology (plutonic), FK2008 models predict decreases in $\Delta^7Li_{f-s}$ values and increases in weathering intensity with increasing MAT. The decrease in $\Delta^7Li_{f-s}$ values with increasing MAT occurs due to two known processes: the decrease in the clay-water fractionation factor (Dupuis et al., 2017; Vigier et al., 2008) and the enhanced dissolution of minerals relative to secondary mineral formation (e.g., Henchiri et al., 2016). The 30 °C range we explore only manifests in a $< 4$‰ range of $\Delta^7Li_{f-s}$ values (11–15 ‰), which agrees with the $\Delta^7Li_{f-s}$ range predicted by the direct effect of temperature on isotope fractionation (Dupuis et al., 2017; Vigier et al., 2008) but only composes one tenth the observed range in $\Delta^7Li_{f-s}$ values. The predicted weathering intensities increase from $> 10^{-0.9}$ to $> 10^{-0.8}$ (10 % range) with increasing MAT. This finding suggests that with erosion held constant, increasing MAT will promote primary mineral dissolution over secondary mineral formation, even though secondary mineral formation is also increasingly catalyzed with increasing temperature.

Lithology, like MAT, influences both $\Delta^7\text{Li}_{f-s}$ values and weathering intensity (Fig. 2.10C). With erosion rates, soil formation rates, and temperature held constant, the model predicts a ~3 ‰ range of $\Delta^7\text{Li}_{f-s}$ values among the five major rock types. Weathering of sedimentary rocks and unconsolidated sediments manifests in $\Delta^7\text{Li}_{f-s}$ values which are ~2 ‰ greater than the weathering of metamorphic, plutonic, and volcanic rocks (~13 ‰). Additionally, minimum weathering intensities increase from sedimentary to metamorphic to volcanic rocks, covering a $10^{-0.2}$ (~20 %) range. These trends among $\Delta^7\text{Li}_{f-s}$ values and weathering intensity arise primarily due to the proportion of plagioclase and primary kaolinite found in each rock type. In our model, the presence of primary kaolinite – with its high Li concentration and large partition coefficient – appears to catalyze secondary kaolinite formation, lowering bulk $\delta^7\text{Li}_{soil}$ values over time while maintaining elevated $\delta^7\text{Li}_f$ values that ultimately yield higher $\Delta^7\text{Li}_{f-s}$ values absent temperature effects; this finding is purely model-derived and thus needs further interrogation through experimentation or observations of natural systems. More sensibly, weathering intensity is driven by the relative dissolution rates of the primary minerals. Rocks with high proportions of plagioclase will yield greater weathering fluxes due to the high dissolution rate of plagioclase. Conversely, kaolinite dissolves relatively slowly and thus rocks with high proportions of kaolinite will yield comparatively smaller weathering fluxes.

Lastly, erosion and deposition, unlike MAT and lithology, primarily influence weathering intensity and have less of an effect on $\Delta^7\text{Li}_{f-s}$ values (Figs. 2.10D and 2.10E). With increasing erosion rates, we observe a decrease in minimum weathering intensities ($10^{-0.1}$ range) and subtle decrease in $\Delta^7\text{Li}_{f-s}$ values by at most 1 ‰. These trends are to be expected; increasing erosion rates will directly decrease weathering intensity and the relative suppression of secondary mineral formation at elevated erosion rates will yield a decrease in $\Delta^7\text{Li}_{f-s}$ values. The inclusion of

deposition with erosion subtly increases both the minimum weathering intensity and $\Delta^7Li_{f-s}$ values relative to the same model without deposition (Fig. 2.10D). In this case, deposition effectively offsets the removal of soil and increases the proportion of primary minerals in the soil, which subtly enhances secondary mineral formation while increasing the net weathering flux from the soil. Contrarily, absent erosion, deposition yields $\Delta^7Li_{f-s}$ values (11 – 12.5 ‰) that are among the lowest values predicted among our observed range (Fig. 2.10E). Without removal of soil, deposition enriches soil in minerals with the lowest dissolution rates (e.g., quartz and kaolinite), which both decreases the rate of secondary mineral formation and decreases bulk $\delta^7Li_{soil}$ values progressively over model time. Notably, the consistent prediction of a weathering intensity of 1 (i.e., when there is no erosion) and its noticeable (albeit subtle) effect on $\Delta^7Li_{f-s}$ values may reveal an insufficiency with characterizing landscapes in terms of weathering intensity (Eq. 2.4), especially since many low relief landscape elements can be net aggradational over time (see Section 2.4.2 for further discussion).

Altogether, these FK2008 model predictions deconvolve the influence of individual catchment properties on predicted weathering intensities and $\Delta^7Li_{f-s}$ values. However, the inability for the model to predict a wider range of $\Delta^7Li_{f-s}$ values may be more revealing. Firstly, the inability of the model to predict $\Delta^7Li_{f-s}$ values $< 10$‰ models suggest that for $\Delta^7Li_{f-s}$ values to be that low, secondary mineral formation must be substantially suppressed. This inference agrees with common conceptions (e.g., Dellinger et al., 2015). In catchments with high relief, this suppression is likely due to short residence times of primary sediments in soils; whereas, in catchments with low relief, this suppression is likely due to the limited availability of primary sediments and the high MAT and MAP that enable secondary mineral dissolution (Fig. 2.6; Dellinger et al., 2015; Henchiri et al., 2016). Moreover, the inability of the model to predict $\Delta^7Li_{f-s}$ values $> 20$ ‰ all but confirms the role

of fluid movement in modulating Li isotope signatures via Rayleigh fractionation (e.g., Fig. 2.1A). Ultimately, this inference underscores that the inclusion of fluid flow in models of mineral transformations within soil and addition/removal of sediments (e.g., FK2008) will allow for a better understanding of the role of catchment properties in modulating the highest $\Delta^7\mathrm{Li}_{f-s}$ values.

### 2.4.2 Transience of weathering regimes

To what extent is the empirical relationship between $\Delta^7\mathrm{Li}_{f-s}$ values and weathering intensity time-transgressive? In modeling weathering intensity via W2012 and FK2008, we assume that either mass transfer within a catchment is at a steady state (i.e., W2012) or we allow a perturbed system to evolve toward a steady state (i.e., FK2008). However, catchments that are perturbed by internal dynamics or external forces undergo transient and nonlinear changes in weathering intensity (Ferrier and West, 2017; Ferrier and Perron, 2020) whose timescales are comparable to relevant silicate weathering responses in the geologic carbon cycle ($> 10^5$ years; Hilton and West, 2020). To explore how transient changes in erosion and deposition manifest in $\Delta^7\mathrm{Li}_{f-s}$ values and weathering intensity, we present findings from a representative time-dependent model (FK2008) where erosion and deposition oscillate out-of-phase over time (Figs. 2.11 and 2.12) while temperature, soil formation rate, and lithology (plutonic) are held constant.

To a first order, these models reveal two important findings: (1) weathering intensity can vary over an order of magnitude while $\Delta^7\mathrm{Li}_{f-s}$ values fluctuate only several per mil (Fig. 2.12B) and (2) deposition, in lieu of high soil formation rates, can yield high silicate weathering fluxes (Fig. 2.11A). As erosion decreases and deposition increases, weathering intensity increases and approaches 1 (Fig. 2.11D), mirroring the topology of the sawtooth-shaped deposition curve. Nadirs in deposition are countered by peaks in the erosion curve, where soil thickness decreases

(Fig. 2.11B), relative proportions of kaolinite in soil slightly increase (Fig. 2.11C), and weathering intensity drops by $10^{-0.7}$ (70%) within 5,000 years of model time (Fig. 2.11). These shifts in weathering intensity are largely driven by the periodicity and magnitude of the maximum deposition and erosion mass fluxes. Despite large fluctuations in erosion and deposition, the changes in $\Delta^7\text{Li}_{f-s}$ values are small (Fig. 2.11E), mirroring the relative consistency of soil mineralogy over the model run (Fig. 2.11C). These predicted $\Delta^7\text{Li}_{f-s}$ values agree with the sensitivity analyses that highlight the greater influence of lithology and temperature (Fig. 2.10B, C).

Together, these results question how empirical relationship between weathering intensity and $\Delta^7\text{Li}_{f-s}$ values are utilized in estimating silicate weathering fluxes in the geologic past. Weathering estimates gleaned from ancient seawater $\delta^7$Li values (e.g., Misra and Froelich, 2012; Washington et al., 2020) consider the cumulative input of Li from continental rivers, which forces us to think about the apportionment of silicate weathering and Li fluxes across landscapes. Canonically, mountain hillslopes are thought to yield the greatest silicate weathering fluxes (e.g., Larsen et al., 2014b) and are inferred to have the greatest effect on seawater $\delta^7$Li values. Mountain hillslopes, however, are shown to respond quickly to environmental perturbations (e.g., Ferrier and West, 2017), albeit heterogeneous among different portions of hillslopes (Ferrier and Perron, 2020). Their quick returns to steady states suggest that any perturbation would be indiscernible over geologic time. Low-relief terrain, such as floodplains, could instead respond over much longer timescales if a large state change occurs (Ferrier and West, 2017). The silicate weathering flux from floodplains, unlike mountain hillslope, are less well parameterized and are more globally variable. For example, 70% of the silicate weathering associated with the Himalaya orogen is generated within the Ganges floodplain (Bickle et al., 2018; Lupker et al., 2012) whereas only 10% is generated in the Amazon floodplain when considering the Amazonian Andes (Bouchez et al., 2014). The deposition of sediments

atop soils in floodplains could perhaps reconcile these differences in silicate weathering yields among transcontinental drainages, but a "top-down" understanding of soil formation will need further inquiry. If floodplains are important loci for silicate weathering fluxes and are vulnerable to state changes, then the relationship between weathering intensity and $\Delta^7\text{Li}_{f-s}$ values in supply-limited weathering may not be time-transgressive. Importantly, absent changes in subsurface fluid flow that could modify $\Delta^7\text{Li}_{f-s}$ values, these results reinforce the idea that steady $\Delta^7\text{Li}_{f-s}$ values does not necessarily indicate unchanging weathering intensity (i.e., non-uniqueness of $\Delta^7\text{Li}_{f-s}$ values in Fig. 2.1B; findings from Henchiri et al., 2016).

### 2.4.3 Li isotope compositions related to catchment-wide denudation mechanisms

From global analyses of catchment properties, river water chemistry, and numerical models of silicate weathering, we determine that differences in the morphometrics properties within transcontinental drainages play a consistently important role in characterizing $\Delta^7\text{Li}_{f-s}$ values and weathering intensity. With this finding, we summarize the differences in weathering intensity predictions and catchment properties to posit the prevailing weathering processes that govern river water chemistry across catchment settings (Fig. 2.13). We broadly characterize samples into one of three geomorphic settings: high relief catchments (Fig. 2.13A), low relief catchments (Fig. 2.13C), and transitional catchments (Fig. 2.13B).

High relief catchments are often small to intermediate in size and silicate weathering is often thought to be kinetically limited (West et al., 2005), meaning that the rate of river incision and physical erosion often exceeds the rate at which minerals can chemically weather within weathering horizons. Rocks resistant to weathering, such as felsic plutonic and metamorphic rocks, often comprise bedrock in the highest relief settings and thus may be responsible for the maintenance of high

relief erosional landscapes. The rate of soil formation, and thus secondary mineral formation, has been observed to keep pace with incision rates in high relief settings (Larsen et al., 2014a) despite elevated erosion rates, but the weathering intensity is generally thought to be low in areas with high erosion (e.g., Bouchez et al., 2012). Lower MAT and MAP in these high elevation settings may contribute to sluggish soil formation. From the comparison between model-generated and reported weathering intensities (Fig. 2.8B), we posit two plausible modes of landscape denudation that are characteristic of high relief catchments: (1) deep weathering (*sensu* West, 2012) or (2) shallow weathering and landslides (*sensu* Ferrier and Kirchner, 2008; Larsen et al., 2014a). In the former scenario, silicate weathering would be less intense but occurring over a deeper swath of the Critical Zone. This mode of denudation is supported by the modest agreement between reported and modeled low weathering intensities in W2012, a model which assumes that relief is analogous to weathering zone thickness. The presence of topographically and tectonically induced bedrock fractures in high relief environments (e.g.,Moon et al., 2017), alongside deeply rooting organisms (e.g., Tune et al., 2020), would allow water, $O_2$, and $CO_2$ to penetrate deeply below the Earth's surface and promote weathering reactions. In the latter scenario, silicate weathering reactions would be highly concentrated to shallow regolith with mass wasting (i.e., landslides) counteracting the high weathering intensity. While the steady-state models in FK2008 greatly overestimate weathering fluxes at low weathering intensities (Fig. 2.8B), it is also plausible that the occurrence of landslides, and thereby erosion, are greatly underestimated. According to empirical relationships between relief and erosion (e.g., Montgomery and Brandon, 2002), erosion rates exponentially increase beyond a relief threshold in some drainage catchments, lending credence to shallow weathering mechanisms. This mechanism would more readily occur in environments where MAP is high enough to support high soil formation rates (Larsen et al., 2014a). Overall, the extent to which either of

these denudation mechanisms generate observed weathering intensities and $\Delta^7Li_{f-s}$ values remains to be tested; the usage of other geochemical proxies for weathering and erosion (e.g., U activity ratios, $^{10}Be/^{9}Be$, low-temperature thermochronometric systems) alongside Li isotope ratios will be likely be needed to make these inferences for a given catchment.

Juxtaposing high relief catchments, low relief catchments are often intermediate to large in area and silicate weathering is thought to be supply-limited (West et al., 2005), meaning that the rate of physical erosion and supply of fresh minerals lags the rate of incongruent weathering reactions in soils. Large catchments often integrate many rock types but are typically dominated by sedimentary rocks or unconsolidated sediments. Diminishing relief in these settings, perhaps influenced by bedrock types and tectonics, reduces the gravitational potential energy of the environment, and thus yields landscapes that tend to be net aggradational. The spatiotemporal understanding of mineral and water transit through low relief environments are less well understood than in high relief settings, although it is widely observed that soil development is primarily a function of the distance sediments are from active channels (e.g., Kraus, 1999). The input of sediment through deposition laterally from river channels may be an important mode of mass transfer (Fig. 2.11) that has received less attention in literature on silicate weathering, yet its importance remains to be tested. Increases in fluid and mineral residence times and the presence of finer-grained sediments catalyzes secondary mineral formation and perhaps yields subtle increases in $\Delta^7Li_{f-s}$ values (Fig. 2.10C). Generally, MAT and MAP tend to be high in these environments, which would enable more intense weathering. Denudation in this environment is largely driven by weathering in soils, as is indicated by FK2008-data comparison of weathering intensity estimates (Fig. 2.8B). Unlike high-relief catchments, low-relief catchments may be more prone to internal and external perturbations that affect weathering on longer timescales.

Moreover, inferring local weathering signals in rivers draining large catchments may be challenging given that river water chemistry integrates weathering occurring upstream of the locally low relief terrain. This further motivates the need to refine silicate weathering and Li fluxes along the length of transcontinental rivers and their influence on oceanic Li isotope compositions through time.

Positioned between high- and low-relief catchments are so-called "transitional" catchments, which contain attributes of both endmember geomorphic environments (Fig. 2.13B). These environments tend to be composed of sedimentary rocks and unconsolidated sediments and have intermediate MAP, MAT, and mean local relief. Weathering in these environments is thought to be kinetically limited, but weathering intensities are intermediate among reported weathering intensities (Fig. 2.1B). The conspicuous inability of W2012 or FK2008 to predict intermediate weathering intensities (Fig. 2.8A) suggest that some combination of denudations mechanisms occurring in high- and low-relief catchments are also operating in transitional catchments. Notably, it is in these transitional catchments where the highest $\Delta^7\text{Li}_{f-s}$ values occur (Fig. 2.4), which implies that the influence of fluid flow on $\Delta^7\text{Li}_{f-s}$ values in these catchments is most salient. The two mechanisms we posit induce these elevated $\Delta^7\text{Li}_{f-s}$ values are hyporheic exchange near active river channels (e.g., Maffre et al., 2020; Pogge von Strandmann and Henderson, 2015) and Rayleigh fractionation along groundwater flow paths (e.g., Bohlin and Bickle, 2019). The former appears most relevant where floodplains begin to develop along fluvial distributive systems river reaches and corresponds with the deposition of freshly eroded sediments (Pogge von Strandmann and Henderson, 2015). Maffre et al. (2020) suggest that in these incipient floodplains, the Li budget is greatest in the dissolved load of rivers and when these waters are introduced in adjacent floodplains during a flood, Rayleigh fractionation enables $\Delta^7\text{Li}_{f-s}$ values to increase beyond the batch fractionation limit. The latter process, which is largely a

model finding (Bohlin and Bickle, 2019) but has been recently observed in fractured bedrock (Golla et al., 2021), illustrates that silicate weathering concomitant with groundwater fluid flow induces a Rayleigh fractionation along deep flow paths. The less frequent occurrence of high $\Delta^7Li_{f-s}$ values in high- and low-relief catchments may support the possibility of groundwater flow in inducing high $\Delta^7Li_{f-s}$ values. At high relief, rates of subsurface fluid flow may exceed the rate of incongruent weathering reactions such that secondary mineral formation imparts less of an effect on $\Delta^7Li_{f-s}$ values, leading to lower values. In low relief environments where fluid flow occurs much more slowly, the rate of incongruent weathering reactions exceeds the rate of fluid flow and therefore $\Delta^7Li_{f-s}$ values approach the limit for batch fractionation (Fig. 2.1A). To discern which process is more relevant for a given sample, information about subsurface structure and hydrology will need to be gleaned. Ultimately, a better grasp of the processes that induce the highest $\Delta^7Li_{f-s}$ values, and how these processes relate back to observable catchment properties, will further enhance our understanding of weathering intensity shifts over geologic time.

## 2.5 Conclusion

This study of a global compilation of river water Li isotope compositions helps to elucidate the relationships of river water chemistry with their drainage catchment climatic, lithologic, and morphometric properties. By employing various statistical techniques, including linear regressions and two-way analysis of variance, we quantify the strength of variable correlations with river water chemistry and the coupling of catchment-wide properties with one another. In general, we find that that river water $\delta^7$Li values cannot be adequately explained by individual catchment properties, but that the effect of climatic (mean annual temperature and precipitation) and morphometric (mean local relief, catchment area, and mean hillslope angles) properties, improves significantly when coupled with the proportion of rock types

in catchments.

We then utilize two weathering models – one which was developed for steady state environments (West, 2012) and another which models soil formation over time (Ferrier and Kirchner, 2008) – to predict the influence of catchment properties on weathering intensity. We find that while the steady-state model better represents weathering in kinetically limited weathering regimes, the time-dependent model better represents weathering in supply-limited weathering regimes. Whereas weathering intensity predictions from the steady-state model (W2012) are equally sensitive to climatic, lithologic, and morphometric information, the predictions from the time-dependent model (FK2008) show a dominant control of morphometric properties, particularly mean local relief and its influence on erosional and depositional mass fluxes.

In unifying catchment properties and weathering intensity predictions, we characterize catchments as one of three catchment types – high-relief, low-relief, and transitional – and discuss plausible denudation mechanisms that influence $\Delta^7\text{Li}_{f-s}$ values and weathering intensity in each. This discussion underscores that while high relief environments are better understood both in terms of denudation mechanisms and Li isotope systematics, more knowledge gaps exist for transitional and low-relief catchments. Transitional catchments tend to yield the highest $\Delta^7\text{Li}_{f-s}$ values of the three catchment types and although the loci of the $\Delta^7\text{Li}_{f-s}$ values and the mechanisms that yield them are uncertain, two compelling hypotheses (Maffre et al., 2020; Pogge von Strandmann and Henderson, 2015) give roadmaps for future investigations. Understanding denudation mechanisms in low-relief catchments remains challenging because (1) silicate weathering fluxes are highly variable in these catchments and less well parameterized, (2) low-relief catchments are susceptible to transient perturbations by internal and external variables, and (3) the chemistry of river water that flows through them are imprinted with inherited, upstream weather-

| Subscript | Description |
|---|---|
| f | Fluid (river water) |
| s | Source rock |
| f-s | Fluid minus source rock (i.e., weathering signal) |
| soil | Soil |
| i | Specific mineral phase |
| N | Total number of mineral phases |
| qtz | quartz |
| plag | plagioclase feldspar |
| kspar | potassium feldspar |
| bt | biotite |
| zir | zircon |
| kao | kaolinite |

Table 2.5: Description of subscripts

ing signals. We ultimately hypothesize that the deposition of sediments from rivers onto adjacent floodplains may be able to resolve the wide-ranging predictions for silicate weathering in low-relief environments. Altogether, our study corroborates the foremost hypothesis of a weathering regime control on $\Delta^7\text{Li}_{f-s}$ values (e.g., Dellinger et al., 2015; Huh et al., 2001). Through our compilation of catchment properties and their input to numerical models, we further this hypothesis and provide a template with which to probe in the environmental influences on river water chemistry that thereby refine our understanding of surface processes and their role in the geologic carbon cycle, past and present.

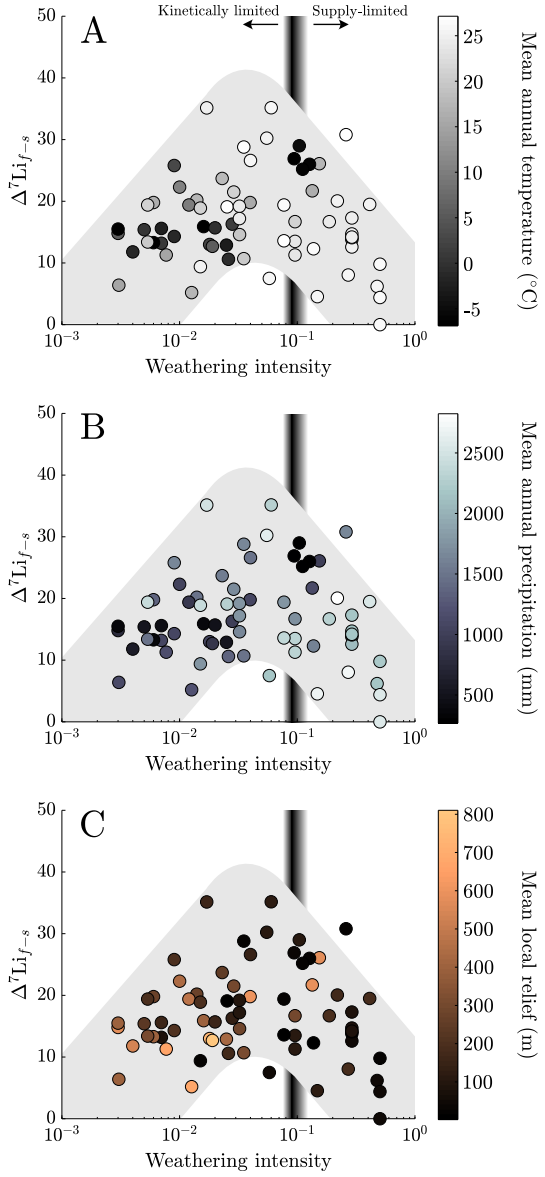


Figure 2.6: Plots of the empirical relationship between $\Delta^7\text{Li}_{f-s}$ values and weathering intensity (Dellinger et al., 2015) with mean catchment properties (A) Mean annual temperature (MAT), (B) Mean annual precipitation (MAP) and (C) mean local relief. The vertical black band corresponds to the boundary between kinetically limited (weathering intensity $< 10^{-1}$) and supply-limited (weathering intensity $> 10^{-1}$) weathering regimes (same bar as in Fig. 1B). Gray shape indicates range of published weathering intensity and $\Delta^7\text{Li}_{f-s}$ values from Dellinger et al. (2015).

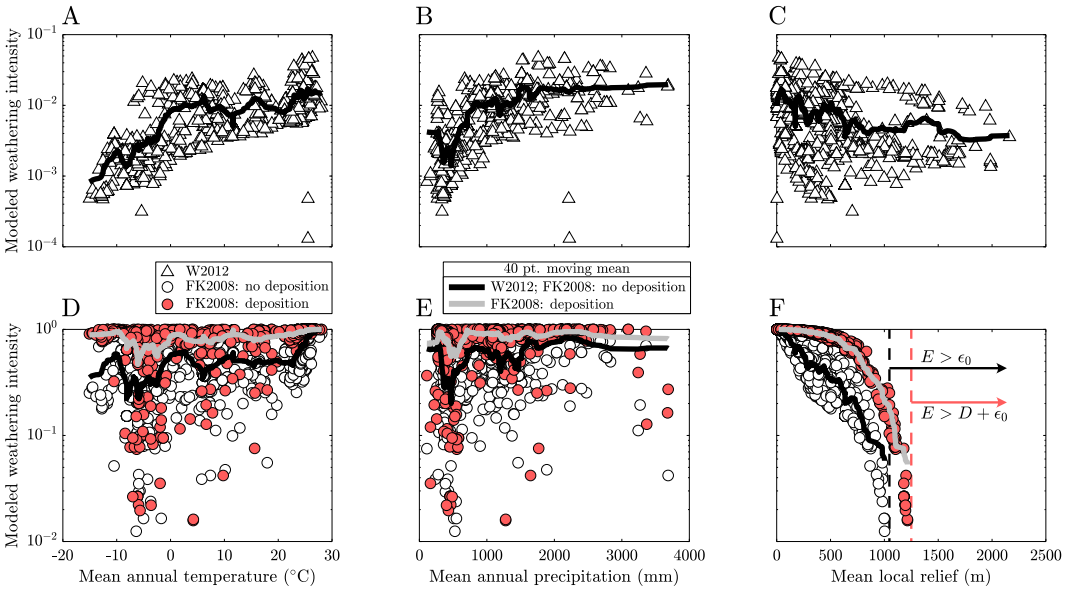


Figure 2.7: Predicted weathering intensity for the dataset plotted as a function of MAT (A, D), MAP (B, E) and mean local relief (C, F) for steady state (W2012; white triangles) and time-dependent (FK2008; colored circles) weathering models. (F) Dashed vertical lines indicate limits for FK2008 model predictions where weathering intensity cannot be predicted due to conditions where the rate of mass removal from soil (erosion $E$) exceeds the rate of mass addition (soil formation $\epsilon_0$ $\pm$ deposition $D$).

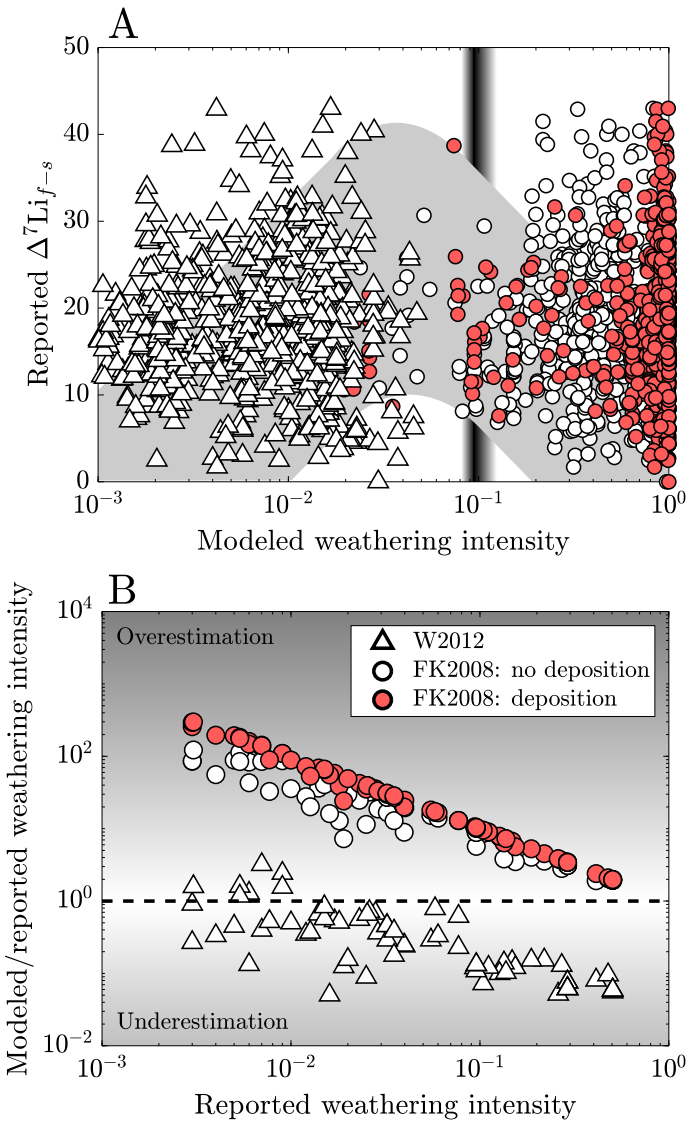


Figure 2.8: (A) Reported $\Delta^7Li_{f-s}$ values vs. modeled weathering intensity for all samples. Gray shape indicates range of published weathering intensity and $\Delta^7Li_{f-s}$ values from Dellinger et al. (2015). Vertical black band indicates boundary between supply-limited ($> 10^{-1}$) and kinetically limited ($< 10^{-1}$) weathering regimes. (B) The ratio of modeled to reported weathering intensity vs. reported weathering intensity for samples with independent weathering intensity estimates. Symbols above the horizontal black dashed line indicate overestimated modeled weathering intensities whereas symbols below indicate underestimated modeled weathering intensities.

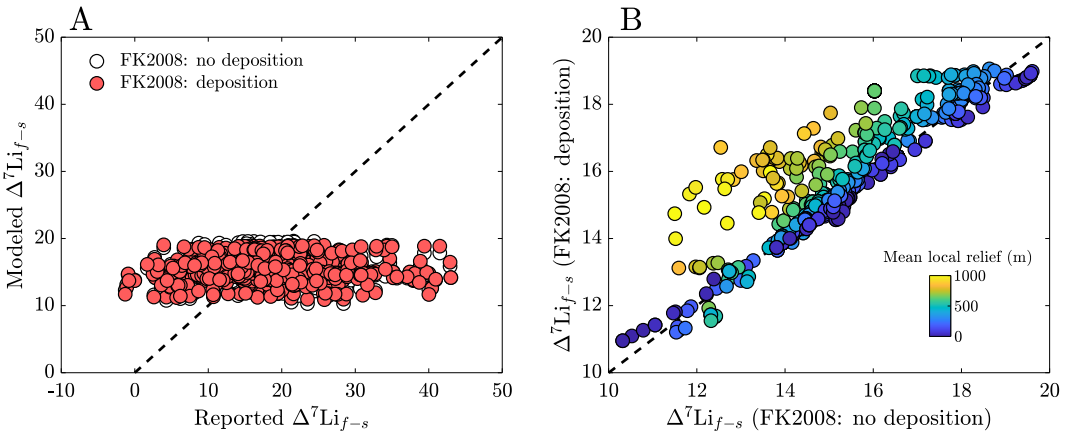


Figure 2.9: (A) Modeled $\Delta^7Li_{f-s}$ values (found with time-dependent FK2008 models) vs. reported $\Delta^7Li_{f-s}$ for all samples. (B) Comparison of modeled $\Delta^7Li_{f-s}$ values for FK2008 models with and without deposition included as a mode of mass transfer. Colors of symbols correspond to catchment-average mean local relief. Black dashed lines in panels A and B are 1:1 lines.

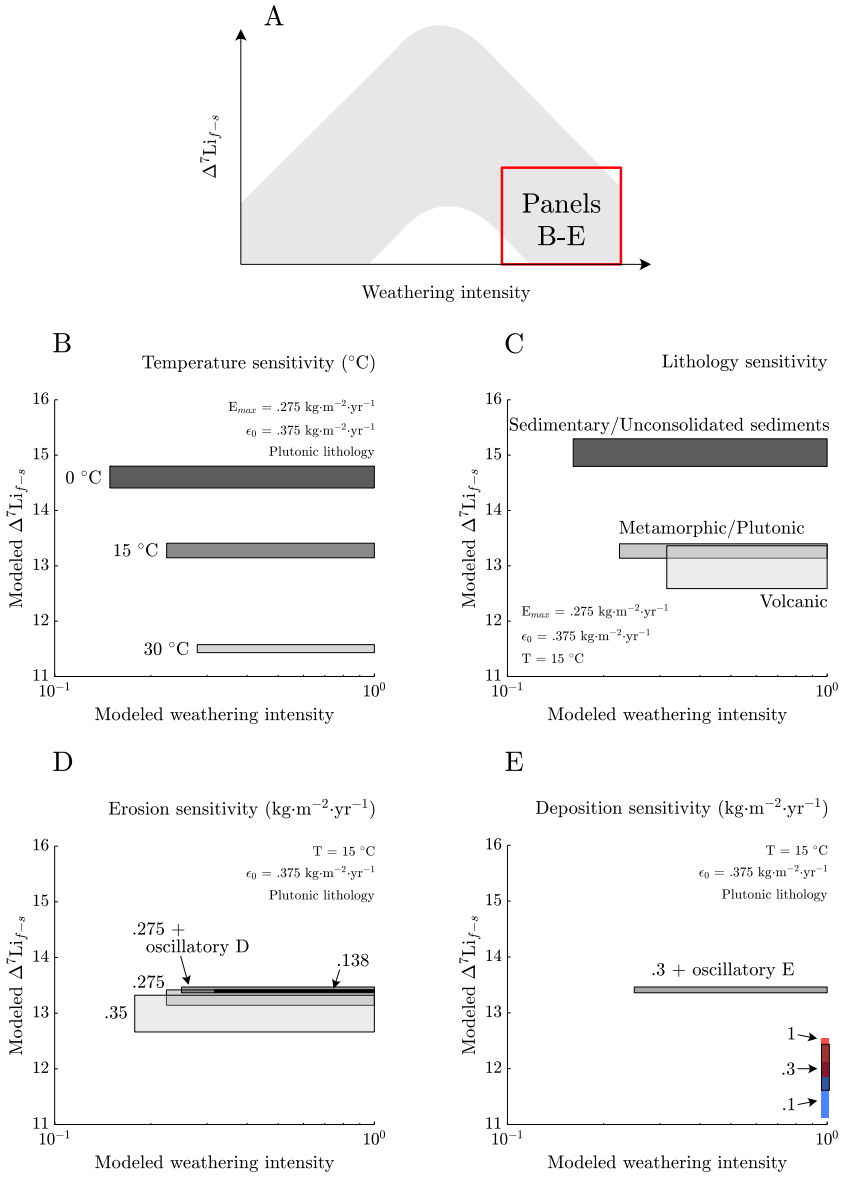


Figure 2.10: The sensitivity of time-dependent modeled $\Delta^7Li_{f-s}$ values and weathering intensities to (B) temperature (C), lithology, (D) erosion, and (E) deposition. All results fall within the red square of $\Delta^7Li_{f-s}$-weathering intensity space (A) and were driven by oscillatory erosion (± deposition). Each rectangle corresponds to range of modeled $\Delta^7Li_{f-s}$ values and weathering intensities as the system approaches a relatively steady state (i.e., between 85-100 kyr of model time). Values or words beside each box correspond to the imposed boundary conditions; all other relevant domain variables, which are held constant through each simulation, are listed within each Cartesian space.

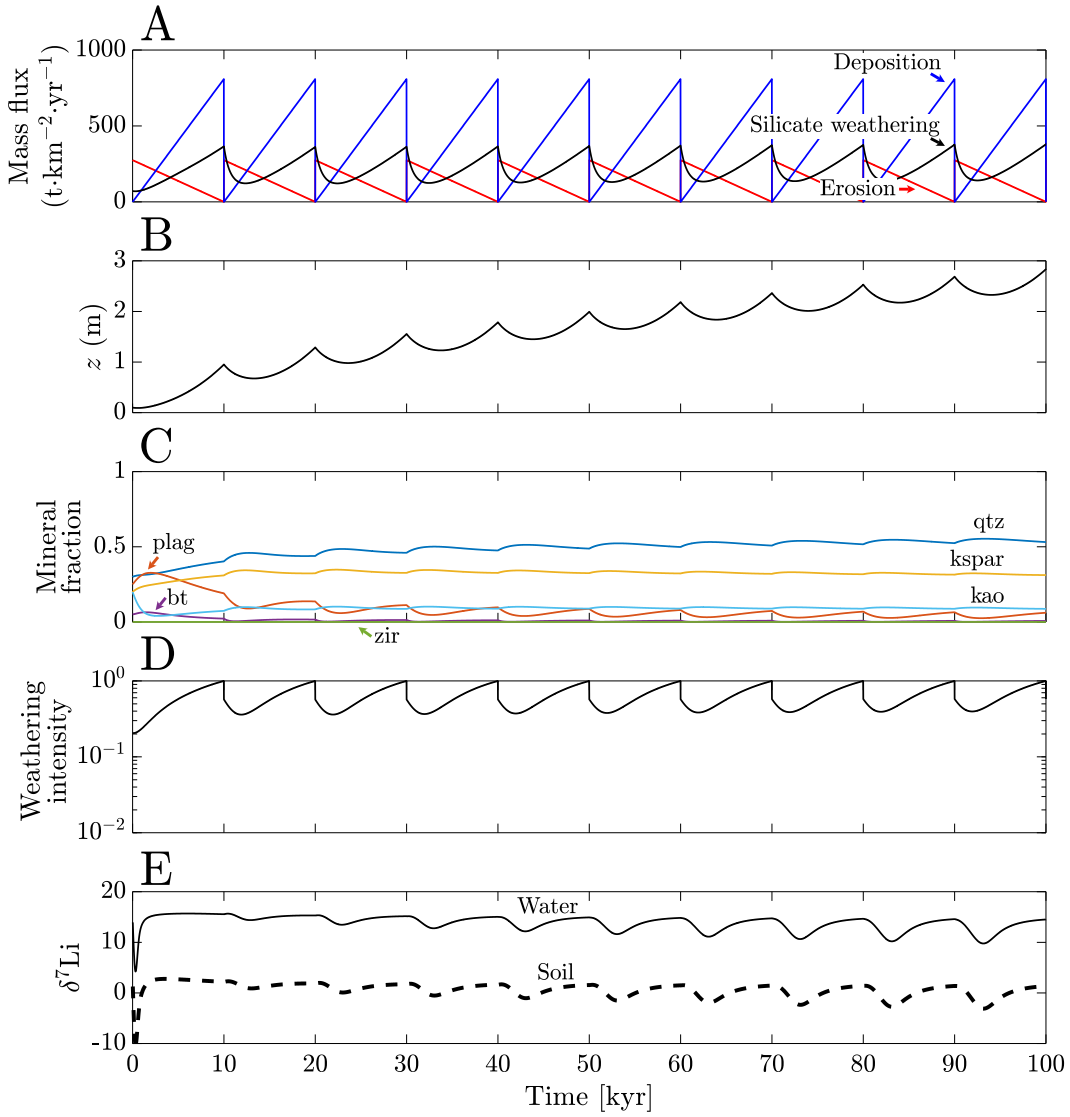


Figure 2.11: Time-dependent model predictions (FK2008) of (A) silicate weathering fluxes (black line and imposed erosion (red line) and deposition (blue line) mass fluxes that vary periodically and out-of-phase over time, and resulting (B) weathering zone thicknesses, (C) mineral fractions in soil, (D) weathering intensity, and (E) $\delta^7\mathrm{Li}_f$ and $\delta^7\mathrm{Li}_{source}$ values. Mineral abbreviations include: qtz (quartz), kspar (potassium feldspar), kao (kaolinite), plag (plagioclase feldspar), bt (biotite), zir (zircon). This model assumes an input plutonic lithology, a constant MAT of 15 °C, and a constant soil formation rate $\epsilon_0$ of 0.375 kg m$^{-2}$ yr$^{-1}$ over 100 kyr of model time. Input deposition rate is roughly equivalent to a 0.3 mm/yr aggradation rate and erosion rate is analogous to one generated in a catchment with a mean local relief of ∼600 m.

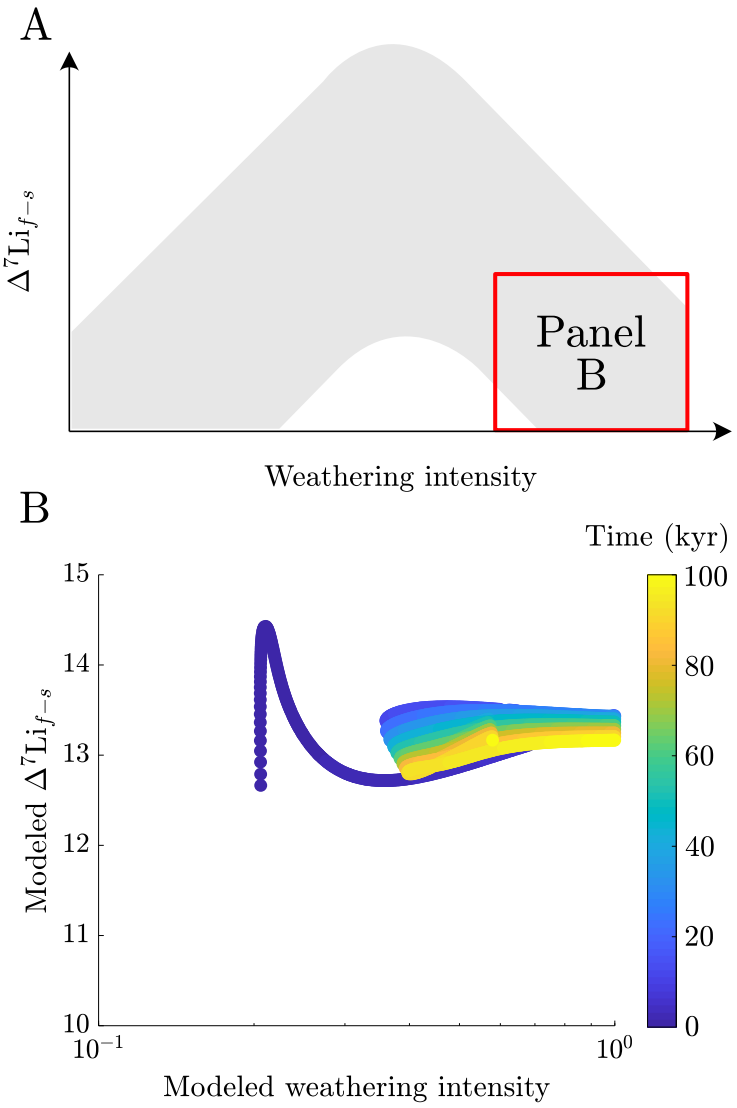


Figure 2.12: (A) Location of panel B within observed range of $\Delta^7Li_{f-s}$ values and weathering intensities, where the gray shape indicates the range of published weathering intensity and $\Delta^7Li_{f-s}$ values from Dellinger et al. (2015). (B) Model predictions of $\Delta^7Li_{f-s}$ and weathering intensity using the transiently imposed erosion and deposition mass fluxes (same model results as presented in Fig. 2.10). The color of the line corresponds to model time (kyr).

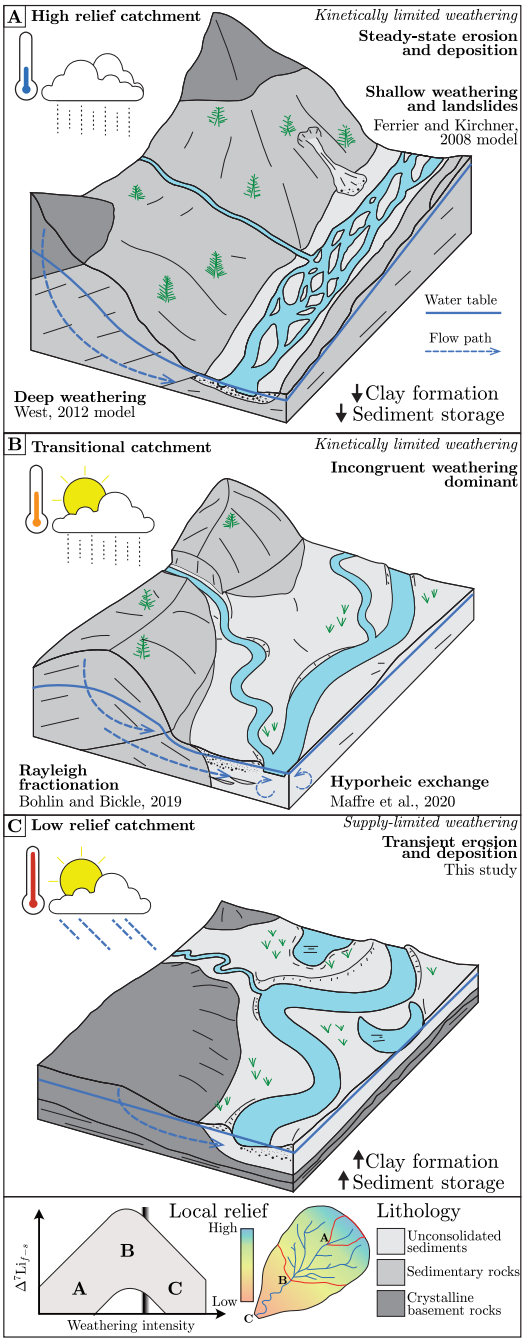


Figure 2.13: Schematic diagrams of key catchment types – (A) high relief catchments, (B) transitional catchments, and (C) low relief catchments – which includes their catchment properties, proposed methods of fluids and solid mass transfer, and what portions of $\Delta^7\mathrm{Li}_{f-s}$-weathering intensity space they likely occupy.

# Chapter 3

# Rapid silicate weathering response in floodplains during the Paleocene-Eocene Thermal Maximum

During hyperthermal events, such as the Paleocene-Eocene Thermal Maximum (PETM), rates of silicate weathering are thought to increase and offset the rapid and massive input of $CO_2$ into the atmosphere and ocean. However, limited quantitative evidence exists of the silicate weathering response on continents to the PETM. Here we show that silicate weathering intensity in the Bighorn Basin, Wyoming (USA) increased during the PETM and remained high during at least the initial stage of recovery, even as atmospheric $pCO_2$ decreased. We quantify weathering intensity by first measuring Li isotope ratios of the clay size fraction of silicate minerals in floodplain deposits. We then compare Li isotope ratios of the floodplain deposits with those of bedrock exposed in the basin-bounding ranges, using trace element ratios to partition the source of floodplain clays between basement rock and Cretaceous shale endmembers. We find that soils that formed farthest from ancient river channels are more sensitive to changes in climate than near-channel soils, demonstrating that the secular change is at least in part controlled by in situ floodplain weathering. The simplest explanation for these changes relates to increased mean

annual temperature, $pCO_2$ and seasonal fluctuations in water table height, all of which promote mineral dissolution and precipitation reactions. Although the sensitivity to climate from weathering on hillslopes is well accepted, these findings newly demonstrate that weathering in floodplains also responds to climate change.

## 3.1 Introduction

The Paleocene-Eocene Thermal Maximum (PETM) was a 190 kyr-long event during which an abrupt input of carbon to the ocean and atmosphere increased global average temperatures by 5–8 °C (McInerney and Wing, 2011; Wing et al., 2005), more than doubled atmospheric $CO_2$ concentrations (Gutjahr et al., 2017; Haynes and Hönisch, 2020; Fig. 3.1A), and profoundly changed marine and terrestrial biomes (McInerney and Wing, 2011; Wing et al., 2005). Although the conditions that induced and sustained the hyperthermal event have been studied extensively (e.g., Bowen et al., 2015; Denis et al., 2021; Gutjahr et al., 2017; Inglis et al., 2021; Lyons et al., 2019), the recovery phase of the event remains less constrained. Silicate weathering and organic carbon (OC) burial are known processes that promote the withdrawal of carbon from the exosphere (i.e., ocean and atmosphere) and are thus posited to have enabled global climate to return to its pre-PETM state (e.g., Bowen and Zachos, 2010; Komar and Zeebe, 2011; Torfstein et al., 2010). Continental erosion rates increased after the onset of the PETM (e.g., Molnar, 2001; John et al., 2012; Sharman et al., 2017) which likely enhanced riverine fluxes of OC and dissolved weathering products to the ocean (e.g., Hilton and West, 2020). The composition of marine sediments (e.g., Dickson et al., 2015; Komar and Zeebe, 2011; Penman et al., 2016; Ravizza et al., 2001; Self-Trail et al., 2012) and models of the carbon and silicon cycles (e.g., Komar and Zeebe, 2021; Panchuk et al., 2008; Penman, 2016) corroborate these increases, but comparatively little is known about how or where silicate weathering responded on continents. To improve upon these marine

records and model findings, more geochemical evidence from nonmarine sedimentary archives needs to be gathered.

Landscapes respond unevenly to climatic perturbations (e.g., Romans et al., 2016; Whipple, 2009), yet a key variable that underpins silicate weathering responses across continents is the supply of fresh, un-weathered minerals to near-surface weathering zones. Mountain hillslopes are a dominant locus for silicate weathering in modern environments (e.g., Larsen et al., 2014b) because incising rivers generate relief that enhances the supply of fresh bedrock to the Earth's surface. The responsiveness of river incision to climate (e.g., Murphy et al., 2016) suggests that silicate weathering in mountain hillslopes may be the primary mechanism by which $CO_2$ is sequestered after hyperthermal events. However, these eroding landscapes are poorly preserved in the geologic record.

In contrast, floodplains are readily preserved in sedimentary records and serve as significant repositories of past Earth surfaces. Yet, the controls of silicate weathering in floodplains are less well understood. Generally, river-borne sediments, having already undergone weathering in the upper reaches of catchments (Dosseto et al., 2006), are delivered to adjacent floodplains during avulsions and overbank deposition. Low supply of fresh sediments and long fluid-rock interaction time, characteristic of floodplains, favor high silicate weathering intensities (e.g., Bouchez et al., 2014; Dellinger et al., 2014, 2017). Globally, however, the resultant silicate weathering flux is variable, amounting to as little as 10% of the net catchment weathering flux in some drainages (e.g., Amazon floodplain; Bouchez et al., 2014) to upwards of 70% in others (e.g., Ganges floodplain; Bickle et al., 2018). Moreover, in ancient floodplain deposits, conflicting evidence exists regarding the silicate weathering response to changes in climate across Paleogene hyperthermal events. Despite the similarity in magnitude and direction of change in climate during these events, some ancient floodplains contain evidence of marked increases in weathering

intensity (Clechenko et al., 2007), whereas others show little change (Wang et al., 2017). Further efforts to refine controls of silicate weathering in floodplains are necessary to evaluate their role in climate modulation.

In this study, we quantify silicate weathering intensities in a well-studied, ancient floodplain in the Bighorn Basin, Wyoming, USA that spans the PETM. We apply a recently developed empirical relationship (Dellinger et al., 2017) which relates the Li isotope composition of river sediments and bedrock (hereafter referred to as source rocks) to silicate weathering intensity. Whereas Dellinger et al. (2017) compares bedrock with sediment suspended in the water column of rivers, we compare bedrock with paleo-floodplain sediments. When geochemical data are contextualized alongside stratigraphic and sedimentological information, we document the variability of silicate weathering intensity in floodplains and underscore the important roles of landscape position and climate.

## 3.2 Geologic setting and samples

All samples were collected in the Bighorn Basin in northern Wyoming, USA: an alluvial, intermontane basin (Dickinson et al., 1988) that formed 70 Ma during the Laramide orogeny (Fig. A.7). Pre- and postdating the PETM, climate in the Bighorn basin is classified as temperate and humid, promoting the growth of deciduous flora such as conifers (McInerney and Wing, 2011; Wing and Harrington, 2001; Wing et al., 2005; Smith et al., 2008). In contrast, climate during the PETM is classified as hot and seasonally wet (e.g., Baczynski et al., 2017), promoting the growth of tropical flora including dicots and palms. The basin contains well-preserved alluvial channel sandstones and floodplain siltstones and mudstones that have undergone variable degrees of pedogenesis.

All paleosols were sampled at Polecat Bench in Powell, WY, which is a well-characterized outcrop positioned along the basin axis in the northernmost extent

of the basin. This site contains sedimentary units that span the latest Paleocene and onset, main body, and recovery phases of the PETM. Stratigraphic elevations were converted to time with respect to the carbon isotope excursion (CIE) using the age model of van der Meulen et al. (2020). In accordance with pedogenic and sedimentologic features, all paleosols were classified as either composite, crevasse splay, or cumulative soils (Bown and Kraus, 1987; Kraus, 1999), which are facies characterizations of soils that describe soil formation in response to episodic (composite, crevasse splay) or continuous (cumulative) sedimentation. These soil facies qualitatively indicate the paleo-landscape position of the soil at the time of formation. Source rock samples were retrieved from outcrops on the flanks of the basin.

## 3.3 Quantifying silicate weathering intensity

The clay-sized fraction ($< 2\mu$m) of paleosols and whole rock powders of source rocks were analyzed for major and trace element concentrations and Li isotope ratios. Using an immobile element mixing model (see Section A.2.3), we identify the proportion of each source rock that is weathered to form secondary clays in paleosol samples. Two endmembers were identified – a shale and feldspar-bearing igneous rock endmember – and we express proportions as fractions where

$$f_{\text{shale}} + f_{\text{igneous}} = 1 \tag{3.1}$$

and $f_{\text{shale}}$ and $f_{\text{igneous}}$ correspond to the fractions of shale and igneous rocks, respectively. The differences between measured $\delta^7\text{Li}_{\text{clay}}$ values and mixing model-determined $\delta^7\text{Li}_{\text{source}}$ values (notated as $\Delta^7\text{Li}_{\text{clay}-\text{source}}$) enabled the quantification of silicate weathering intensities (Dellinger et al., 2017), which is mathematically

expressed as

$$\text{Weathering intensity} = \frac{W}{W+E}. \tag{3.2}$$

and approaches a maximum value of 1 as silicate weathering intensity increases. All descriptions of analytical and computational methods can be found in the Appendix.

The measured $\delta^7\text{Li}_{\text{clay}}$ values range from -2.3 to +0.6 ‰. Based on source rock mixing methods (see Section A.2.3 for detailed methods), calculated $\delta^7\text{Li}_{\text{source}}$ values range from 1.1 to 2.4 ‰. In contrast to the $\delta^7\text{Li}_{\text{source}}$ values which that are roughly constant across the PETM, $\delta^7\text{Li}_{\text{clay}}$ values steadily decrease through the main body and into the recovery phase of the event (Fig. 3.1B). As a result, predicted weathering intensities increase by 0.15 on average during the main body of the event and remain high into the recovery phase (Fig. 3.1C). It is worth noting that predicted negative weathering intensities are empirical artifacts which arise when clay and source $\delta^7$Li values are within $\sim$ 1‰ of one another (Dellinger et al., 2017); however, we elect to report negative weathering intensities to convey the relative differences among all samples.

When samples are grouped in accordance with their soil facies (composite, crevasse splay, or cumulative soils), predicted weathering intensities show consistent inverse correlations with the fraction of primary shale ($f_{\text{shale}}$) (Fig. 3.2), where higher $f_{\text{shale}}$ yields lower weathering intensities. Within a given soil facies, samples that predate or coincide with the onset phases are regressed with steeper negative slopes, whereas samples within the body and recovery phases are regressed with shallower negative slopes. Among all soil facies, soils that formed closer to the ancient river channel are regressed with shallower negative slopes, whereas soils that formed more distal are regressed with steeper negative slopes (Fig. 3.2).

## 3.4 Influence of climate and landscape position on floodplain weathering

The Li isotope data indicate a rapid and significant increase in silicate weathering intensity in response to the climatic perturbation. This stepwise increase in weathering intensity during the PETM coincides with major shifts in atmospheric $pCO_2$ (Gutjahr et al., 2017; Haynes and Hönisch, 2020), hydroclimate (Kraus et al., 2013, 2015; Smith et al., 2008), floral composition (Wing and Harrington, 2001; Wing et al., 2005), and floodplain architecture (Abdul Aziz et al., 2008; Foreman, 2014; Kraus et al., 2015) in the Bighorn Basin. The >3 ‰ negative excursion in $\delta^7Li_{clay}$ values is likely driven by changes in weathering resulting from these environmental changes because sediment aggradation rates (Clyde et al., 2007; van der Meulen et al., 2020) and provenance (DeCelles et al., 1991a; May et al., 2013; Neasham and Vondra, 1972; steady $\delta^7Li_{source}$ values in this study (Fig. 3.1B)) remained constant across the PETM.

Several lines of evidence suggest that a combination of environmental variables is necessary to explain these weathering trends. First, the outright control of temperature/$pCO_2$ on observed trends can be ruled out because silicate weathering intensity a) fluctuates during the main body of the PETM when temperature/$pCO_2$ are relatively steady and b) remains high in the recovery phase as temperature/$pCO_2$ have returned to pre-PETM levels. Second, distinct weathering relationships are found when the fraction of shale-derived sediment in the paleosol ($f_{shale}$), climate, and soil facies are considered together (Fig. 3.2). Shales, which are lithified byproducts of past continental weathering, weather less readily at Earth's surface than primary igneous rock-derived minerals like plagioclase or biotite (e.g., White and Buss, 2014), explaining the consistent inverse relationships between weathering intensity and $f_{shale}$. This lithologic control is then modulated by climate and landscape position. High temperatures and $pCO_2$ enable more in-

tense silicate weathering (e.g., Winnick and Maher, 2018) that effectively subdue the lithologic control on weathering intensity. For all soil facies during the main body of the PETM, the flattened slopes in weathering intensity-$f_{\text{shale}}$ space indicates a reduced effect of $f_{\text{shale}}$ on weathering intensity. Lastly, the difference in weathering trends between varying climate states is most pronounced in soils that formed far from the channel. Composite and crevasse splay soils, which are coarser grained, better drained, and topographically high within floodplains (e.g., Kraus, 1999), form in oxidizing conditions that more readily facilitate silicate weathering reactions. Cumulative soils, in contrast, tend to be finer grained and more poorly drained, favoring reducing conditions and slow water movement that keep silicate minerals from chemically weathering. Therefore, in this alluvial system, when climate does change, more limitations of silicate weathering are removed in cumulative soils than their near-channel counterparts, yielding a stronger silicate weathering response.

The simplest explanation for these weathering trends is the fluctuation of the water table in response to increased seasonality during the PETM (Fig. 3.3). Alongside increases in mean annual temperature (MAT) and $p\text{CO}_2$ during the main body, mean annual precipitation (MAP) in the Bighorn Basin decreased but became more seasonal (Kraus and Hasiotis, 2006; Kraus et al., 2015; Smith et al., 2008). Large rainfall events and increased evapotranspiration in the basin led to better-drained soils and large fluctuations in water table height (Kraus et al., 2013; Smith et al., 2008). As a result, soil water contents would change widely throughout a year, perturbing the saturation state of the aqueous solutions in soil that ultimately catalyzed mineral dissolution and precipitation reactions. In contrast to well-drained proximal soils, distal soils retain water due to high clay content (i.e., due to high matric potentials) and therefore require greater changes in in water table height to enable oxidative weathering. Periods of poor soil drainage and high MAP during the

main body of the PETM may also explain the occurrences of low silicate weathering intensity. We postulate that the relatively high silicate weathering intensity during the recovery phase is due to sustained seasonality of rainfall (Kraus et al., 2015) that promotes intense weathering. Although unproven, it is also possible that with the incipient return of conifer forests alongside seasonal precipitation, an increase in root mass sustained high soil $pCO_2$ and transiently increased weathering rates (e.g., Algeo and Scheckler, 2010) despite atmospheric $pCO_2$ returning to pre-PETM levels. A third possibility is that detrital floodplain sediments from upstream comprise a significant proportion of paleosol clay-sized fractions that mask an undetected decrease in silicate weathering intensity during the recovery phase. However, the consistency of weathering trends among soil facies suggest that the detrital component is minimal. And, if these detrital clay-sized sediments are derived from the hinterland, those which have higher $\delta^7$Li values than authigenic clays, the inferred silicate weathering intensities presented herein would thus represent minimum values. It is possible that a return to low silicate weathering intensity occurs further beyond 150 kyr (Fig. 3.3), which could be tested via analysis of samples further up-section.

Altogether, these findings newly demonstrate that floodplain weathering dynamically responds to climate change. Unlike weathering in mountain hillslopes whose climatic sensitivity is tied to the kinetics of silicate mineral dissolution (e.g., Bufe et al., 2021), floodplain weathering involves mineral residence times long enough to counter these dissolution kinetics (e.g., Dosseto et al., 2006; Torres et al., 2017, 2020). Instead, weathering in floodplains is sensitive to climatically driven changes in water flow through soils where better soil drainage begets more intense weathering. The rapid and large weathering response to climate change in the Bighorn Basin during the PETM might be characteristic of intermontane basins whose steady supply of less weathered silicate sediments from adjacent uplifts (Clyde et al., 2007;

van der Meulen et al., 2020) does not limit silicate weathering. These findings ultimately expand upon recent studies that argue for floodplains as a carbon sinks (e.g., Torres et al., 2016; Bufe et al., 2021) and underscore the relevance of floodplain biogeochemical cycling in the carbon cycle over much wider timescales than previously thought.

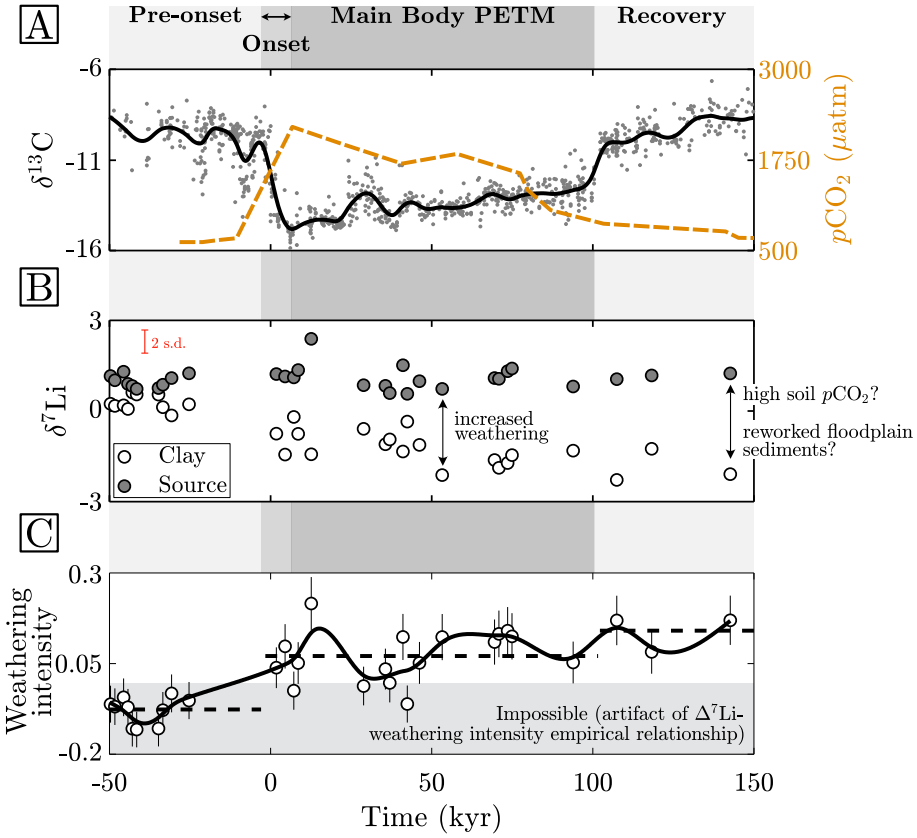


Figure 3.1: Atmospheric and soil chemistry across the PETM. Gray vertical bands represent key time intervals across the event (McInerney and Wing, 2011; van der Meulen et al., 2020) and time is presented relative to the onset of the carbon isotope excursion. A) Compilation of pedogenic carbonate $\delta^{13}$C values from the Bighorn basin (van der Meulen et al., 2020) and model-derived atmospheric $p$CO$_2$ partial pressures (Haynes and Hönisch, 2020). The black line corresponds to locally weighted mean carbonate $\delta^{13}$C values with a 2.5 % averaging window. B) Measured paleosol clay ($< 2\mu$m size fraction) $\delta^7$Li values and mixing model-determined source rock $\delta^7$Li values for each paleosol. The red error bar corresponds to a maximum, conservative error for each data (0.4 ‰, 2 standard deviations). C) Empirically determined silicate weathering intensity from $\Delta^7\text{Li}_{\text{clay}-\text{source}}$. Error (1) accounts for the error in $\Delta^7\text{Li}_{\text{clay}-\text{source}}$ and the $\Delta^7\text{Li}_{\text{clay}-\text{source}}$-weathering intensity empirical relationship (Dellinger et al., 2017). Weathering intensity $< 0$ cannot be realized and are artifacts of the empirical relationship. The black dashed lines are mean weathering intensities over different time intervals (pre-onset, onset + main body, recovery), and the black line corresponds to locally weighted mean weathering intensities with a 2.5 % averaging window.

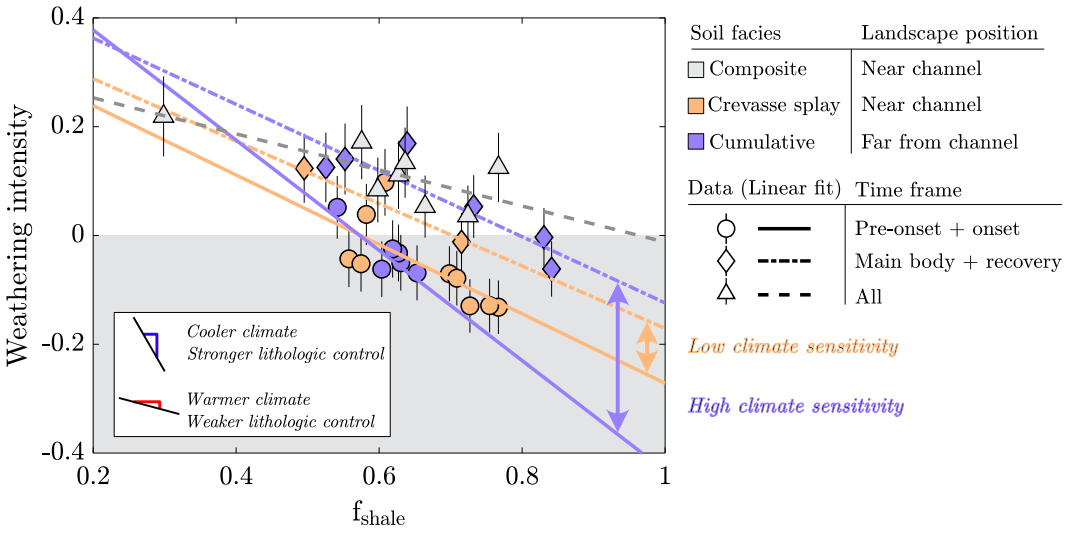


Figure 3.2: Weathering intensity as a function of the fraction of primary shale sediments ($f_{\text{shale}}$) from which secondary clays formed (error bars are $1\sigma$). Data are grouped according to soil type and time intervals of the PETM, and lines correspond to linear fits through corresponding data groups. The gray shaded region indicates artificial weathering intensity predictions that are $< 0$. Linear fits with steeper negative slopes broadly correspond to stronger lithologic controls during cooler climates whereas shallower negative slopes broadly correspond to weaker lithologic controls during warmer climates.

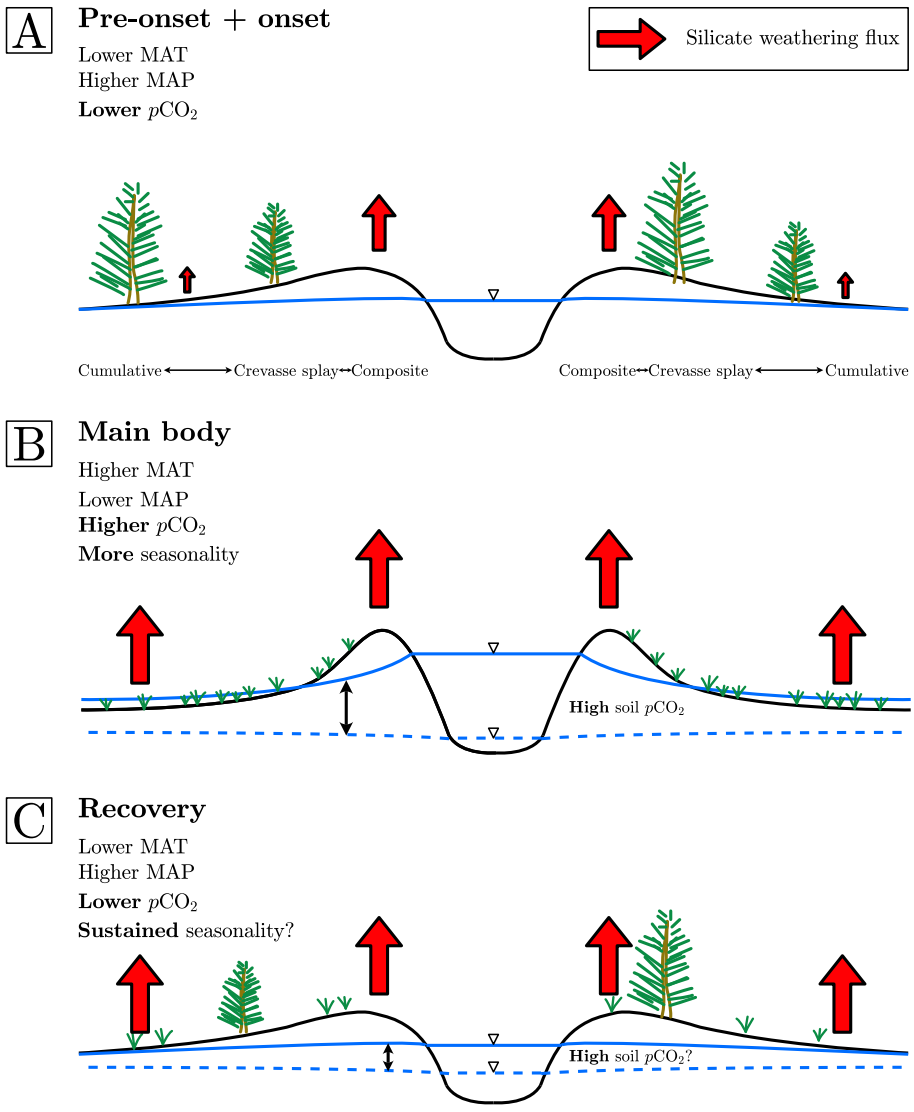


Figure 3.3: Conceptual cross-sections of floodplains in the Bighorn basin spanning the pre-onset and onset (A), main body (B), and recovery (C) phases of the PETM. The relative location of each soil facies (composite, crevasse splay, and cumulative) is listed beneath cross section in panel A but applies to each cross-section. Blue lines correspond to the elevation(s) of the water table (fluctuating in panels B and C). Red arrows indicate locations of silicate weathering fluxes in the floodplain and the sizes are their relative magnitudes (larger = greater).

# Chapter 4

# Sediment transport and silicate weathering in the Huerfano Basin (Colorado, USA) during the latest Paleocene and Early Eocene

Silicate weathering imposes a negative feedback in the geologic carbon cycle and stabilizes Earth's climate on $10^5$-$10^6$-year timescales. Its sensitivity to geologic and environmental conditions at the Earth's surface results in orders-of-magnitude variability across continents today. Moreover, these combined effects of geology and climate on silicate weathering are challenging to disentangle when considering silicate weathering in the geologic past, which ultimately hamper how silicate weathering is included in carbon cycle models. To adequately refine controls of silicate weathering, thorough studies of nonmarine sedimentary basins are warranted. In this study, we measure the elemental and Li isotope compositions of sediments in the Huerfano Basin: a Laramide basin in the Western United States that contains latest Paleocene and early Eocene strata. To interrogate the controls of silicate weathering, we select clay-sized ($< 2\mu$m) sediments in overbank deposits and bulk sandstones for analysis, where the former is hypothesized to capture *in situ* weathering signals and the latter is hypothesized to reflect primary sediment compositions.

When we synthesize our measurements with previously published bedrock

geochemical data, we first distinguish that the range of observed clay and sandstone chemistry can be explained by the chemistry of intrusive rocks in the hinterland. Whereas clays are geochemically similar to mafic and intermediate rocks, sandstones are most geochemically similar to intermediate and felsic rocks. We attribute these lithologic differences to the sorting of sediments during deposition, where more weatherable, finer-grained mafic sediments are more readily included in overbank deposits while less weatherable, coarser-grained felsic sediments compose channel sandstones. Although containing different proportions of source rock sediments, overbank clays and sandstones have remarkably comparable up-section trends in $\delta^7$Li values. The simplest explanation for their isotopic similarity is that they both contain similar Li-rich minerals/sediments that dominate the bulk $\delta^7$Li value. This control is intimated by 1) the significant relationship between sandstone $\delta^7$Li values and percentages of metasedimentary lithic fragments in sandstones and 2) the known high concentrations of Li in biotite that frequently compose overbank deposits in the basin.

Importantly, these comparable up-section trends and the inconsistent relationships between clay $\delta^7$Li values and other weathering-sensitive proxies (e.g., Mg/Ti, K/Ti, magnetic coercivity) suggest that silicate weathering intensity is low in the basin. We posit that weathering is limited in the Huerfano Basin due to the short residence time of sediments in floodplains, which is plausibly a result of poor sediment cohesion controlled by source rock mineralogy. Although climatically and tectonically driven sediment transfer cannot be disregarded as a control, this newly identified lithologic limitation on silicate weathering is consistent with sedimentological information and ultimately underscores the importance of surface processes in modulating silicate weathering.

## 4.1 Introduction

Silicate weathering is a central process in Earth systems models and is canonically thought to impose a negative feedback in the geologic carbon cycle (Berner et al., 1983; Chamberlin, 1899; Walker et al., 1981). In essence, high atmospheric $pCO_2$ facilitates the leaching of Ca and Mg from silicate minerals that, upon its delivery by rivers to the ocean, promotes the formation of marine carbonates, acting as a net atmospheric $pCO_2$ sink that thus weakens silicate weathering. This feedback is consistent with thermodynamic controls of $CO_2$ on silicate weathering rates (e.g., Penman et al., 2020; Winnick and Maher, 2018) and the response of silicate weathering to hyperthermal (e.g., Chapter 3) and ocean anoxic events (e.g., Pogge von Strandmann et al., 2013) of the last 100 Ma. However, it is increasingly recognized that silicate weathering is directly modified by climate (Kump et al., 2000; Maher and Chamberlain, 2014; Fang et al., 2019), tectonics (Raymo and Ruddiman, 1992; Misra and Froelich, 2012), lithology (Macdonald et al., 2019; Park et al., 2020), terrestrial biomass (D'Antonio et al., 2019; Hahm et al., 2014; Ibarra et al., 2019; Tune et al., 2020), and landscape configuration (Bufe et al., 2021; Larsen et al., 2014b; Pogge von Strandmann and Henderson, 2015; Torres et al., 2016). These modifications are evidenced by the wide range of silicate weathering fluxes observed in rivers globally despite the global uniformity of atmospheric $pCO_2$ (Gaillardet et al., 1999; Tipper et al., 2021). Moreover, as these environmental and geologic conditions change and equilibrium climate states change with them, the silicate weathering feedback is thus thought to vary through geologic time (Caves et al., 2016; Lee et al., 2019; Penman et al., 2020; Rugenstein et al., 2019). To further extend our understanding of silicate weathering during different equilibrium climate states and over wider geologic conditions, continental archives of past Earth surfaces need further investigation.

Sedimentary deposits in intermontane basins are records of tectonic, climatic,

and eustatic processes that contribute to basin development, capturing many controls of silicate weathering. The Laramide orogeny in North America was brought forth by flat-slab subduction of the Farallon plate, transferring deformation through the overlying North American plate (e.g., Bird, 1998) that yielded a series of north-south trending nonmarine basins (Dickinson et al., 1988; Lawton, 2008). The orogeny continued to develop occurring between ~75 and 35 Ma, and the sediments filling these Laramide basins serve as important archives of changes in the Earth system during the late Mesozoic and early Cenozoic eras. Paleocene- and Eocene-aged strata are particularly well preserved and outcrop as extensive badlands exposures in several Laramide basins.

Global climate in the Paleocene and Eocene epochs is classified as a warmhouse or hothouse (Westerhold et al., 2020) due to high atmospheric $pCO_2$ levels (Rae et al., 2021) and the absence of polar ice (Zachos et al., 2001). Notably, the late Paleocene and Early Eocene were punctuated by hyperthermal events, where geologically rapid input of endogenic $CO_2$ to the ocean and atmosphere caused extreme changes in climate (Carmichael et al., 2018; Rush et al., 2021; Wing et al., 2005), surface processes (e.g., Duller et al., 2019; Foreman et al., 2012; Foreman, 2014; Kraus et al., 2015; Pujalte et al., 2015), and marine and nonmarine biota (Bowen et al., 2002; McInerney and Wing, 2011; Self-Trail et al., 2012). Silicate weathering rates are shown to increase globally (e.g., Dickson et al., 2015; John et al., 2012; Komar and Zeebe, 2011; Penman, 2016; Ravizza et al., 2001) and within Laramide basins (e.g., Clechenko et al., 2007; Chapter 3) during the events. Yet, the perceptibly low silicate weathering rates before the events (Chapter 3) and between hyperthermal events (Wang et al., 2017) suggest that either equilibrium climate conditions during the Paleocene and Eocene could not sustain high silicate weathering rates, or that other limiting factors at the catchment scale inhibit elevated weathering rates.

In this study, we analyze the chemical and isotopic composition of fluvial de-

posits in the Huerfano Basin (Colorado, USA) to assess the provenance, deposition, and chemical weathering of silicate minerals during the latest Paleocene and early Eocene. We target bulk channel sandstone deposits and clays ($< 2$ $\mu$m grains) in overbank deposits for analysis to gauge integrated source rock compositions and *in situ* weathering signals, respectively. Alongside traditional measurements of major and trace element concentrations, we measure Li isotope ratios of these sediments because of their utility in quantitatively describing the mode and intensity of silicate weathering (Dellinger et al., 2017 and references therein). These analyses are interpreted in the context of published magnetic and petrographic data from these sedimentary deposits(Rasmussen, 2016; Rasmussen and Foreman, 2017; Rasmussen et al., 2020) and are compared to bulk elemental data of rocks that crop out in the basin-bounding mountain ranges (Armbrustmacher, 1984, 1988; Boardman and Condie, 1986; Noblett and Staub, 1990; Parker and Sharp, 1970; Van Gosen, 2020). These compositional data, synthesized with sedimentological information, allow for a detailed assessment of silicate weathering and its potential relationships with climate, lithology, tectonics, and sediment transport in the basin.

## 4.2 Geologic setting

The Huerfano Basin is one of the southeastern-most Laramide basins (Fig. 4.1A), situated between the Sangre de Cristo Uplift to the west and the Wet Mountains to the northeast. Its formation is often genetically linked with the nearby Raton Basin (Bush et al., 2016; Cather et al., 2004; Chapin et al., 2014), but recent studies argue that the Huerfano Basin is a unique depocenter (Rasmussen and Foreman, 2017; Rasmussen et al., 2020) containing alluvial sequences spanning the latest Paleocene and Early Eocene. Paleocurrents, derived primarily from trough cross-bedding in sandstones, indicate a consistent southward drainage throughout the section (Cather et al., 2004; Dickinson et al., 1988; Rasmussen and Foreman, 2017).

Detrital zircon (DZ) spectra among the Paleocene and Early Eocene are nearly identical (Rasmussen and Foreman, 2017). Interestingly, U-Pb ages younger than ∼517 Ma are absent in detrital zircon samples, and suggest that any Paleozoic through Mesozoic sedimentary cover in the basin-bounding ranges was eroded and deposited farther downstream of the Huerfano Basin. Moreover, the distinct DZ peaks alongside cobble censuses and sandstone petrography indicate the provenance of sediment from solely Proterozoic basement and Cambrian-aged plutons in the Wet Mountains (Rasmussen and Foreman, 2017). The crystalline units in the Wet Mountains mostly consist of granites, syenites, and metasedimentary paragneisses, but many of these plutonic units are crosscut by or commingle with mafic and ultramafic suites that consist of gabbros, lamprophyres, pyroxenites, and amphibolites (Armbrustmacher, 1984, 1988; Boardman and Condie, 1986; Noblett and Staub, 1990; Park et al., 2020; Van Gosen, 2020). Felsic volcaniclastic units, and some intermediate ones, also crop out in the Wet Mountains. The felsic intrusive units are dominantly represented in sandstone deposits (Rasmussen and Foreman, 2017).

Across the three formations that compose the Huerfano Basin, including the Poison Canyon, Cuchara, and Huerfano formations, lithofacies are dominated by interbedded layers of channel-fill sandstones and conglomerates and overbank mudstones and siltstones (Fig. 4.1B; see Rasmussen et al., 2020 for a thorough review). Quartz-rich sandstones and conglomerates exhibit a wide range of sedimentary structures and colors. The laterally continuous sheet sandstone deposits and abundant rip-up clasts of the Poison Canyon and Cuchara formations indicate steep river gradients and mobile river channels that actively reworked floodplain sediments during these time intervals (Rasmussen et al., 2020). The heavily bioturbated sandstones of the Huerfano Formation, in contrast, indicate single-threaded rivers within well-drained, broad floodplains. Although sediment provenance is the same for the three formations, the proportion of sediment sources among the forma-

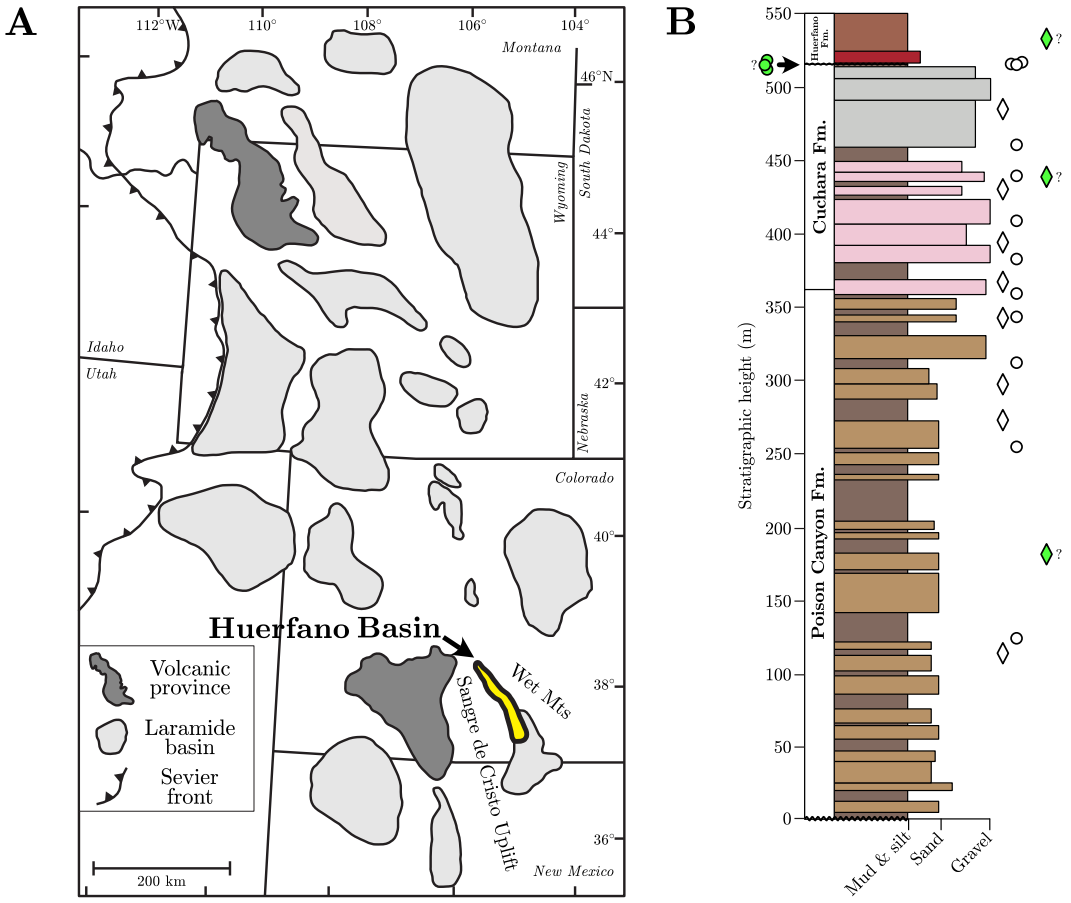


Figure 4.1: A) Laramide basins of the Western US (modified after Dickinson et al., 1988 and Rasmussen et al., 2020). Names and locations of major uplifts are listed beside the Huerfano Basin. B) Stratigraphy of the Huerfano Basin (modified after Rasmussen et al., 2020). White circles and diamonds correspond to the stratigraphic height of mudstone/siltstone clays and bulk sandstones analyzed in this study, respectively. Green circles and green diamonds are samples that come from a nearby locality and do not have specific stratigraphic heights in this section; their locations correspond to the formation they comprise, where three clay samples at the interpreted unconformity between the Cuchara and Huerfano Formations (Rasmussen and Foreman, 2017; Rasmussen et al., 2020) crop out in the Cuchara Formation stratigraphically higher than the extent of the Cuchara Formation in this section. The brown, pink, drab gray, and red layers correspond to the color sandstone layers (Rasmussen and Foreman, 2017; Rasmussen et al., 2020).

tions vary. As determined through sandstone petrography and clast counts in previous work (Rasmussen and Foreman, 2017), the proportion of alkali feldspar-bearing granite grains and metasedimentary (lithic) grains increase significantly from the Poison Canyon to the Huerfano Formation. These up-section changes in source rock proportions are hypothesized to be the result of one or more periods of increased uplift in the Wet Mountains (Rasmussen et al., 2020). Overbank mudstones and siltstones are often drab-colored, mica-rich, and appear to have undergone low degrees of pedogenesis; they are classified as Entisols and Inceptisols (Rasmussen and Foreman, 2017; Rasmussen et al., 2020; Robinson, 1966). Coercivity measurements of overbank deposits, which convey the relative proportion of oxidized ferrimagnetic minerals (e.g., goethite, hematite, maghemite) to magnetite, suggest episodes of increased oxidative weathering in the middle of the Cuchara Formation and in the Huerfano Formation. Thus, the stacking pattern of the channel-fill and overbank deposits – notably the acyclical amalgamation of fluvial channel belts – are thought to be modulated by external factors (climate and/or tectonics) rather than internal dynamics (e.g., river avulsions; Hajek and Straub, 2016) between the Paleocene Poison Canyon Formation and Early Eocene Cuchara/Huerfano formations (Rasmussen et al., 2020).

Despite this wealth of sedimentological information, temporal and climatic constraints are less well determined. The dearth of index fossils, pedogenic carbonate nodules for stable C isotope measurements, Paleocene- or Eocene-aged zircons for maximum depositional ages, and the absence of large C isotope excursions in organic matter (which can be diagnostic of hyperthermal events, e.g., Baczynski et al., 2013) make it challenging to pinpoint when in the Paleocene and Eocene these sediments were deposited (Rasmussen and Foreman, 2017; Rasmussen et al., 2020). By correlating observations in the Huerfano Basin with nearby Laramide Basins that contain better temporal constraints, Rasmussen et al. (2020) propose that the

Poison Canyon and Cuchara formations developed in the latest Paleocene (∼57-56 Ma) and the Huerfano Formation deposited through Wasatchian-7 of the North American land mammal age (∼53 Ma, i.e., Early Eocene). Yet, the amount of time represented by the unconformity between Cuchara and Huerfano Formations is uncertain. Climate in the Huerfano Basin during this time interval is largely informed quantitatively by abundant proxy data in nearby basins (e.g., Snell et al., 2013) and global climate models (e.g., Sewall and Sloan, 2006). Global climate models for the Paleocene in nearby Raton Basin predict mean annual temperatures of 10–12 °C and mean annual precipitations of 730 – 1100 mm (Sewall and Sloan, 2006). Eocene climate in the basin is less understood, but the increased occurrence of well-drained soils suggests higher temperatures and more seasonal rainfall than in the Paleocene (Rasmussen et al., 2020). Overall, climate in the Huerfano Basin proceeds from more temperate in the Paleocene to more tropical in the Eocene, tracking with increases in MAT observed globally and in nearby basins (e.g., Snell et al., 2013; Wolfe and Upchurch, 1987).

## 4.3 Methods

### 4.3.1 Sample preparation

Overbank mudstones/siltstones and channel sandstones required different preparation prior to chemical and isotopic analyses. The target mass of sample for geochemical analyses was based on minimum mass constraint for Li isotope measurements (∼50 ng Li) and assumed Li concentrations of the analytes (conservative minimum estimates of 1 ppm and 5 ppm for bulk sandstones and overbank clays, respectively). To selectively extract clay-sized sediments from overbank deposits, approximately 10 g of bulk sample were disaggregated in clean low-density polyethylene tubes by deionized (DI) water for at least 24 hours. Once disaggregated, samples were

transferred to centrifuge tubes using a 10 mg sample:300 g DI water ratio. To isolate clay-size fractions, samples were centrifuged for 45 seconds at 900 rpm, which left clays in suspension. To collect the clays, solution with suspended clays was transferred to another centrifuge tube and centrifuged for 40 minutes at 2400 rpm. Around 20 mg of clay from each sample were processed for geochemical analysis (see Section A.3). Before full dissolution, all clays were treated with a 1M ammonium chloride solution (using a 1 mL solution:5 mg sample ratio following similar protocols of Dosseto et al., 2015) and agitated for 1 hour (repeated 3 times) to remove all exchangeable cations. These cations, although typically containing small amounts of Li relative to crystallographically bound Li (e.g., Li et al., 2020), are susceptible to post-depositional exchange with fluids and therefore selectively removed. All solution was discarded between steps. Other partial dissolution steps to remove carbonate, Fe/Mn oxide, and organic fractions were excluded because negligible amounts of Li are found in those fractions in humid soils (Li et al., 2020). Furthermore, some reagents used to selectively dissolve non-silicate fractions have been shown to dissolve phyllosilicate minerals (e.g., Whalley and Grant, 1994). All pre-treated clays were rinsed in doubly deionized (18.2 m$\Omega$) water, repeated 3 times with solution discarded between steps, before full dissolution.

Most sandstone samples were fissile and disaggregated into loose sediments. Approximately 5 grams of well-mixed sandstone sediments were gathered and subsequently powdered in a diamonite mortar and pestle. Approximately 45–75 mg of powder for each sandstone sample were used for geochemical analysis. Most Li in siliciclastic sediments is found in silicate minerals, and not in carbonates (e.g., Kisakűrek et al., 2005) nor sorbed to organic matter (Li et al., 2020). Thus, the sandstones were not treated with reagents to selectively dissolve non-silicate phases.

Once weighed, samples were reacted in Teflon beakers with a series of strong acids to attack Si-O bonds. The sequence involved reactions with concentrated HF,

concentrated HF + concentrated $HNO_3$, and 6N HCl at 110 °C. Whereas the first 2 steps required ∼100 hours each, the third step required only 24 hours. All steps were repeated if significant solid residue remained after the complete dissolution. Upon samples being fully dissolved, they were reconstituted in 6N $HNO_3$ and inspected for residuum. If fully in solution, samples were split into two aliquots: one for Li isotope analysis (90 % v/v), and another for major and trace element analysis (10 % v/v).

### 4.3.2 Major and trace element chemistry

Major and trace element concentrations were measured at the University of Texas at Austin with an Agilent 7500ce quadrupole ICP-MS. All samples in 6N $HNO_3$ were diluted to 2 % (v/v) $HNO_3$ solutions and introduced into the instrument in solution. Uncertainties for elements Al, Mg, Ti, and K were <6 % and Li and Zr were <12 %, based on replicate analyses of both in-house standards and the Geological Survey of Japan JR-1 (rhyolite) and NIST1643f international standards.

### 4.3.3 Li isotope chemistry

To selectively extract Li and remove cations prior to isotope measurements, samples underwent cation chromatography following the procedure of Magna et al. (2004). All samples were reconstituted in the 0.67N $HNO_3$ + methanol (30% v/v) and centrifuged prior to chemistry. The eluent was loaded on columns packed with BioRad® AG 50W-X8 (200–400 mesh) cation exchange resin. Eluate was collected before and after the Li elution to assure that Li yields were > 99 %. After cation chromatography, all samples were dried on a hot plate and reconstituted in 2% (v/v) $HNO_3$ for isotope analysis. Li isotope ratios were measured at the University of Texas at Austin with a Nu Plasma 3 Multi Collector ICP-MS in solution mode. All measured $^{7}Li/^{6}Li$ ratios were converted to delta values (in units of ‰) following

a standard-sample-standard bracketing method where

$$\delta^7\mathrm{Li}_{\mathrm{sample}} = \left\{ \frac{\left(\frac{^7\mathrm{Li}}{^6\mathrm{Li}}\right)_{\mathrm{sample}}}{\left[\left(\frac{^7\mathrm{Li}}{^6\mathrm{Li}}\right)_{\mathrm{standard,i-1}} + \left(\frac{^7\mathrm{Li}}{^6\mathrm{Li}}\right)_{\mathrm{standard,i+1}}\right]/2} \right\} \times 1000 \qquad (4.1)$$

and "standard i-1" and "standard i+1" correspond to measured IRMM-016 isotope standards before and after the "sample" unknown, respectively. All delta values computed in Eq. 4.1 are then converted to delta values relative to the NIST RM 8454 lithium carbonate (LSVEC) standard (Brand et al., 2014). During each session of cation chromatography, at least one matrix-matched analytical standard (i.e., JR-1 rhyolites) was processed alongside unknowns. Over the time in which unknowns were analyzed, the long-term average $\delta^7\mathrm{Li}_{\mathrm{JR-1}}$ value was 4.0 ‰ ± 0.4 (2 s.d.; N = 16) – compared to a reported value of 4.0 ‰ ± 0.3 (Oi et al., 1997) – and $\delta^7\mathrm{Li}_{\mathrm{LSVEC}}$ value was 0 ‰ ± 0.2 (2 s.d.; N = 34). In-run standard error ($2\sigma$) for unknowns was ∼0.1 ‰. As conservative estimate, we apply the long-term error for JR-1 (0.4 ‰) to all data and subsequent interpretations.

## 4.4 Results

### 4.4.1 Major element ratios

Major and trace element concentrations reveal distinct geochemical arrays for overbank clays and sandstones (Fig. 4.2; see Section A.3 for complete geochemical data). These differences are prevalent in two element ratio spaces: one often utilized to depict weathering trends (Fig. 4.2A), and another used to determine the proportion of bedrock sources in sedimentary deposits (Fig. 4.2B). In the former space, clays exhibit a comparatively wide range of Mg/Ti values (0.7–8.7) and a narrower range of K/Ti (0.9–4.0) whereas sandstones span a relatively narrower range of Mg/Ti

(0.4–5.6) (albeit comparable to clays) and a large range K/Ti (9.3–106.4; note that one sandstone sample is not shown in Fig. 4.2B). The decrease in K/Ti and Mg/Ti often correlates with increased weathering intensity (e.g., Bastian et al., 2017, 2019) because K and Mg are progressively leached from primary minerals and excluded from authigenic phyllosilicates (e.g., kaolinite and gibbsite) while Ti remains mineralogically bound due to its low solubility in water at Earth surface temperatures. Clays and sandstones both exhibit monotonic relationships in K/Ti-Mg/Ti space, which reflects that Ca and Mg are affected similarly by given processes and thus lends credence to decreases in K/Ti or Mg/Ti being weathering signals. However, both arrays overlap significantly with source rock compositions. Many felsic and intermediate source rocks have high K/Ti and lower Mg/Ti, overlapping and spanning the range of sandstones elemental ratios. Similarly, the clay array overlaps significantly with mafic values. Clay K/Ti trend marginally higher than the source rocks and some clay Mg/Ti are lower than the minimum mafic source rock Mg/Ti (Fig. 4.3).

The immobile element ratios of clays, sandstones, and source rocks depict a similar story (Fig. 4.2B). In Ti/Al-Zr/Al space, clays form a near-vertical array (having a wide variability in Ti/Al) whereas sandstones form a near-horizontal array (having a wide variability in Zr/Al). With increasing stratigraphic height (i.e., over time), clay composition shifts toward higher Ti/Al and sandstone compositions shift toward lower Zr/Al. In this space, intermediate and mafic source rocks have distinctly low Zr/Al and extend toward high Ti/Al, characteristically above the clay array. The felsic and intermediate source rocks span a much wider range of Ti/Al and encompass nearly all sandstones and clay samples. With notably low Zr/Al, hornblende-bearing syenites overlap nearly the entire range of clay values. Felsic rocks without perceptible hornblende, such as felsic volcaniclastics and granites, tend to have lower Ti/Al and higher Zr/Al.

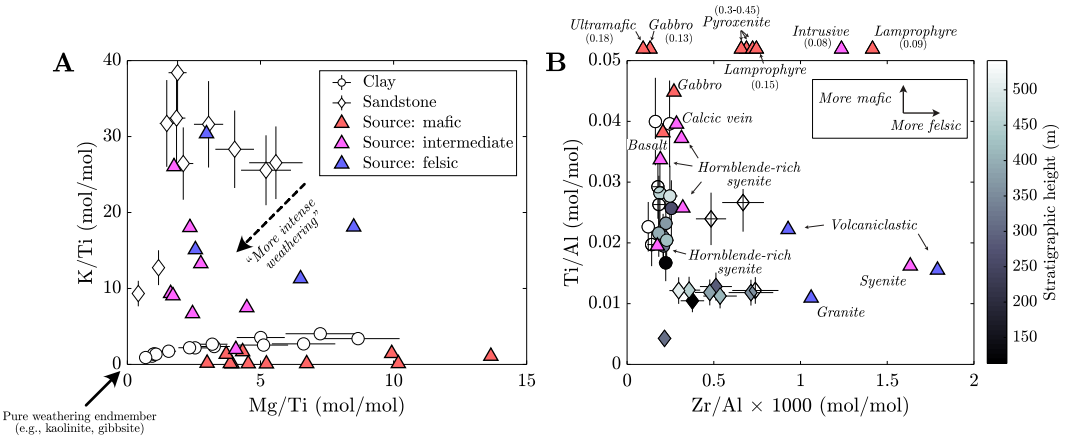


Figure 4.2: Major and trace element ratios of overbank clays, sandstones, and potential sources. All elemental data of source rocks are literature values (Armbrustmacher, 1984, 1988; Boardman and Condie, 1986; Noblett and Staub, 1990; Parker and Sharp, 1970; Van Gosen, 2020). A) K/Ti vs. Mg/Ti of samples, typically used to interrogate weathering intensity. B) Ti/Al vs. Zr/Al x 1000 of samples, used to determine the proportion of source rocks that compose basin sediments (overbank clays and sandstones). The color of clay and sandstone symbols correspond to their stratigraphic heights. Samples with Ti/Al $>$ 0.05 listed above with their Ti/Al values listed in parentheses. Their x-axis location corresponds with their Zr/Al.

### 4.4.2 Stratigraphic trends in Li isotope ratios and Mg/Ti

Li isotope ratios and Mg/Ti of clays and sandstones are shown stratigraphically (Fig. 4.3). Clay $\delta^7$Li values span -0.9 to +9.2 ‰ whereas sandstone $\delta^7$Li values span +1.9 to +13.0 ‰, nearly encompassing the reported range of river suspended and bedload $\delta^7$Li values globally (Tomascak et al., 2016). The range of clay $\delta^7$Li values in the Poison Canyon Formation is narrower than the range in the Cuchara Formation (Fig. 4.3A, B). Conversely, the range of sandstone $\delta^7$Li values is largest in the Poison Canyon Formation and narrows up-section into the Cuchara Formation. We suppose that the wide range of sandstone $\delta^7$Li values to the occurrence of high-$\delta^7$Li-valued outliers (see Section 4.5.1 for further discussion). Once accounting for those outliers, the up-section trends between sandstone and clay $\delta^7$Li values are noticeably similar. Clay and sandstone $\delta^7$Li values steadily increase upward

through the Poison Canyon Formation and into the Cuchara Formation, decrease by upwards of 7 ‰ about half-way through the Cuchara Formation, increase by as much as 10‰ around when the gray sandstones were being deposited in the Cuchara Formation, and ultimately remain positive into the Huerfano Formation. Three clay deposits without stratigraphic information (considered to be latest Paleocene) are consistently low with $\delta^7$Li values from -0.9 to -0.1 ‰ (Fig. 4.3B). Up-section, clay $\delta^7$Li values are generally lower than sandstone $\delta^7$Li values.

Stratigraphically, clay and sandstone Mg/Ti follow comparable up-section trends as well (Fig. 4.3C). Clay Mg/Ti are highest in the Poison Canyon Formation and progressively decrease through Cuchara Formation and into the Huerfano Formation. Sandstone Mg/Ti is low in the lower and middle portions of the Poison Canyon Formation, increases stepwise toward the end of the Poison Canyon Formation, and then follows a similar decreasing trajectory in Mg/Ti values through the Cuchara Formation. The difference in clay Mg/Ti and sandstone Mg/Ti is greatest in the Poison Canyon Formation and then tapers up-section, similar to clay and sandstone $\delta^7$Li values.

## 4.5 Discussion

### 4.5.1 Lithologic and mineralogical controls on sediment chemistry

The elemental and isotopic data from overbank clays and channel sandstone deposits, alongside mineralogical information (e.g. Rasmussen and Foreman, 2017; Robinson, 1966) point toward a lithologic control on the chemistry of sedimentary deposits in the basin. The distinct arrays that clays and sandstones form in both mobile (Fig. 4.2A) and immobile (Fig. 4.2B) element ratio spaces show that overbank and channel-fill deposits are composed of sediments with varying chemistry. The sandstones consistently exhibit a geochemical similarity with felsic and inter-

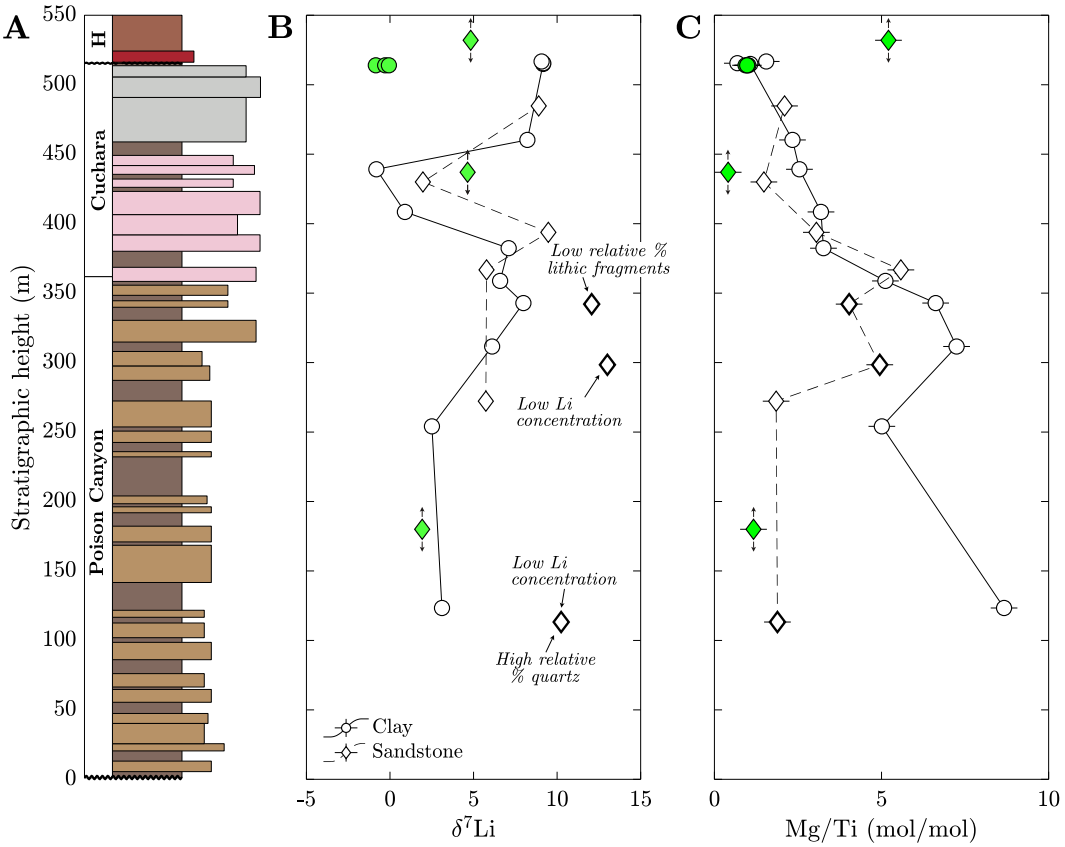


Figure 4.3: Isotopic and geochemical data of basin sediments considered stratigraphically. A) Huerfano Basin stratigraphy (same as in Fig. 4.1B). H corresponds to the Huerfano Formation. B) Clay and sandstone $\delta^7$Li values ($2\sigma$ error bars for $\delta^7$Li values are smaller than symbols). Symbols for sandstones with outlying $\delta^7$Li values have bolded rims and green-colored symbols are samples without clear stratigraphic heights. C) Clay and sandstone Mg/Ti. Bolded diamonds are sandstones with outlying $\delta^7$Li values and green-colored symbols are samples without clear stratigraphic heights.

mediate source rocks, whereas clays in overbank deposits exhibit strong geochemical similarities with more mafic sediments and hornblende-rich syenites. The disparity of sediment chemistry within modern fluvial environments is commonplace, as evidenced by depth-dependent changes in the chemistry and grain size of suspended river sediments (e.g., Bouchez et al., 2011; Garzanti et al., 2011) and differences

in sediment provenance as a function of river suspended sediment grain size (e.g., Cullers et al., 1987; Malkowski et al., 2019). Experiments have shown that sediment sorting can lead to geochemical and mineralogical disparities in sedimentary deposits (Pyles et al., 2013), which is likely due to the significant correlation between grain size and sediment chemistry (Bouchez et al., 2011; Garzanti et al., 2011).

We therefore posit that the distinct geochemical affinities of clays and sandstones are driven by sediment sorting during deposition, which separates coarse-grained felsic/intermediate bedrock-derived sediments from fine-grained mafic bedrock-derived sediments. The absence of mafic clasts and the low relative proportion of metasedimentary lithic grains in sandstones and conglomerates (Rasmussen and Foreman, 2017), alongside high fractions of mica in overbank deposits (Robinson, 1966), are consistent with this hypothesis. Furthermore, because mafic minerals are known to weather more rapidly than felsic minerals (e.g., Brantley, 2004; White and Buss, 2014) and would likely be finer grained than felsic sediments at a given location in the catchment, it is plausible that mafic minerals would remain in suspension preferentially and thus be deposited in floodplains. Of all source rocks, it appears that hornblende-rich syenites could serve as an endmember sediment source for both overbank deposits and channel-fill sandstones. For this to be possible, differential weathering of hornblende-rich syenites should be taking place to some extent. The Cambrian syenites in the Wet Mountains are composed of plagioclase feldspar, potassium feldspar, biotite, and hornblende (Armbrustmacher, 1984, 1988): minerals which have different natural dissolutions rates at Earth surface conditions and different crystal structures. If these syenites were to weather along grain boundaries and be subjected to sorting, sheet and chain silicates (like biotite and hornblende) would be preferentially included in overbank deposits while framework silicates (feldspar) would be included in channel sandstones. This interpretation is consistent with apparent differences in floodplain depositional patterns when com-

pared to other Laramide basins. In the Eocene Willwood Formation of the Bighorn Basin floodplain strata are composed of both well-developed paleosol mudrocks and a heterolithic suite of claystones, siltstones, and sandstones, with the latter representing major crevasse splay events wherein both bedload and suspended load sediment are provided to the floodplain (Kraus et al., 2015). Willwood Formation fluvial channel movement was characterized by an initial pulse of fluvial sediment to the floodplain that deposited several meters of sandstones and siltstones prior to channel avulsion (Kraus et al., 2015). In contrast, Paleogene strata of the Huerfano Basin are comparatively poor in these crevasse splay (avulsion deposits *sensu* Kraus et al., 2015), and typical thicknesses are less than a meter (Rasmussen et al., 2020). This observation suggests sediment provision to the Huerfano Basin floodplains may have been dominated by overbank flooding that would create a flux to the floodplain of the suspended sediment load.

Considering the distinct chemistry of clays and sandstones, the shared up-section trends in $\delta^7$Li values and Mg/Ti is especially striking. We propose that when clays and sandstones follow similar up-section trends, overbank deposits and sandstones contain the same Li- and Mg-rich phases that dominate the Li isotope and Mg/Ti signals, even though their other mineralogical compositions differ from each other. Evidence for this is found when the elemental and isotopic composition of sandstone are compared to results from sandstone petrography (Fig. 4.4; Rasmussen, 2016). There is a significant inverse correlation between sandstone $\delta^7$Li values and the percent lithic fragments, where these lithic fragments are typically metasedimentary in origin and composed of alkali feldspar, biotite, and minor amphibole (Rasmussen and Foreman, 2017). The lowest percentages of lithic fragments often correspond with high percentages of quartz. With respect to other minerals found in granites and paragneisses, quartz has the highest observed $\delta^7$Li values and lowest Li concentrations (Zhang et al., 2021). It is thus notable that the three

sandstone outliers (Fig. 4.3B; 4.4) solely occur at high $\delta^7$Li values where samples either have high quartz contents or low Li concentrations. Quartz is seldom the primary mineral from which secondary clays form (feldspar and phyllosilicates are predominant), which means that sandstones composed of nearly all quartz are not representative of source sediments for authigenic minerals in overbank deposits.

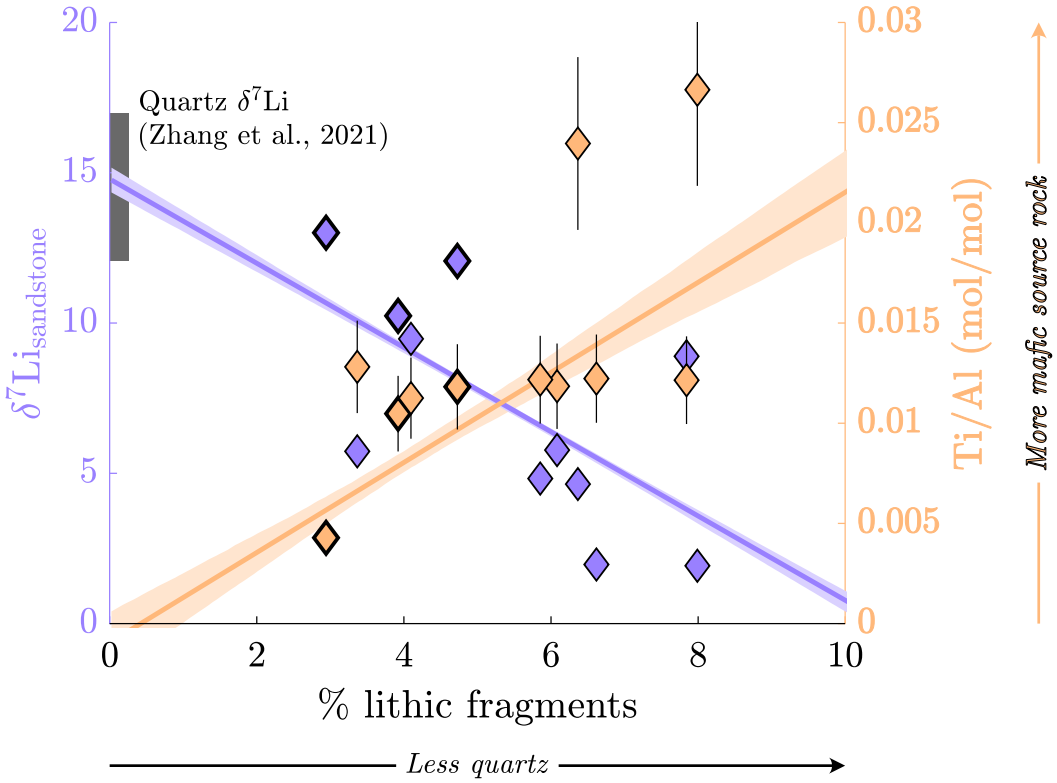


Figure 4.4: Sandstone chemistry compared to sandstone petrography. Bolded black diamonds correspond to the interpreted sandstone outliers from Fig. 3B. An increase in percent lithic grains corresponds with a decrease in percent quartz grains. Left axis: $\delta^7$Li$_{sandstone}$ values vs. % lithic fragments determined via sandstone petrography ($2\sigma$ error bars for $\delta^7$Li values are smaller than symbols). Linear fit through all data (purple line) and 66% confidence interval (translucent purple envelope) shown. The gray bar corresponds to the median range of quartz $\delta^7$Li values from Zhang et al. (2021). Right axis: Ti/Al vs. % percent lithic fragments. Greater Ti/Al trends toward the mafic source rock endmembers. Linear fit through all data (orange line) and 66% confidence interval (translucent orange envelope) shown.

Ultimately, we designate those samples as outliers because quartz-rich sandstones are exceptionally unlike overbank deposits and therefore compositionally incomparable. Moreover, modest increases in lithic fragment contents yield significant decreases in $\delta^7$Li values (Fig. 4.4), suggesting that these lithic grains have higher Li concentrations and lower $\delta^7$Li values than quartz sediments. The increase in sandstone Ti/Al with increasing lithic fragments indicate that sandstones with greater lithic fragments trend geochemically toward intermediate and mafic source rock compositions, i.e., more like clays. These lithic fragments can contain higher proportions of Li- and Mg-rich minerals like amphibole and biotite. Therefore, upon inclusion in sandstones, these lithic fragments—or minerals that commonly compose lithic fragments—bridge the apparent geochemical disparity between sandstone and overbank clays. The determination of modal mineralogy through X-ray diffraction of both sandstones and overbank deposits are needed to corroborate this inference.

There are two potential explanations for the increased up-section similarity between clay and sandstone geochemistry. One reason highlights the potential influence pf progressive reworking of floodplain sediments by rivers. In a study of rivers flowing through the Wet Mountains, Cullers et al. (1987) demonstrated that the chemistry of river suspended clays and silts well integrates the chemistry of exposed catchment rocks, whereas river suspended sands are more geochemically like Holocene soils near the active river channel. It is therefore possible that the increased similarity between clay and sandstone chemistry (i.e., $\delta^7$Li values and Mg/Ti) into the Cuchara and Huerfano Formations is caused by the progressive reworking of floodplain sediments that incrementally enriches sandstone deposits in mafic/intermediate sediments rich in Li and Mg. However, the second and more reasonable explanation for the up-section improved comparability is due to changes in source rock proportions entering the basin. Over time, the proportion of lithic fragments in sandstones increases significantly, from $\sim$13 % in the Poison Canyon

Formation to nearly 30 % in the Huerfano Formation (Rasmussen and Foreman, 2017). Thus, it is likely that when sandstones contain more lithic fragments, their bulk $\delta^7$Li values and Mg/Ti begin looking more like those of overbank deposits.

### 4.5.2 What limits weathering in the Huerfano Basin?

The Li isotope, elemental, and sedimentological compositions of basin sediments highlight the foremost control of source rock lithology (i.e., mineralogy) on secondary mineral composition. Given this strong control, it appears that silicate weathering plays a subsidiary role in sediment composition or that this mineralogical signature completely masks a weathering signal. When secondary clays form from the weathering of primary silicates, they preferentially incorporate $^6$Li over $^7$Li and thus have lower $\delta^7$Li values than the rocks from which they form (e.g., Hindshaw et al., 2019; Pistiner and Henderson, 2003). The progressive decrease in clay $\delta^7$Li values relative to source rock $\delta^7$Li values corresponds with higher silicate weathering intensity (Dellinger et al., 2017), where differences of 2–3 ‰ are significant and a change of 1 ‰ in either can correlate to an order-of-magnitude change in silicate weathering intensity. Taking clay and sandstone $\delta^7$Li values at face value, one could infer that the common occurrence of clay $\delta^7$Li values less than sandstone $\delta^7$Li values (as large as 3 ‰ different) indicates high silicate weathering intensity and that up-section changes in the $\delta^7$Li value difference indicate changes in weathering intensity over time. However, the elemental data (Fig. 4.2) imply that sandstones are not necessarily representative of integrated source rock compositions. Thus, it may not be judicious to quantify silicate weathering intensity from the comparison of clay and sandstone $\delta^7$Li values, especially when sandstones lack lithic fragments. Also, large fluctuations of clay $\delta^7$Li values $> 7$ ‰would involve extreme changes in weathering that have not been observed during other climatic perturbations (e.g., Pogge von Strandmann et al., 2013; Chapter 3), notwithstanding the similar fluctu-

ations in sandstone $\delta^7$Li values that suggest a non-weathering control of up-section $\delta^7$Li trends.

Moreover, when proxies for silicate weathering are considered against one another (Figs. 4.5 and 4.6), there is little evidence that clay $\delta^7$Li values and elemental compositions are driven by silicate weathering. Clay K/Ti and Mg/Ti each show an inconsistent and non-unique trend with clay $\delta^7$Li values (Fig. 4.5); low Mg/Ti and K/Ti values, which typically indicate high weathering intensities (e.g., Bastian et al., 2017, 2019), occur at both low and high clay $\delta^7$Li values. Strong positive correlations between clay $\delta^7$Li values and Mg/Ti or K/Ti would be expected if both primarily reflected silicate weathering. The comparison between clay $\delta^7$Li values and overbank magnetic data corroborate the limited effects of weathering on sediment chemistry (Fig. 4.6). Increases in clay $\delta^7$Li values coincide with increases in both saturation and coercivity, where the former underscores the concentration of ferrimagnetic minerals (Fig. 4.6A) and the latter shows the proportion of ferrimagnetic minerals that are oxidative weathering products (Fig. 4.6B). In this space, had clay $\delta^7$Li values been unambiguously driven by silicate weathering, decreases in $\delta^7$Li values would coincide with increases in coercivity. This lack of an inverse correlation further implies that chemistry of input sediments, rather than *in situ* weathering, drive changes in $\delta^7$Li values and Mg/Ti.

When the chemical and mineralogical composition of basin sediments are ultimately connected to sedimentological information, the simplest conclusion to draw is that despite warmhouse/hothouse conditions, silicate weathering was minimal in the Huerfano Basin during the early Paleogene. The paucity of temporal information and quantitative climate information in this basin limits our ability to probe the capacity of climate and soil hydrology in modulating silicate weathering. Moreover, the lack of Li isotope data for source rocks in the Wet Mountains inhibits the quantification of silicate weathering intensity (Dellinger et al., 2017), which is

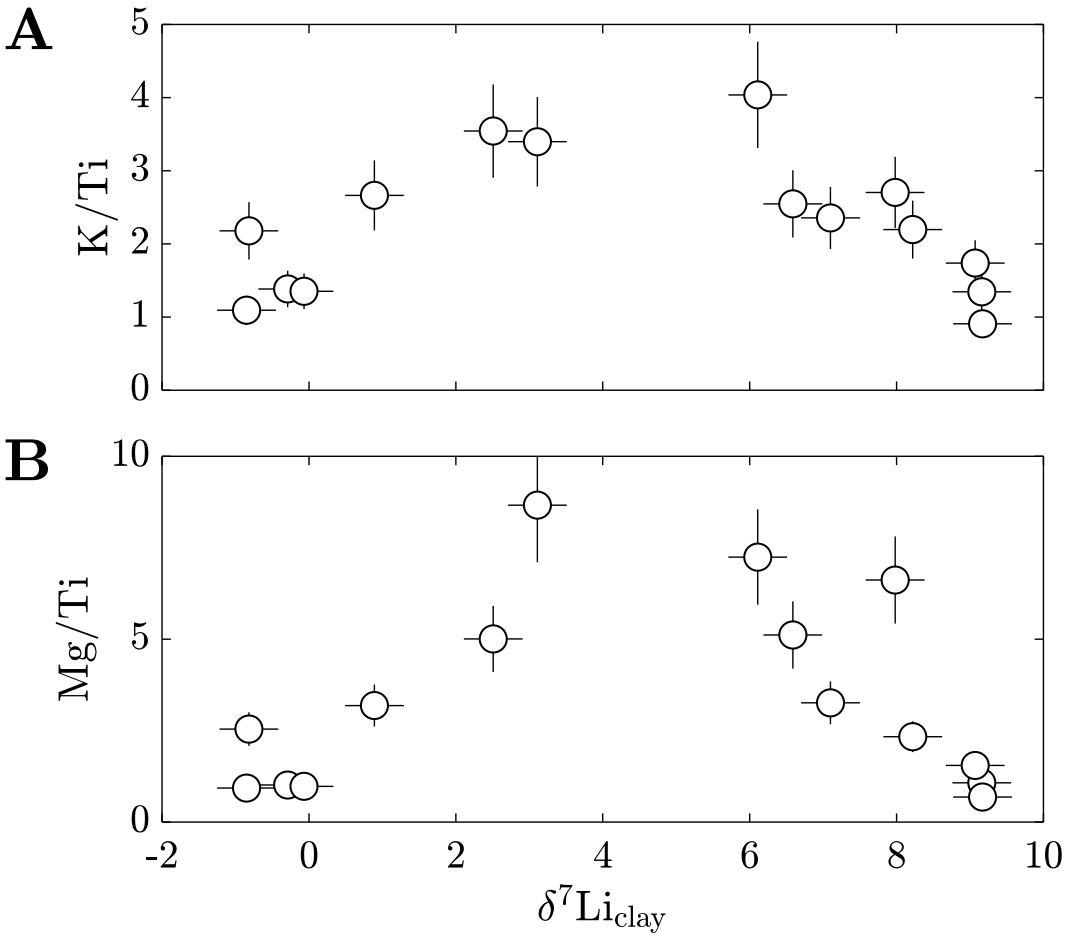


Figure 4.5: Commonly used, weathering-sensitive geochemical data of overbank clays. A) K/Ti vs. $\delta^7Li_{clay}$ values; B) Mg/Ti vs. $\delta^7Li_{clay}$ values.

more judicious than inferring weathering intensity from clay $\delta^7$Li values alone. Yet, the stratigraphy in the Huerfano Basin reinforces the idea that silicate weathering intensity was low in the basin and further intimates that source rock compositions played an important role in limiting weathering. One key criterion for high weathering intensity is long residences times of sediments at the Earth's surface (Dosseto et al., 2006). In alluvial systems that have accommodation for sediments to aggrade, sediment cohesion plays a vital role in stabilizing landscapes and thereby allowing

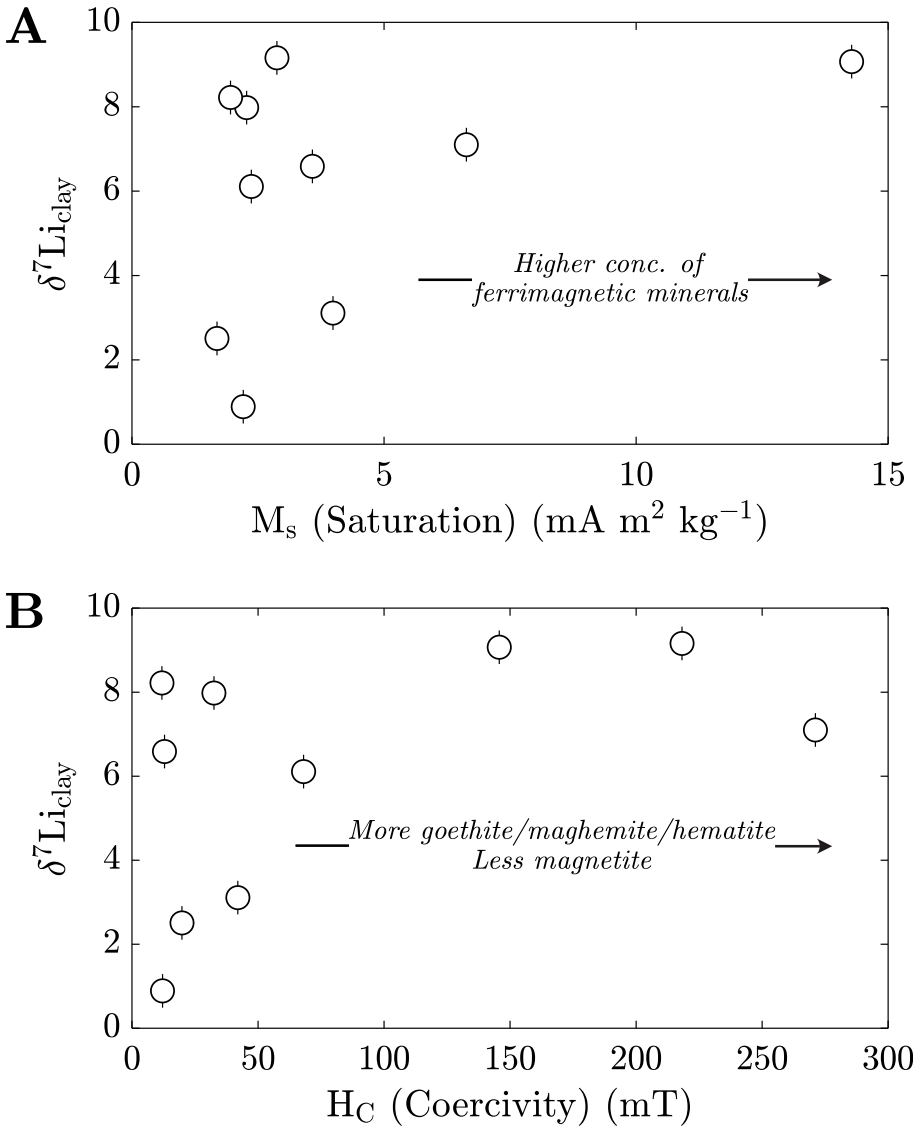


Figure 4.6: Clay chemistry and magnetic data. A) $\delta^7\mathrm{Lic}_{\mathrm{clay}}$ values vs. bulk mudstone/siltstone saturation, where high saturations indicate higher concentrations of ferrimagnetic minerals. B) $\delta^7\mathrm{Li}_{\mathrm{clay}}$ values vs. bulk mudstone/siltstone coercivity, where high coercivities indicate higher proportions of oxidized ferrimagnetic minerals, like goethite, maghemite, and/or hematite, relative to unoxidized ferrimagnetic minerals, like magnetite.

for sediments to remain exposed to Earth surface conditions for longer amounts of time (e.g., Hajek and Straub, 2016; Hobson and Dahlgren, 1998). The input of sediments from crystalline bedrock in the Wet Mountains (Rasmussen and Foreman, 2017), alongside short transport distances from the hinterland to the basin, limit the amount of fine-grained sediment that could be generated. Nearby Laramide basins, including the Raton Basin, have been interpreted to steadily accumulate sediments through the early Paleogene (Bush et al., 2016), suggesting that there was at least some accommodation for sediments to accumulate and weather in the floodplain. Yet, the incoming coarse grains to the floodplain may not have cohered well, allowing for rivers to avulse and meander across the floodplain and effectively transmit sediments through the alluvial system faster than the rates at which they chemically weather (Fig. 4.7). The occurrence of sheet sandstones and weakly developed overbank soils support this idea, and any climatically or tectonically induced influx of sediments from the Wet Mountains would only exacerbate river avulsions and floodplain erosion.

The implication of limited weathering of fresh, igneous-derived sediments is partly paradoxical because the supply of fresh, un-weathered crystalline bedrock is thought to be an essential criterion for maximizing silicate weathering fluxes from landscapes (e.g., Gaillardet et al., 1999; West et al., 2005). These geologic conditions in the Huerfano Basin are not necessarily representative of most drainage catchments on Earth that often have a wide range of rock types exposed within them. Yet, these findings introduce an intriguing caveat in considering the optimal conditions for generating large silicate weathering fluxes in a drainage catchment, where silicate weathering is often thought to be limited by the supply of fresh sediments and not landscape stability.

## 4.6 Conclusion

In this study, we present a detailed analysis of silicate weathering in the Huerfano Basin by integrating new elemental (major and trace) and isotopic (Li) analyses of basin sediments with previously published magnetic data of overbank deposits, elemental data of bedrock, and sedimentologic information. When elemental data of basin deposits are compared with those of bedrock, we determine that the chemistry of basin sediments primarily reflects source rock lithology and sediment transport. Although sediment provenance remains constant in the basin, clays in overbank deposits show a strong geochemical affinity for intermediate and mafic bedrock whereas channel sandstones are most like intermediate and felsic bedrock. Clays and sandstones form distinct geochemical arrays in immobile element spaces (i.e., Ti/Al vs. Zr/Al) but appear to share a mutual source rock endmember that is geochemically comparable to the intermediate, hornblende-rich syenites from the Wet Mountains. We propose that sorting of primary sediments during deposition drives this geochemical disparity, where more weatherable, fine-grained mafic and intermediate sediments are deposited into floodplains while less weatherable, coarse-grained intermediate and felsic sediments are deposited as channel fill (Fig. 4.7).

Despite forming from distinct mineralogical sources, overbank clays and sandstones exhibit markedly similar up-section trends in weathering-sensitive proxies. Clay and sandstone $\delta^7$Li values vary up-section by as much as 10 ‰ and these variations occur at similar stratigraphic heights. Similarly, clay and sandstone Mg/Ti, although significantly different in the lower portions of the stratigraphic section, become progressively similar up-section. The inconsistent relationship between $\delta^7$Li values and Mg/Ti underline that these trends are inconsistent with silicate weathering as a primary control. We propose that for stratigraphically adjacent overbank clays and sandstones to have such similar isotopic and geochemical compositions, both deposits must share a mineralogical phase that is concentrated in Li and Mg,

such as amphibole, pyroxene, or biotite . Whereas metasedimentary lithic fragments would be the host of Li and Mg for sandstones, fine-grained hornblende (amphibole), pyroxene, or biotite would be the host for overbank deposits.

Ultimately, we conclude that sediments in the Huerfano Basin underwent very little weathering, which agrees with findings from nearby Laramide basins during this time interval (Chapter 3; Wang et al., 2017). However, we propose the limited weathering is due to the short residence time of sediments in floodplains. These inferences from geochemical and isotopic data are consistent with basin stratigraphy, which contains evidence of thin, weakly developed soils and mobile river channels. Because of the limited temporal constraints in the basin, we cannot rule out the possibility of climate and/or tectonics influencing sediment transfer through the basin. However, an alternative and novel explanation for low weathering intensity is the lack of sediment cohesion controlled by the intrinsic properties of source rock sediments. Stripped of their sedimentary cover, the Wet Mountains supplied crystalline bedrock that was thermodynamically poised to undergo intense chemical weathering. However, without the input of fine-grained sediments to the basin, sediments did not cohere, preventing landscape stabilization, soil development, and intense weathering. It is entirely plausible that the locus of intense weathering existed farther downstream where the progressive weathering of sediments and decreased local relief allowed for the development of robust, stable floodplains. If this were the case, then the unroofing of crystalline bedrock would still yield a large silicate weathering flux despite the limited weathering in the upper reaches of a drainage catchment. Nevertheless, these results provide a new, sedimentological perspective of silicate weathering and lay the groundwork for future studies to test this potential limiting mechanism.

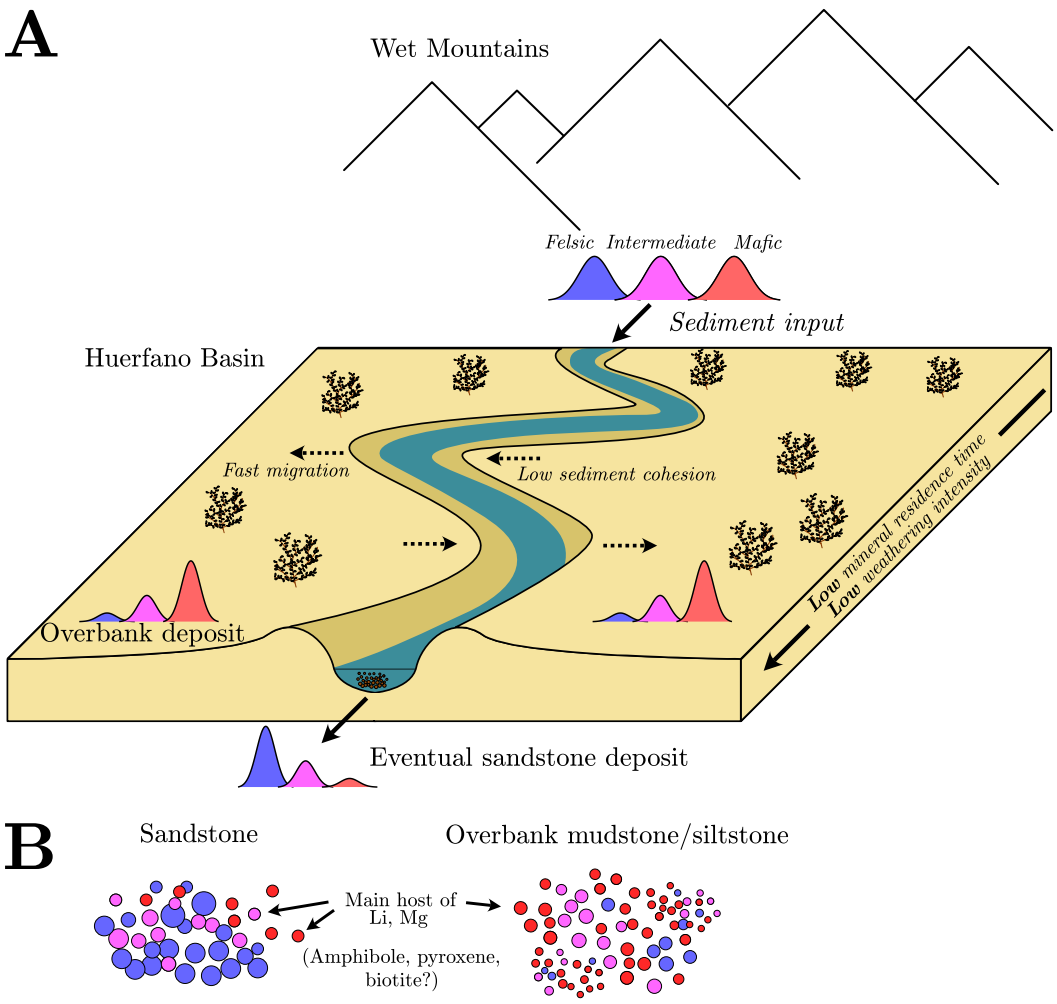


Figure 4.7: Conceptual diagram of sediment chemistry, transport, and weathering in the Huerfano Basin. A) The Wet Mountains are the sole sediment source of Paleocene and Eocene sediments to the Huerfano Basin. Those sediments undergo very little chemical weathering, which we posit is due to low mineral residences times in the basin. Differences in chemistry between overbank clays and sandstones are driven by sorting during deposition, with overbank deposits containing primarily mafic sediments and sandstones containing primarily felsic sediments. B) Interpreted sediment grain size distributions and chemistries for sandstones and overbank mudstones and siltstones. Up-section similarities in clay and sandstone $\delta^7$Li values and Mg/Ti are proposed to be due to the mutual presence of Li and Mg-rich mafic-to-intermediate minerals, like amphibole, pyroxene, and biotite, that comprise both deposits.

# Chapter 5

# Conclusions

Silicate weathering is a fundamental Earth system process because it modifies the physical and chemical composition of Earth's crust, modulates the chemical composition of the ocean, and influences nutrient cycles that affect both marine and terrestrial biota. These broad connections to various components of the Earth, despite motivating focused investigation for over a century, make silicate weathering greatly challenging to characterize theoretically. Improvements in measuring nontraditional isotope ratios, such as Li isotope ratios, have made available new methods that facilitate our understanding of silicate weathering and its controls. As these measurements become more routine, there is an increased need to both scrutinize underlying mechanisms within these isotope system and to determine the extent of these systems' capabilities. The overarching objective of this dissertation is to understand how geologic and environmental conditions, and the processes that they promote, can manifest in a Li isotope composition of water or sediments.

In Chapter 2, a global compilation of river water Li isotope compositions is investigated through statistical and modeling techniques. A central and important finding from this study is that there is not an individual catchment variable that can adequately describe the global range of observed $\delta^7\mathrm{Li}_f$ values. However unsurprising this finding is, this study is the first attempt at directly link catchment-

average properties with a global dataset of $\delta^7Li_f$ values and thereby corroborate the null hypothesis regarding multiple controls of silicate weathering. In addition, the numerical models more or less corroborate the weathering regime hypothesis (e.g., Dellinger et al., 2015), which suggests that $\delta^7Li_f$ values are closely related to catchment-scale denudation mechanisms. This finding, again, fits neatly within existing paradigms for silicate weathering. However, Chapter 2 addresses several important knowledge gaps, namely in how catchment properties are related denudation mechanisms and thus how *processes* are ultimately imprinted on river water Li isotope compositions. The conceptual framework that concludes this study highlights several avenues of future research and how Li isotopes, among other geochemical proxies, can be used to further refine catchment-scale denudation. These avenues include 1) the discernment of shallow (i.e., soil) weathering from groundwater (i.e., deep) weathering in mountain hillslopes/transitional catchments and 2) the role of transient, external perturbations in modulating weathering in low-relief environments, like floodplains or shields. Ultimately, this study reinforces the idea that multiple weathering-sensitive geochemical proxies will be needed to address many outstanding questions (e.g., Frings, 2019), especially those highlighted herein.

Chapters 3 and 4 work in concert. Both are studies of silicate weathering in intermontane basins during the Paleocene and Eocene epochs, and both utilize Li isotopes, major and trace element analyses, and sedimentological information to deduce controls of silicate weathering. The focus of Chapter 3 is to discern how silicate weathering intensity changes in response to the Paleocene-Eocene Thermal Maximum in the Bighorn Basin. The geochemical and isotopic data, in conjunction with sedimentological information, newly illuminate that floodplain weathering can actively respond to sudden changes in climate. Weathering in floodplains is often overlooked when considering climatic perturbations because in these environment, it is suggested that the supply of fresh, un-weathered sediments is low, and that they

therefore would not respond actively to a sudden change. However, these findings illustrate that better soil drainage due to seasonal rainfall may catalyze weathering reactions and expand the zone (i.e., depth into soil) over which oxidative weathering occurs. Through both the development of theory for floodplain weathering and observations of other ancient floodplain deposits that span the PETM, future studies should explore how widely applicable these findings in the Bighorn Basin are to other low-relief environments.

Chapter 4 acts as a foil to Chapter 3 due to the distinctly crystalline source rocks contained in the hinterland of the Huerfano Basin. This study highlights that despite tropical climates and high atmospheric $pCO_2$, silicate weathering in the Huerfano Basin is notably limited. The evidence for limited weathering comes from the comparable up-section trends in sandstone and clay $\delta^7$Li values, despite the fact that they are composed of primary sediments with distinct compositions. The comparable up-section trends suggest Li is predominantly hosted in one mineral phase that is mutually found in sandstones and clay. Although needing further evidence, this finding highlights a potential pitfall in Li isotope studies when source rock and mineral-specific chemistries are not fully characterized. Two potential hypotheses are developed to describe the limited weathering in the Huerfano Basin and both are derived from basin stratigraphy. The first hypothesis suggests that the lack of sediment cohesion, due to the absence of clay-sized source sediments, stunted the development of mature soils. The second suggests that sediment influxes from the mountains, perhaps due to the proximity of the basin to the hinterland, were too large to allow for extensive periods of silicate weathering before the burial of sediments. Thermochronologic constraints of uplift in the Wet Mountains, either from detrital grains or minerals in bedrock, will enable hypothesis testing.

Lastly, one particularly rich avenue of future research (which would benefit future research objectives related to Chapters 3 and 4) is the synthesis of high-

resolution global climate models (e.g., Community Atmosphere Model; Neale et al., 2010), landscape evolution models (e.g., Landlab; Barnhart et al., 2020), and reactive transport models (e.g. CrunchFlow; Steefel and Maher, 2009) to evaluate the co-evolution of climate, landscapes, and soil chemistry on $10^4$- to $10^5$-year timescales. These synthesized models, benchmarked against geochemical and sedimentological observations in sedimentary basins, could enable an understanding of silicate weathering on timescales that are seldom resolvable from the geologic record or the modern.

# Appendices

## A.1 Li isotope composition of river water informed by catchment properties

### A.1.1 Comparison between Upper Continental Crust (UCC) and calculated source rock chemistry

We compare UCC source rock $\delta^7$Li values with $\delta^7$Li source values based off a weighted average of exposed source rock compositions. Our assumed rock Li concentrations and $\delta^7$Li values are median values of those reported in Tomascak et al. (2016) and our assumed Na concentrations are values reported in Rudnick and Gao (2003) (Table A.1). Source rock Li/Na and $\delta^7$Li values are found through these formulations

$$\left(\frac{\mathrm{Li}}{\mathrm{Na}}\right)_{\mathrm{source}} = \sum_i \chi_i \left(\frac{\mathrm{Li}}{\mathrm{Na}}\right)_i \tag{A.1}$$

and

$$\left(\frac{\mathrm{Li}}{\mathrm{Na}}\right)_{\mathrm{source}} \delta^7\mathrm{Li}_{\mathrm{source}} = \sum_i \chi_i \delta^7\mathrm{Li}_i \left(\frac{\mathrm{Li}}{\mathrm{Na}}\right)_i \tag{A.2}$$

where $i$ corresponds to a given rock type (sedimentary, volcanic, plutonic, metamorphic, or unconsolidated sediments) and $\chi_i$ is the volumetric proportion of the rock type i [$km^2/km^2$].

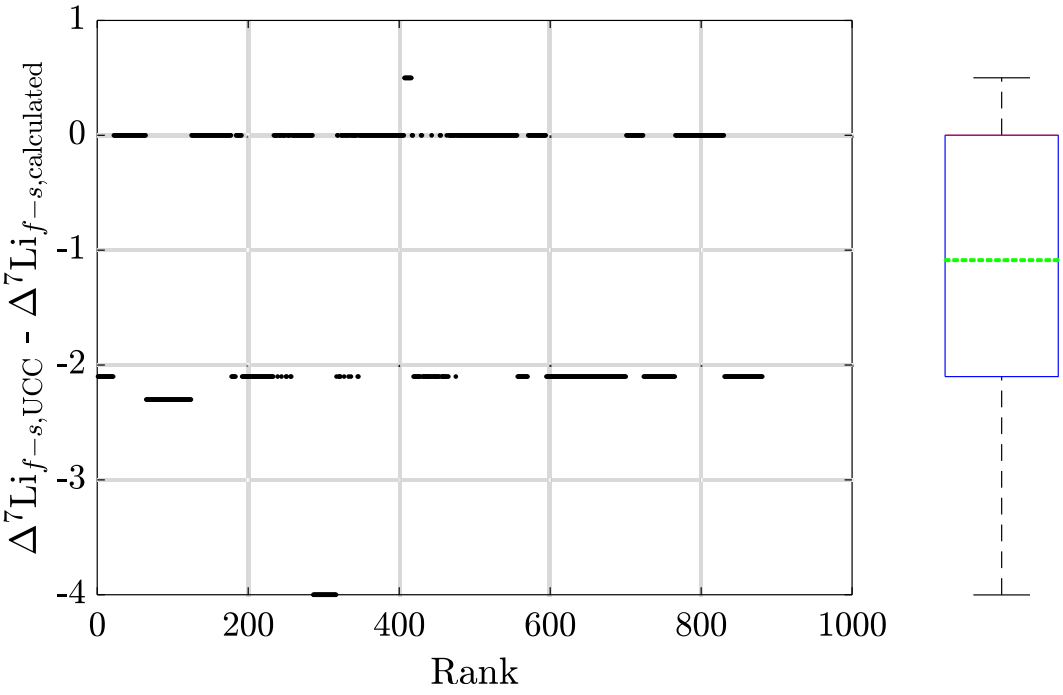


Figure A.1: Plot of the difference between our simplified $\Delta^7Li_{f-s}$ (i.e., one using either reported $\delta^7Li_{source}$ values or assumed UCC range) and $\Delta^7Li_{f-s}$ computed using a weighted mean of rock proportions in each catchment (all presumed $\delta^7Li_{source}$ values and $Li_{source}$ concentrations are derived from median values reported in Tomascak et al., 2016). The box plot to the shows the quantile limits with the red line corresponding to the median and the green dashed line corresponding to the mean.

### A.1.2 Two-way ANOVA

Two-way ANOVA enables us to assess the strength of variable correlations using categorical data, allowing us to consider the effect of lithology on geochemical data. For each catchment variable (i.e. independent variable), we define categories in which geochemical data ($\Delta^7Li_{f-s}$ and $\log_{10}$ Li/Na) are grouped and then test the differ-

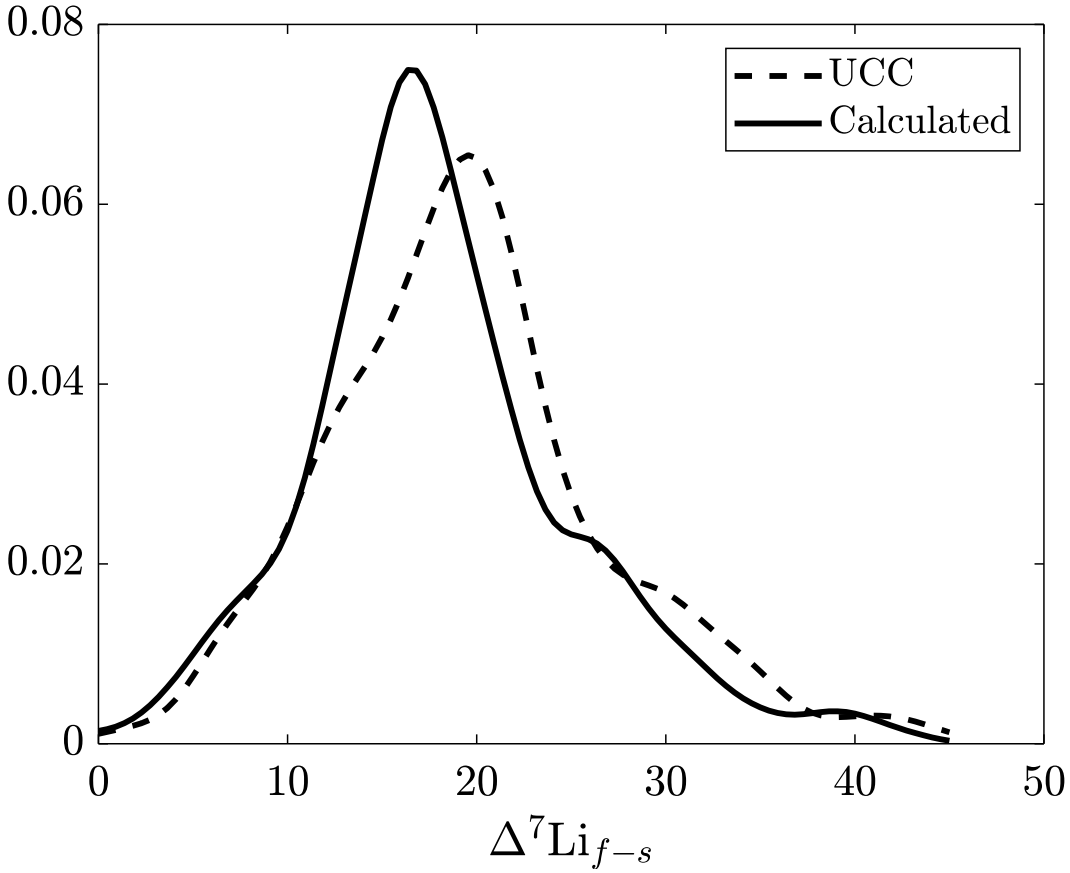


Figure A.2: Kernel density plots of $\Delta^7\mathrm{Li}_{f-s}$ with two separate $\delta^7\mathrm{Li}_{source}$ value computations (see Section A.1.1 for explanations).

ence among category medians and distributions. We perform a two-sided Wilcoxon rank sum test to assess whether two categories contain data from continuous distributions with equal medians. If all category medians and distributions are distinct at the 5% significance level (p-value $< 0.05$), the catchment variable has a statistically significant "main effect" on the geochemical data. Two-way ANOVA further enables us to determine if "interaction effects" exist, meaning that two catchment variables with their combined categories yield geochemical data with distinct medians and distributions. We define 3 to 4 categories for each catchment variable. For example, there are three categories for mean annual temperature (MAT): -20–0 °C, 0–20 °C,

and 20–40 °C (see Fig. A.1.5 for categories of other catchment variables).

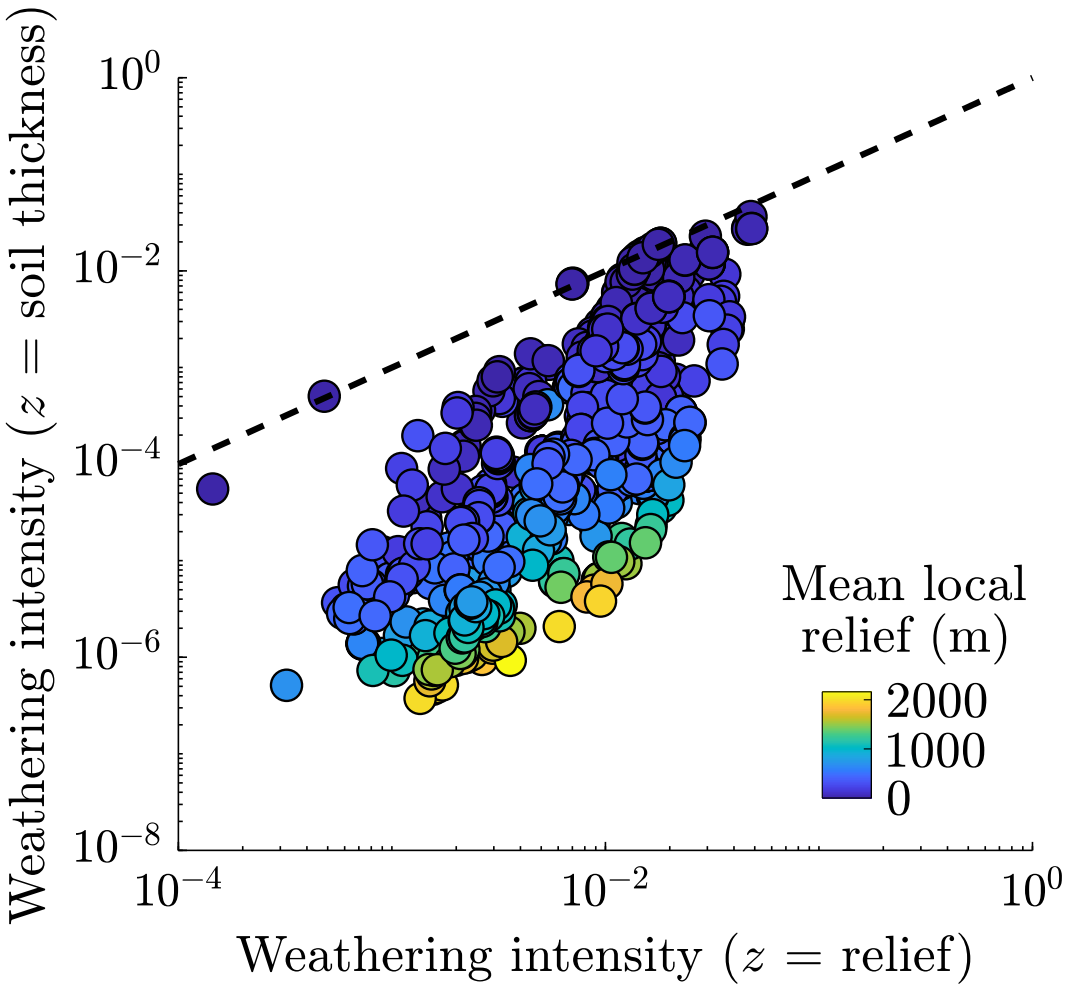


Figure A.3: Weathering intensity predictions with the steady state weathering model (West, 2012) assuming weathering zone thickness $z$ is equal to mean local relief or soil thickness (using Heimsath et al., 1997 formulation). All other input variables are equal between the models. Black dashed line corresponds to the 1:1 line.

### A.1.3 Mass balance calculations for Li isotope predictions

We adapt the time-dependent weathering expression (Eq. 2.10) to predict changes in $[\mathrm{Li}]_f$, $\delta^7\mathrm{Li}_f$ values, and $\delta^7\mathrm{Li}_{source}$ values. The chemistry of water is going to

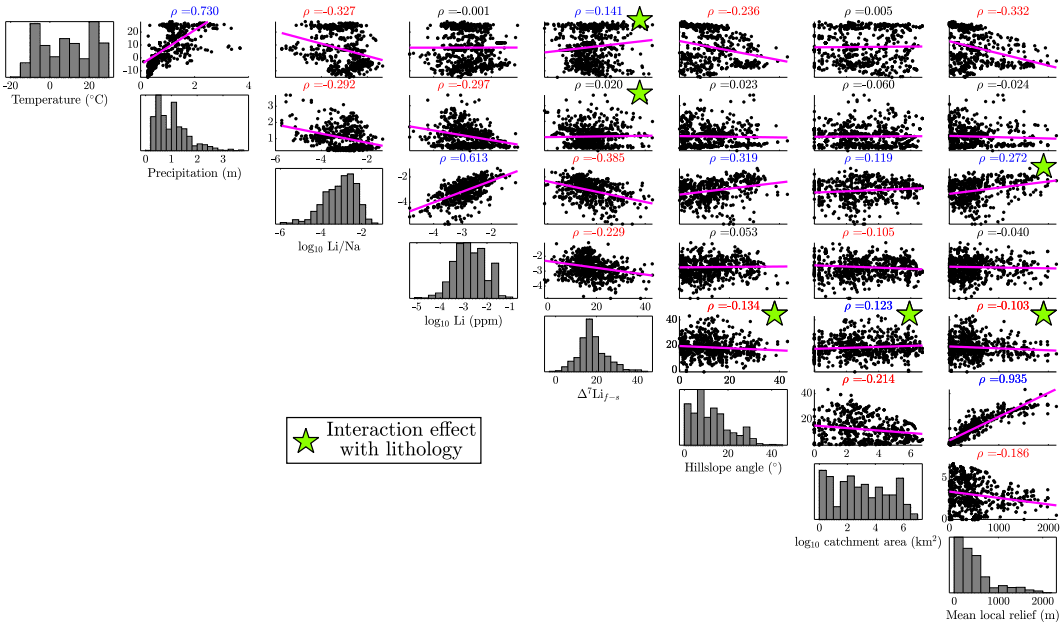


Figure A.4: Correlation plots and histograms of all continuous catchment variables. All bivariate plots found in each row contain the same variable on the y-axis whereas each column contains that variable on the x-axis. Magenta lines represent least squares linear regressions and all values in the title of bivariate plots are Spearman's $\rho$. where values $> 0.1$ have a significant monotonic relationship that are either positive (blue), negative (red) correlations, or are $< 0.1$ and lack a significant monotonic relationship (black). Green stars indicate a significant interaction effect of a catchment variable and lithology on river water chemistry, as determined by ANOVA (p-value $< 0.05$).

reflect the competing processes of mineral dissolution and formation. Whereas Li input due to mineral dissolution will directly reflect the chemistry of soil minerals, Li uptake from water due to the formation of secondary minerals will be modified by the volumetric partition coefficient $K_{Li}$ (ppm ppm-1) of those phases, which is expressed for each mineral phase as

$$K_{Li} = \frac{[Li]_{soil,i}}{[Li]_f}. \tag{A.3}$$

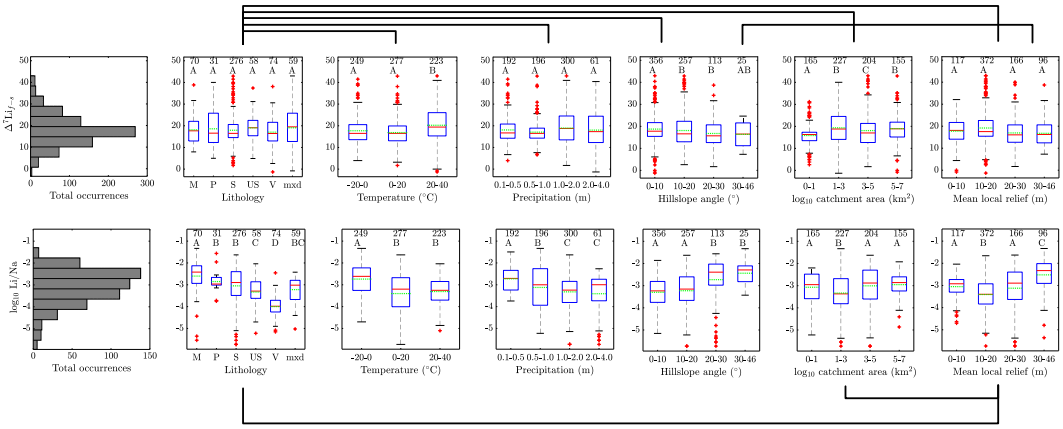


Figure A.5: Two-way analysis of variance (ANOVA) results for global $\Delta^7\text{Li}_{f-s}$ and $\log_{10}$ Li/Na. The leftmost plots are histograms of $\Delta^7\text{Li}_{f-s}$ and $\log_{10}$ Li/Na and the rest of each row contains those geochemical observations categorically binned for each primary catchment variable, shown as box-and-whisker plots. Horizontal lines on box-and-whisker plot correspond to a quartile limit and the green dashed lines are mean variables for that data subpopulation. Red plus signs are outliers. The number above each box corresponds to the total number of values in the distribution and letters above indicate the "Wilcoxon" group that each group falls in; as such, bins with the same letter are statistically indistinguishable. Black brackets connecting each catchment variable pair indicate statistically significant variable interactions (p-value $< 0.05$), akin to the bolded green borders in Fig. 2.3. Lithology abbreviations include metamorphic (M), plutonic (P), sedimentary (S), unconsolidated sediment (US), volcanic (V), and mixed (mxd) bedrock dominated catchments.

We assume that volumetric partition coefficients are constant although they can exhibit a wide range of values due to mineral stoichiometry (e.g.,Bohlin and Bickle, 2019; Tardy et al., 1972). We can thus express a modification of the time-dependent weathering equation which include [Li]f and substitutions related to Eq. A.3:

$$[\text{Li}]_f W = z \sum_i^N \exp\left(\frac{E_{a_i}}{\text{R}T} - \frac{E_{a_i}}{\text{R}T_0}\right)\left\{\kappa_i A_i [X_i]_s [\text{Li}]_{soil,i} w_i \rho_i - \text{K}_{\text{Li},i}[\text{Li}]_f \eta_i s_i w_i\right\}. \quad \text{(A.4)}$$

We follow a similar approach for tracking $\delta^7$Lif values, which must also account for isotopic fractionation due to secondary mineral formation. In this case, we can

express the relationship between $\delta^7\mathrm{Li}_f$ to $\delta^7\mathrm{Li}_{s,i}$ assuming an equilibrium isotopic fractionation such that

$$1000\log\alpha_{soil,i-f} \approx \delta^7\mathrm{Li}_{soil,i} - \delta^7\mathrm{Li}_f \tag{A.5}$$

where $\alpha_{soil,i-f}$ is the equilibrium fractionation factor between the newly formed secondary mineral and water, which is also a function of temperature. With Eq. A.5, we can adapt Eq. A.4 to come to a similar expression that includes isotopic compositions, expressed as

$$[\mathrm{Li}]_f\delta^7[\mathrm{Li}]_f W = z\sum_i^N \exp\Big(\frac{E_{a_i}}{\mathrm{R}T} - \frac{E_{a_i}}{\mathrm{R}T_0}\Big)\Big\{\kappa_i A_i [X_i]_s [\mathrm{Li}]_{soil,i}\delta^7[\mathrm{Li}]_{soil,i} w_i\rho_i - \cdots$$
$$\mathrm{K}_{\mathrm{Li},i}[\mathrm{Li}]_f[1000\log\alpha_{soil,i-f}(T) + \delta^7\mathrm{Li}_f]\eta_i s_i w_i\Big\}. \tag{A.6}$$

Eq. A.4 and A.6 are rearranged and solved for $[\mathrm{Li}]_f$ and $\delta^7\mathrm{Li}_f$ in sequence. Lastly, we update $\delta^7\mathrm{Li}_s$ values at each time step to reflect the formation of secondary minerals in the soil. To do so, we first calculate the relative proportion $f_i$ of newly formed secondary minerals (subscript new), primary minerals (subscript *source*), pre-existing minerals in the soil (subscript *old*), each expressed as such:

$$f_{new,i} = \cdots$$
$$\frac{\exp\Big(\frac{E_{a_i}}{\mathrm{R}T} - \frac{E_{a_i}}{\mathrm{R}T_0}\Big)\frac{\eta_i s_i}{\rho_{soil}}}{\exp\Big(\frac{E_{a_i}}{\mathrm{R}T} - \frac{E_{a_i}}{\mathrm{R}T_0}\Big)\Big\{\frac{\eta_i s_i}{\rho_{soil}} + \kappa_i A_i [X_i]_{soil}\Big\} + \frac{E}{\rho_{soil} z}[X_i]_{soil} + \frac{D+\epsilon_0\exp(-\alpha z)}{\rho_{soil} z}[X_i]_{source}}; \tag{A.7}$$

$$f_{source,i} = \cdots$$
$$\frac{\frac{D+\epsilon_0 \exp(-\alpha z)}{\rho_{soil} z}[X_i]_{source}}{\exp\left(\frac{E_{a_i}}{\mathrm{R}T} - \frac{E_{a_i}}{\mathrm{R}T_0}\right)\left\{\frac{\eta_i s_i}{\rho_{soil}} + \kappa_i A_i [X_i]_{soil}\right\} + \frac{E}{\rho_{soil} z}[X_i]_{soil} + \frac{D+\epsilon_0 \exp(-\alpha z)}{\rho_{soil} z}[X_i]_{source}}; \tag{A.8}$$

$$f_{old,i} = \cdots$$
$$\frac{[X_i]_{soil}\left\{\exp\left(\frac{E_{a_i}}{\mathrm{R}T} - \frac{E_{a_i}}{\mathrm{R}T_0}\right)\kappa_i A_i + \frac{E}{\rho_{soil} z}\right\}}{\exp\left(\frac{E_{a_i}}{\mathrm{R}T} - \frac{E_{a_i}}{\mathrm{R}T_0}\right)\left\{\frac{\eta_i s_i}{\rho_{soil}} + \kappa_i A_i [X_i]_{soil}\right\} + \frac{E}{\rho_{soil} z}[X_i]_{soil} + \frac{D+\epsilon_0 \exp(-\alpha z)}{\rho_{soil} z}[X_i]_{source}}. \tag{A.9}$$

With these proportions determined, new mineral-specific $\mathrm{Li}_s$ and $\delta^7\mathrm{Li}_s$ values can be calculated where

$$[\mathrm{Li}]_{soil,i} = [\mathrm{Li}]_{soil_{old},i} f_{old,i} + [\mathrm{Li}]_{source,i} f_{source,i} + \mathrm{K}_{\mathrm{Li},i}[\mathrm{Li}]_f f_{new,i} \tag{A.10}$$

and

$$[\mathrm{Li}]_{soil,i}\delta^7\mathrm{Li}_{soil,i} = [\mathrm{Li}]_{soil_{old},i}\delta^7\mathrm{Li}_{soil_{old},i} f_{old,i} + [\mathrm{Li}]_{source,i}\delta^7\mathrm{Li}_{source,i} f_{source,i} + \mathrm{K}_{\mathrm{Li},i}[\mathrm{Li}]_f(\delta^7\mathrm{Li}_f + 1000\log\alpha_{soil,i-f}(T)) f_{new,i}. \tag{A.11}$$

Note that subscript $s_{old}$ corresponds to the value of the pre-existing soil. Once those changes are accounted for, we express the bulk soil $\delta^7\mathrm{Li}$ value as

$$\delta^7\mathrm{Li}_{soil} = \sum_{i+1}^{N} [X_i]_{soil} w_i [\mathrm{Li}]_{soil,i} \delta^7\mathrm{Li}_{soil,i}. \tag{A.12}$$

Eq. A.12 ultimately enables us to express Li isotopes compositions as $\Delta^7 Li_{f-s}$ values.

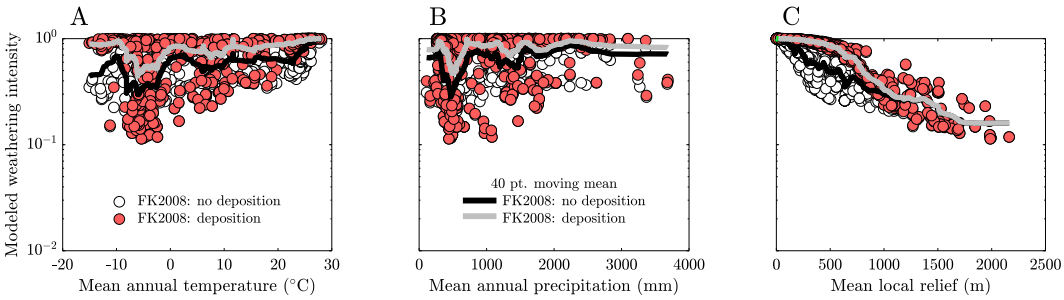


Figure A.6: Modeled weathering intensities as a function of MAT (A), MAP (B), and mean local relief (C) using the FK2008 model and the highest known soil production rate $\epsilon_0$ =15 kg m$^{-2}$ yr$^{-1}$ (Larsen et al., 2014a).

### A.1.4 "README" for Li isotope database

#### File description

This Excel spread (available publicly here) contains information regarding river water chemistry (Li isotope data, Li concentration data, Na concentration data) and properties of their drainage catchments.

1. Empty cells in the spreadsheet mean that either the study did not report the geochemical data or catchment properties could not be determined for those samples.

2. Each **row** corresponds to an individual sample and each **column** corresponds to a certain descriptor of that river water sample.

#### Column descriptions

1. Some studies do not report the Li isotope composition of bedrock. If they do not, we assign a range of values (a minimum and a maximum). Studies that

have the range bedrock $\delta^7$Li values (Li isotope composition) of [1, 3.2] do not report **any** bedrock data and studies that have other ranges report bedrock data but do NOT pair the individual bedrock $\delta^7$Li values with a river water $\delta^7$Li value.

2. For each catchment property (excluding lithologic information) we report the minimum, maximum, mean, and standard deviation of the given catchment property.

   (a) **T** corresponds to **mean annual temperature (°C)**

   (b) **P** corresponds to **mean annual precipitation (mm/yr)**

   (c) **FL** corresponds to **mean flow length (m)**

   (d) **R** corresponds to **mean local relief (m)**

3. For lithologic information, we report the fraction (a number between 0 and 1) of the catchment that is composed of that rock type.

   (a) **su** corresponds to **unconsolidated sediments**

   (b) **ss** corresponds to **siliciclastic sedimentary rocks**

   (c) **sm** corresponds to **mixed sedimentary rocks**

   (d) **py** corresponds to **pyroclastic sedimentary rocks**

   (e) **sc** corresponds to **carbonate sedimentary rocks**

   (f) **ev** corresponds to **evaporites**

   (g) **mt** corresponds to **metamorphic rocks**

   (h) **pa** corresponds to **acidic (felsic) plutonic rocks**

   (i) **pi** corresponds to **intermediate plutonic rocks**

   (j) **pb** corresponds to **basic (mafic) plutonic rocks**

   (k) **va** corresponds to **acidic (felsic) volcanic rocks**

| Rock type | Li (ppm) | Na (ppm) | $\delta^7$Li (‰ LSVEC) |
|---|---|---|---|
| Sedimentary | 70 | 24259 | -1.0 |
| Unconsolidated sediments | 40 | 24259 | -0.5 |
| Metamorphic | 20 | 24159 | 0 |
| Plutonic | 40 | 22774 | 1.0 |
| Volcanic | 15 | 24259 | 4.0 |

Table A.1: Li concentration, Na concentrations, and $\delta^7$Li values used for $\delta^7\text{Li}_{\text{source}}$ computation from catchment lithology.

(l) **vi** corresponds to **intermediate volcanic rocks**

(m) **vb** corresponds to **basic (mafic) volcanic rocks**

(n) **ig** corresponds to **ice and glaciers**

(o) **wb** corresponds to **water bodies**

(p) **nd** corresponds to **no data**

4. Other variables whose column headers require description:

   (a) **W (t km2 yr)** corresponds to **reported silicate weathering fluxes** in units of t $\text{km}^{-2}$ $\text{yr}^{-1}$

   (b) **W/D** corresponds to **reported weathering intensity**

**Miscellany**

1. Any stream order value of -9999 indicates that the catchment was too small for a stream order to be determined.

| Mineral | Li (ppm) | $\delta^7$Li (‰ LSVEC) | 1000 log$\alpha_{s-f}(T)^a$ | $K_{Li}$ (ppm ppm$^{-1}$) |
|---|---|---|---|---|
| Quartz | 5 | 15.0 | 1 | 1 |
| Plagioclase feldspar | 10 | 3.0 | 1 | 1 |
| Potassium feldspar | 20 | 3.0 | 1 | 1 |
| Biotite | 25 | 3.0 | 1 | 1 |
| Zircon | 5 | 3.0 | 1 | 1 |
| Kaolinite | 200 | -2.0 | $-\frac{1.63\times10^6}{T^2}+2.04$ | $200^b$ |

[a]Temperature-dependent equation for each mineral when forming from aqueous solution; [b]Value exhibits a 2-3 order-of-magnitude range (Bohlin and Bickle, 2019; Tardy et al., 1972). We elect to use a value on the lower end of the range since high values mask other underlying dynamics that the model reveals.

Table A.2: Mineral specific values for Li isotope calculations in time-dependent weathering equations

## A.2 Rapid silicate weathering response in floodplains during the Paleocene-Eocene Thermal Maximum

### Expanded geologic setting and sampling protocol

The Bighorn Basin formed in response to the uplifts of the Bighorn, Owl Creek, and Beartooth Mountains that bound the basin on the east, south, and west, respectively. These mountains were the primary contributors of sediment to the basin (Fig. A.7). Rapid exhumation of the Bighorn and Beartooth Mountains during the early to middle Paleocene induced dramatic basin subsidence preceding the PETM (Fan and Carrapa, 2014), offering accommodation for sediments that led to the coeval development of an axially draining alluvial system (Kraus, 1980; Kraus and Middleton, 1987). Each basement-cored uplift that flanks the basin exhumes Precambrian basement composed of gneiss and granite and overlying Paleozoic through Mesozoic sedimentary sequences composed of limestone, dolomite, arkose, and shale (e.g., DeCelles et al., 1991a; Thomas, 1965). Sediment accumulation rates in the basin are relatively constant through the late Paleocene and early Eocene (0.25–0.33 mm/yr; Clyde et al., 2007; 0.37 mm/yr; van der Meulen et al., 2020). Paleocurrents

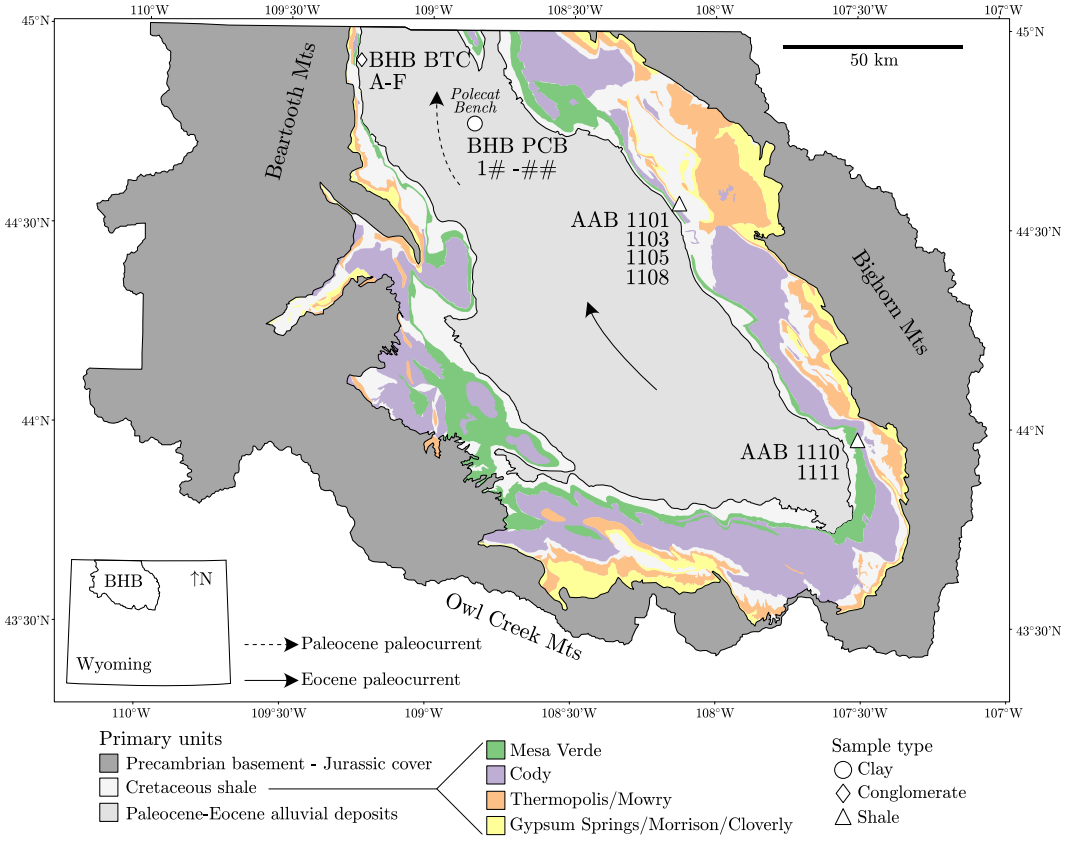


Figure A.7: Simplified geologic map of the Bighorn Basin after Love and Christiansen (1985). Shades of gray correspond to primary geologic units and colored formations correspond to Cretaceous shale formations analyzed in this study. All light gray area within the Cretaceous shale units correspond to geochemically uncharacterized units in this study. Letters beside the upward triangles, open circle, and diamond correspond to the names of samples gathered at each locality. Polecat Bench, in Powell, WY, is the primary locality of the study and where all paleosols were sampled. Inset: map of Wyoming, USA, and the location of the Bighorn Basin (BHB).

indicate northward drainage during the Paleocene transitioning to north and westward drainage during the Eocene (Bown and Kraus, 1981; Foreman, 2014; Neasham and Vondra, 1972) (Fig. A.7). Sediment provenance remains consistent across the PETM (May et al., 2013) and indicates the ultimate drainage of the basin into the

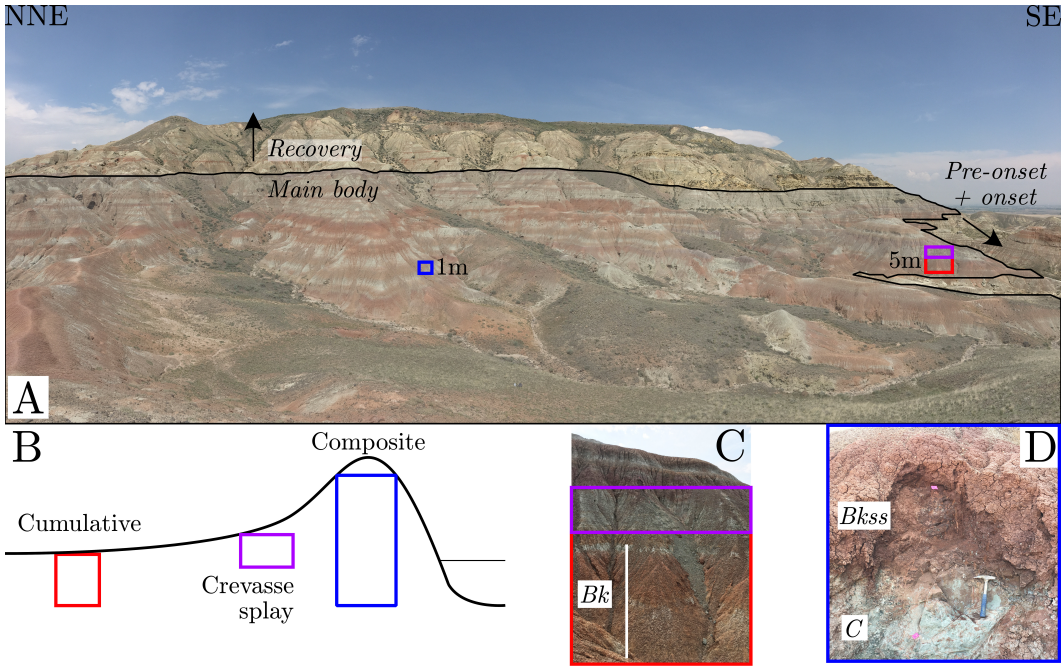


Figure A.8: Ancient floodplain deposits at Polecat Bench (location of white circle in Fig. A.7). A) Panoramic view of a section of Polecat Bench characterized in this study, spanning a view of the locality from north northeast (NNE) to southeast (SE). Key time intervals (pre-onset, onset, main body, and recovery) are shown, with the grayed middle portion representing the main body phase. The blue box corresponds to a composite soil, the red box corresponds to a cumulative soil, and the purple box corresponds to a crevasse splay soil. The vertical length of the blue box and red box spans approximately 1 and 5 meters, respectively. B) Schematic half space of a cross-section through a floodplain (after Kraus, 1999). Cumulative soils form farther from the ancient channel and topographically lower than composite and crevasse splay soils, which are closer to the ancient channel. C) Example cumulative and crevasse splay soils. The length of the white bar corresponds to an entire cumulative paleosol. The soil horizon is listed beside the white line (approx. 4m in length) corresponding to a large Bk soil horizon. D) Example composite soil. A drab green C horizon underlies a red/purple Bkss horizon. Rock hammer for scale.

present-day Gulf of Mexico during the Eocene (Sharman et al., 2017).

All Paleocene and Eocene sedimentary deposits come from the Willwood formation, which is broadly characterized as a progradational avulsion channel belt (Hajek and Wolinsky, 2012). Paleosols across the PETM showcase a range of colors,

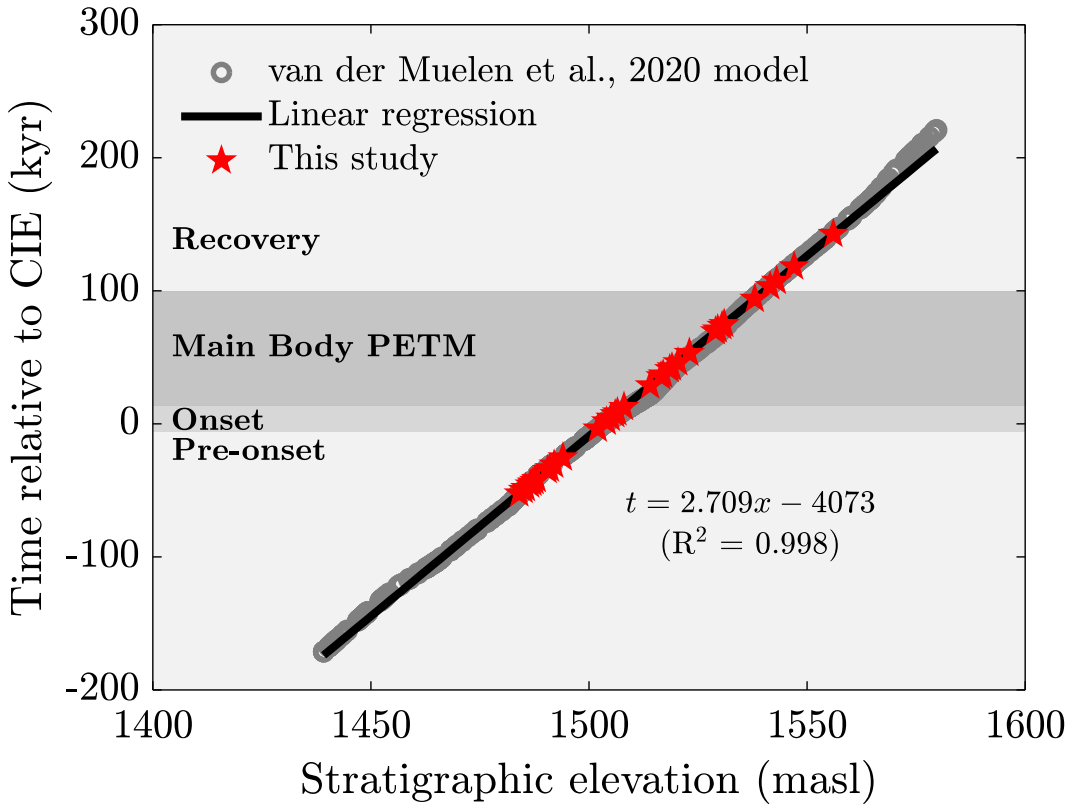


Figure A.9: Age model from van der Meulen et al. (2020) used to determine time relative to carbon isotope excursion (CIE) for samples analyzed in this study. The data were regressed linearly which enabled the determination of time for each sample (red stars) given their stratigraphic elevation. The equation for the linear regression (and associated $R^2$ value) and key time intervals (pre-onset, onset, main body, and recovery) are shown.

sedimentary structures, ichnofabrics, and mineralogical compositions, all suggesting heterogeneous soil development, soil drainage, and hydroclimate through space and time (Abdul Aziz et al., 2008; Abels et al., 2013; Foreman, 2014; Kraus et al., 2013, 2015; Kraus and Hasiotis, 2006; Kraus and Riggins, 2007; Smith et al., 2008). The resultant "pedofacies" concept was largely established from observations of pedogenesis within overbank and avulsion deposits in the Willwood formation (e.g., Bown and Kraus, 1987; Kraus, 1999; Kraus and Aslan, 1993), where it is argued that

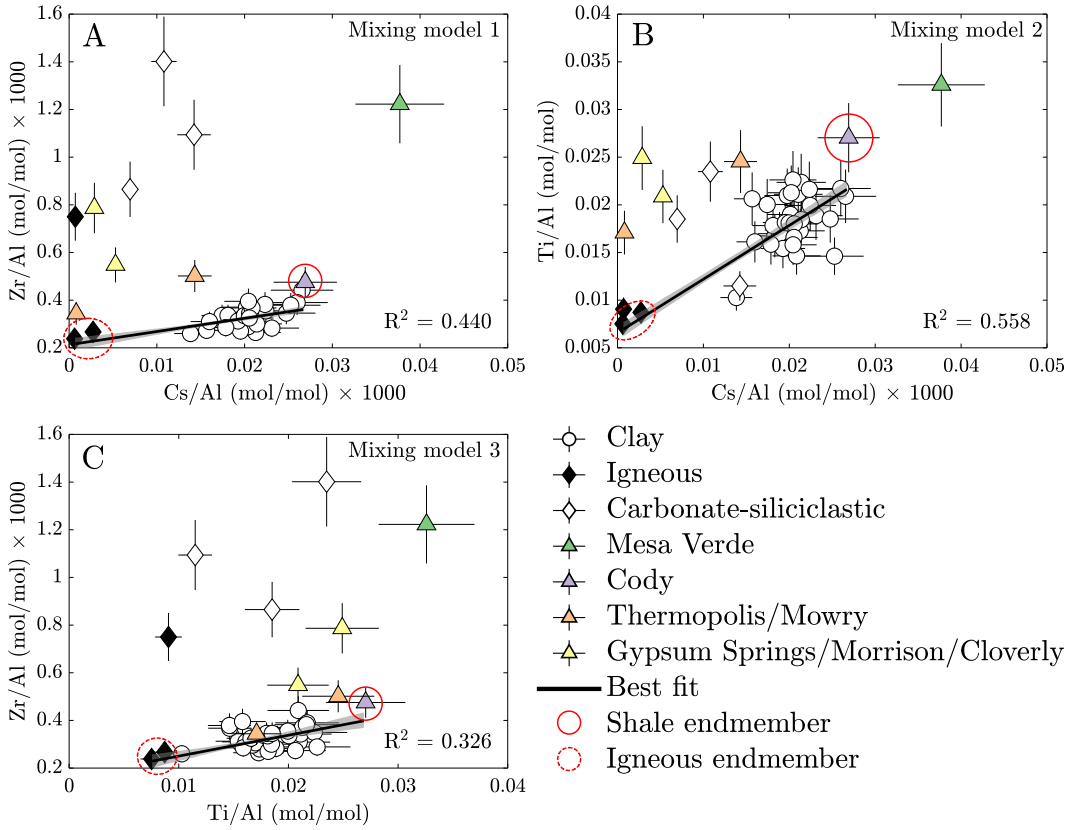


Figure A.10: Immobile element ratios of clays, conglomerate clasts (which contain igneous rock and carbonate clasts), and shales used for computing the source rock proportions for each clay sample. The three combinations of immobile element ratios (panels A, B, and C) are referred to as mixing models 1, 2, and 3, respectively. All immobile element ratios are in units of mole/mole. Error bars correspond to the propagated error (1 standard deviation) of numerator and denominator values. The black line in is the best fit line between the clays and identified endmembers (Cody shale, feldspar- and biotite-bearing igneous conglomerate clasts), and the gray envelope around the line is the 66% confidence interval. The linear fit in mixing model 2 has the highest $R^2$ value and thus is used to compute $f_{\text{shale}}$ and $\delta^7\text{Li}_{\text{source}}$ values.

the degree of soil development is a function of sediment supply and lateral location of the soil from the ancient channel (Fig. A.8). In this pedofacies framework, soils that form proximally to the ancient channel (termed composite soils) tend to

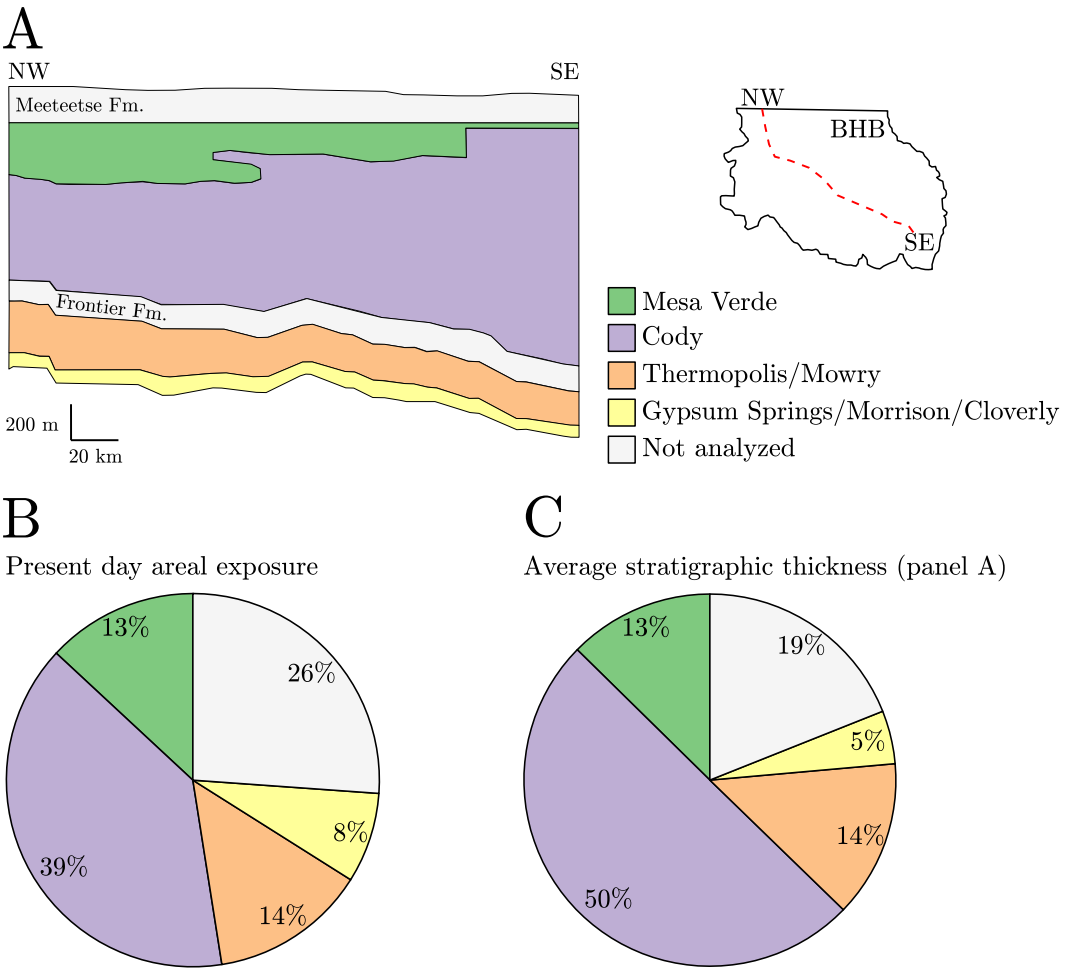


Figure A.11: Stratigraphic information of Cretaceous shale units in the Bighorn Basin. A) Cross-section stratigraphy of Cretaceous shale units along NW-SE transect through the Bighorn Basin (modified after Finn, 2019). B) Percentages of all exposed Cretaceous shale units (Fig. A.1). C) Percentage of Cretaceous shale in subsurface based off stratigraphic thicknesses (panel A).

contain a series of stacked coarse-grained C horizons and overlying truncated B horizons as subsequent deposition arrests soil development. In contrast, soils that form distally from the ancient channel (termed cumulative soils) tend to contain finer sediments and thick B horizons as the rate of pedogenesis is thought to match the slow and steady supply of overbank sediments. Composite soils tend to be better

drained and more oxidized than cumulative soils, but soil drainage can vary within a given pedofacies, as demonstrated by gradients in color along a given stratigraphic horizon. Lastly, in addition to these endmembers, heterolithic deposits (interpreted as crevasse splays; Kraus et al., 2015) crop out consistently within the lowermost Willwood and undergo pedogenesis (e.g., Kraus et al., 2013). All pedogenically modified crevasse splay deposits are interpreted as forming proximally to ancient channels.

At Polecat Bench, where all paleosols were sampled, outcrops were trenched 0.5–1m below modern soils to expose unaltered, lithified mudstones and siltstones. Samples were characterized in terms of bulk grain size, color, sedimentary structures, and presence/absence of nodular authigenic minerals (carbonates, Fe/Mn-oxides) and rhizoliths. This information was used to classify each deposit as a composite, cumulative, or crevasse splay soils. Approximately 10s of grams of material were gathered for each sample. Stratigraphic thicknesses were measured with a Jacob's staff and sighting lens. Stratigraphic elevations were determined by superimposing sample GPS coordinates onto a GIS map stack in ArcScene and eliminating bedding dip. Paleosol descriptions, measured thicknesses, and the location of key marker beds were used to corroborate these elevations. These elevations were lastly converted to time with respect to the carbon isotope excursion using the age model of van der Meulen et al. (2020) (Fig. A.9).

In addition to sampling paleosols, synorogenic conglomerate clasts of the Beartooth conglomerate (DeCelles et al., 1991b) in nearby Clarks Fork Canyon (44°51'5.78"N, 109°18'14.43"W) were gathered. Six different clast types were identified (Table A.9) and were inferred to integrate the Precambrian through Mesozoic source rocks within the basin-bounding mountain ranges. Cretaceous shales, whose exposure during the Paleocene and Eocene were possibly more widespread (e.g., Baczynski et al., 2016), were also analyzed. Shale samples in this study crop out on

the eastern flank of the basin (Fig. A.8).

## Analytical methods

### A.2.1 Sample preparation

There are two different analytes in this study that require different sample preparation: (i) clay-sized ($< 2\mu$m) fractions from paleosols; and (ii) bulk source rocks. The mass of sample required for geochemical analyses was determined by considering our minimum mass constraint for accurate and precise Li isotope measurements (50 ng Li). To selectively extract clay-sized sediments, approximately 10 g of paleosol matrices were disaggregated in deionized water for at least 24 hours. Once disaggregated, samples were centrifuged to isolate clay-size fractions. Around 20 mg of clay from each sample were processed for geochemical analysis. Before full dissolution, all clays were treated with a 1M ammonium chloride solution (using a 1 mL solution:5 mg sample ratio *sensu* Dosseto et al., 2015) and agitated for 1 hour (repeated 3 times) to remove all exchangeable cations that are susceptible to post-depositional exchange with fluids. All solution was discarded between steps. Other partial dissolution steps to remove carbonate, Fe/Mn oxide, and organic fractions were excluded because negligible amounts of Li are found in those fractions in well-drained soils (Li et al., 2020) and some reagents used to selectively dissolve non-silicate fractions have been shown to dissolve phyllosilicate minerals (e.g., Whalley and Grant, 1994). All pre-treated clays were rinsed 3 times in doubly deionized (18.2 m$\Omega$) water before full dissolution.

Bulk source rocks were cut with a water saw where fresh, un-oxidized portions of the sample were targeted for geochemical analysis. All cut rock samples were subsequently powdered in a diamonite mortar and pestle. Approximately 45–75 mg of powder for each rock sample were used for geochemical analysis.

All samples underwent a sequence of strong acid dissolutions involving con-

centrated HF, concentrated HF + concentrated $HNO_3$, and 6N HCl. All steps were repeated if significant solid residue remained after dissolution. Upon samples being fully dissolved, all were reconstituted in 6N HNO3 and inspected for residuum. If fully in solution, samples were split into two aliquots: one for major and trace element analysis (10 % v/v) and another for Li isotope analysis (90 % v/v).

### A.2.2 Major and trace element analysis

Major and trace element concentrations were measured at the University of Texas at Austin with an Agilent 7500ce quadrupole ICP-MS. All samples in 6N $HNO_3$ were diluted to 2 % (v/v) $HNO_3$ solutions and introduced into the ICP-MS in solution. Uncertainties for elements Ca, Al, Mg, Ti, and K were <6 % and Li, Cs, and Zr were <12 %, based on replicate analyses of both in-house standards and the Geological Survey of Japan JR-1 (rhyolite) and NIST1643f international standards.

### A.2.3 Li isotope ratios

To selectively extract Li from other cations prior to isotope measurements, samples underwent cation chromatography following Magna et al. (2004). All samples were reconstituted in 0.67N $HN_3$ + methanol (30% v/v) and centrifuged prior to being loaded on columns packed with BioRad® AG 50W-X8 (200–400 mesh) cation exchange resin. Eluate was collected before and after the Li elution to assure that Li yields were >99%. After cation chromatography, all samples were reconstituted in 2% (v/v) $HNO_3$ for isotope analysis in solution mode. Li isotope ratios were measured at the University of Texas at Austin with a Nu Plasma 3 Multi Collector ICP-MS. All measured $^{7}Li/^{6}Li$ ratios were converted to delta values (in units of ‰)

following a commonplace standard-sample-standard bracketing method where

$$\delta^7\mathrm{Li}_{\mathrm{sample}} = \left\{ \frac{\left(\frac{^7\mathrm{Li}}{^6\mathrm{Li}}\right)_{\mathrm{sample}}}{\left[\left(\frac{^7\mathrm{Li}}{^6\mathrm{Li}}\right)_{\mathrm{standard,i-1}} + \left(\frac{^7\mathrm{Li}}{^6\mathrm{Li}}\right)_{\mathrm{standard,i+1}}\right]/2} \right\} \times 1000 \qquad \text{(A.13)}$$

and "standard i-1" and "standard i+1" correspond to measured IRMM-016 isotope standards before and after the "sample" unknown, respectively. All delta values computed in Eq. A.13 are then converted to delta values relative to LSVEC standard. During each session of cation chromatography, at least one matrix-matched analytical standard (i.e., JR-1 rhyolites) was processed alongside unknowns. Over the time in which unknowns were analyzed, the long-term average $\delta^7\mathrm{Li}_{\mathrm{JR-1}}$ value was 4.0 ‰ ± 0.4 (2 s.d.; N = 16) – compared to a reported value of 4.0 ‰ ± 0.3 (Oi et al., 1997) – and $\delta^7\mathrm{Li}_{\mathrm{LSVEC}}$ value was 0 ‰ ± 0.2 (2 s.d.; N = 34). In-run standard error ($2\sigma$) for unknowns was ~0.1 ‰. The long-term error for JR-1 (0.4 ‰) is applied to all unknown values as a conservative estimate.

### Immobile element mixing models

The immobile element compositions of clays, when compared to the immobile element compositions of conglomerates and shales, can be used to quantify the proportion of source rocks that are weathered to form secondary (authigenic) clays (e.g., Dellinger et al., 2017). We select three immobile element ratios – Zr/Al, Ti/Al, and Cs/Al – and use them to produce three distinct mixing spaces (Fig. A.10). In these spaces, the distance of clays to conglomerate clasts and shales corresponds to a source rock proportion, where shorter distances indicate greater proportions of that endmember. We find that two endmembers consistently bookend the array of clay specimens (Fig. A.10) – the relatively abundant and well-exposed Cody shale (Fig. A.11) and two feldspar- and biotite-bearing granite clasts from the Beartooth

conglomerate (Table A.9) – and therefore elect to perform simple binary mixing. To compute distances, we first normalize the x- and y-coordinates of each sample such that the range of distances in both directions spans between 0 and 1. A line is then fitted between the shale endmember and the average of the two igneous rock endmembers and each clay sample is perpendicularly projected onto that line. We compute the proportions of shale and igneous rocks using the lever rule and present the proportions as fractions ($f_{\text{shale}}$ and $f_{\text{igneous}}$ as shown in Eq. 3.1). With these fractions, we are then able to compute the Li concentration and isotopic composition of source rocks for each clay sample where

$$\frac{[\text{Li}]}{[\text{Al}]}_{\text{source}} = f_{\text{shale}} \frac{[\text{Li}]}{[\text{Al}]}_{\text{shale}} + f_{\text{igneous}} \frac{[\text{Li}]}{[\text{Al}]}_{\text{igneous}}, \tag{A.14}$$

$$\frac{[\text{Li}]}{[\text{Al}]}_{\text{source}} \delta^7\text{Li}_{\text{source}} = f_{\text{shale}} \frac{[\text{Li}]}{[\text{Al}]}_{\text{shale}} \delta^7\text{Li}_{\text{shale}} + f_{\text{igneous}} \frac{[\text{Li}]}{[\text{Al}]}_{\text{igneous}} \delta^7\text{Li}_{\text{igneous}}, \tag{A.15}$$

[Li] (mol) is the molar concentration of Li, [Al] (mol) is the molar concentration of Al, and $\delta^7\text{Li}_{shale}$ and $\delta^7\text{Li}_{igneous}$(‰ LSVEC) are the measured Li isotope compositions of shale and igneous endmembers, respectively, in delta notation (Eq. A.13).

### Error propagation for silicate weathering intensity calculations

Once $\delta^7$Li¬source values are computed, the empirical relationship from Dellinger et al. (2017) is used to convert $\Delta^7\text{Li}_{\text{clay}-\text{source}}$ (equal to $\delta^7\text{Li}_{\text{clay}}$ - $\delta^7\text{Li}_{\text{source}}$) to silicate weathering intensity. This relationship ($R^2 = 0.730$) is mathematically expressed as

$$\text{Weathering intensity} = (-0.986 \pm 0.0915)\Delta^7\text{Li}_{\text{clay}-\text{source}} + \cdots (-0.150 \pm 0.039) \tag{A.16}$$

which includes the error (1 standard deviation) on the slopes and y-intercept. For each clay sample, the error on $\delta^7\text{Li}_{\text{clay}}$ value, $\delta^7\text{Li}_{\text{source}}$ value, and the slope and y-intercept of Eq. A.16 are propagated using a Monte Carlo approach. In this approach, we define normal distributions for $\Delta^7\text{Li}_{\text{clay}-\text{source}}$, the slope of Eq. A.16, and the y-intercept of Eq. A.16 based of their median values and standard deviations. Random values from each of the three normal distributions are selected and then passed as input to Eq. A.16 to compute a weathering intensity. This random selection and weathering intensity calculation is repeated 50,000 times. We compute the mean, median, maximum, minimum, standard deviation, standard error, maximum, 0.25 quantile, and 0.75 quantile values of the computed weathering intensities. We present the mean and standard deviation weathering intensities, which is shown in Fig. 3.1.

| Sample Name | Latitude (°) | Longitude (°) | Elevation (m) | Lithology | Formation | Soil facies | Color |
|---|---|---|---|---|---|---|---|
| BHB-PCB-19-0.2 | 44.763883 | -108.878419 | 1484 | Mudstone | Willwood | cumulative | red |
| BHB-PCB-19-01 | 44.763908 | -108.878406 | 1485 | Mudstone | Willwood | cumulative | gray/orange |
| BHB-PCB-19-01.5 | 44.763928 | -108.878397 | 1485.5 | Mudstone | Willwood | cumulative | gray |
| BHB-PCB-19-02.5 | 44.764103 | -108.878761 | 1486.5 | Mudstone | Willwood | crevasse | gray |
| BHB-PCB-19-03 | 44.764111 | -108.878753 | 1487 | Mudstone | Willwood | crevasse | gray/orange |
| BHB-PCB-19-03.5 | 44.764114 | -108.878744 | 1487.5 | Mudstone | Willwood | crevasse | gray/orange |
| BHB-PCB-19-04 | 44.764122 | -108.878733 | 1488 | Mudstone | Willwood | crevasse | gray |
| BHB-PCB-19-06.5 | 44.764150 | -108.878697 | 1490.5 | Mudstone | Willwood | crevasse | gray |
| BHB-PCB-19-07 | 44.764183 | -108.878700 | 1491 | Mudstone | Willwood | crevasse | gray |
| BHB-PCB-19-08 | 44.764200 | -108.878694 | 1492 | Mudstone | Willwood | cumulative | gray |
| BHB-PCB-19-11 | 44.764256 | -108.878656 | 1494 | Mudstone | Willwood | crevasse | gray |
| BHB-PCB-18-16 | 44.763992 | -108.880206 | 1504 | Mudstone | Willwood | crevasse | red |
| BHB-PCB-18-17 | 44.764006 | -108.880214 | 1505 | Mudstone | Willwood | crevasse | red |
| BHB-PCB-19-22 | 44.764325 | -108.879125 | 1506 | Siltstone | Willwood | cumulative | gray |
| BHB-PCB-19-22.5 | 44.764333 | -108.879133 | 1506.5 | Mudstone | Willwood | cumulative | red |
| BHB-PCB-19-25 | 44.764361 | -108.879167 | 1508 | Siltstone | Willwood | composite | gray |
| BHB-PCB-18-19 | 44.764297 | -108.880211 | 1514 | Mudstone | Willwood | crevasse | red |
| BHB-PCB-18-20C | 44.764239 | -108.880183 | 1516.5 | Mudstone | Willwood | composite | red |
| BHB-PCB-19-32 | 44.764456 | -108.879278 | 1517 | Mudstone | Willwood | cumulative | red/purple |
| BHB-PCB-19-33.5 | 44.764444 | -108.879247 | 1518.5 | Mudstone | Willwood | crevasse | gray |
| BHB-PCB-18-21A | 44.764272 | -108.880178 | 1519 | Mudstone | Willwood | cumulative | red |
| BHB-PCB-19-36 | 44.764039 | -108.883503 | 1520.4 | Mudstone | Willwood | composite | red/purple |
| BHB-PCB-19-38 | 44.764619 | -108.884797 | 1523 | Mudstone | Willwood | composite | brown/red |
| BHB-PCB-19-42 | 44.764850 | -108.884819 | 1529 | Siltstone | Willwood | composite | gray |
| BHB-PCB-19-42.5 | 44.764858 | -108.884842 | 1529.5 | Mudstone | Willwood | composite | red |
| BHB-PCB-19-43.5 | 44.764869 | -108.884864 | 1530.5 | Mudstone | Willwood | cumulative | red |
| BHB-PCB-19-44 | 44.764883 | -108.884875 | 1531 | Mudstone | Willwood | cumulative | red |
| BHB-PCB-19-47.5 | 44.765214 | -108.884850 | 1538 | Mudstone | Willwood | cumulative | brown/red |
| BHB-PCB-19-68.5 | 44.765400 | -108.885161 | 1543 | Mudstone | Willwood | cumulative | gray |
| BHB-PCB-19-73.5 | 44.765511 | -108.885158 | 1547 | Siltstone | Willwood | composite | gray |
| BHB-PCB-19-78.5 | 44.765542 | -108.886269 | 1556 | Mudstone | Willwood | composite | brown/red |

Table A.3: Bighorn Basin clay sample information

| Sample Name | Sample mass (g) | $\delta^7$Li | Li | B | Na | Mg | Al | Si |
|---|---|---|---|---|---|---|---|---|
| BHB-PCB-19-0.2 | 0.0223 | 0.0 | 2.04E+04 | 1.97E+04 | 2.52E+05 | 5.43E+06 | 4.35E+07 | 3.11E+04 |
| BHB-PCB-19-01 | 0.0219 | 0.2 | 2.41E+04 | 2.41E+04 | 3.03E+05 | 6.03E+06 | 5.34E+07 | 2.47E+04 |
| BHB-PCB-19-01.5 | 0.0214 | 0.2 | 2.45E+04 | 2.33E+04 | 3.63E+05 | 6.01E+06 | 5.27E+07 | 1.72E+04 |
| BHB-PCB-19-02.5 | 0.0281 | 0.2 | 1.65E+04 | 1.91E+04 | 2.32E+05 | 4.83E+06 | 4.07E+07 | 1.38E+04 |
| BHB-PCB-19-03 | 0.0244 | 0.1 | 2.79E+04 | 2.88E+04 | 6.46E+05 | 7.34E+06 | 6.09E+07 | 1.63E+04 |
| BHB-PCB-19-03.5 | 0.0251 | 0.6 | 2.18E+04 | 1.56E+04 | 5.58E+05 | 5.67E+06 | 4.53E+07 | 2.21E+04 |
| BHB-PCB-19-04 | 0.0248 | 0.5 | 2.37E+04 | 2.68E+04 | 8.05E+05 | 6.60E+06 | 4.97E+07 | 1.67E+04 |
| BHB-PCB-19-06.5 | 0.0204 | 0.5 | 2.69E+04 | 2.49E+04 | 3.90E+05 | 5.86E+06 | 5.36E+07 | 3.46E+04 |
| BHB-PCB-19-07 | 0.0229 | 0.1 | 2.77E+04 | 2.67E+04 | 2.76E+05 | 5.97E+06 | 5.25E+07 | 2.23E+04 |
| BHB-PCB-19-08 | 0.0271 | -0.1 | 2.25E+04 | 1.79E+04 | 5.83E+05 | 6.28E+06 | 4.63E+07 | 3.59E+04 |
| BHB-PCB-19-11 | 0.027 | 0.2 | 1.75E+04 | 1.40E+04 | 2.44E+05 | 5.62E+06 | 4.53E+07 | 1.54E+04 |
| BHB-PCB-18-16 | 0.0274 | -0.8 | 4.05E+04 | 3.05E+04 | 6.30E+05 | 1.34E+07 | 8.84E+07 | 1.59E+04 |
| BHB-PCB-18-17 | 0.0223 | -1.4 | 6.68E+04 | 3.98E+04 | 1.67E+06 | 2.04E+07 | 1.09E+08 | 2.15E+04 |
| BHB-PCB-19-22 | 0.0271 | -0.2 | 1.42E+04 | 1.61E+04 | 1.49E+05 | 4.64E+06 | 3.35E+07 | 1.34E+04 |
| BHB-PCB-19-22.5 | 0.0212 | -0.8 | 1.49E+04 | 1.27E+04 | 1.55E+05 | 5.04E+06 | 3.57E+07 | 2.29E+04 |
| BHB-PCB-19-25 | 0.023 | -1.4 | 5.45E+03 | 5.53E+03 | 7.60E+04 | 2.43E+06 | 1.50E+07 | 8.13E+03 |
| BHB-PCB-18-19 | 0.0526 | -0.6 | 4.71E+04 | 4.77E+04 | 1.38E+06 | 1.55E+07 | 1.01E+08 | 2.20E+04 |
| BHB-PCB-18-20C | 0.0409 | -1.1 | 4.79E+04 | 6.60E+04 | 6.91E+05 | 1.53E+07 | 1.04E+08 | 1.35E+04 |
| BHB-PCB-19-32 | 0.0224 | -0.9 | 1.75E+04 | 2.84E+04 | 1.40E+05 | 4.27E+06 | 2.96E+07 | 8.25E+03 |
| BHB-PCB-19-33.5 | 0.028 | -1.3 | 1.15E+04 | 1.56E+04 | 1.62E+05 | 3.90E+06 | 2.73E+07 | 5.34E+03 |
| BHB-PCB-18-21A | 0.0258 | -0.4 | 4.60E+04 | 4.14E+04 | 6.52E+05 | 1.19E+07 | 7.97E+07 | 1.35E+04 |
| BHB-PCB-19-36 | 0.0229 | -1.1 | 1.93E+04 | 2.01E+04 | 1.88E+05 | 6.40E+06 | 4.20E+07 | 6.97E+03 |
| BHB-PCB-19-38 | 0.0173 | -2.1 | 2.31E+04 | 2.28E+04 | 2.90E+05 | 7.33E+06 | 4.24E+07 | 1.40E+04 |
| BHB-PCB-19-42 | 0.021 | -1.6 | 2.86E+04 | 3.46E+04 | 3.00E+05 | 8.32E+06 | 5.98E+07 | 1.00E+04 |
| BHB-PCB-19-42.5 | 0.0227 | -1.9 | 1.63E+04 | 2.19E+04 | 1.39E+05 | 4.55E+06 | 3.54E+07 | 6.72E+03 |
| BHB-PCB-19-43.5 | 0.02 | -1.7 | 1.09E+04 | 1.80E+04 | 6.59E+04 | 2.62E+06 | 2.11E+07 | 5.74E+03 |
| BHB-PCB-19-44 | 0.0204 | -1.5 | 5.60E+03 | 8.20E+03 | 5.28E+04 | 4.33E+06 | 1.30E+07 | 4.27E+03 |
| BHB-PCB-19-47.5 | 0.0213 | -1.3 | 1.55E+04 | 2.19E+04 | 1.87E+05 | 4.96E+06 | 3.03E+07 | 1.93E+04 |
| BHB-PCB-19-68.5 | 0.0185 | -2.3 | 1.19E+04 | 1.69E+04 | 8.33E+04 | 2.87E+06 | 2.08E+07 | 6.76E+03 |
| BHB-PCB-19-73.5 | 0.0203 | -1.3 | 1.88E+04 | 1.58E+04 | 1.68E+05 | 4.38E+06 | 3.60E+07 | 7.03E+03 |
| BHB-PCB-19-78.5 | 0.0215 | -2.1 | 9.24E+03 | 1.27E+04 | 7.74E+04 | 2.64E+06 | 1.99E+07 | 4.30E+03 |

Table A.4: Bighorn Basin clay elemental and isotopic data (1/5). All elements are in units of ppb. bdl: below detection limit. $\delta^7$Li units are ‰ LSVEC.

| Sample Name | P | K | Ca | Ti | V | Cr | Mn | Fe | Co |
|---|---|---|---|---|---|---|---|---|---|
| BHB-PCB-19-0.2 | 8.30E+04 | 8.88E+06 | 7.61E+04 | 1.33E+06 | 6.02E+04 | 4.33E+04 | 6.22E+04 | 2.12E+07 | 4.95E+03 |
| BHB-PCB-19-01 | 7.48E+04 | 9.62E+06 | 8.62E+04 | 1.65E+06 | 7.46E+04 | 4.75E+04 | 6.54E+04 | 1.83E+07 | 4.74E+03 |
| BHB-PCB-19-01.5 | 7.82E+04 | 1.19E+07 | 1.20E+05 | 1.78E+06 | 6.52E+04 | 3.92E+04 | 7.37E+04 | 2.01E+07 | 5.30E+03 |
| BHB-PCB-19-02.5 | 7.89E+04 | 7.05E+06 | 1.22E+05 | 1.21E+06 | 5.58E+04 | 3.49E+04 | 6.14E+04 | 1.66E+07 | 3.68E+03 |
| BHB-PCB-19-03 | 2.67E+05 | 1.42E+07 | 9.48E+05 | 2.27E+06 | 7.62E+04 | 5.42E+04 | 1.15E+05 | 2.49E+07 | 6.49E+03 |
| BHB-PCB-19-03.5 | 2.23E+05 | 9.81E+06 | 7.15E+05 | 1.69E+06 | 6.22E+04 | 4.18E+04 | 9.61E+04 | 1.56E+07 | 5.62E+03 |
| BHB-PCB-19-04 | 2.36E+05 | 1.21E+07 | 1.03E+06 | 1.97E+06 | 6.56E+04 | 4.86E+04 | 1.22E+05 | 2.08E+07 | 6.41E+03 |
| BHB-PCB-19-06.5 | 8.43E+04 | 1.10E+07 | 1.09E+05 | 2.15E+06 | 7.72E+04 | 5.12E+04 | 7.17E+04 | 2.51E+07 | 4.75E+03 |
| BHB-PCB-19-07 | 1.11E+05 | 9.72E+06 | 7.28E+04 | 1.76E+06 | 7.38E+04 | 5.01E+04 | 7.20E+04 | 2.91E+07 | 4.63E+03 |
| BHB-PCB-19-08 | 1.26E+05 | 1.01E+07 | 4.01E+05 | 1.65E+06 | 6.81E+04 | 4.50E+04 | 1.14E+05 | 1.58E+07 | 5.61E+03 |
| BHB-PCB-19-11 | 6.85E+04 | 9.18E+06 | 8.11E+04 | 1.37E+06 | 5.96E+04 | 3.68E+04 | 6.47E+04 | 2.13E+07 | 3.68E+03 |
| BHB-PCB-18-16 | 2.49E+05 | 1.76E+07 | 6.28E+05 | 2.80E+06 | 1.33E+05 | 8.46E+04 | 1.86E+05 | 3.64E+07 | 9.38E+03 |
| BHB-PCB-18-17 | 3.65E+05 | 1.71E+07 | 8.02E+05 | 4.00E+06 | 1.90E+05 | 1.63E+05 | 3.34E+05 | 5.93E+07 | 2.06E+04 |
| BHB-PCB-19-22 | 4.96E+04 | 6.04E+06 | 4.21E+04 | 1.08E+06 | 4.13E+04 | 2.80E+04 | 3.77E+04 | 1.47E+07 | 2.78E+03 |
| BHB-PCB-19-22.5 | 5.33E+04 | 6.86E+06 | 4.63E+04 | 9.77E+05 | 4.41E+04 | 2.90E+04 | 4.57E+04 | 1.46E+07 | 3.21E+03 |
| BHB-PCB-19-25 | 3.09E+04 | 2.09E+06 | 2.21E+05 | 2.74E+05 | 2.58E+04 | 1.70E+04 | 2.64E+04 | 6.91E+06 | 1.81E+03 |
| BHB-PCB-18-19 | 5.47E+05 | 2.19E+07 | 1.52E+06 | 3.81E+06 | 1.35E+05 | 1.00E+05 | 2.10E+05 | 4.59E+07 | 1.18E+04 |
| BHB-PCB-18-20C | 2.99E+05 | 2.20E+07 | 8.08E+05 | 3.69E+06 | 1.84E+05 | 1.09E+05 | 1.59E+05 | 6.52E+07 | 1.10E+04 |
| BHB-PCB-19-32 | 7.46E+04 | 6.55E+06 | 4.19E+05 | 1.10E+06 | 5.02E+04 | 3.51E+04 | 5.02E+04 | 2.05E+07 | 4.19E+03 |
| BHB-PCB-19-33.5 | 4.12E+04 | 4.44E+06 | 2.53E+05 | 7.81E+05 | 5.06E+04 | 3.26E+04 | 4.95E+04 | 9.60E+06 | 4.05E+03 |
| BHB-PCB-18-21A | 2.75E+05 | 1.74E+07 | 7.58E+05 | 3.07E+06 | 1.39E+05 | 8.74E+04 | 1.67E+05 | 4.18E+07 | 1.17E+04 |
| BHB-PCB-19-36 | 5.79E+04 | 8.96E+06 | 2.60E+05 | 1.37E+06 | 6.00E+04 | 5.71E+04 | 7.52E+04 | 2.67E+07 | 6.88E+03 |
| BHB-PCB-19-38 | 8.31E+04 | 9.29E+06 | 4.71E+05 | 1.63E+06 | 7.75E+04 | 5.66E+04 | 1.73E+05 | 2.16E+07 | 1.37E+04 |
| BHB-PCB-19-42 | 1.24E+05 | 1.09E+07 | 3.51E+05 | 1.92E+06 | 9.80E+04 | 6.35E+04 | 1.20E+05 | 2.79E+07 | 7.73E+03 |
| BHB-PCB-19-42.5 | 7.19E+04 | 6.59E+06 | 2.56E+05 | 1.13E+06 | 5.84E+04 | 3.62E+04 | 5.98E+04 | 2.26E+07 | 3.72E+03 |
| BHB-PCB-19-43.5 | 6.63E+04 | 3.39E+06 | 2.39E+05 | 5.48E+05 | 2.82E+04 | 1.94E+04 | 4.14E+04 | 1.16E+07 | 2.70E+03 |
| BHB-PCB-19-44 | 3.28E+04 | 2.21E+06 | 2.28E+05 | 3.66E+05 | 2.15E+04 | 1.36E+04 | 2.54E+04 | 7.59E+06 | 1.61E+03 |
| BHB-PCB-19-47.5 | 7.52E+04 | 6.53E+06 | 2.92E+05 | 9.95E+05 | 4.46E+04 | 3.58E+04 | 5.11E+04 | 1.79E+07 | 4.03E+03 |
| BHB-PCB-19-68.5 | 5.92E+04 | 4.23E+06 | 1.68E+05 | 5.40E+05 | 3.70E+04 | 2.28E+04 | 2.76E+04 | 1.14E+07 | 2.47E+03 |
| BHB-PCB-19-73.5 | 8.02E+04 | 6.51E+06 | 2.60E+05 | 1.06E+06 | 5.90E+04 | 3.79E+04 | 5.83E+04 | 2.13E+07 | 4.18E+03 |
| BHB-PCB-19-78.5 | 5.83E+04 | 3.72E+06 | 2.30E+05 | 5.57E+05 | 3.48E+04 | 2.05E+04 | 3.40E+04 | 1.19E+07 | 2.23E+03 |

Table A.5: Bighorn Basin clay elemental and isotopic data (2/5). All elements are in units of ppb. bdl: below detection limit.

| Sample Name | Ni | Cu | Zn | As | Se | Rb | Sr | Zr | Mo |
|---|---|---|---|---|---|---|---|---|---|
| BHB-PCB-19-0.2 | 1.48E+04 | 9.55E+03 | 4.01E+04 | 1.94E+03 | 4.57E+01 | 6.03E+04 | 1.95E+04 | 3.89E+04 | 2.53E+02 |
| BHB-PCB-19-01 | 1.68E+04 | 1.58E+04 | 5.01E+04 | 2.06E+03 | 8.58E+01 | 7.03E+04 | 2.55E+04 | 5.06E+04 | 2.95E+02 |
| BHB-PCB-19-01.5 | 1.79E+04 | 1.51E+04 | 5.28E+04 | 1.86E+03 | 1.16E+02 | 7.43E+04 | 3.07E+04 | 5.93E+04 | 3.52E+02 |
| BHB-PCB-19-02.5 | 1.24E+04 | 1.13E+04 | 4.39E+04 | 2.15E+03 | 7.50E+01 | 5.27E+04 | 1.89E+04 | 4.09E+04 | 4.48E+02 |
| BHB-PCB-19-03 | 2.02E+04 | 1.79E+04 | 5.76E+04 | 3.17E+03 | 9.11E+01 | 8.16E+04 | 3.39E+04 | 6.36E+04 | 3.41E+02 |
| BHB-PCB-19-03.5 | 1.65E+04 | 1.58E+04 | 4.74E+04 | 2.52E+03 | 1.11E+02 | 6.68E+04 | 2.66E+04 | 5.25E+04 | 2.37E+02 |
| BHB-PCB-19-04 | 1.94E+04 | 1.64E+04 | 5.23E+04 | 3.13E+03 | 1.47E+02 | 7.43E+04 | 2.99E+04 | 5.87E+04 | 3.09E+02 |
| BHB-PCB-19-06.5 | 1.55E+04 | 1.59E+04 | 4.63E+04 | 3.38E+03 | 9.63E+01 | 7.22E+04 | 2.95E+04 | 5.24E+04 | 9.44E+02 |
| BHB-PCB-19-07 | 1.55E+04 | 1.38E+04 | 4.35E+04 | 4.05E+03 | 1.05E+02 | 7.39E+04 | 2.70E+04 | 5.01E+04 | 9.23E+02 |
| BHB-PCB-19-08 | 1.64E+04 | 1.60E+04 | 5.87E+04 | 3.22E+03 | 2.12E+02 | 5.86E+04 | 2.68E+04 | 5.26E+04 | 3.08E+02 |
| BHB-PCB-19-11 | 1.24E+04 | 9.96E+03 | 3.42E+04 | 2.26E+03 | 1.04E+02 | 6.18E+04 | 2.40E+04 | 4.69E+04 | 6.67E+02 |
| BHB-PCB-18-16 | 3.23E+04 | 3.65E+04 | 8.55E+04 | 5.41E+03 | 1.75E+02 | 1.13E+05 | 5.28E+04 | 1.00E+05 | 4.26E+02 |
| BHB-PCB-18-17 | 6.33E+04 | 9.04E+04 | 1.27E+05 | 5.46E+03 | 4.31E+02 | 1.27E+05 | 5.08E+04 | 1.01E+05 | 9.09E+02 |
| BHB-PCB-19-22 | 9.94E+03 | 8.36E+03 | 2.79E+04 | 1.86E+03 | 2.10E+01 | 4.63E+04 | 1.47E+04 | 3.06E+04 | 4.14E+02 |
| BHB-PCB-19-22.5 | 1.25E+04 | 1.21E+04 | 3.67E+04 | 1.24E+03 | 4.11E+01 | 5.02E+04 | 1.36E+04 | 3.78E+04 | 6.04E+02 |
| BHB-PCB-19-25 | 5.33E+03 | 8.49E+03 | 1.59E+04 | 6.13E+02 | 1.25E+01 | 1.48E+04 | 3.70E+03 | 1.32E+04 | 4.84E+01 |
| BHB-PCB-18-19 | 3.86E+04 | 3.92E+04 | 1.06E+05 | 6.26E+03 | 4.13E+02 | 1.47E+05 | 6.85E+04 | 1.27E+05 | 5.69E+02 |
| BHB-PCB-18-20C | 3.64E+04 | 2.75E+04 | 1.20E+05 | 1.14E+04 | 2.06E+02 | 1.64E+05 | 5.91E+04 | 1.25E+05 | 1.14E+03 |
| BHB-PCB-19-32 | 1.45E+04 | 1.12E+04 | 4.11E+04 | 2.34E+03 | 9.40E+01 | 5.48E+04 | 1.90E+04 | 4.42E+04 | 3.02E+02 |
| BHB-PCB-19-33.5 | 1.17E+04 | 1.57E+04 | 3.24E+04 | 8.26E+02 | 7.63E+01 | 3.11E+04 | 1.07E+04 | 2.86E+04 | 1.42E+02 |
| BHB-PCB-18-21A | 3.77E+04 | 3.44E+04 | 1.08E+05 | 6.34E+03 | 2.51E+02 | 1.47E+05 | 7.29E+04 | 1.05E+05 | 8.99E+02 |
| BHB-PCB-19-36 | 2.50E+04 | 1.66E+04 | 5.29E+04 | 1.79E+03 | 1.45E+02 | 7.20E+04 | 1.59E+04 | 4.27E+04 | 1.94E+02 |
| BHB-PCB-19-38 | 2.52E+04 | 3.25E+04 | 7.55E+04 | 2.40E+03 | 1.03E+02 | 6.96E+04 | 2.18E+04 | 5.48E+04 | 3.51E+02 |
| BHB-PCB-19-42 | 2.51E+04 | 3.46E+04 | 6.55E+04 | 2.59E+03 | 1.43E+02 | 8.40E+04 | 2.82E+04 | 6.78E+04 | 3.65E+02 |
| BHB-PCB-19-42.5 | 1.37E+04 | 1.36E+04 | 3.89E+04 | 3.61E+03 | 4.29E+01 | 5.12E+04 | 1.69E+04 | 4.14E+04 | 3.59E+02 |
| BHB-PCB-19-43.5 | 9.22E+03 | 1.08E+04 | 2.55E+04 | 1.39E+03 | 7.48E+01 | 3.05E+04 | 1.11E+04 | 2.62E+04 | 1.77E+02 |
| BHB-PCB-19-44 | 5.75E+03 | 4.57E+03 | 1.44E+04 | 1.06E+03 | 5.20E+01 | 1.60E+04 | 5.52E+03 | 1.25E+04 | 1.19E+02 |
| BHB-PCB-19-47.5 | 1.44E+04 | 1.56E+04 | 3.91E+04 | 1.69E+03 | 9.06E+01 | 5.26E+04 | 1.87E+04 | 3.54E+04 | 1.25E+02 |
| BHB-PCB-19-68.5 | 9.22E+03 | 1.03E+04 | 2.47E+04 | 1.30E+03 | 6.32E+01 | 3.34E+04 | 1.06E+04 | 2.67E+04 | 1.31E+02 |
| BHB-PCB-19-73.5 | 1.46E+04 | 1.85E+04 | 3.72E+04 | 3.06E+03 | 3.28E+02 | 4.94E+04 | 1.80E+04 | 3.96E+04 | 1.21E+03 |
| BHB-PCB-19-78.5 | 7.06E+03 | 1.09E+04 | 2.36E+04 | 1.52E+03 | 1.11E+02 | 2.73E+04 | 1.04E+04 | 2.66E+04 | 1.85E+02 |

Table A.6: Bighorn Basin clay elemental and isotopic data (3/5). All elements are in units of ppb. bdl: below detection limit.

| Sample Name | Ag | Sn | Sb | Cs | Ba | Tl |
|---|---|---|---|---|---|---|
| BHB-PCB-19-0.2 | 1.67E+02 | 1.37E+03 | 3.61E+02 | 4.56E+03 | 1.33E+05 | 4.07E+02 |
| BHB-PCB-19-01 | 1.76E+02 | 1.87E+03 | 3.04E+02 | 5.21E+03 | 1.56E+05 | 4.72E+02 |
| BHB-PCB-19-01.5 | 2.08E+02 | 1.79E+03 | 3.62E+02 | 5.23E+03 | 1.79E+05 | 5.07E+02 |
| BHB-PCB-19-02.5 | 1.43E+02 | 1.32E+03 | 2.81E+02 | 3.68E+03 | 1.23E+05 | 3.25E+02 |
| BHB-PCB-19-03 | 2.73E+02 | 2.02E+03 | 4.33E+02 | 5.92E+03 | 2.29E+05 | 5.51E+02 |
| BHB-PCB-19-03.5 | 2.71E+02 | 1.47E+03 | 3.31E+02 | 4.69E+03 | 1.89E+05 | 4.59E+02 |
| BHB-PCB-19-04 | 2.61E+02 | 1.68E+03 | 4.20E+02 | 5.23E+03 | 2.24E+05 | 5.47E+02 |
| BHB-PCB-19-06.5 | 1.94E+02 | 1.71E+03 | 6.21E+02 | 5.39E+03 | 1.85E+05 | 4.99E+02 |
| BHB-PCB-19-07 | 2.37E+02 | 1.88E+03 | 9.38E+02 | 5.97E+03 | 1.64E+05 | 5.27E+02 |
| BHB-PCB-19-08 | 2.33E+02 | 1.48E+03 | 4.23E+02 | 3.98E+03 | 1.66E+05 | 3.92E+02 |
| BHB-PCB-19-11 | 1.76E+02 | 1.68E+03 | 3.26E+02 | 4.21E+03 | 1.38E+05 | 3.51E+02 |
| BHB-PCB-18-16 | 2.44E+02 | 3.28E+03 | 6.89E+02 | 7.88E+03 | 2.77E+05 | 6.72E+02 |
| BHB-PCB-18-17 | 2.85E+02 | 5.42E+03 | 7.39E+02 | 8.43E+03 | 3.47E+05 | 8.12E+02 |
| BHB-PCB-19-22 | 5.38E+02 | 1.12E+03 | 4.82E+02 | 3.22E+03 | 9.41E+04 | 2.89E+02 |
| BHB-PCB-19-22.5 | 1.86E+02 | 1.27E+03 | 2.14E+02 | 3.39E+03 | 9.25E+04 | 2.97E+02 |
| BHB-PCB-19-25 | 4.27E+01 | 5.49E+02 | 7.83E+01 | 1.02E+03 | 2.44E+04 | 8.68E+01 |
| BHB-PCB-18-19 | 3.46E+02 | 3.64E+03 | 8.52E+02 | 1.01E+04 | 3.91E+05 | 9.20E+02 |
| BHB-PCB-18-20C | 3.29E+02 | 4.54E+03 | 1.58E+03 | 1.15E+04 | 3.64E+05 | 9.53E+02 |
| BHB-PCB-19-32 | 1.29E+02 | 1.53E+03 | 5.43E+02 | 3.87E+03 | 1.13E+05 | 3.26E+02 |
| BHB-PCB-19-33.5 | 8.03E+01 | 1.01E+03 | 1.16E+02 | 2.15E+03 | 7.15E+04 | 1.93E+02 |
| BHB-PCB-18-21A | 3.01E+02 | 3.33E+03 | 9.35E+02 | 1.02E+04 | 3.48E+05 | 9.19E+02 |
| BHB-PCB-19-36 | 1.21E+02 | 1.58E+03 | 3.98E+02 | 4.43E+03 | 1.36E+05 | 4.48E+02 |
| BHB-PCB-19-38 | 1.52E+02 | 1.79E+03 | 2.98E+02 | 4.66E+03 | 1.56E+05 | 4.60E+02 |
| BHB-PCB-19-42 | 1.89E+02 | 2.28E+03 | 4.42E+02 | 5.88E+03 | 1.76E+05 | 5.31E+02 |
| BHB-PCB-19-42.5 | 1.28E+02 | 1.38E+03 | 4.84E+02 | 3.59E+03 | 9.99E+04 | 3.02E+02 |
| BHB-PCB-19-43.5 | 7.22E+01 | 8.94E+02 | 2.66E+02 | 2.17E+03 | 6.08E+04 | 1.93E+02 |
| BHB-PCB-19-44 | 2.56E+01 | 4.85E+02 | 1.09E+02 | 1.14E+03 | 4.16E+04 | 1.09E+02 |
| BHB-PCB-19-47.5 | 1.28E+02 | 1.16E+03 | 2.32E+02 | 3.69E+03 | 1.06E+05 | 3.31E+02 |
| BHB-PCB-19-68.5 | 1.86E+02 | 9.29E+02 | 2.29E+02 | 2.59E+03 | 6.12E+04 | 2.07E+02 |
| BHB-PCB-19-73.5 | 1.66E+02 | 1.29E+03 | 5.46E+02 | 3.64E+03 | 1.07E+05 | 3.22E+02 |
| BHB-PCB-19-78.5 | 7.56E+01 | 7.62E+02 | 2.49E+02 | 2.00E+03 | 5.31E+04 | 1.63E+02 |

Table A.7: Bighorn Basin clay elemental and isotopic data (4/5). All elements are in units of ppb. bdl: below detection limit.

| Sample Name | Pb | Bi | Th | U |
|---|---|---|---|---|
| BHB-PCB-19-0.2 | 9.63E+03 | 2.11E+02 | 5.38E+03 | 1.06E+03 |
| BHB-PCB-19-01 | 1.02E+04 | 2.62E+02 | 6.56E+03 | 1.52E+03 |
| BHB-PCB-19-01.5 | 1.20E+04 | 2.35E+02 | 6.91E+03 | 1.87E+03 |
| BHB-PCB-19-02.5 | 1.02E+04 | 1.90E+02 | 5.32E+03 | 1.12E+03 |
| BHB-PCB-19-03 | 1.30E+04 | 2.74E+02 | 8.37E+03 | 1.88E+03 |
| BHB-PCB-19-03.5 | 1.23E+04 | 2.38E+02 | 6.17E+03 | 1.53E+03 |
| BHB-PCB-19-04 | 1.29E+04 | 2.62E+02 | 7.13E+03 | 1.65E+03 |
| BHB-PCB-19-06.5 | 1.10E+04 | 3.03E+02 | 7.52E+03 | 2.10E+03 |
| BHB-PCB-19-07 | 1.61E+04 | 3.65E+02 | 8.87E+03 | 2.26E+03 |
| BHB-PCB-19-08 | 1.27E+04 | 2.38E+02 | 6.07E+03 | 1.62E+03 |
| BHB-PCB-19-11 | 7.79E+03 | 1.93E+02 | 6.31E+03 | 1.22E+03 |
| BHB-PCB-18-16 | 1.91E+04 | 4.34E+02 | 1.24E+04 | 2.76E+03 |
| BHB-PCB-18-17 | 2.89E+04 | 4.35E+02 | 3.03E+04 | 4.18E+03 |
| BHB-PCB-19-22 | 6.84E+03 | 2.01E+02 | 4.76E+03 | 9.13E+02 |
| BHB-PCB-19-22.5 | 7.50E+03 | 2.07E+02 | 4.85E+03 | 1.16E+03 |
| BHB-PCB-19-25 | 2.78E+03 | 6.58E+01 | 1.46E+03 | 3.63E+02 |
| BHB-PCB-18-19 | 3.45E+04 | 4.22E+02 | 1.61E+04 | 3.34E+03 |
| BHB-PCB-18-20C | 3.37E+04 | 6.10E+02 | 1.78E+04 | 3.60E+03 |
| BHB-PCB-19-32 | 1.38E+04 | 2.54E+02 | 5.80E+03 | 1.21E+03 |
| BHB-PCB-19-33.5 | 5.25E+03 | 1.16E+02 | 3.26E+03 | 9.29E+02 |
| BHB-PCB-18-21A | 2.46E+04 | 4.27E+02 | 1.27E+04 | 2.90E+03 |
| BHB-PCB-19-36 | 9.13E+03 | 2.22E+02 | 5.74E+03 | 1.53E+03 |
| BHB-PCB-19-38 | 2.04E+04 | 1.79E+02 | 6.78E+03 | 4.01E+03 |
| BHB-PCB-19-42 | 1.78E+04 | 3.34E+02 | 7.84E+03 | 3.78E+03 |
| BHB-PCB-19-42.5 | 1.49E+04 | 2.40E+02 | 5.66E+03 | 1.36E+03 |
| BHB-PCB-19-43.5 | 7.95E+03 | 1.48E+02 | 3.91E+03 | 7.41E+02 |
| BHB-PCB-19-44 | 6.14E+03 | 7.34E+01 | 3.61E+03 | 3.81E+02 |
| BHB-PCB-19-47.5 | 7.93E+03 | 1.51E+02 | 4.55E+03 | 8.03E+02 |
| BHB-PCB-19-68.5 | 5.04E+03 | 1.41E+02 | 3.48E+03 | 6.32E+02 |
| BHB-PCB-19-73.5 | 1.06E+04 | 2.19E+02 | 5.14E+03 | 9.74E+02 |
| BHB-PCB-19-78.5 | 6.60E+03 | 1.27E+02 | 3.43E+03 | 7.05E+02 |

Table A.8: Bighorn Basin clay elemental and isotopic data (5/5). All elements are in units of ppb. bdl: below detection limit.

| Sample Name | Latitude (°) | Longitude (°) | Sample Type | Lithology | Formation |
|---|---|---|---|---|---|
| AAB 1110 | 43.957967 | -107.514767 | Shale | Shale | Mesa Verde |
| AAB 1101 | 44.533883 | -108.082850 | Shale | Shale | Thermopolis/Mowry |
| AAB 1105 | 44.572917 | -108.127667 | Shale | Shale | Gypsum Springs/Morrison/Cloverly |
| AAB 1111 | 43.964667 | -107.517367 | Shale | Shale | Cody |
| AAB 1108 | 44.584250 | -108.151250 | Shale | Shale | Thermopolis/Mowry |
| AAB 1103 | 44.571150 | -108.124817 | Shale | Shale | Gypsum Springs/Morrison/Cloverly |
| BHB-BTC-A | 44.851606 | -109.304008 | Conglomerate | Igneous | Fort Union |
| BHB-BTC-B | 44.851606 | -109.304008 | Conglomerate | Igneous | Fort Union |
| BHB-BTC-C | 44.851606 | -109.304008 | Conglomerate | Carbonate-siliciclastic | Fort Union |
| BHB-BTC-D | 44.851606 | -109.304008 | Conglomerate | Carbonate-siliciclastic | Fort Union |
| BHB-BTC-E | 44.851606 | -109.304008 | Conglomerate | Carbonate-siliciclastic | Fort Union |
| BHB-BTC-F | 44.851606 | -109.304008 | Conglomerate | Igneous | Fort Union |

Table A.9: Bighorn Basin source rock information

| Sample Name | Sample mass (g) | $\delta^7$Li | Li | B | Na | Mg | Al | Si |
|---|---|---|---|---|---|---|---|---|
| AAB 1110 | 0.0407 | 4.1 | 2.41E+04 | 2.12E+04 | 6.31E+05 | 3.62E+06 | 5.76E+07 | bdl |
| AAB 1101 | 0.0453 | 3.9 | 3.16E+04 | 2.03E+04 | 5.45E+06 | 5.63E+06 | 1.06E+08 | 1.48E+03 |
| AAB 1105 | 0.049 | -2.7 | 3.30E+04 | 5.79E+04 | 2.17E+07 | 1.38E+07 | 9.30E+07 | 2.95E+03 |
| AAB 1111 | 0.0441 | 0.3 | 3.94E+04 | 2.36E+04 | 4.82E+06 | 2.40E+07 | 9.05E+07 | 5.72E+03 |
| AAB 1108 | 0.0956 | -4.1 | 9.82E+04 | 6.79E+04 | 1.26E+07 | 1.65E+07 | 1.72E+08 | 1.14E+05 |
| AAB 1103 | 0.0706 | 11.3 | 1.78E+03 | 3.78E+04 | 1.05E+07 | 9.01E+06 | 7.39E+07 | 7.93E+04 |
| BHB-BTC-A | 0.0779 | 9.5 | 1.73E+04 | 7.19E+03 | 3.19E+07 | 4.31E+06 | 7.09E+07 | 5.63E+03 |
| BHB-BTC-B | 0.0733 | 4.3 | 1.83E+04 | 2.90E+03 | 2.70E+07 | 3.77E+06 | 9.12E+07 | 6.86E+03 |
| BHB-BTC-C | 0.0643 | 23.9 | 4.77E+03 | 8.10E+03 | 2.07E+05 | 3.57E+06 | 7.99E+06 | bdl |
| BHB-BTC-D | 0.0809 | 19.1 | 7.78E+03 | 1.75E+04 | 3.83E+05 | 4.34E+06 | 2.61E+07 | 1.10E+03 |
| BHB-BTC-E | 0.0484 | 25.1 | 1.46E+04 | 1.08E+04 | 5.10E+05 | 2.99E+06 | 2.25E+07 | bdl |
| BHB-BTC-F | 0.0552 | 5.8 | 1.64E+04 | bdl | 4.78E+07 | 3.42E+06 | 1.41E+08 | 5.82E+03 |

Table A.10: Bighorn Basin source rock elemental and isotopic data (1/5). All elements are in units of ppb. bdl: below detection limit. $\delta^7$Li values in units of ‰ LSVEC.

| Sample Name | P | K | Ca | Ti | V | Cr | Mn | Fe | Co |
|---|---|---|---|---|---|---|---|---|---|
| AAB 1110 | 2.41E+05 | 2.77E+07 | 2.32E+05 | 3.33E+06 | 7.10E+04 | 6.75E+04 | 1.14E+05 | 1.61E+07 | 6.52E+03 |
| AAB 1101 | 7.73E+05 | 6.28E+07 | 3.83E+06 | 4.60E+06 | 8.52E+04 | 4.31E+04 | 1.02E+05 | 2.72E+07 | 5.89E+03 |
| AAB 1105 | 4.67E+04 | 4.08E+06 | 4.86E+06 | 3.44E+06 | 8.49E+04 | 1.47E+04 | 2.31E+05 | 3.65E+07 | 7.62E+03 |
| AAB 1111 | 7.73E+05 | 2.53E+07 | 1.21E+07 | 4.34E+06 | 1.29E+05 | 8.38E+04 | 1.76E+05 | 5.04E+07 | 8.73E+03 |
| AAB 1108 | 6.14E+05 | 3.97E+07 | 2.34E+06 | 5.22E+06 | 1.85E+05 | 8.76E+04 | 2.42E+05 | 3.91E+07 | 1.02E+04 |
| AAB 1103 | 1.59E+05 | 2.07E+07 | 4.39E+06 | 3.26E+06 | 5.41E+04 | 2.71E+04 | 1.87E+05 | 2.32E+07 | 8.39E+03 |
| BHB-BTC-A | 1.48E+05 | 9.01E+06 | 1.52E+07 | 1.14E+06 | 1.10E+04 | 1.86E+03 | 1.30E+05 | 1.15E+07 | 2.83E+03 |
| BHB-BTC-B | 4.59E+05 | 5.69E+07 | 1.25E+07 | 1.41E+06 | 1.87E+04 | 2.54E+03 | 2.08E+05 | 1.43E+07 | 4.81E+03 |
| BHB-BTC-C | 7.18E+05 | 9.09E+06 | 3.86E+08 | 3.33E+05 | 1.44E+04 | 5.92E+03 | 1.41E+06 | 1.60E+07 | 5.19E+03 |
| BHB-BTC-D | 2.10E+06 | 2.53E+07 | 3.17E+08 | 8.57E+05 | 1.68E+04 | 1.60E+04 | 1.19E+06 | 1.62E+07 | 4.19E+03 |
| BHB-BTC-E | 1.90E+06 | 2.69E+07 | 2.65E+08 | 4.60E+05 | 9.45E+03 | 7.69E+03 | 2.14E+06 | 1.11E+07 | 3.47E+03 |
| BHB-BTC-F | 2.48E+05 | 6.17E+07 | 1.74E+07 | 1.88E+06 | 1.15E+04 | 1.71E+03 | 1.52E+05 | 2.19E+07 | 4.30E+03 |

Table A.11: Bighorn Basin source rock elemental and isotopic data (2/5). All elements are in units of ppb. bdl: below detection limit.

| Sample Name | Ni | Cu | Zn | As | Se | Rb | Sr | Zr | Mo |
|---|---|---|---|---|---|---|---|---|---|
| AAB 1110 | 2.41E+04 | 1.25E+04 | 7.95E+04 | 5.84E+03 | 7.57E+02 | 1.04E+05 | 4.07E+04 | 2.38E+05 | bdl |
| AAB 1101 | 1.89E+04 | 1.82E+04 | 8.27E+04 | 8.76E+03 | 1.93E+03 | 1.56E+05 | 9.87E+04 | 1.79E+05 | 3.80E+03 |
| AAB 1105 | 7.30E+03 | 2.91E+04 | 4.32E+04 | 5.85E+03 | 5.77E+02 | 2.12E+04 | 1.60E+05 | 1.72E+05 | 2.36E+03 |
| AAB 1111 | 2.07E+04 | 3.26E+04 | 8.38E+04 | 1.09E+04 | 5.06E+02 | 1.27E+05 | 6.19E+04 | 1.45E+05 | 9.99E+02 |
| AAB 1108 | 3.64E+04 | 3.55E+04 | 1.37E+05 | 8.32E+03 | 1.65E+03 | 2.53E+05 | 2.09E+05 | 2.00E+05 | 1.06E+03 |
| AAB 1103 | 1.02E+04 | 3.19E+04 | 5.03E+04 | 3.91E+03 | 1.54E+03 | 1.57E+04 | 1.77E+05 | 1.96E+05 | 1.37E+03 |
| BHB-BTC-A | 2.99E+03 | 1.86E+03 | 2.09E+04 | 4.52E+02 | 3.52E+01 | 2.52E+04 | 5.78E+05 | 1.80E+05 | bdl |
| BHB-BTC-B | 7.09E+03 | 2.90E+03 | 3.29E+04 | 6.24E+03 | 7.62E+02 | 1.56E+05 | 3.45E+05 | 8.23E+04 | bdl |
| BHB-BTC-C | 1.09E+04 | 6.83E+03 | 5.56E+03 | 3.69E+03 | 1.85E+02 | 1.62E+04 | 2.19E+05 | 3.78E+04 | bdl |
| BHB-BTC-D | 9.28E+03 | 5.23E+03 | 7.70E+03 | 3.75E+03 | 1.60E+02 | 4.47E+04 | 1.98E+05 | 7.63E+04 | bdl |
| BHB-BTC-E | 8.36E+03 | 2.21E+03 | 1.04E+04 | 3.26E+03 | 1.85E+02 | 5.92E+04 | 1.82E+05 | 8.34E+04 | bdl |
| BHB-BTC-F | 6.40E+03 | 4.39E+03 | 2.97E+04 | 9.68E+02 | 1.77E+02 | 8.72E+04 | 3.98E+05 | 1.14E+05 | bdl |

Table A.12: Bighorn Basin source rock elemental and isotopic data (3/5). All elements are in units of ppb. bdl: below detection limit.

| Sample Name | Ag | Sn | Sb | Cs | Ba | Tl |
|---|---|---|---|---|---|---|
| AAB 1110 | 7.43E+02 | 2.23E+03 | 1.48E+03 | 1.07E+04 | 5.01E+05 | 7.69E+02 |
| AAB 1101 | 6.64E+02 | 2.45E+03 | 8.97E+02 | 7.46E+03 | 7.55E+05 | 1.38E+03 |
| AAB 1105 | 5.33E+02 | 2.43E+03 | 1.38E+03 | 2.42E+03 | 9.16E+05 | 2.40E+02 |
| AAB 1111 | 6.80E+02 | 2.90E+03 | 8.57E+02 | 1.20E+04 | 4.46E+05 | 9.82E+02 |
| AAB 1108 | 7.67E+02 | 6.60E+02 | 3.74E+03 | 6.84E+02 | 1.37E+04 | 1.07E+06 |
| AAB 1103 | 5.74E+02 | 3.34E+02 | 1.94E+03 | 1.05E+03 | 3.29E+02 | 3.16E+05 |
| BHB-BTC-A | 4.47E+02 | 3.51E+02 | bdl | 2.45E+02 | 5.52E+05 | 1.42E+02 |
| BHB-BTC-B | 2.24E+02 | 1.16E+03 | 1.10E+01 | 1.22E+03 | 3.02E+06 | 8.51E+02 |
| BHB-BTC-C | 1.28E+02 | 1.59E+02 | 5.98E+01 | 4.25E+02 | 8.07E+04 | 4.71E+01 |
| BHB-BTC-D | 2.43E+02 | 4.76E+02 | 1.64E+02 | 8.93E+02 | 2.30E+05 | 1.50E+02 |
| BHB-BTC-E | 2.56E+02 | bdl | 1.12E+02 | 1.58E+03 | 3.37E+05 | 2.34E+02 |
| BHB-BTC-F | 2.89E+02 | 5.93E+02 | bdl | 4.34E+02 | 3.30E+06 | 4.69E+02 |

Table A.13: Bighorn Basin source rock elemental and isotopic data (4/5). All elements are in units of ppb. bdl: below detection limit.

| Sample Name | Pb | Bi | Th | U |
|---|---|---|---|---|
| AAB 1110 | 1.86E+04 | 4.53E+02 | 1.04E+04 | 4.87E+03 |
| AAB 1101 | 1.66E+04 | 3.18E+02 | 1.16E+04 | 5.77E+03 |
| AAB 1105 | 1.65E+04 | 3.54E+02 | 7.28E+03 | 1.41E+03 |
| AAB 1111 | 3.11E+04 | 7.24E+02 | 1.13E+04 | 3.22E+03 |
| AAB 1108 | 6.92E+02 | 3.22E+04 | 6.26E+02 | 2.52E+04 |
| AAB 1103 | 3.76E+02 | 1.91E+04 | 4.00E+02 | 3.16E+04 |
| BHB-BTC-A | 5.15E+03 | bdl | 3.74E+02 | 6.04E+02 |
| BHB-BTC-B | 3.83E+04 | 7.79E+00 | 7.45E+04 | 2.18E+03 |
| BHB-BTC-C | 5.21E+03 | 3.92E+01 | 1.79E+03 | 6.60E+02 |
| BHB-BTC-D | 5.74E+03 | 3.61E+01 | 4.30E+03 | 1.67E+03 |
| BHB-BTC-E | 6.29E+03 | 6.76E+01 | 4.48E+03 | 1.80E+03 |
| BHB-BTC-F | 2.48E+04 | bdl | 2.43E+04 | 2.01E+03 |

Table A.14: Bighorn Basin source rock elemental and isotopic data (5/5). All elements are in units of ppb. bdl: below detection limit.

## A.3 Sediment transport and silicate weathering in the Huerfano Basin (Colorado, USA) during the latest Paleocene and Early Eocene

| Study | Rock type | Chemistry | Ti/Al (mol/mol) | Zr/Al × 1000 (mol/mol) | CsAl × 1000 (mol/mol) | Mg/Ti (mol/mol) | K/Ti (mol/mol) | Li/Al × 1000 (mol/mol) |
|---|---|---|---|---|---|---|---|---|
| Noblett and Staub, 1990 | Lamprophyre | Mafic | 0.092 | 1.438 | | 4.329 | 1.687 | |
| Noblett and Staub, 1990 | Intrusive | Intermediate | 0.080 | 1.262 | | 4.073 | 1.978 | |
| Noblett and Staub, 1990 | granite | Felsic | 0.011 | 1.061 | | 2.972 | 30.382 | |
| Boardman and Condie, 1986 | Gabbro | Mafic | 0.045 | 0.270 | | 13.653 | 1.089 | |
| Boardman and Condie, 1986 | Basalt volcaniclastic | Mafic | 0.038 | 0.206 | | 9.930 | 1.448 | |
| Boardman and Condie, 1986 | Lithic volcaniclastic | Felsic | 0.016 | 1.790 | | 8.502 | 18.106 | |
| Boardman and Condie, 1986 | Bedded volcaniclastic | Felsic | 0.022 | 0.928 | | 6.506 | 11.294 | |
| Parker and Sharp, 1970 | Syenite | Felsic | 0.026 | | | 1.624 | 9.350 | |
| Parker and Sharp, 1970 | Gabbro | Mafic | 0.206 | | | 2.995 | 0.173 | |
| Parker and Sharp, 1970 | Pyroxenite | Mafic | 0.227 | | | 10.177 | 0.115 | |
| Van Gosen, 2020 | Pyroxenite | Mafic | 0.300 | 0.725 | 0.00053 | 6.735 | 0.110 | |
| Van Gosen, 2020 | Pyroxenite | Mafic | 0.452 | 0.695 | 0.00025 | 3.932 | 0.0792 | |
| Van Gosen, 2020 | gabbro | Mafic | 0.129 | 0.179 | | 4.539 | 0.098 | |
| Van Gosen, 2020 | Pyroxenite | Mafic | 0.356 | 0.759 | 0.00045 | 5.222 | 0.080 | 0.941 |
| Van Gosen, 2020 | Syenite | Felsic | 0.016 | 1.633 | 0.00219 | 2.348 | 18.034 | 0.860 |
| Van Gosen, 2020 | Syenite | Felsic | 0.012 | 3.422 | 0.00172 | 1.751 | 26.050 | 1.397 |
| Van Gosen, 2020 | Syenite | Felsic | 0.004 | 2.671 | 0.00237 | 0.328 | 64.274 | 2.353 |
| Van Gosen, 2020 | Syenite | Felsic | 0.026 | 0.321 | 0.00236 | 2.757 | 13.277 | |
| Van Gosen, 2020 | Ultramafic rock | Mafic | 0.178 | 0.140 | 0.00038 | 3.867 | 0.129 | |
| Van Gosen, 2020 | Syenite | Felsic | 0.019 | 0.174 | 0.00119 | 2.555 | 15.121 | |
| Van Gosen, 2020 | Calcic vein | Intermediate | 0.040 | 0.285 | 0.00406 | 4.486 | 7.487 | 1.516 |
| Van Gosen, 2020 | Lamprophyre | Mafic | 0.150 | 0.781 | 0.00325 | 3.712 | 1.347 | 0.518 |
| Van Gosen, 2020 | Syenite | Felsic | 0.037 | 0.314 | 0.00119 | 2.447 | 6.696 | |
| Van Gosen, 2020 | Syenite | Felsic | 0.034 | 0.192 | 0.00206 | 1.711 | 9.052 | 0.381 |

Table A.15: Wet Mountain source rock elemental ratios

| Sample name | Lithology | Formation | Stratigraphic height (m) |
|---|---|---|---|
| Cuch-4 Black Mtn #1 | Claystone | Cuchara | |
| Cuch-4 Black Mtn #2 | Claystone | Cuchara | |
| Cuch-4 Black Mtn #3 | Claystone | Cuchara | |
| PCSS-030 | Claystone | Poison Canyon | 123.35 |
| PCSS-117 | Claystone | Poison Canyon | 254.1 |
| PCSS-151 | Claystone | Poison Canyon | 311.57 |
| PCSS-174 | Claystone | Poison Canyon | 342.84 |
| PCSS-198 | Silty claystone | Poison Canyon | 358.79 |
| PCSS-221 | Silty claystone | Cuchara | 382.35 |
| PCSS-233 | Claystone | Cuchara | 408.44 |
| PCSS-257 | Rip-up claystone | Cuchara | 439.14 |
| PCSS-290 | Clayey siltstone | Cuchara | 460.28 |
| PCSS-294 | Siltstone | Huerfano | 514.97 |
| PCSS-297 | Clayey siltstone | Huerfano | 515.52 |
| PCSS-303 | Siltstone | Huerfano | 516.75 |
| PCSS-53 | Sandstone | Poison Canyon | 113.23 |
| PCSS-133 | Sandstone | Poison Canyon | 272.22 |
| PCSS-140 | Sandstone | Poison Canyon | 298.41 |
| PCSS-169 | Sandstone | Poison Canyon | 342.07 |
| PCSS-197 | Sandstone | Poison Canyon | 366.75 |
| PCSS-208 | Sandstone | Cuchara | 393.74 |
| PCSS-224 | Sandstone | Cuchara | 430.01 |
| PCSS-250 | Sandstone | Cuchara | 484.73 |
| HF-1 Black Mtn | Sandstone | Huerfano | |
| PC-2 Black Mtn | Sandstone | Poison Canyon | |
| Cuch-6 Black Mtn | Sandstone | Cuchara | |

Table A.16: Huerfano Basin sample type and stratigraphy

| Sample name | Qm | Qp | K | P | Lm | Lv | Ls | Lu | Total | Coercivity | Saturation |
|---|---|---|---|---|---|---|---|---|---|---|---|
| Cuch-4 Black Mtn #1 | | | | | | | | | | | |
| Cuch-4 Black Mtn #2 | | | | | | | | | | | |
| Cuch-4 Black Mtn #3 | | | | | | | | | | | |
| PCSS-030 | | | | | | | | | | 41.986 | 3.986 |
| PCSS-117 | | | | | | | | | | 19.826 | 1.685 |
| PCSS-151 | | | | | | | | | | 68.067 | 2.367 |
| PCSS-174 | | | | | | | | | | 32.500 | 2.274 |
| PCSS-198 | | | | | | | | | | 12.887 | 3.577 |
| PCSS-221 | | | | | | | | | | 271.131 | 6.632 |
| PCSS-233 | | | | | | | | | | 12.102 | 2.206 |
| PCSS-257 | | | | | | | | | | | |
| PCSS-290 | | | | | | | | | | 11.869 | 1.955 |
| PCSS-294 | | | | | | | | | | 218.218 | 2.875 |
| PCSS-297 | | | | | | | | | | | |
| PCSS-303 | | | | | | | | | | 145.704 | 14.275 |
| PCSS-53 | 171 | 71 | 143 | 7 | 5 | 3 | 2 | 6 | 408 | | |
| PCSS-133 | 134 | 79 | 173 | 16 | 4 | 2 | 1 | 7 | 416 | | |
| PCSS-140 | 97 | 71 | 123 | 6 | 3 | 0 | 1 | 5 | 306 | | |
| PCSS-169 | 156 | 31 | 185 | 11 | 15 | 0 | 0 | 4 | 402 | | |
| PCSS-197 | 193 | 36 | 148 | 9 | 16 | 0 | 0 | 9 | 411 | | |
| PCSS-208 | 164 | 48 | 178 | 8 | 5 | 3 | 2 | 7 | 415 | | |
| PCSS-224 | 191 | 29 | 155 | 6 | 16 | 0 | 1 | 10 | 408 | | |
| PCSS-250 | 166 | 58 | 149 | 3 | 19 | 0 | 0 | 13 | 408 | | |
| HF-1 Black Mtn | 193 | 30 | 158 | 5 | 4 | 2 | 0 | 18 | 410 | | |
| PC-2 Black Mtn | 171 | 38 | 162 | 9 | 13 | 0 | 2 | 18 | 413 | | |
| Cuch-6 Black Mtn | 140 | 73 | 139 | 1 | 11 | 0 | 0 | 13 | 377 | | |

Table A.17: Huerfano Basin sandstone petrography and magnetic data. All sandstone petrographic data come from Rasmussen, 2016 (Qm: quartz; Qp: polycrystalline quartz; K: potassium feldspar; P: plagioclase; Lm: metamorphic lithic fragments; Lv: volcanic lithic fragments; Ls- sedimentary lithic fragments; Lu- unclassified lithic fragments) and all magnetic data comes from Rasmussen et al., 2020 (Coercivity units [=] mT; Saturation units [=] mA $m^2$ $kg^{-1}$).

| Sample name | $\delta^7$Li (‰) | Li | B | Na | Mg | Al | Si | P | K |
|---|---|---|---|---|---|---|---|---|---|
| Cuch-4 Black Mtn #1 | -0.9 | 2.2E+04 | 8.4E+03 | 6.1E+04 | 1.5E+06 | 8.9E+07 | 4.3E+03 | 1.5E+05 | 2.8E+06 |
| Cuch-4 Black Mtn #2 | -0.3 | 1.4E+04 | 6.7E+03 | 5.1E+04 | 1.2E+06 | 5.1E+07 | 1.2E+03 | 1.4E+05 | 2.7E+06 |
| Cuch-4 Black Mtn #3 | -0.1 | 2.2E+04 | 1.0E+04 | 7.8E+04 | 1.8E+06 | 6.8E+07 | 1.5E+03 | 3.1E+05 | 3.9E+06 |
| PCSS-030 | 3.1 | 1.4E+04 | 7.4E+03 | 7.1E+04 | 4.5E+06 | 3.5E+07 | bdl | 6.8E+04 | 2.9E+06 |
| PCSS-117 | 2.5 | 1.0E+04 | 4.6E+03 | 8.8E+04 | 3.3E+06 | 2.8E+07 | 1.3E+03 | 1.1E+05 | 3.7E+06 |
| PCSS-151 | 6.1 | 1.8E+04 | 7.2E+03 | 1.0E+05 | 4.7E+06 | 3.7E+07 | bdl | 5.5E+04 | 4.2E+06 |
| PCSS-174 | 8.0 | 1.6E+04 | 4.3E+03 | 3.8E+04 | 2.7E+06 | 2.2E+07 | bdl | 6.8E+04 | 1.8E+06 |
| PCSS-198 | 6.6 | 2.3E+04 | 5.0E+03 | 3.2E+05 | 3.6E+06 | 3.4E+07 | bdl | 5.9E+04 | 2.9E+06 |
| PCSS-221 | 7.1 | 1.6E+04 | 7.5E+03 | 1.2E+05 | 3.3E+06 | 5.2E+07 | 1.9E+03 | 8.5E+04 | 3.8E+06 |
| PCSS-233 | 0.9 | 1.1E+04 | 4.9E+03 | 2.2E+05 | 2.3E+06 | 3.9E+07 | 2.7E+03 | 7.5E+04 | 3.0E+06 |
| PCSS-257 | -0.8 | 1.1E+04 | 4.2E+03 | 9.4E+04 | 2.1E+06 | 3.3E+07 | bdl | 4.9E+04 | 2.9E+06 |
| PCSS-290 | 8.2 | 2.1E+04 | 7.6E+03 | 3.3E+05 | 3.1E+06 | 5.3E+07 | 1.1E+03 | 9.2E+04 | 4.7E+06 |
| PCSS-294 | 9.2 | 3.1E+04 | 7.5E+03 | 9.8E+04 | 2.7E+06 | 7.1E+07 | 7.2E+03 | 1.5E+05 | 5.5E+06 |
| PCSS-297 | 9.2 | 1.2E+04 | 4.5E+03 | 3.8E+04 | 1.1E+06 | 4.3E+07 | 2.9E+03 | 1.3E+05 | 2.3E+06 |
| PCSS-303 | 9.1 | 2.7E+04 | 8.0E+03 | 1.3E+05 | 2.9E+06 | 9.3E+07 | 3.7E+03 | 1.6E+05 | 5.3E+06 |
| PCSS-53 | 10.2 | 5.4E+03 | 2.5E+03 | 1.5E+07 | 1.3E+06 | 7.2E+07 | 2.4E+04 | 2.2E+05 | 4.2E+07 |
| PCSS-133 | 5.7 | 1.4E+04 | 8.5E+03 | 1.6E+07 | 1.6E+06 | 7.6E+07 | 4.2E+05 | 2.4E+05 | 4.6E+07 |
| PCSS-140 | 13.0 | 5.8E+03 | 6.8E+03 | 1.5E+07 | 1.5E+06 | 7.7E+07 | 5.3E+05 | 5.3E+04 | 5.1E+07 |
| PCSS-169 | 12.1 | 1.0E+04 | 6.3E+03 | 1.4E+07 | 3.1E+06 | 7.2E+07 | 5.9E+05 | 2.1E+05 | 3.5E+07 |
| PCSS-197 | 5.8 | 1.1E+04 | 4.8E+03 | 1.3E+07 | 4.0E+06 | 6.7E+07 | 2.3E+04 | 1.9E+05 | 3.1E+07 |
| PCSS-208 | 9.5 | 5.5E+03 | 4.7E+03 | 1.2E+07 | 2.2E+06 | 7.1E+07 | 1.6E+05 | 1.9E+05 | 3.7E+07 |
| PCSS-224 | 2.0 | 5.5E+03 | 3.7E+03 | 1.0E+07 | 1.1E+06 | 7.0E+07 | 2.9E+04 | 1.2E+05 | 4.0E+07 |
| PCSS-250 | 8.9 | 1.3E+04 | 5.5E+03 | 1.5E+06 | 2.1E+06 | 9.3E+07 | 3.5E+04 | 1.4E+05 | 4.3E+07 |
| HF-1 Black Mtn | 4.8 | 8.0E+03 | 3.7E+03 | 1.1E+07 | 3.7E+06 | 6.4E+07 | 2.0E+04 | 3.7E+05 | 2.9E+07 |
| PC-2 Black Mtn | 1.9 | 8.5E+03 | 5.6E+03 | 1.6E+07 | 1.9E+06 | 6.8E+07 | 2.4E+04 | 4.9E+05 | 3.4E+07 |
| Cuch-6 Black Mtn | 4.6 | 1.5E+04 | 1.3E+04 | 7.7E+05 | 8.7E+05 | 9.9E+07 | 1.6E+04 | 1.7E+05 | 3.2E+07 |

Table A.18: Huerfano Basin Li isotope and elemental data (1/4). All elements are in units of ppb. bdl: below detection limit.

| Sample name | Ca | Ti | V | Cr | Mn | Fe | Co | Ni | Cu |
|---|---|---|---|---|---|---|---|---|---|
| Cuch-4 Black Mtn #1 | bdl | 3.1E+06 | 5.1E+04 | 3.6E+04 | 9.4E+04 | 2.3E+07 | 7.7E+03 | 5.6E+03 | 1.1E+04 |
| Cuch-4 Black Mtn #2 | bdl | 2.4E+06 | 4.6E+04 | 6.5E+04 | 4.1E+04 | 1.5E+07 | 5.4E+03 | 3.5E+03 | 6.6E+03 |
| Cuch-4 Black Mtn #3 | bdl | 3.5E+06 | 6.0E+04 | 8.8E+04 | 7.3E+04 | 2.1E+07 | 6.3E+03 | 4.9E+03 | 8.6E+03 |
| PCSS-030 | 5.0E+04 | 1.0E+06 | 4.8E+04 | 3.1E+04 | 1.0E+05 | 2.1E+07 | 5.4E+03 | 1.1E+04 | 2.7E+04 |
| PCSS-117 | 5.0E+04 | 1.3E+06 | 3.9E+04 | 2.3E+04 | 8.1E+04 | 1.7E+07 | 4.3E+03 | 1.2E+04 | 1.6E+04 |
| PCSS-151 | 4.7E+04 | 1.3E+06 | 4.4E+04 | 2.9E+04 | 1.1E+05 | 1.9E+07 | 5.4E+03 | 1.2E+04 | 2.5E+04 |
| PCSS-174 | bdl | 8.0E+05 | 3.5E+04 | 2.2E+04 | 5.9E+04 | 1.4E+07 | 2.8E+03 | 8.2E+03 | 3.6E+04 |
| PCSS-198 | 8.1E+04 | 1.4E+06 | 4.4E+04 | 3.0E+04 | 9.7E+04 | 1.5E+07 | 6.8E+03 | 1.2E+04 | 1.9E+04 |
| PCSS-221 | bdl | 2.0E+06 | 6.5E+04 | 4.3E+04 | 6.1E+04 | 2.6E+07 | 8.5E+03 | 1.9E+04 | 3.0E+04 |
| PCSS-233 | bdl | 1.4E+06 | 5.9E+04 | 3.8E+04 | 5.3E+04 | 8.2E+06 | 6.5E+03 | 1.4E+04 | 4.0E+04 |
| PCSS-257 | bdl | 1.6E+06 | 3.4E+04 | 1.3E+05 | 3.7E+04 | 1.3E+07 | 7.0E+03 | 1.6E+04 | 8.4E+03 |
| PCSS-290 | 4.9E+04 | 2.6E+06 | 5.1E+04 | 4.6E+04 | 1.0E+05 | 1.3E+07 | 1.6E+04 | 2.0E+04 | 4.6E+04 |
| PCSS-294 | 4.5E+04 | 5.0E+06 | 1.1E+05 | 7.6E+04 | 6.7E+04 | 3.3E+07 | 6.4E+03 | 2.5E+04 | 4.1E+04 |
| PCSS-297 | bdl | 3.1E+06 | 6.9E+04 | 5.0E+04 | 3.6E+04 | 1.8E+07 | 2.9E+03 | 1.6E+04 | 3.4E+04 |
| PCSS-303 | bdl | 3.7E+06 | 8.4E+04 | 7.0E+04 | 1.1E+05 | 3.7E+07 | 8.3E+03 | 1.6E+04 | 2.6E+04 |
| PCSS-53 | 4.2E+07 | 1.3E+06 | 2.3E+04 | 2.3E+04 | 3.6E+06 | 1.0E+07 | 1.9E+03 | 4.6E+03 | 5.3E+03 |
| PCSS-133 | 2.6E+06 | 1.7E+06 | 3.0E+04 | 2.4E+04 | 1.9E+05 | 3.3E+07 | 5.3E+03 | 9.6E+03 | 4.4E+03 |
| PCSS-140 | 1.6E+06 | 5.8E+05 | 3.5E+04 | 1.2E+04 | 5.5E+04 | 7.5E+06 | 2.4E+03 | 4.5E+03 | 4.5E+03 |
| PCSS-169 | 9.5E+07 | 1.5E+06 | 3.5E+04 | 2.3E+04 | 2.5E+06 | 1.7E+07 | 5.0E+03 | 2.4E+04 | 8.2E+03 |
| PCSS-197 | 8.4E+07 | 1.4E+06 | 3.7E+04 | 3.0E+04 | 2.3E+06 | 1.6E+07 | 4.3E+03 | 1.1E+04 | 1.1E+04 |
| PCSS-208 | 5.9E+07 | 1.4E+06 | 4.6E+04 | 2.6E+04 | 1.5E+06 | 8.2E+06 | 3.8E+03 | 5.9E+03 | 6.6E+03 |
| PCSS-224 | 6.5E+07 | 1.5E+06 | 2.8E+04 | 2.7E+04 | 3.6E+06 | 1.0E+07 | 3.5E+03 | 6.8E+03 | 7.0E+03 |
| PCSS-250 | 1.3E+06 | 2.0E+06 | 6.8E+04 | 4.9E+04 | 4.1E+05 | 1.7E+07 | 5.4E+03 | 1.2E+04 | 1.3E+04 |
| HF-1 Black Mtn | 9.6E+07 | 1.4E+06 | 4.0E+04 | 2.0E+04 | 8.4E+06 | 9.9E+06 | 3.8E+03 | 7.4E+03 | 1.2E+04 |
| PC-2 Black Mtn | 6.8E+07 | 3.2E+06 | 5.0E+04 | 3.8E+04 | 1.9E+06 | 1.2E+07 | 4.5E+03 | 7.4E+03 | 6.3E+03 |
| Cuch-6 Black Mtn | 3.0E+06 | 4.2E+06 | 6.0E+04 | 4.4E+04 | 3.3E+05 | 2.1E+07 | 2.1E+03 | 3.6E+03 | 7.5E+03 |

Table A.19: Huerfano Basin elemental data (2/4). All elements are in units of ppb. bdl: below detection limit.

| Sample name | Zn | As | Se | Rb | Sr | Zr | Mo | Ag | Cd |
|---|---|---|---|---|---|---|---|---|---|
| Cuch-4 Black Mtn #1 | 2.1E+04 | 3.6E+03 | 2.8E+02 | 1.8E+04 | 1.2E+04 | 4.3E+04 | 3.7E+03 | 1.3E+02 | 8.1E+01 |
| Cuch-4 Black Mtn #2 | 1.6E+04 | 4.2E+03 | 2.1E+02 | 1.7E+04 | 1.5E+04 | 3.2E+04 | 2.9E+03 | 1.0E+02 | 7.3E+01 |
| Cuch-4 Black Mtn #3 | 2.2E+04 | 8.7E+03 | 6.4E+02 | 2.6E+04 | 4.1E+04 | 4.1E+04 | 3.0E+03 | 1.4E+02 | 1.1E+02 |
| PCSS-030 | 3.7E+04 | 1.4E+03 | 2.8E+02 | 2.1E+04 | 5.8E+03 | 2.6E+04 | 2.1E+03 | 7.9E+01 | 1.4E+02 |
| PCSS-117 | 2.7E+04 | 3.1E+03 | 2.8E+02 | 3.0E+04 | 9.0E+03 | 2.4E+04 | 1.9E+03 | 7.0E+01 | 4.6E+01 |
| PCSS-151 | 3.9E+04 | 9.0E+02 | 2.0E+02 | 2.5E+04 | 6.7E+03 | 2.6E+04 | 2.0E+03 | 7.6E+01 | 8.9E+01 |
| PCSS-174 | 2.9E+04 | 1.7E+03 | 2.3E+02 | 1.4E+04 | 4.3E+03 | 1.5E+04 | 2.7E+03 | 4.9E+01 | 9.5E+01 |
| PCSS-198 | 4.0E+04 | 1.1E+03 | 9.2E+01 | 2.1E+04 | 8.2E+03 | 2.6E+04 | 1.5E+03 | 7.2E+01 | 1.0E+02 |
| PCSS-221 | 5.0E+04 | 1.7E+03 | 3.0E+02 | 3.0E+04 | 8.0E+03 | 3.2E+04 | 3.7E+03 | 9.6E+01 | 8.3E+01 |
| PCSS-233 | 4.3E+04 | 1.9E+03 | 2.2E+02 | 2.1E+04 | 7.5E+03 | 3.0E+04 | 1.1E+03 | 8.1E+01 | 1.2E+02 |
| PCSS-257 | 3.9E+04 | 5.5E+02 | 3.9E+01 | 2.1E+04 | 6.9E+03 | 2.1E+04 | 1.5E+03 | 5.8E+01 | 3.9E+01 |
| PCSS-290 | 1.2E+05 | 3.2E+03 | 2.8E+02 | 3.9E+04 | 1.3E+04 | 4.4E+04 | 1.9E+03 | 1.3E+02 | 2.6E+02 |
| PCSS-294 | 7.3E+04 | 4.2E+03 | 3.7E+02 | 4.3E+04 | 1.3E+04 | 3.9E+04 | 3.2E+03 | 1.3E+02 | 1.2E+02 |
| PCSS-297 | 3.4E+04 | 2.4E+03 | 1.7E+02 | 1.6E+04 | 4.4E+03 | 3.6E+04 | 3.2E+03 | 9.9E+01 | 8.5E+01 |
| PCSS-303 | 6.5E+04 | 1.1E+03 | 3.6E+02 | 4.1E+04 | 1.2E+04 | 3.8E+04 | 2.4E+03 | 1.4E+02 | 9.4E+01 |
| PCSS-53 | 1.5E+04 | 1.1E+03 | 1.0E+02 | 9.0E+04 | 2.1E+05 | 9.2E+04 | 3.2E+02 | 2.8E+02 | 2.7E+02 |
| PCSS-133 | 3.3E+04 | 3.1E+03 | 4.7E+02 | 9.8E+04 | 1.6E+05 | 1.3E+05 | 5.2E+02 | 4.7E+02 | 3.8E+02 |
| PCSS-140 | 1.9E+04 | 1.1E+03 | 1.7E+02 | 1.0E+05 | 2.1E+05 | 5.6E+04 | 9.5E+01 | 1.7E+02 | 1.3E+02 |
| PCSS-169 | 2.6E+04 | 2.5E+03 | 1.2E+02 | 7.8E+04 | 2.0E+05 | 1.7E+05 | 7.4E+02 | 5.8E+02 | 7.9E+02 |
| PCSS-197 | 2.8E+04 | 1.5E+03 | 9.4E+01 | 8.4E+04 | 2.1E+05 | 1.1E+05 | 2.9E+02 | 3.2E+02 | 2.7E+02 |
| PCSS-208 | 2.1E+04 | 1.8E+03 | 6.5E+01 | 8.3E+04 | 2.0E+05 | 1.3E+05 | 2.6E+01 | 3.8E+02 | 4.0E+02 |
| PCSS-224 | 2.3E+04 | 1.1E+03 | 3.6E+01 | 9.6E+04 | 1.9E+05 | 8.5E+04 | 1.8E+02 | 2.5E+02 | 6.2E+02 |
| PCSS-250 | 5.8E+04 | 1.6E+03 | 1.6E+02 | 1.2E+05 | 1.5E+05 | 9.3E+04 | 6.7E+02 | 3.1E+02 | 1.8E+02 |
| HF-1 Black Mtn | 1.9E+04 | 1.1E+03 | 4.7E+01 | 7.4E+04 | 2.7E+05 | 1.6E+05 | 3.1E+03 | 4.8E+02 | 7.2E+02 |
| PC-2 Black Mtn | 2.6E+04 | 1.9E+03 | 2.1E+02 | 8.6E+04 | 2.6E+05 | 1.5E+05 | 3.7E+02 | 4.3E+02 | 2.9E+02 |
| Cuch-6 Black Mtn | 2.5E+04 | 4.9E+03 | 3.3E+02 | 8.3E+04 | 1.0E+05 | 1.6E+05 | 2.8E+02 | 4.3E+02 | 2.8E+02 |

Table A.20: Huerfano Basin elemental data (3/4). All elements are in units of ppb. bdl: below detection limit.

| Sample name | Sn | Sb | Cs | Ba | Tl | Pb | Bi | Th | U |
|---|---|---|---|---|---|---|---|---|---|
| Cuch-4 Black Mtn #1 | 2.0E+03 | 2.7E+02 | 1.3E+03 | 2.7E+04 | 1.2E+02 | 1.7E+04 | 1.9E+02 | 7.9E+03 | 1.3E+03 |
| Cuch-4 Black Mtn #2 | 1.7E+03 | 2.5E+02 | 1.1E+03 | 2.8E+04 | 1.2E+02 | 1.7E+04 | 2.0E+02 | 7.2E+03 | 9.7E+02 |
| Cuch-4 Black Mtn #3 | 2.5E+03 | 3.3E+02 | 1.7E+03 | 5.1E+04 | 1.9E+02 | 3.1E+04 | 2.9E+02 | 1.5E+04 | 1.8E+03 |
| PCSS-030 | 1.2E+03 | 1.2E+02 | 1.0E+03 | 4.3E+04 | 1.3E+02 | 9.0E+03 | 1.7E+02 | 4.4E+03 | 1.3E+03 |
| PCSS-117 | 9.6E+02 | 1.2E+02 | 1.5E+03 | 8.0E+04 | 2.0E+02 | 8.3E+03 | 1.1E+02 | 3.6E+03 | 1.5E+03 |
| PCSS-151 | 1.2E+03 | 1.1E+02 | 1.3E+03 | 7.5E+04 | 1.5E+02 | 7.8E+03 | 1.3E+02 | 3.5E+03 | 1.3E+03 |
| PCSS-174 | 9.0E+02 | 1.1E+02 | 7.0E+02 | 3.1E+04 | 7.7E+01 | 7.9E+03 | 1.8E+02 | 4.2E+03 | 1.2E+03 |
| PCSS-198 | 1.1E+03 | 6.4E+01 | 9.6E+02 | 7.1E+04 | 1.3E+02 | 6.7E+03 | 1.5E+02 | 4.0E+03 | 1.3E+03 |
| PCSS-221 | 1.6E+03 | 1.4E+02 | 1.6E+03 | 5.9E+04 | 1.7E+02 | 9.1E+03 | 2.1E+02 | 5.2E+03 | 1.8E+03 |
| PCSS-233 | 1.4E+03 | 1.5E+02 | 9.0E+02 | 6.3E+04 | 1.4E+02 | 8.7E+03 | 1.7E+02 | 5.0E+03 | 2.4E+03 |
| PCSS-257 | 1.1E+03 | 5.7E+01 | 9.7E+02 | 6.6E+04 | 1.4E+02 | 5.6E+03 | 1.3E+02 | 3.4E+03 | 7.8E+02 |
| PCSS-290 | 1.6E+03 | 2.7E+02 | 1.6E+03 | 1.1E+05 | 2.9E+02 | 1.4E+04 | 2.0E+02 | 7.4E+03 | 3.2E+03 |
| PCSS-294 | 2.9E+03 | 3.5E+02 | 1.9E+03 | 8.7E+04 | 2.6E+02 | 2.7E+04 | 2.9E+02 | 1.5E+04 | 3.4E+03 |
| PCSS-297 | 2.0E+03 | 1.1E+02 | 5.1E+02 | 2.5E+04 | 7.6E+01 | 1.0E+04 | 1.7E+02 | 5.8E+03 | 1.6E+03 |
| PCSS-303 | 2.1E+03 | 2.1E+02 | 1.5E+03 | 1.2E+05 | 2.3E+02 | 2.1E+04 | 2.2E+02 | 4.4E+03 | 2.1E+03 |
| PCSS-53 | 6.8E+02 | 2.0E+02 | 4.8E+02 | 1.5E+06 | 3.3E+02 | 1.4E+04 | 2.1E+01 | 2.3E+03 | 9.3E+02 |
| PCSS-133 | 1.0E+03 | 1.6E+02 | 5.7E+02 | 1.5E+06 | 4.3E+02 | 1.8E+04 | 2.0E+01 | 3.9E+03 | 2.3E+03 |
| PCSS-140 | 3.5E+02 | 7.4E+01 | 7.4E+02 | 1.8E+06 | 4.4E+02 | 2.1E+04 | 1.6E+01 | 1.8E+03 | 7.8E+02 |
| PCSS-169 | 7.0E+02 | 1.2E+02 | 6.3E+02 | 1.3E+06 | 4.5E+02 | 1.4E+04 | 2.7E+01 | 3.9E+03 | 1.3E+03 |
| PCSS-197 | 7.3E+02 | 8.4E+01 | 7.7E+02 | 1.2E+06 | 3.4E+02 | 1.3E+04 | 2.7E+01 | 2.4E+03 | 1.2E+03 |
| PCSS-208 | 6.1E+02 | 6.1E+01 | 4.9E+02 | 1.5E+06 | 3.3E+02 | 1.6E+04 | 1.7E+01 | 2.1E+03 | 8.9E+02 |
| PCSS-224 | 7.1E+02 | 9.6E+01 | 6.1E+02 | 1.4E+06 | 3.6E+02 | 1.8E+04 | 2.9E+01 | 2.3E+03 | 7.8E+02 |
| PCSS-250 | 9.1E+02 | 1.3E+02 | 1.1E+03 | 1.7E+06 | 5.9E+02 | 2.2E+04 | 4.4E+01 | 3.1E+03 | 1.7E+03 |
| HF-1 Black Mtn | 5.7E+02 | 1.3E+02 | 4.6E+02 | 2.0E+06 | 3.0E+02 | 1.3E+04 | 2.8E+01 | 4.6E+03 | 1.0E+03 |
| PC-2 Black Mtn | 9.6E+02 | 1.1E+02 | 5.2E+02 | 1.4E+06 | 3.2E+02 | 1.6E+04 | 3.2E+01 | 3.5E+03 | 1.3E+03 |
| Cuch-6 Black Mtn | 1.6E+03 | 1.6E+02 | 1.0E+03 | 1.2E+06 | 3.5E+02 | 2.0E+04 | 6.1E+01 | 5.9E+03 | 2.0E+03 |

Table A.21: Huerfano Basin elemental data (4/4). All elements are in units of ppb. bdl: below detection limit.

# Bibliography

Abdul Aziz, H., Hilgen, F. J., Luijk, G. M. v., Sluijs, A., Kraus, M. J., Pares, J. M., and Gingerich, P. D. (2008). Astronomical climate control on paleosol stacking patterns in the upper Paleocene–lower Eocene Willwood Formation, Bighorn Basin, Wyoming. *Geology*, 36(7):531–534.

Abels, H. A., Kraus, M. J., and Gingerich, P. D. (2013). Precession-scale cyclicity in the fluvial lower Eocene Willwood Formation of the Bighorn Basin, Wyoming (USA). *Sedimentology*, 60(6):1467–1483.

Algeo, T. J. and Scheckler, S. E. (2010). Land plant evolution and weathering rate changes in the Devonian. *Journal of Earth Science*, 21(Suppl 1):75–78.

Armbrustmacher, T. J. (1984). Alkaline rock complexes in the Wet Mountains area, Custer and Fremont counties, Colorado. Technical Report 1269, U.S. Geological Survey Professional Paper.

Armbrustmacher, T. J. (1988). Geology and resources of thorium and associated elements in the Wet Mountains area, Fremont and Custer Counties, Colorado. Technical Report 1049-F, U.S. Geological Survey Professional Paper.

Baczynski, A. A., McInerney, F. A., Wing, S. L., Kraus, M. J., Bloch, J. I., Boyer, D. M., Secord, R., Morse, P. E., and Fricke, H. C. (2013). Chemostratigraphic implications of spatial variation in the Paleocene-Eocene Thermal Maximum car-

bon isotope excursion, SE Bighorn Basin, Wyoming. *Geochemistry, Geophysics, Geosystems*, 14(10):4133–4152.

Baczynski, A. A., McInerney, F. A., Wing, S. L., Kraus, M. J., Bloch, J. I., and Secord, R. (2017). Constraining paleohydrologic change during the Paleocene-Eocene Thermal Maximum in the continental interior of North America. *Palaeogeography, Palaeoclimatology, Palaeoecology*, 465:237–246.

Baczynski, A. A., McInerney, F. A., Wing, S. L., Kraus, M. J., Morse, P. E., Bloch, J. I., Chung, A. H., and Freeman, K. H. (2016). Distortion of carbon isotope excursion in bulk soil organic matter during the Paleocene-Eocene thermal maximum. *GSA Bulletin*, 128(9-10):1352–1366.

Bagard, M.-L., West, A. J., Newman, K., and Basu, A. R. (2015). Lithium isotope fractionation in the Ganges–Brahmaputra floodplain and implications for groundwater impact on seawater isotopic composition. *Earth and Planetary Science Letters*, 432:404–414.

Barnhart, K. R., Hutton, E. W., Tucker, G. E., Gasparini, N. M., Istanbulluoglu, E., Hobley, D. E., Lyons, N. J., Mouchene, M., Nudurupati, S. S., Adams, J. M., et al. (2020). Landlab v2. 0: a software package for Earth surface dynamics. *Earth Surface Dynamics*, 8(2):379–397.

Bastian, L., Revel, M., Bayon, G., Dufour, A., and Vigier, N. (2017). Abrupt response of chemical weathering to Late Quaternary hydroclimate changes in northeast Africa. *Scientific Reports*, 7(1):44231.

Bastian, L., Vigier, N., Revel, M., Yirgu, G., Ayalew, D., and Pik, R. (2019). Chemical erosion rates in the upper Blue Nile Basin and related atmospheric CO2 consumption. *Chemical Geology*, 518:19–31.

Berner, R. A., Lasaga, A. C., and Garrels, R. M. (1983). The carbonate-silicate geochemical cycle and its effect on atmospheric carbon dioxide over the past 100 million years. *American Journal of Science*, 283:641–683.

Bickle, M. J., Chapman, H. J., Tipper, E., Galy, A., Rocha, C. L. D. L., and Ahmad, T. (2018). Chemical weathering outputs from the flood plain of the Ganga. *Geochimica et Cosmochimica Acta*, 225:146–175.

Bird, P. (1998). Kinematic history of the Laramide orogeny in latitudes 35–49 N, western United States. *Tectonics*, 17(5):780–801.

Boardman, S. J. and Condie, K. C. (1986). Early Proterozoic bimodal volcanic rocks in central Colorado, USA, Part II: Geochemistry, petrogenesis and tectonic setting. *Precambrian Research*, 34(1):37–68.

Bohlin, M. S. and Bickle, M. J. (2019). The reactive transport of Li as a monitor of weathering processes in kinetically limited weathering regimes. *Earth and Planetary Science Letters*, 511:233–243.

Bouchez, J., Blanckenburg, F. v., and Schuessler, J. A. (2013). Modeling novel stable isotope ratios in the weathering zone. *American Journal of Science*, 313(4):267–308.

Bouchez, J., Gaillardet, J., and Blanckenburg, F. v. (2014). Weathering Intensity in Lowland River Basins: From the Andes to the Amazon Mouth. *Procedia Earth and Planetary Science*, 10:280–286.

Bouchez, J., Gaillardet, J., France-Lanord, C., Maurice, L., and Dutra-Maia, P. (2011). Grain size control of river suspended sediment geochemistry: Clues from Amazon River depth profiles. *Geochemistry, Geophysics, Geosystems*, 12(3).

Bouchez, J., Gaillardet, J., Lupker, M., Louvat, P., France-Lanord, C., Maurice, L.,

Armijos, E., and Moquet, J.-S. (2012). Floodplains of large rivers: Weathering reactors or simple silos? *Chemical Geology*, 332:166–184.

Bowen, G. J., Clyde, W. C., Koch, P. L., Ting, S., Alroy, J., Tsubamoto, T., Wang, Y., and Wang, Y. (2002). Mammalian dispersal at the Paleocene/Eocene boundary. *Science*, 295(5562):2062–2065.

Bowen, G. J., Maibauer, B. J., Kraus, M. J., Röhl, U., Westerhold, T., Steimke, A., Gingerich, P. D., Wing, S. L., and Clyde, W. C. (2015). Two massive, rapid releases of carbon during the onset of the Palaeocene–Eocene thermal maximum. *Nature Geoscience*, 8(1):44–47.

Bowen, G. J. and Zachos, J. C. (2010). Rapid carbon sequestration at the termination of the Palaeocene–Eocene Thermal Maximum. *Nature Geoscience*, 3(12):866–869.

Bown, T. M. and Kraus, M. J. (1981). Lower Eocene alluvial paleosols (Willwood Formation, northwest Wyoming, USA) and their significance for paleoecology, paleoclimatology, and basin analysis. *Palaeogeography, Palaeoclimatology, Palaeoecology*, 34:1–30.

Bown, T. M. and Kraus, M. J. (1987). Integration of channel and floodplain suites; I, Developmental sequence and lateral relations of alluvial Paleosols. *Journal of Sedimentary Research*, 57(4):587–601.

Brady, P. V. and Carroll, S. A. (1994). Direct effects of $CO_2$ and temperature on silicate weathering: Possible implications for climate control. *Geochimica et Cosmochimica Acta*, 58(7):1853–1856.

Brand, W. A., Coplen, T. B., Vogl, J., Rosner, M., and Prohaska, T. (2014). Assessment of international reference materials for isotope-ratio analysis (IUPAC Technical Report). *Pure and Applied Chemistry*, 86(3):425–467.

Brantley, S. (2004). Reaction Kinetics of Primary Rock-forming Minerals under Ambient Conditions. *Treatise on Geochemistry*, pages 73–117.

Bufe, A., Hovius, N., Emberson, R., Rugenstein, J. K. C., Galy, A., Hassenruck-Gudipati, H. J., and Chang, J.-M. (2021). Co-variation of silicate, carbonate and sulfide weathering drives CO2 release with erosion. *Nature Geoscience*, 14(4):211–216.

Bush, M. A., Horton, B. K., Murphy, M. A., and Stockli, D. F. (2016). Detrital record of initial basement exhumation along the Laramide deformation front, southern Rocky Mountains. *Tectonics*, 35(9):2117–2130.

Carmichael, M. J., Pancost, R. D., and Lunt, D. J. (2018). Changes in the occurrence of extreme precipitation events at the Paleocene–Eocene thermal maximum. *Earth and Planetary Science Letters*, 501:24–36.

Cather, S. M., Mack, G., and Giles, K. (2004). Laramide orogeny in central and northern New Mexico and southern Colorado. *The Geology of New Mexico, A Geologic History: New Mexico Geological Society Special Publication*, 11:203–248.

Caves, J. K., Jost, A. B., Lau, K. V., and Maher, K. (2016). Cenozoic carbon cycle imbalances and a variable weathering feedback. *Earth and Planetary Science Letters*, 450:152–163.

Chamberlin, T. C. (1899). An attempt to frame a working hypothesis of the cause of glacial periods on an atmospheric basis. *The Journal of Geology*, 7(6):545–584.

Chapin, C. E., Kelley, S. A., and Cather, S. M. (2014). The Rocky Mountain Front, southwestern USA. *Geosphere*, 10(5):1043–1060.

Choi, H.-B., Ryu, J.-S., Shin, W.-J., and Vigier, N. (2019). The impact of anthropogenic inputs on lithium content in river and tap water. *Nature Communications*, 10(1):5371.

Clechenko, E. R., Kelly, D. C., Harrington, G. J., and Stiles, C. A. (2007). Terrestrial records of a regional weathering profile at the Paleocene-Eocene boundary in the Williston Basin of North Dakota. *GSA Bulletin*, 119(3-4):428–442.

Clergue, C., Dellinger, M., Buss, H., Gaillardet, J., Benedetti, M., and Dessert, C. (2015). Influence of atmospheric deposits and secondary minerals on Li isotopes budget in a highly weathered catchment, Guadeloupe (Lesser Antilles). *Chemical Geology*, 414:28–41.

Clyde, W. C., Hamzi, W., Finarelli, J. A., Wing, S. L., Schankler, D., and Chew, A. (2007). Basin-wide magnetostratigraphic framework for the Bighorn Basin, Wyoming. *GSA Bulletin*, 119(7-8):848–859.

Colleps, C. L., McKenzie, N. R., Stockli, D. F., Hughes, N. C., Singh, B. P., Webb, A. A. G., Myrow, P. M., Planavsky, N. J., and Horton, B. K. (2018). Zircon (U-Th)/He thermochronometric constraints on Himalayan Thrust Belt exhumation, bedrock weathering, and Cenozoic seawater chemistry. *Geochemistry, Geophysics, Geosystems*, 19(1):257–271.

Cullers, R. L., Barrett, T., Carlson, R., and Robinson, B. (1987). Rare-earth element and mineralogic changes in Holocene soil and stream sediment: A case study in the Wet Mountains, Colorado, U.S.A. *Chemical Geology*, 63(3-4):275–297.

DeCelles, P. G., Gray, M. B., Ridgway, K. D., Cole, R. B., Pivnik, D. A., Pequera, N., and Srivastava, P. (1991a). Controls on synorogenic alluvial-fan architecture, Beartooth Conglomerate (Palaeocene), Wyoming and Montana. *Sedimentology*, 38(4):567–590.

DeCelles, P. G., Gray, M. B., Ridgway, K. D., Cole, R. B., Srivastava, P., Pequera, N., and Pivnik, D. A. (1991b). Kinematic history of a foreland uplift from Pale-

ocene synorogenic conglomerate, Beartooth Range, Wyoming and Montana. *GSA Bulletin*, 103(11):1458–1475.

Dellinger, M., Bouchez, J., Gaillardet, J., Faure, L., and Moureau, J. (2017). Tracing weathering regimes using the lithium isotope composition of detrital sediments. *Geology*, 45(5):411–414.

Dellinger, M., Gaillardet, J., Bouchez, J., Calmels, D., Galy, V., Hilton, R. G., Louvat, P., and France-Lanord, C. (2014). Lithium isotopes in large rivers reveal the cannibalistic nature of modern continental weathering and erosion. *Earth and Planetary Science Letters*, 401:359–372.

Dellinger, M., Gaillardet, J., Bouchez, J., Calmels, D., Louvat, P., Dosseto, A., Gorge, C., Alanoca, L., and Maurice, L. (2015). Riverine Li isotope fractionation in the Amazon River basin controlled by the weathering regimes. *Geochimica et Cosmochimica Acta*, 164:71–93.

Denis, E. H., Maibauer, B. J., Bowen, G. J., Jardine, P. E., Harrington, G. J., Baczynski, A. A., McInerney, F. A., Collinson, M. E., Belcher, C. M., Wing, S. L., and Freeman, K. H. (2021). Decreased soil carbon in a warming world: Degraded pyrogenic carbon during the Paleocene-Eocene Thermal Maximum, Bighorn Basin, Wyoming. *Earth and Planetary Science Letters*, 566:116970.

Dickinson, W. R., Klute, M. A., Hayes, M. J., Janecke, S. U., Lundin, E. R., McKittrick, M. A., and Olivares, M. D. (1988). Paleogeographic and paleotectonic setting of Laramide sedimentary basins in the central Rocky Mountain region. *GSA Bulletin*, 100(7):1023–1039.

Dickson, A. J., Cohen, A. S., Coe, A. L., Davies, M., Shcherbinina, E. A., and Gavrilov, Y. O. (2015). Evidence for weathering and volcanism during the PETM

from Arctic Ocean and Peri-Tethys osmium isotope records. *Palaeogeography, Palaeoclimatology, Palaeoecology*, 438:300–307.

Dosseto, A., Bourdon, B., Gaillardet, J., Maurice-Bourgoin, L., and Allegre, C. J. (2006). Weathering and transport of sediments in the Bolivian Andes: Time constraints from uranium-series isotopes. *Earth and Planetary Science Letters*, 248(3-4):759–771.

Dosseto, A., Vigier, N., Joannes-Boyau, R., Moffat, I., Singh, T., and Srivastava, P. (2015). Rapid response of silicate weathering rates to climate change in the Himalaya. *Geochemical Perspectives Letters*, pages 10–19.

Duller, R. A., Armitage, J. J., Manners, H. R., Grimes, S., and Jones, T. D. (2019). Delayed sedimentary response to abrupt climate change at the Paleocene-Eocene boundary, northern Spain. *Geology*, 47(2):159–162.

Dupuis, R., Benoit, M., Tuckerman, M. E., and Méheut, M. (2017). Importance of a Fully Anharmonic Treatment of Equilibrium Isotope Fractionation Properties of Dissolved Ionic Species As Evidenced by Li + (aq). *Accounts of Chemical Research*, 50(7):1597–1605.

D'Antonio, M. P., Ibarra, D. E., and Boyce, C. K. (2019). Land plant evolution decreased, rather than increased, weathering rates. *Geology*, 48(1):29–33.

Fan, M. and Carrapa, B. (2014). Late Cretaceous–early Eocene Laramide uplift, exhumation, and basin subsidence in Wyoming: Crustal responses to flat slab subduction. *Tectonics*, 33(4):509–529.

Fang, X., Galy, A., Yang, Y., Zhang, W., Ye, C., and Song, C. (2019). Paleogene global cooling—induced temperature feedback on chemical weathering, as recorded in the northern Tibetan Plateau. *Geology*, 47(10):992–996.

Ferrier, K. L. and Kirchner, J. W. (2008). Effects of physical erosion on chemical denudation rates: A numerical modeling study of soil-mantled hillslopes. *Earth and Planetary Science Letters*, 272(3-4):591–599.

Ferrier, K. L. and Perron, J. T. (2020). The Importance of Hillslope Scale in Responses of Chemical Erosion Rate to Changes in Tectonics and Climate. *Journal of Geophysical Research: Earth Surface*, 125(9).

Ferrier, K. L. and West, N. (2017). Responses of chemical erosion rates to transient perturbations in physical erosion rates, and implications for relationships between chemical and physical erosion rates in regolith-mantled hillslopes. *Earth and Planetary Science Letters*, 474:447–456.

Fick, S. E. and Hijmans, R. J. (2017). Worldclim 2: new 1-km spatial resolution climate surfaces for global land areas. *International journal of climatology*, 37(12):4302–4315.

Finn, T. M. (2019). Stratigraphic cross sections of the Niobrara Interval of the Upper Cretaceous Cody Shale in the Bighorn Basin, Wyoming and Montana. Technical report, US Geological Survey.

Foreman, B. Z. (2014). Climate-driven generation of a fluvial sheet sand body at the Paleocene–Eocene boundary in north-west Wyoming (USA). *Basin Research*, 26(2):225–241.

Foreman, B. Z., Heller, P. L., and Clementz, M. T. (2012). Fluvial response to abrupt global warming at the Palaeocene/Eocene boundary. *Nature*, 491(7422):92–95.

Frings, P. J. (2019). Palaeoweathering: How Do Weathering Rates Vary with Climate? *Elements*, 15(4):259–265.

Gaillardet, J., Dupré, B., Louvat, P., and Allègre, C. (1999). Global silicate weathering and $CO_2$ consumption rates deduced from the chemistry of large rivers. *Chemical Geology*, 159(1-4):3–30.

Garzanti, E., Andó, S., France-Lanord, C., Censi, P., Vignola, P., Galy, V., and Lupker, M. (2011). Mineralogical and chemical variability of fluvial sediments 2. Suspended-load silt (Ganga–Brahmaputra, Bangladesh). *Earth and Planetary Science Letters*, 302(1-2):107–120.

Godsey, S. E., Kirchner, J. W., and Clow, D. W. (2009). Concentration–discharge relationships reflect chemostatic characteristics of US catchments. *Hydrological Processes: An International Journal*, 23(13):1844–1864.

Golla, J. K., Kuessner, M. L., Henehan, M. J., Bouchez, J., Rempe, D. M., and Druhan, J. L. (2021). The evolution of lithium isotope signatures in fluids draining actively weathering hillslopes. *Earth and Planetary Science Letters*, 567:116988.

Gou, L.-F., Jin, Z., Strandmann, P. v. P. A., Li, G., Qu, Y.-X., Xiao, J., Deng, L., and Galy, A. (2019). Li isotopes in the middle Yellow River: Seasonal variability, sources and fractionation. *Geochimica et Cosmochimica Acta*, 248:88–108.

Greenlee, D. D. (1987). Raster and vector processing for scanned linework. *Photogrammetric Engineering and Remote Sensing*, 53:1383–1387.

Gutjahr, M., Ridgwell, A., Sexton, P. F., Anagnostou, E., Pearson, P. N., Pälike, H., Norris, R. D., Thomas, E., and Foster, G. L. (2017). Very large release of mostly volcanic carbon during the Palaeocene–Eocene Thermal Maximum. *Nature*, 548(7669):573–577.

Hahm, W. J., Riebe, C. S., Lukens, C. E., and Araki, S. (2014). Bedrock composition regulates mountain ecosystems and landscape evolution. *Proceedings of the National Academy of Sciences*, 111(9):3338–3343.

Hajek, E. A. and Straub, K. M. (2016). Autogenic Sedimentation in Clastic Stratigraphy. *Annual Review of Earth and Planetary Sciences*, 45(1):1–29.

Hajek, E. A. and Wolinsky, M. A. (2012). Simplified process modeling of river avulsion and alluvial architecture: Connecting models and field data. *Sedimentary Geology*, 257:1–30.

Hartmann, J. and Moosdorf, N. (2012). The new global lithological map database GLiM: A representation of rock properties at the Earth surface. *Geochemistry, Geophysics, Geosystems*, 13(12).

Haynes, L. L. and Hönisch, B. (2020). The seawater carbon inventory at the Paleocene–Eocene Thermal Maximum. *Proceedings of the National Academy of Sciences*, 117(39):24088–24095.

Heimsath, A. M., Dietrich, W. E., Nishiizumi, K., and Finkel, R. C. (1997). The soil production function and landscape equilibrium. *Nature*, 388(6640):358–361.

Henchiri, S., Clergue, C., Dellinger, M., Gaillardet, J., Louvat, P., and Bouchez, J. (2014). The Influence of Hydrothermal Activity on the Li Isotopic Signature of Rivers Draining Volcanic Areas. *Procedia Earth and Planetary Science*, 10:223–230.

Henchiri, S., Gaillardet, J., Dellinger, M., Bouchez, J., and Spencer, R. G. M. (2016). Riverine dissolved lithium isotopic signatures in low-relief central Africa and their link to weathering regimes. *Geophysical Research Letters*, 43(9):4391–4399.

Hilton, R. G. and West, A. J. (2020). Mountains, erosion and the carbon cycle. *Nature Reviews Earth & Environment*, 1(6):284–299.

Hindshaw, R. S., Aciego, S. M., and Tipper, E. T. (2018). Li and U Isotopes as a Potential Tool for Monitoring Active Layer Deepening in Permafrost Dominated Catchments. *Frontiers in Earth Science*, 6:102.

Hindshaw, R. S., Tosca, R., Goût, T. L., Farnan, I., Tosca, N. J., and Tipper, E. T. (2019). Experimental constraints on Li isotope fractionation during clay formation. *Geochimica et Cosmochimica Acta*, 250:219–237.

Hobson, W. and Dahlgren, R. (1998). A quantitative study of pedogenesis in California vernal pool wetlands. *Quantifying soil hydromorphology*, 54:107–127.

Howard, A. D., Dietrich, W. E., and Seidl, M. A. (1994). Modeling fluvial erosion on regional to continental scales. *Journal of Geophysical Research: Solid Earth*, 99(B7):13971–13986.

Huh, Y., Chan, L.-H., and Edmond, J. M. (2001). Lithium isotopes as a probe of weathering processes: Orinoco River. *Earth and Planetary Science Letters*, 194(1-2):189–199.

Huh, Y., Chan, L.-H., Zhang, L., and Edmond, J. M. (1998). Lithium and its isotopes in major world rivers: implications for weathering and the oceanic budget. *Geochimica et Cosmochimica Acta*, 62(12):2039–2051.

Ibarra, D. E., Caves, J. K., Moon, S., Thomas, D. L., Hartmann, J., Chamberlain, C. P., and Maher, K. (2016). Differential weathering of basaltic and granitic catchments from concentration–discharge relationships. *Geochimica et Cosmochimica Acta*, 190:265–293.

Ibarra, D. E., Rugenstein, J. K. C., Bachan, A., Baresch, A., Lau, K. V., Thomas, D. L., Lee, J.-E., Boyce, C. K., and Chamberlain, C. P. (2019). Modeling the consequences of land plant evolution on silicate weathering. *American Journal of Science*, 319(1):1–43.

Inglis, G. N., Rohrssen, M., Kennedy, E. M., Crouch, E. M., Raine, J. I., Strogen, D. P., Naafs, B. D. A., Collinson, M. E., and Pancost, R. D. (2021). Terrestrial

methane cycle perturbations during the onset of the Paleocene-Eocene Thermal Maximum. *Geology*, 49(5):520–524.

Jenson, S. K. and Domingue, J. O. (1988). Extracting topographic structure from digital elevation data for geographic information system analysis. *Photogrammetric engineering and remote sensing*, 54(11):1593–1600.

John, C. M., Banerjee, N. R., Longstaffe, F. J., Sica, C., Law, K. R., and Zachos, J. C. (2012). Clay assemblage and oxygen isotopic constraints on the weathering response to the Paleocene-Eocene thermal maximum, east coast of North America. *Geology*, 40(7):591–594.

Kisakűrek, B., James, R. H., and Harris, N. B. (2005). Li and $\delta^7$Li in Himalayan rivers: Proxies for silicate weathering? *Earth and Planetary Science Letters*, 237(3-4):387–401.

Komar, N. and Zeebe, R. (2011). Oceanic calcium changes from enhanced weathering during the Paleocene-Eocene thermal maximum: No effect on calcium-based proxies. *Paleoceanography*, 26(3).

Komar, N. and Zeebe, R. E. (2021). Reconciling atmospheric CO2, weathering, and calcite compensation depth across the Cenozoic. *Science Advances*, 7(4):eabd4876.

Kraus, M. J. (1980). Genesis of a fluvial sheet sandstone, Willwood Formation, northwest Wyoming. *Early Cenozoic Paleontology and Stratigraphy of the Bighorn Basin, Wyoming. University of Michigan Papers on Paleontology*, 24:87–94.

Kraus, M. J. (1999). Paleosols in clastic sedimentary rocks: their geologic applications. *Earth-Science Reviews*, 47(1-2):41–70.

Kraus, M. J. and Aslan, A. (1993). Eocene hydromorphic Paleosols; significance for interpreting ancient floodplain processes. *Journal of Sedimentary Research*, 63(3):453–463.

Kraus, M. J. and Hasiotis, S. T. (2006). Significance of Different Modes of Rhizolith Preservation to Interpreting Paleoenvironmental and Paleohydrologic Settings: Examples from Paleogene Paleosols, Bighorn Basin, Wyoming, U.S.A. *Journal of Sedimentary Research*, 76(4):633–646.

Kraus, M. J., McInerney, F. A., Wing, S. L., Secord, R., Baczynski, A. A., and Bloch, J. I. (2013). Paleohydrologic response to continental warming during the Paleocene–Eocene Thermal Maximum, Bighorn Basin, Wyoming. *Palaeogeography, Palaeoclimatology, Palaeoecology*, 370:196–208.

Kraus, M. J. and Middleton, L. T. (1987). Contrasting architecture of two alluvial suites in different structural settings. *Special Publications of SEPM*.

Kraus, M. J. and Riggins, S. (2007). Transient drying during the Paleocene–Eocene Thermal Maximum (PETM): Analysis of paleosols in the bighorn basin, Wyoming. *Palaeogeography, Palaeoclimatology, Palaeoecology*, 245(3-4):444–461.

Kraus, M. J., Woody, D. T., Smith, J. J., and Dukic, V. (2015). Alluvial response to the Paleocene–Eocene Thermal Maximum climatic event, Polecat Bench, Wyoming (U.S.A.). *Palaeogeography, Palaeoclimatology, Palaeoecology*, 435:177–192.

Kump, L. R., Brantley, S. L., and Arthur, M. A. (2000). Chemical Weathering, Atmospheric CO2, and Climate. *Annual Review of Earth and Planetary Sciences*, 28(1):611–667.

Larsen, I. J., Almond, P. C., Eger, A., Stone, J. O., Montgomery, D. R., and Malcolm, B. (2014a). Rapid Soil Production and Weathering in the Southern Alps, New Zealand. *Science*, 343(6171):637–640.

Larsen, I. J., Montgomery, D. R., and Greenberg, H. M. (2014b). The contribution of mountains to global denudation. *Geology*, 42(6):527–530.

Lawton, T. F. (2008). Laramide sedimentary basins. *Sedimentary basins of the world*, 5:429–450.

Lee, C.-T. A., Jiang, H., Dasgupta, R., and Torres, M. (2019). A framework for understanding whole-earth carbon cycling. In *Deep Carbon: Past to Present*, pages 313–357. Cambridge University Press.

Lemarchand, E., Chabaux, F., Vigier, N., Millot, R., and Pierret, M.-C. (2010). Lithium isotope systematics in a forested granitic catchment (Strengbach, Vosges Mountains, France). *Geochimica et Cosmochimica Acta*, 74(16):4612–4628.

Li, G., Hartmann, J., Derry, L. A., West, A. J., You, C.-F., Long, X., Zhan, T., Li, L., Li, G., Qiu, W., et al. (2016). Temperature dependence of basalt weathering. *Earth and Planetary Science Letters*, 443:59–69.

Li, G. and West, A. J. (2014). Evolution of Cenozoic seawater lithium isotopes: Coupling of global denudation regime and shifting seawater sinks. *Earth and Planetary Science Letters*, 401:284–293.

Li, W., Liu, X.-M., and Chadwick, O. A. (2020). Lithium isotope behavior in Hawaiian regoliths: Soil-atmosphere-biosphere exchanges. *Geochimica et Cosmochimica Acta*, 285:175–192.

Liu, X.-M., Wanner, C., Rudnick, R. L., and McDonough, W. F. (2015). Processes controlling $\delta^7$Li in rivers illuminated by study of streams and groundwaters draining basalts. *Earth and Planetary Science Letters*, 409:212–224.

Longley, M. (2018). Lithium as a proxy for Silicate Weathering during the Southeast Asian Monsoon. Undergraduate thesis, Yale University.

Love, J. and Christiansen, A. (1985). Geologic Map of Wyoming: US Geologic Survey, Scale 1:500,000.

Lupker, M., France-Lanord, C., Galy, V., Lavé, J., Gaillardet, J., Gajurel, A. P., Guilmette, C., Rahman, M., Singh, S. K., and Sinha, R. (2012). Predominant floodplain over mountain weathering of Himalayan sediments (Ganga basin). *Geochimica et Cosmochimica Acta*, 84:410–432.

Lyons, S. L., Baczynski, A. A., Babila, T. L., Bralower, T. J., Hajek, E. A., Kump, L. R., Polites, E. G., Self-Trail, J. M., Trampush, S. M., Vornlocher, J. R., Zachos, J. C., and Freeman, K. H. (2019). Palaeocene–Eocene Thermal Maximum prolonged by fossil carbon oxidation. *Nature Geoscience*, 12(1):54–60.

Macdonald, F. A., Swanson-Hysell, N. L., Park, Y., Lisiecki, L., and Jagoutz, O. (2019). Arc-continent collisions in the tropics set Earth's climate state. *Science*, 364(6436):eaav5300.

Maffre, P., Goddéris, Y., Vigier, N., Moquet, J.-S., and Carretier, S. (2020). Modelling the riverine $\delta^7$Li variability throughout the Amazon Basin. *Chemical Geology*, 532:119336.

Magna, T., Wiechert, U. H., and Halliday, A. N. (2004). Low-blank isotope ratio measurement of small samples of lithium using multiple-collector ICPMS. *International Journal of Mass Spectrometry*, 239(1):67–76.

Maher, K. (2010). The dependence of chemical weathering rates on fluid residence time. *Earth and Planetary Science Letters*, 294(1-2):101–110.

Maher, K. and Chamberlain, C. P. (2014). Hydrologic Regulation of Chemical Weathering and the Geologic Carbon Cycle. *Science*, 343(6178):1502–1504.

Malkowski, M. A., Sharman, G. R., Johnstone, S. A., Grove, M. J., Kimbrough, D. L., and Graham, S. A. (2019). Dilution and propagation of provenance trends

in sand and mud: Geochemistry and detrital zircon geochronology of modern sediment from central California (USA). *American Journal of Science*, 319(10):846–902.

Małoszewski, P. and Zuber, A. (1982). Determining the turnover time of groundwater systems with the aid of environmental tracers: 1. models and their applicability. *Journal of hydrology*, 57(3-4):207–231.

Manaka, T., Araoka, D., Yoshimura, T., Hossain, H. Z., Nishio, Y., Suzuki, A., and Kawahata, H. (2017). Downstream and seasonal changes of lithium isotope ratios in the Ganges-Brahmaputra river system. *Geochemistry, Geophysics, Geosystems*, 18(8):3003–3015.

May, S. R., Gray, G. G., Summa, L. L., Stewart, N. R., Gehrels, G. E., and Pecha, M. E. (2013). Detrital zircon geochronology from the Bighorn Basin, Wyoming, USA: Implications for tectonostratigraphic evolution and paleogeography. *GSA Bulletin*, 125(9-10):1403–1422.

McGuire, K. J., McDonnell, J. J., Weiler, M., Kendall, C., McGlynn, B. L., Welker, J. M., and Seibert, J. (2005). The role of topography on catchment-scale water residence time. *Water Resources Research*, 41(5).

McInerney, F. A. and Wing, S. L. (2011). The Paleocene-Eocene Thermal Maximum: A Perturbation of Carbon Cycle, Climate, and Biosphere with Implications for the Future. *Earth and Planetary Sciences*, 39(1):489–516.

Meier, C., Osenbrück, K., Seitz, H.-M., and Weise, S. M. (2017). First lithium isotope data from rivers and subsurface water in the Pamirs. *Procedia Earth and Planetary Science*, 17:574–577.

Millot, R. and Négrel, P. (2021). Lithium isotopes in the Loire River Basin (France):

Hydrogeochemical characterizations at two complementary scales. *Applied Geochemistry*, 125:104831.

Millot, R., Scaillet, B., and Sanjuan, B. (2010). Lithium isotopes in island arc geothermal systems: Guadeloupe, Martinique (French West Indies) and experimental approach. *Geochimica et Cosmochimica Acta*, 74(6):1852–1871.

Misra, S. and Froelich, P. N. (2012). Lithium Isotope History of Cenozoic Seawater: Changes in Silicate Weathering and Reverse Weathering. *Science*, 335(6070):818–823.

Molnar, P. (2001). Climate change, flooding in arid environments, and erosion rates. *Geology*, 29(12):1071–1074.

Montgomery, D. R. and Brandon, M. T. (2002). Topographic controls on erosion rates in tectonically active mountain ranges. *Earth and Planetary Science Letters*, 201(3-4):481–489.

Moon, S., Perron, J., Martel, S., Holbrook, W., and St. Clair, J. (2017). A model of three-dimensional topographic stresses with implications for bedrock fractures, surface processes, and landscape evolution. *Journal of Geophysical Research: Earth Surface*, 122(4):823–846.

Murphy, B. P., Johnson, J. P., Gasparini, N. M., and Sklar, L. S. (2016). Chemical weathering as a mechanism for the climatic control of bedrock river incision. *Nature*, 532(7598):223–227.

Murphy, M. J., Porcelli, D., Pogge von Strandmann, P. A., Hirst, C. A., Kutscher, L., Katchinoff, J. A., Mörth, C.-M., Maximov, T., and Andersson, P. S. (2019). Tracing silicate weathering processes in the permafrost-dominated Lena River watershed using lithium isotopes. *Geochimica et Cosmochimica Acta*, 245:154–171.

Neale, R. B., Chen, C.-C., Gettelman, A., Lauritzen, P. H., Park, S., Williamson, D. L., Conley, A. J., Garcia, R., Kinnison, D., Lamarque, J.-F., et al. (2010). Description of the NCAR community atmosphere model (CAM 5.0). *NCAR Tech. Note NCAR/TN-486+ STR*, 1(1):1–12.

Neasham, J. W. and Vondra, C. F. (1972). Stratigraphy and Petrology of the Lower Eocene Willwood Formation, Bighorn Basin, Wyoming. *GSA Bulletin*, 83(7):2167–2180.

Noblett, J. B. and Staub, M. W. (1990). Mid-Proterozoic lamprophyre commingled with late-stage granitic dikes of the anorogenic San Isabel batholith, Wet Mountains, Colorado. *Geology*, 18(2):120–123.

Oi, T., Odagiri, T., and Nomura, M. (1997). Extraction of lithium from GSJ rock reference samples and determination of their lithium isotopic compositions. *Analytica chimica acta*, 340(1-3):221–225.

Panchuk, K., Ridgwell, A., and Kump, L. (2008). Sedimentary response to Paleocene-Eocene Thermal Maximum carbon release: A model-data comparison. *Geology*, 36(4):315–318.

Park, Y., Maffre, P., Goddéris, Y., Macdonald, F. A., Anttila, E. S., and Swanson-Hysell, N. L. (2020). Emergence of the Southeast Asian islands as a driver for Neogene cooling. *Proceedings of the National Academy of Sciences*, 117(41):25319–25326.

Parker, R. L. and Sharp, W. N. (1970). Mafic-ultramafic igneous rocks and associated carbonatites of the Gem Park Complex, Custer and Fremont Counties, Colorado. Technical Report 649, U.S. Geological Survey Professional Paper.

Penman, D. E. (2016). Silicate weathering and North Atlantic silica burial during the Paleocene-Eocene thermal maximum. *Geology*, 44(9):731–734.

Penman, D. E., Rugenstein, J. K. C., Ibarra, D. E., and Winnick, M. J. (2020). Silicate weathering as a feedback and forcing in Earth's climate and carbon cycle. *Earth-Science Reviews*, 209:103298.

Penman, D. E., Turner, S. K., Sexton, P. F., Norris, R. D., Dickson, A. J., Boulila, S., Ridgwell, A., Zeebe, R. E., Zachos, J. C., Cameron, A., et al. (2016). An abyssal carbonate compensation depth overshoot in the aftermath of the Palaeocene–Eocene Thermal Maximum. *Nature Geoscience*, 9(8):575–580.

Peucker-Ehrenbrink, B. and Ravizza, G. (2000). The marine osmium isotope record. *Terra Nova*, 12(5):205–219.

Pistiner, J. S. and Henderson, G. M. (2003). Lithium-isotope fractionation during continental weathering processes. *Earth and Planetary Science Letters*, 214(1-2):327–339.

Pogge von Strandmann, P. A., Burton, K. W., James, R. H., Calsteren, P. v., and Gislason, S. R. (2010). Assessing the role of climate on uranium and lithium isotope behaviour in rivers draining a basaltic terrain. *Chemical Geology*, 270(1-4):227–239.

Pogge von Strandmann, P. A., Burton, K. W., James, R. H., Calsteren, P. v., Gíslason, S. R., and Mokadem, F. (2006). Riverine behaviour of uranium and lithium isotopes in an actively glaciated basaltic terrain. *Earth and Planetary Science Letters*, 251(1-2):134–147.

Pogge von Strandmann, P. A., Burton, K. W., Opfergelt, S., Eiríksdóttir, E. S., Murphy, M. J., Einarsson, A., and Gislason, S. R. (2016). The effect of hydrothermal spring weathering processes and primary productivity on lithium isotopes: Lake Myvatn, Iceland. *Chemical Geology*, 445:4–13.

Pogge von Strandmann, P. A., Fraser, W. T., Hammond, S. J., Tarbuck, G., Wood, I. G., Oelkers, E. H., and Murphy, M. J. (2019). Experimental determination of Li isotope behaviour during basalt weathering. *Chemical Geology*, 517:34–43.

Pogge von Strandmann, P. A., Frings, P. J., and Murphy, M. J. (2017a). Lithium isotope behaviour during weathering in the Ganges Alluvial Plain. *Geochimica et Cosmochimica Acta*, 198:17–31.

Pogge von Strandmann, P. A. and Henderson, G. M. (2015). The Li isotope response to mountain uplift. *Geology*, 43(1):67–70.

Pogge von Strandmann, P. A., Vaks, A., Bar-Matthews, M., Ayalon, A., Jacob, E., and Henderson, G. M. (2017b). Lithium isotopes in speleothems: Temperature-controlled variation in silicate weathering during glacial cycles. *Earth and Planetary Science Letters*, 469:64–74.

Pogge von Strandmann, P. A. E., Desrochers, A., Murphy, M. J., Finlay, A. J., Selby, D., and Lenton, T. M. (2017c). Global climate stabilisation by chemical weathering during the Hirnantian glaciation. *Geochemical Perspectives Letters*, pages 230–237.

Pogge von Strandmann, P. A. E., Jenkyns, H. C., and Woodfine, R. G. (2013). Lithium isotope evidence for enhanced weathering during Oceanic Anoxic Event 2. *Nature Geoscience*, 6(8):668–672.

Pogge von Strandmann, P. A. E., Kasemann, S. A., and Wimpenny, J. B. (2020). Lithium and Lithium Isotopes in Earth's Surface Cycles. *Elements*, 16(4):253–258.

Portenga, E. W. and Bierman, P. R. (2011). Understanding Earth's eroding surface with 10Be. *GSA Today*, 21(8):4–10.

Pujalte, V., Baceta, J., and Schmitz, B. (2015). A massive input of coarse-grained siliciclastics in the Pyrenean Basin during the PETM: the missing ingredient in

a coeval abrupt change in hydrological regime. *Climate of the Past*, 11(12):1653–1672.

Pyles, D. R., Straub, K. M., and Stammer, J. G. (2013). Spatial variations in the composition of turbidites due to hydrodynamic fractionation. *Geophysical Research Letters*, 40(15):3919–3923.

Rad, S., Rivé, K., Vittecoq, B., Cerdan, O., and Allègre, C. J. (2013). Chemical weathering and erosion rates in the Lesser Antilles: An overview in Guadeloupe, Martinique and Dominica. *Journal of South American Earth Sciences*, 45:331–344.

Rae, J. W., Zhang, Y. G., Liu, X., Foster, G. L., Stoll, H. M., and Whiteford, R. D. (2021). Atmospheric $CO_2$ over the Past 66 Million Years from Marine Archives. *Annual Review of Earth and Planetary Sciences*, 49.

Rasmussen, D. M. (2016). Depositional Environments and Provenance of Early Paleogene Strata in the Huerfano Basin: Implications for Uplift of the Wet Mountains, Colorado, USA. Master's thesis, Western Washington University.

Rasmussen, D. M. and Foreman, B. Z. (2017). Provenance of lower Paleogene strata in the Huerfano Basin: Implications for uplift of the Wet Mountains, Colorado, USA. *Journal of Sedimentary Research*, 87(6):579–593.

Rasmussen, D. M., Foreman, B. Z., Fricke, H. C., Snell, K., Gipson, L., and Housen, B. (2020). The early Paleogene stratigraphic evolution of the Huerfano Basin, Colorado. *Rocky Mountain Geology*, 55(1):1–26.

Ravizza, G., Norris, R., Blusztajn, J., and Aubry, M.-P. (2001). An osmium isotope excursion associated with the late Paleocene thermal maximum: Evidence of intensified chemical weathering. *Paleoceanography*, 16(2):155–163.

Raymo, M. E. and Ruddiman, W. F. (1992). Tectonic forcing of late cenozoic climate. *Nature*, 359(6391):117–122.

Riebe, C. S., Hahm, W. J., and Brantley, S. L. (2017). Controls on deep critical zone architecture: a historical review and four testable hypotheses. *Earth Surface Processes and Landforms*, 42(1):128–156.

Robinson, P. (1966). *Fossil Mammalia of the Huerfano Formation, Eocene, of Colorado*, volume 21. Peabody Museum of Natural History, Yale University.

Romans, B. W., Castelltort, S., Covault, J. A., Fildani, A., and Walsh, J. (2016). Environmental signal propagation in sedimentary systems across timescales. *Earth-Science Reviews*, 153:7–29.

Rudnick, R. and Gao, S. (2003). Composition of the continental crust. *Treatise on Geochemistry*, 3:1–64.

Rugenstein, J. K. C., Ibarra, D. E., and Blanckenburg, F. v. (2019). Neogene cooling driven by land surface reactivity rather than increased weathering fluxes. *Nature*, 571(7763):99–102.

Rush, W. D., Kiehl, J. T., Shields, C. A., and Zachos, J. C. (2021). Increased frequency of extreme precipitation events in the North Atlantic during the PETM: Observations and theory. *Palaeogeography, Palaeoclimatology, Palaeoecology*, 568:110289.

Ryu, J.-S., Vigier, N., Lee, S.-W., Lee, K.-S., and Chadwick, O. A. (2014). Variation of lithium isotope geochemistry during basalt weathering and secondary mineral transformations in Hawaii. *Geochimica et Cosmochimica Acta*, 145:103–115.

Sauzéat, L., Rudnick, R. L., Chauvel, C., Garçon, M., and Tang, M. (2015). New perspectives on the Li isotopic composition of the upper continental crust and its weathering signature. *Earth and Planetary Science Letters*, 428:181–192.

Schmitt, A.-D., Vigier, N., Lemarchand, D., Millot, R., Stille, P., and Chabaux, F. (2012). Processes controlling the stable isotope compositions of Li, B, Mg and Ca in plants, soils and waters: A review. *Comptes Rendus Geoscience*, 344(11-12):704–722.

Self-Trail, J. M., Powars, D. S., Watkins, D. K., and Wandless, G. A. (2012). Calcareous nannofossil assemblage changes across the Paleocene–Eocene Thermal Maximum: Evidence from a shelf setting. *Marine Micropaleontology*, 92:61–80.

Sewall, J. O. and Sloan, L. C. (2006). Come a little bit closer: A high-resolution climate study of the early Paleogene Laramide foreland. *Geology*, 34(2):81–84.

Sharman, G. R., Covault, J. A., Stockli, D. F., Wroblewski, A. F.-J., and Bush, M. A. (2017). Early Cenozoic drainage reorganization of the United States Western Interior–Gulf of Mexico sediment routing system. *Geology*, 45(2):187–190.

Small, E. E., Blom, T., Hancock, G. S., Hynek, B. M., and Wobus, C. W. (2015). Variability of rock erodibility in bedrock-floored stream channels based on abrasion mill experiments. *Journal of Geophysical Research: Earth Surface*, 120(8):1455–1469.

Smith, J. J., Hasiotis, S. T., Kraus, M. J., and Woody, D. T. (2008). Relationship of Floodplain Ichnocoenoses to Paleopedology, Paleohydrology, and Paleoclimate in the Willwood Formation, Wyoming, During the Paleoceneeocene Thermal Maximum. *PALAIOS*, 23(10):683–699.

Snell, K. E., Thrasher, B. L., Eiler, J. M., Koch, P. L., Sloan, L. C., and Tabor, N. J. (2013). Hot summers in the Bighorn Basin during the early Paleogene. *Geology*, 41(1):55–58.

Steefel, C. I. and Maher, K. (2009). Fluid-rock interaction: A reactive transport approach. *Reviews in mineralogy and geochemistry*, 70(1):485–532.

Tarboton, D. G., Bras, R. L., and Rodriguez-Iturbe, I. (1991). On the extraction of channel networks from digital elevation data. *Hydrological processes*, 5(1):81–100.

Tardy, Y., Krempp, G., and Trauth, N. (1972). Le lithium dans les minéraux argileux des sédiments et des sols. *Geochimica et Cosmochimica Acta*, 36(4):397–412.

Teng, F.-Z., McDonough, W., Rudnick, R., Dalpé, C., Tomascak, P., Chappell, B., and Gao, S. (2004). Lithium isotopic composition and concentration of the upper continental crust. *Geochimica et Cosmochimica Acta*, 68(20):4167–4178.

Thomas, L. E. (1965). Sedimentation and structural development of Big Horn basin. *AAPG Bulletin*, 49(11):1867–1877.

Tipper, E. T., Stevenson, E. I., Alcock, V., Knight, A. C. G., Baronas, J. J., Hilton, R. G., Bickle, M. J., Larkin, C. S., Feng, L., Relph, K. E., and Hughes, G. (2021). Global silicate weathering flux overestimated because of sediment–water cation exchange. *Proceedings of the National Academy of Sciences*, 118(1):e2016430118.

Tomascak, P. B., Magna, T., and Dohmen, R. (2016). *Advances in lithium isotope geochemistry*. Springer.

Torfstein, A., Winckler, G., and Tripati, A. (2010). Productivity feedback did not terminate the Paleocene-Eocene Thermal Maximum (PETM). *Climate of the Past*, 6(2):265–272.

Torres, M. A., Kemeny, P. C., Lamb, M. P., Cole, T. L., and Fischer, W. W. (2020). Long-Term Storage and Age-Biased Export of Fluvial Organic Carbon: Field Evidence From West Iceland. *Geochemistry, Geophysics, Geosystems*, 21(4).

Torres, M. A., Limaye, A. B., Ganti, V., Lamb, M. P., West, A. J., and Fischer, W. W. (2017). Model predictions of long-lived storage of organic carbon in river deposits. *Earth Surface Dynamics*, 5(4):711–730.

Torres, M. A., West, A. J., Clark, K. E., Paris, G., Bouchez, J., Ponton, C., Feakins, S. J., Galy, V., and Adkins, J. F. (2016). The acid and alkalinity budgets of weathering in the Andes–Amazon system: Insights into the erosional control of global biogeochemical cycles. *Earth and Planetary Science Letters*, 450:381–391.

Tune, A. K., Druhan, J. L., Wang, J., Bennett, P. C., and Rempe, D. M. (2020). Carbon Dioxide Production in Bedrock Beneath Soils Substantially Contributes to Forest Carbon Cycling. *Journal of Geophysical Research: Biogeosciences*, 125(12).

Urey, H. C. (1952). The planets: their origin and development. *Mrs. Hepsa Ely Silliman Memorial Lectures*.

van der Meulen, B., Gingerich, P. D., Lourens, L. J., Meijer, N., Broekhuizen, S. v., Ginneken, S. v., and Abels, H. A. (2020). Carbon isotope and mammal recovery from extreme greenhouse warming at the Paleocene–Eocene boundary in astronomically-calibrated fluvial strata, Bighorn Basin, Wyoming, USA. *Earth and Planetary Science Letters*, 534:116044.

Van Gosen, B. S. (2020). Whole-rock geochemical data for alkaline intrusive rocks in the Wet Mountains area of Custer and Fremont Counties, south-central Colorado, USA. =https://doi.org/10.5066/P99YBJLX.

Verdin, K., Hall, F., Collatz, G., Meeson, B., Los, S., Brown de Colstoun, E., and Landis, D. (2011). ISLSCP II HYDRO1k elevation-derived products. *ORNL DAAC*.

Vigier, N., Decarreau, A., Millot, R., Carignan, J., Petit, S., and France-Lanord, C. (2008). Quantifying Li isotope fractionation during smectite formation and implications for the Li cycle. *Geochimica et Cosmochimica Acta*, 72(3):780–792.

Vigier, N., Gislason, S., Burton, K., Millot, R., and Mokadem, F. (2009). The

relationship between riverine lithium isotope composition and silicate weathering rates in Iceland. *Earth and Planetary Science Letters*, 287(3-4):434–441.

Vigier, N. and Goddéris, Y. (2015). A new approach for modeling Cenozoic oceanic lithium isotope paleo-variations: the key role of climate. *Climate of the Past*, 11(4):635–645.

Walker, J. C., Hays, P., and Kasting, J. F. (1981). A negative feedback mechanism for the long-term stabilization of earth's surface temperature. *Journal of Geophysical Research: Oceans*, 86(C10):9776–9782.

Wang, C., Adriaens, R., Hong, H., Elsen, J., Vandenberghe, N., Lourens, L. J., Gingerich, P. D., and Abels, H. A. (2017). Clay mineralogical constraints on weathering in response to early Eocene hyperthermal events in the Bighorn Basin, Wyoming (Western Interior, USA). *GSA Bulletin*, 129(7-8):997–1011.

Wang, Q.-L., Chetelat, B., Zhao, Z.-Q., Ding, H., Li, S.-L., Wang, B.-L., Li, J., and Liu, X.-L. (2015). Behavior of lithium isotopes in the Changjiang River system: Sources effects and response to weathering and erosion. *Geochimica et Cosmochimica Acta*, 151:117–132.

Wanner, C., Sonnenthal, E. L., and Liu, X.-M. (2014). Seawater $\delta^7$Li: A direct proxy for global $CO_2$ consumption by continental silicate weathering? *Chemical Geology*, 381:154–167.

Washington, K. E., West, A. J., Kalderon-Asael, B., Katchinoff, J. A., Stevenson, E. I., and Planavsky, N. J. (2020). Lithium isotope composition of modern and fossilized Cenozoic brachiopods. *Geology*, 48(11):1058–1061.

West, A. J. (2012). Thickness of the chemical weathering zone and implications for erosional and climatic drivers of weathering and for carbon-cycle feedbacks. *Geology*, 40(9):811–814.

West, A. J., Galy, A., and Bickle, M. (2005). Tectonic and climatic controls on silicate weathering. *Earth and Planetary Science Letters*, 235(1-2):211–228.

Westerhold, T., Marwan, N., Drury, A. J., Liebrand, D., Agnini, C., Anagnostou, E., Barnet, J. S., Bohaty, S. M., De Vleeschouwer, D., Florindo, F., et al. (2020). An astronomically dated record of Earth's climate and its predictability over the last 66 million years. *Science*, 369(6509):1383–1387.

Weynell, M., Wiechert, U., and Schuessler, J. A. (2017). Lithium isotopes and implications on chemical weathering in the catchment of Lake Donggi Cona, northeastern Tibetan Plateau. *Geochimica et Cosmochimica Acta*, 213:155–177.

Whalley, C. and Grant, A. (1994). Assessment of the phase selectivity of the European Community Bureau of Reference (BCR) sequential extraction procedure for metals in sediment. *Analytica Chimica Acta*, 291(3):287–295.

Whipple, K. X. (2009). The influence of climate on the tectonic evolution of mountain belts. *Nature Geoscience*, 2(2):97–104.

White, A. and Buss, H. (2014). Natural weathering rates of silicate minerals. *Treatise on Geochemistry, Second Edition. Elsevier, Oxford*, pages 115–155.

Wimpenny, J., Gíslason, S. R., James, R. H., Gannoun, A., Pogge von Strandmann, P. A., and Burton, K. W. (2010). The behaviour of Li and Mg isotopes during primary phase dissolution and secondary mineral formation in basalt. *Geochimica et Cosmochimica Acta*, 74(18):5259–5279.

Wing, S. L. and Harrington, G. J. (2001). Floral response to rapid warming in the earliest eocene and implications for concurrent faunal change. *Paleobiology*, 27(3):539–563.

Wing, S. L., Harrington, G. J., Smith, F. A., Bloch, J. I., Boyer, D. M., and

Freeman, K. H. (2005). Transient Floral Change and Rapid Global Warming at the Paleocene-Eocene Boundary. *Science*, 310(5750):993–996.

Winnick, M., Druhan, J. L., and Maher, K. (2019). Weathering Regimes and Lithium Isotope Signals of Mineral Dissolution and Precipitation: A Reactive Transport Perspective. In *AGU Fall Meeting Abstracts*, volume 2019, pages U21A–02.

Winnick, M. J. and Maher, K. (2018). Relationships between $CO_2$, thermodynamic limits on silicate weathering, and the strength of the silicate weathering feedback. *Earth and Planetary Science Letters*, 485:111–120.

Witherow, R. A., Lyons, W. B., and Henderson, G. M. (2010). Lithium isotopic composition of the McMurdo Dry Valleys aquatic systems. *Chemical Geology*, 275(3-4):139–147.

Wolfe, J. A. and Upchurch, G. R. (1987). Leaf assemblages across the Cretaceous-Tertiary boundary in the Raton Basin, New Mexico and Colorado. *Proceedings of the National Academy of Sciences*, 84(15):5096–5100.

Zachos, J., Pagani, M., Sloan, L., Thomas, E., and Billups, K. (2001). Trends, Rhythms, and Aberrations in Global Climate 65 Ma to Present. *Science*, 292(5517):686–693.

Zhang, J.-W., Zhao, Z.-Q., Yan, Y.-N., Cui, L.-F., Wang, Q.-L., Meng, J.-L., Li, X.-D., and Liu, C.-Q. (2021). Lithium and its isotopes behavior during incipient weathering of granite in the eastern Tibetan Plateau, China. *Chemical Geology*, 559:119969.

# Vita

Evan was born in Glen Cove, New York, raised in Bay Shore, New York, and did most of his schooling in Bethpage, New York, eating lots of everything bagels and rooting for bad professional sports franchises along the way. His fondest memories almost exclusively involve the beach (Field 3 at Robert Moses, always) and the long bike rides he did with his friends along the Bethpage bike path to Jones Beach. After graduating high school in 2011, he enrolled in Boston University where he would switch into a Geophysics & Planetary Sciences degree track after a brief stint as an engineering major. Attending his Mineralogy professor's running office hours in 2013 fundamentally changed his trajectory and outlook, leading to a deep interest in unpacking Earth's complicated past and preserving its future. He would graduate in 2015, enroll as a Master's student at UT-Austin, and then re-enroll as a PhD student in 2017 after completing his MS. His research interests evolved immensely over his six years at UT; he even considered studying gar scales. After graduation, he will begin a postdoctoral fellowship at Rice University and stumble into a whole new set of research (and life) problems. If not working, he's likely on a run, listening to shoegaze, or wishing he could talk about music with anyone that will listen.

This dissertation was typeset with LaTeX $2_\varepsilon$[1] by the author.

[1] LaTeX $2_\varepsilon$ is an extension of LaTeX. LaTeX is a collection of macros for TeX. TeX is a trademark of the American Mathematical Society. The macros used in formatting this dissertation were written by Dinesh Das, Department of Computer Sciences, The University of Texas at Austin, and extended by Bert Kay, James A. Bednar, Ayman El-Khashab, Gus Kivotidis, J.J. Muñoz, Alex Toto, Andrew Flanagan, Margaux Mango, Nicole Warner, and Sean Creamer.